Experimental and numerical investigation of moisture effects on bending behaviors and damage mechanisms of composite sandwich structures by acoustic emission and infraRed thermography

Yuan Wu

Université Fédérale
Toulouse Midi-Pyrénées

THÈSE

En vue de l'obtention du

DOCTORAT DE L'UNIVERSITÉ DE TOULOUSE

Délivré par l'Université Toulouse 3 - Paul Sabatier

Présentée et soutenue par

YUAN WU

Le 5 juillet 2022

Experimental and Numerical Investigation of Moisture Effects on Bending Behaviors and Damage Mechanisms of Composite Sandwich Structures by Acoustic Emission and InfraRed Thermography

Ecole doctorale : **MEGEP - Mécanique, Energétique, Génie civil, Procédés**

Spécialité : **Génie mécanique, mécanique des matériaux**

Unité de recherche:
ICA - Institut Clément Ader

Thèse dirigée par
Xiaojing GONG, Marie-laetitia PASTOR et Marianne PERRIN

Jury

Mme Nathalie GODIN	**McF-HDR, INSA Lyon**	**Rapporteure**
M.Jean-Claude GRANDIDIER	**Professeur, ISAE ENSMA Poitier**	**Rapporteur**
M.Olivier SICOT	**Professeur, ISAT UB**	**Examinateur**
M.Pascal CASARI	**Professeur, Université de Nantes**	**Examinateur invité**
Mme Xiaojing GONG	**Professeur, Université Toulouse III**	**Directrice de thèse**
Mme Marie-Laetitia PASTOR	**McF, Université Toulouse III**	**Co-directrice de thèse**
Mme Marianne PERRIN	**McF, Université Toulouse III**	**Co-directrice de thèse**

Acknowledgements

Firstly, I would like to express my sincere gratitude to my supervisors Prof. Xiaojing Gong, Dr. Marie-Laetitia Pastor and Dr. Marianne Perrin for their support and help of my Ph.D thesis. Without them, I cannot finish all the related research work very well. I am really grateful for their guidance, motivation and patience in the theoretical analysis and experimental investigations. During the past three years, I have learned from them that curiosity, pursuit of knowledge and understanding will be always a strong drive in my study and life. Thanks to all of them, I have lived a very happy, fulfilling and meaningful life during my whole Ph.D in France.

I would also like to express my sincere appreciation to Prof. Pascal Casari for his support in offering all the sandwich materials, fabricating all the sandwich specimens and proposing the new ideas about the experimental configurations in my thesis.

I also want to express my sincere gratitude to Dr. Nathalie Godin, Prof. Jean-Claude Grandidier and Prof. Olivier Sicot for their willingness to be the reviewers of my thesis and the members of the jury.

My sincere thanks also go to Mr. Frederic Leroy, Prof. Florent Eyma and Dr. Rémi Curti for their kind help of fabricating the specimens and dealing with the problems of machines in the experiments.

I also thank very much my colleagues in the lab for the discussions of the research, for their accompany in the past three years, especially during the period of Covid-19. They have given me a lot of encouragement and kindness which have motivated me.

I also thank the China Scholarship Council for financial support for three years to cover all my living cost in France. I am really grateful for Education Section of the Embassy of the People's Republic of China in the French Republic, “Union des Chercheurs et des Etudiants Chinois en France”, Université Toulouse III, IUT Tarbes, IUT Saint-Nazaire, Tarbes local government, local friendly citizens and all the Chinese people and students in Tarbes for all their support and assistance.

Last but not least, I would like to thank my close family members and friends for supporting me spiritually throughout writing this thesis. They are always the drive of power in my life.

The research work never ends, and I will continue my pursuit of the science with the love of all the nice people I have met in my life. Many thanks for all encounters.

Contents

Abstract 1
Résumé 3
General Introduction 5
Chapter 1. Literature Review 9
1.1. Introduction 11
1.2. Overviews of balsa/honeycomb sandwich structures 11
1.2.1. Constituents of composite sandwich structures 11
1.2.2. Applications of balsa/honeycomb sandwich structures 16
1.2.3. Fabrication process of balsa/honeycomb sandwich structures 18
1.2.4. Challenges and perspectives of balsa/honeycomb sandwich structures 20
1.3. Damage mechanisms of balsa/honeycomb sandwich structures under bending load 21
1.3.1. Theoretical sandwich theory 21
1.3.2. Damage mechanisms of sandwich structures 22
1.3.3. Moisture effects on damage mechanisms of sandwich structures 27
1.3.4. Conclusions and challenges 31
1.4. NDT techniques for monitoring damage mechanisms of sandwich structures 32
1.4.1. Overviews of NDT techniques for composite structures 32
1.4.2. Monitoring damages by Acoustic Emission (AE) 33
1.4.3. Monitoring damages by InfraRed Thermography (IRT) 44
1.4.4. Coupling of AE and IRT techniques 52
1.5. Numerical analysis of bending behaviors of balsa/honeycomb sandwich structures 55
1.5.1. Finite Element Modeling (FEM) of balsa/honeycomb sandwich structures 55
1.5.2. Damage models for laminated skins 56
1.5.3. Damage models for balsa/honeycomb cores 59
1.6. Chapter summary 62
Chapter 2. Preliminary tests monitored by AE and IRT on dry and wet sandwiches 64

2.1. Introduction 67
2.2. Materials and specimens 67
2.2.1. Material properties 67
2.2.2. Fabrication process 68
2.2.3. Specimen cutting and geometries of specimens 71
2.3. Characterization of AE wave propagation properties in sandwich panels 73
2.3.1. Characterization of AE wave velocity in sandwich panels 73
2.3.2. Characterization of AE attenuation properties in sandwich panels 89
2.4. Moisture effects on preliminary AE and IRT signals 93
2.4.1. Moisture absorption tests monitored by active AE and IRT methods 93
2.4.2. Moisture absorption behaviors 95
2.4.3. Moisture effects on AE wave propagation properties 99
2.4.4. Moisture effects on temperature variation rate in active IRT tests 105
2.5. Chapter summary 109
Chapter 3. Static 4-point bending behaviors of GFRP-balsa sandwich 112
3.1. Introduction 114
3.2. Static 4-point bending tests monitored by AE and IRT 114
3.2.1. Experimental setup 114
3.2.2. Moisture effects on bending behaviors 116
3.2.3. Moisture effects on damage mechanisms observed by microscope 120
3.2.4. Moisture effects on damage initiation and evolution monitored by IRT 125
3.2.5. Moisture effects on damage characterization by AE 130
3.2.6. Experimental conclusions 147
3.3. Numerical analysis of 4-point bending behaviors 147
3.3.1. Abaqus model establishment 147
3.3.2. Progressive Damage Analysis (PDA) model 149

3.3.3. Prediction of 4-point bending behaviors by PDA model 150
3.3.4. Numerical conclusions 163
3.4. Chapter summary 164
Chapter 4. Static 4-point bending behaviors of CFRP-honeycomb sandwich 167
4.1. Introduction 169
4.2. Static 4-point bending tests monitored by AE and IRT 169
4.2.1. Experimental setup 169
4.2.2. Moisture effects on bending behaviors 170
4.2.3. Damage mechanisms observed by microscope 172
4.2.4. Damage localizations by IRT and AE 175
4.2.5. Moisture effects on damage initiation identification by AE 188
4.2.6. Experimental conclusions 191
4.3. Numerical analysis of 4-point bending behaviors 191
4.3.1. Abaqus model establishment 191
4.3.2. Equivalent elastic-plastic and shear damage model 193
4.3.3. Prediction of 4-point bending behaviors 195
4.3.4. Numerical conclusions 205
4.4. Chapter summary 205
Conclusions and Perspectives 207
References 210
Annex 1 225
Annex 2 226
Relevant Publications 233

List of Figures

Fig. 1-1. Presentation of the short and long fiber reinforced composite [1]..... 12

Fig. 1-2. Constituents of a typical honeycomb sandwich structure [6]. 12

Fig. 1-3. Micrographs of balsa wood and the three types of cells [22]. 15

Fig. 1-4. Hexagonal honeycomb cells in L and W directions [26-27]. 15

Fig. 1-5. Schematic of a pyramidal lattice truss core sandwich panel [20]. 16

Fig. 1-6. GFRP-balsa sandwich applied in the ship hull [38]. 17

Fig. 1-7. CFRP-honeycomb sandwich applications in the aircraft A380 [39]. 17

Fig. 1-8. BALTEK® SB balsa panels from 3A Composites Core Materials [46]. 19

Fig. 1-9. Expansion process of the honeycomb panel [50]. 20

Fig. 1-10. Stress distributions of bending and shear stresses in a sandwich beam [58]. 21

Fig. 1-11. Damage modes of CFRP-balsa sandwich under 3-point bending: a) Failure modes; Fracture area (magnification 25X): b) upper skin; c) balsa core; d) lower skin [56]. 23

Fig. 1-12. 4-point bending behaviors and damage modes of GFRP-balsa sandwich [70]. 24

Fig. 1-13. 3-point bending force-displacement curve of Aluminum-Nomex honeycomb sandwich [73]. 25

Fig. 1-14. Damage modes of CFRP-honeycomb sandwich under static 3-point loading [74]..25

Fig. 1-15. Damage modes of Aluminum-honeycomb sandwich under static 4-point loading [75]. 26

Fig. 1-16. Damage modes of Nomex honeycomb sandwich under static 4-point loading [76]. 26

Fig. 1-17. Moisture effects on fiber/matrix interface of composite laminates [78]..... 27

Fig. 1-18. Normalized compressive property change after immersion in sea and tap water [55]. 28

Fig. 1-19. Rate curves of moisture absorption and liberation of two fibers [82]. 29

Fig. 1-20. Variation of hygroscopic stresses through the thickness of the sandwich plate [36]. 30

Fig. 1-21. Dry (gray) and wet (black) interfacial fracture properties of different DCB sandwich beams [85]. 31

Fig. 1-22. Experimental setup of AE system under 4-point bending loading [100]..... 34

Fig. 1-23. Characteristics of one hit of acoustic emission wave [104]..... 34

Fig. 1-24. An example of iteration procedure of K-means algorithm [112]. 37

Fig. 1-25. Damage initiation detection in glass/epoxy DCB specimen by different AE parameters [104]..... 40

Fig. 1-26. Compression response and AE cumulative counts of glass/epoxy composite laminates [117]. 41

Fig. 1-27. Linear source location by two sensors [124]. 42

Fig. 1-28. Active Lock-in IRT system heated by halogen lamps [133]. 45

Fig. 1-29. Radiation received by the IR camera [135]. 46

Fig. 1-30. Moisture detection setup by active IRT for honeycomb panel in reflection mode [148]. 50

Fig. 1-31. Temperature change rates of water filled and dry honeycomb panels [148]. 50

Fig. 1-32. Three moisture detection directions using active IRT method [140]. 51

Fig. 1-33. Experimental setup in the 4-point bending fracture test monitored by passive IRT [162]. 52

Fig. 1-34. Three damage evolution stages of Glass/Epoxy during bending fatigue by IRT and AE [141]..... 54

Fig. 1-35. Global and local material coordinates of honeycomb panel [73]. 55

Fig. 1-36. 3D stress components and orthogonal material directions for a timber element [171]. 56

Fig. 1-37. Bilinear traction-separation law of damage evolution criterion in Abaqus [172]. .. 58

Fig. 1-38. Bilinear constitutive law of representative cohesive element [177]. 59

Fig. 1-39. Crack propagation in wood and basic fracture modes [182]. 60

Fig. 2-1. The two kinds of sandwich panels..... 68

Fig. 2-2. Schematic of vacuum bag molding of composite laminates..... 69

Fig. 2-3. 3-layer CFRP laminated skin before curing. 69

Fig. 2-4. Bonding of cured CFRP skin and honeycomb core..... 70

Fig. 2-5. Co-curing process of GFRP-balsa sandwich panel..... 71

Fig. 2-6. Geometry shape of triple dog-bone GFRP-balsa sandwich specimens. 73

Fig. 2-7. Geometry shape of triple dog-bone CFRP-honeycomb sandwich specimens. 73

Fig. 2-8. Positions of the sensors and source (in 0^o direction) on the tested sandwich panels. 74

Fig. 2-9. AE timing parameters of the waveform signals [107]. 75

Fig. 2-10. Positions of sensors and source on the tested panel between 0^o and 90^o. 76

Fig. 2-11. Influence of sensor distance on measured AE wave velocities in [0^o/90^o/0^o] CFRP panel. 78

Fig. 2-12. Measured AE wave velocities and calculated values in [0^o/90^o/0^o] CFRP panel. ... 78

Fig. 2-13. Influence of sensor distance on measured AE wave velocities in CFRP-honeycomb sandwich A. 79

Fig. 2-14. Measured AE wave velocities and calculated values in CFRP-honeycomb sandwich A. 80

Fig. 2-15. Measured AE wave velocities in sandwich A and CFRP skin panel. 81

Fig. 2-16. Correlation ratio of AE wave velocity in CFRP-honeycomb sandwich A over that in the skin. 83

Fig. 2-17. Measured AE wave velocities in different CFRP-honeycomb sandwich panels..... 83

Fig. 2-18. Correlation ratio of AE wave velocity in CFRP-honeycomb sandwiches over that in the skins. 85

Fig. 2-19. Influence of sensor distance on measured AE wave velocities in 3-layer woven GFRP panel. 85

Fig. 2-20. Measured AE wave velocities and calculated values in 3-layer woven GFRP panel. 86

Fig. 2-21. Influence of sensor distance on measured AE wave velocities in GFRP-balsa sandwich panel. 87

Fig. 2-22. Measured AE wave velocities and calculated values in GFRP-balsa sandwich panel. 87

Fig. 2-23. Comparison of acoustic wave velocities in GFRP-balsa sandwich, GFRP skin and balsa core. 88

Fig. 2-24. Correlation ratio of AE wave velocity in GFRP-balsa sandwich over that in the skin. 89

Fig. 2-25. AE attenuation properties in 3-layer CFRP skin along different directions. 90

Fig. 2-26. AE attenuation properties in CFRP-honeycomb sandwich panel A along different directions. 91

Fig. 2-27. AE attenuation properties in 3-layer GFRP panel along different directions. 92

Fig. 2-28. AE attenuation properties in GFRP-balsa sandwich and pure balsa panels. 92

Fig. 2-29. AE Hsu-Nielsen test setup for monitoring moisture effects on sandwich structures. 94

Fig. 2-30. Experimental setup of active reflection IRT tests. 95

Fig. 2-31. Moisture absorption behavior of GFRP-balsa sandwich specimens. 97

Fig. 2-32. Moisture absorption behavior of CFRP-honeycomb sandwich specimens. 98

Fig. 2-33. Correlations between AE wave velocity and MC of GFRP-balsa sandwich. 100

Fig. 2-34. Correlations between AE attenuation and MC of GFRP-balsa sandwich. 102

Fig. 2-35. Moisture effects on attenuation coefficient of GFRP-balsa sandwich. 103

Fig. 2-36. Correlations between AE wave velocity and MC of CFRP-honeycomb sandwich. 104

Fig. 2-37. Correlation between AE attenuation and MC of CFRP-honeycomb sandwich. 105

Fig. 2-38. Moisture effects on attenuation coefficient of CFRP-honeycomb sandwich. 105

Fig. 2-39. Moisture effects on active IRT test of GFRP-balsa sandwich. 107

Fig. 2-40. Moisture effects on active IRT test of CFRP-honeycomb sandwich. 108

Fig. 3-1. 4-point bending test setup monitored by AE and IRT techniques. 115

Fig. 3-2. Static 4-point bending behaviors of GFRP-balsa sandwich specimens. 117

Fig. 3-3. Interfaces of balsa blocks in dry and wet GFRP-balsa sandwich specimens. 117

Fig. 3-4. Comparison of fracture surfaces of wet and dry GFRP-balsa sandwich specimens. 120

Fig. 3-5. Moisture effects on microscope images of 50% MC specimen Wet 2 before 4-point bending tests. 121

Fig. 3-6. Upper skin damage images of dry and wet specimens after 4-point bending tests. 122

Fig. 3-7. Skin/core damage images of dry and wet specimens after 4-point bending tests.... 124

Fig. 3-8. Cumulative heat source (J/m^3) field images and damage photos of specimen Dry 1. 128

Fig. 3-9. Cumulative heat source (J/m^3) field images and damage photos of 50% MC specimen Wet 2. 129

Fig. 3-10. Cumulative heat source (J/m^3) field images and damage photos of 120% MC specimen Wet 5. 130

Fig. 3-11. Moisture effects on cumulative hits number of GFRP-balsa sandwich. 131

Fig. 3-12. Moisture effects on cumulative energy of GFRP-balsa sandwich. 131

Fig. 3-13. Damage localizations in dry and wet GFRP-balsa sandwiches by AE. 134

Fig. 3-14. DB and Tou coefficients of GFRP-balsa sandwiches in the first clustering process. 135

Fig. 3-15. Two clusters after first clustering process of dry and wet GFRP-balsa sandwiches. 138

Fig. 3-16. Peak frequency vs. Amplitude of Cluster 0 of dry and wet GFRP-balsa sandwiches. 139

Fig. 3-17. Duration vs. Amplitude of Cluster 0 of dry and wet GFRP-balsa sandwiches..... 139

Fig. 3-18. Cumulative counts of Cluster I vs. time of dry and wet GFRP-balsa sandwiches. 141

Fig. 3-19. DB and Tou coefficients of GFRP-balsa sandwiches in the second clustering process. 142

Fig. 3-20. AE amplitude distributions of dry and wet GFRP-balsa sandwiches. 143

Fig. 3-21. AE peak frequency distributions of dry and wet GFRP-balsa sandwiches. 144

Fig. 3-22. Peak frequency vs. Amplitude of dry and wet GFRP-balsa sandwiches. 145

Fig. 3-23. Duration vs. Amplitude of dry and wet GFRP-balsa sandwiches. 146

Fig. 3-24. Abaqus model of GFRP-balsa sandwich under 4-point bending. 148

Fig. 3-25. Comparison of bending stiffness of simulation and test results of GFRP-balsa sandwich. 151

Fig. 3-26. Numerical Force/Displacement curves and experimental curves of GFRP-balsa sandwich under 4-point bending. 154

Fig. 3-27. Damage evolution prediction of dry sandwich by Abaqus simulation model Dry S2. 156

Fig. 3-28. Damage evolution prediction of 50% MC wet sandwich by Abaqus model W50 S2. 156

Fig. 3-29. Damage evolution prediction of 120% MC wet sandwich by Abaqus model W120 S2. 157

Fig. 3-30. Stress distributions of dry sandwich by Abaqus model Dry S2. 159

Fig. 3-31. Stress distributions of 50% MC wet sandwich by Abaqus model W50 S2. 160

Fig. 3-32. Stress distributions of 120% MC wet sandwich by Abaqus model W120 S2. 161

Fig. 3-33. Stress distributions of lower skins of dry and wet sandwich models at the final fracture moment. 163

Fig. 4-1. 4-point bending test setup monitored by AE and IRT for CFRP-honeycomb sandwich. 170

Fig. 4-2. Static 4-point bending behaviors of CFRP-honeycomb sandwich specimens..... 171

Fig. 4-3. Honeycomb cell wall surfaces of dry and wet CFRP-honeycomb sandwich under bending. 173

Fig. 4-4. Core damage images of dry and wet CFRP-honeycomb sandwich after 4-point bending tests. 174

Fig. 4-5. Skin images of dry and wet CFRP-honeycomb sandwich after 4-point bending tests. 175

Fig. 4-6. Temperature variation (°C) images in CFRP-honeycomb sandwich specimen Dry H2. 177

Fig. 4-7. Temperature variation (°C) images in CFRP-honeycomb sandwich specimen Wet H1 (5.5% MC). 179

Fig. 4-8. Damage localizations of specimen Dry H2 by AE amplitude and IRT. 182

Fig. 4-9. Damage localizations of specimen Wet H1 (5.5% MC) by AE amplitude and IRT. 184

Fig. 4-10. Damage localizations (Unit of X position: m) of specimen Dry H2 by AE. 186

Fig. 4-11. Damage localizations (Unit of X position: m) of 5.5% MC specimen Wet H1 by AE. 188

Fig. 4-12. Cumulative hits number of dry and wet CFRP-honeycomb sandwiches. 189

Fig. 4-13. Cumulative energy of dry and wet CFRP-honeycomb sandwiches..... 190

Fig. 4-14. Cumulative counts of dry and wet CFRP-honeycomb sandwiches. 190

Fig. 4-15. Abaqus model of CFRP-honeycomb sandwich under 4-point bending..... 192

Fig. 4-16. Schematic diagram of elastic-plastic material with progressive damage [214]..... 193

Fig. 4-17. Damage degradation law as a function of plastic displacement in damage evolution model [164]. 195

Fig. 4-18. Comparison of simulation and test results of dry and wet CFRP-honeycomb sandwich. 197

Fig. 4-19. Damage evolution prediction of dry sandwich by Abaqus simulation model Dry HS1. 199

Fig. 4-20. Damage evolution prediction of wet sandwich by Abaqus simulation model Wet HS3. 200

Fig. 4-21. Stress distributions in zone 2 of dry sandwich by Abaqus simulation model Dry HS1. 202

Fig. 4-22. Stress distributions in zone 2 of wet sandwich by Abaqus simulation model Wet HS3. 204

Fig. 4-23. Stress variation of Cell 1 in zone 2 of dry sandwich by Abaqus simulation model Dry HS1..... 204

Fig. 4-24. Stress variation of Cell 2 in zone 2 of wet sandwich by Abaqus simulation model Wet HS3..... 205

List of Tables

Table 1-1. Advantages and limitations of different NDT techniques [88-92]..... 32

Table 1-2. Characteristics of AE parameters of composite sandwich structures [116-121]. ... 39

Table 1-3. Failure criteria and corresponding damage variables for wood material [69]. 61

Table 2-1. Material parameters of glass and carbon fibers for skins..... 68

Table 2-2. Equivalent material parameters of balsa wood for cores. 68

Table 2-3. Equivalent material parameters of honeycomb for cores..... 68

Table 2-4. Dimensions of GFRP-balsa sandwich panels. 72

Table 2-5. Dimensions of CFRP-honeycomb sandwich panels. 72

Table 2-6. AE acquisition parameters for all sandwiches in active Hsu-Nielsen tests [113]... 74

Table 2-7. IRT acquisition parameters for dry sandwich in active reflection tests. 95

Table 2-8. Material parameters of woven glass fiber skin of dry and wet GFRP-balsa sandwiches. 101

Table 2-9. Material parameters of carbon fiber skin of dry and wet CFRP-honeycomb sandwich. 104

Table 3-1. AE acquisition parameters for GFRP-balsa sandwiches under 4-point bending. . 115

Table 3-2. IRT acquisition parameters for GFRP-balsa sandwiches in 4-point bending tests. 116

Table 3-3. Average bending stiffness and fracture load of dry and wet GFRP-balsa sandwiches. 116

Table 3-4. Moisture effects on thermal coefficients of GFRP-balsa sandwich..... 125

Table 3-5. AE characteristics of dry GFRP-balsa sandwiches under 4-point bending. 146

Table 3-6. Dominance of different damage mechanisms of GFRP-balsa sandwiches under 4-point bending..... 147

Table 3-7. Strength values of dry and wet woven GFRP skin [212-213]. 152

Table 3-8. Fracture energy values of PDA models of dry and wet woven GFRP skin in Abaqus. 152

Table 4-1. AE acquisition parameters for CFRP-honeycomb sandwiches under 4-point bending. 170

Table 4-2. IRT acquisition parameters for CFRP-honeycomb sandwiches under 4-point bending. 170

Table 4-3. Groups of different fracture strain of dry honeycomb in Abaqus. 195

Table 4-4. Groups of different fracture energy of dry honeycomb in Abaqus. 195

Table 4-5. Different groups of fracture energy of wet honeycomb in Abaqus. 196

Nomenclature

D_b	bending stiffness of the sandwich	D_f	bending stiffness of the skin to its neutral axis
D_c	bending stiffness of the core	D_o	bending stiffness of the skin to the neutral axis of the entire sandwich
E_c	Young's modulus of the core	E_f	Young's modulus of the skin
h_f	thickness of the skin	h_c	thickness of the core
h_s	thickness of the sandwich	h	sum of thicknesses of the skin and the core
b	width of the sandwich beam	A	cross-section area of a sandwich beam
Q	shear stiffness of the sandwich	G	shear modulus of the core
σ_f	skin stress	M	bending moment of the sandwich
I_z	inertia moment of the sandwich	F	applied force
τ_c	core shear stress	L	distance between the two external supports
G_C	critical fracture energy	L_e	distance between the internal loadings and the external supports
R_{DB}	Davis-Bouldin validity index	Tou	Tou criterion index
k	class number	$d_{i/j/k}$	average distances within the class i, j and k
D_{ij}	distance between the class i and j	α_λ	spectral absorptance
ρ_λ	spectral reflectance	τ_λ	spectral transmittance
ε	emissivity	W_λ	power emitted per unit area per unit wavelength by a real body
$W_{\lambda b}$	power emitted per unit area per unit wavelength by a black body	W	power emitted per unit area per unit wavelength by an object
σ	Stefan-Boltzmann constant	T	temperature
ΔT	temperature difference	C_{tr}	temperature contrast ($\Delta T/T$)

E_{obj}	emission from the target object	E_{refl}	emission from the surroundings and reflected by the object
E_{atm}	emission from the atmosphere	ε_{obj}	emissivity of the object
τ_{atm}	transmissivity of the atmosphere	T_{obj}	temperature of the object
T_{refl}	reflected temperature	T_{atm}	atmosphere temperature
ρ	mass density	C	specific heat capacity
r_{ext}	external heat supply	s_t	overall heat source produced by the material
$\mathbf{k}$	thermal conductivity tensor	$\boldsymbol{\sigma}$	Cauchy stress tensor
d_{me}	intrinsic dissipation heat source	$\mathbf{D_{EU}}$	Eulerian strain rate tensor
s_{the}	thermoelastic coupling between temperature and strain	s_{int}	other thermomechanical coupling between the temperature and internal variables
ψ	Helmholtz free energy	$\boldsymbol{\varepsilon}$	strain tensor
α	thermal expansion coefficient	τ_{th}	time increment characterizing heat convection between specimen and environment
σ_{ij}	components of the stress tensor	T_w	temperature in the wet specimen
T_d	temperature in the dry specimen	F_6	longitudinal shear strength
F_{1t}	longitudinal tensile strength in fiber direction	F_{1c}	longitudinal compressive strength in fiber direction
F_{2t}	transverse tensile strength in fiber direction	F_{2c}	transverse compressive strength in fiber direction
F_4	transverse shear strength	β	contribution of shear stress to the fiber failure
F_f^t	damage index due to longitudinal tensile stress	F_f^c	damage index due to longitudinal compressive stress
F_m^t	damage index due to transverse tensile stress	F_m^c	damage index due to transverse compressive stress

δ_{eq}^{0}	equivalent displacement	σ_{eq}^{0}	equivalent stress
G_i^c	critical energy release rate	D	distance between the two sensors S_1 and S_2
t_2, t_1	arrival times at each sensor	E_{11}	in-plane longitudinal elastic modulus
C_L	longitudinal wave velocity	ν	Poisson's ratio
$E_x(\theta)$	Young's modulus in direction x, associated with the angle θ	$\nu_{yx}(\theta)$	Poisson's ratio in direction x, associated with the angle θ
f_1	corrective factor of acoustic wave velocity	$C_L(\theta)$	longitudinal wave velocity in direction x, associated with the angle θ
MC	Moisture Content	R	correlation ratio of wave velocity in the sandwich over that in the skin
M_i	mass of wet specimen	M_0	initial mass after drying process
$p_{MC}(0^\circ)$	attenuation coefficient	ρ_{MC}	density of wet sandwich
$\nu_{MC}(0^\circ)$	Poisson's ratio of wet sandwich in 0° direction	$C_{LD}(0^\circ)$	AE wave velocity in the dry specimen before water immersion
$\nu_D(0^\circ)$	Poisson's ratio of dry sandwich in 0° direction	$C_{LMC}(0^\circ)$	AE wave velocity in wet sandwich measured in specimen length direction
ρ_D	density of dry sandwich	$\bar{\varepsilon}_0^{pl}$	equivalent plastic strain
$\bar{\varepsilon}_f^{pl}$	equivalent strain at complete failure	$G_i^c(MC)$	fracture energy rate of wet sandwich
D_{me}	Cumulative irreversible damage index		

Abstract

Thanks to the excellent specific stiffness and strength, as well as lower costs, the sandwich structures with composites skins, such as glass fiber reinforced polymer (GFRP)-balsa and carbon fiber reinforced polymer (CFRP)-honeycomb sandwich panels, have attracted more and more attention in marine and aviation industries. Generally, the skins of sandwich structures mainly take the bending load, while the core carries the transverse shear stresses. The objectives of this thesis are to characterize the moisture effects on bending behaviors and damage mechanisms of GFRP-balsa and CFRP-honeycomb sandwich structures under 4-point bending experimentally and numerically, with the help of Acoustic Emission (AE) and InfraRed Thermography (IRT).

To better study the bending behaviors of sandwich structures by AE and IRT, firstly, by the preliminary Hsu-Nielsen tests, a new strategy of rapid determination of AE wave propagation velocity in any direction is firstly proposed for most usually used composite sandwich structures, based on the measurements of velocity in only one direction in the composite skin. And then, a new methodology is proposed to predict the elastic modulus of the skin of the wet sandwich structure based on the relationships between Moisture Content (MC), AE wave velocity and elastic modulus. Finally, static 4-point bending tests are monitored by IRT and AE to verify the good consistency between bending stiffness reduction and elastic modulus prediction of the wet sandwich by the new proposed method. A damage characterization approach coupling characteristics of AE amplitude, peak frequency and duration via K-means clustering algorithm is also developed to identify the damage sequence and classify damage modes of sandwich structures under bending loading.

In order to predict the bending behaviors of the sandwich structures, numerical models in Abaqus have been developed by introducing the variation of material parameters of the skin due to moisture absorption, such as the elastic modulus, strength and fracture energy. It is demonstrated that the tested bending stiffness, strength and damage evolution process can be correctly simulated by the numerical models. In addition, the damage localizations by numerical models have a good concordance with the observations by IRT and AE.

Consequently, the accuracy of the numerical models and the feasibility of AE and IRT to identify damage mechanisms of sandwich structures have been demonstrated. The results lay a critical foundation for the future dialogue between experimental and numerical analysis of sandwich structures.

Keywords: sandwich structures, moisture effects, damage mechanisms, Acoustic Emission (AE), InfraRed Thermography (IRT), numerical models.

Résumé

Grâce à leurs propriétés spécifiques exceptionnelles aussi bien en rigidité qu'en résistance, à leurs faibles coûts, les structures sandwichs avec les peaux en composites stratifiés, telles que les panneaux en fibres de verre (GFRP)-balsa et en fibres de carbone (CFRP)-nid d'abeille, sont de plus en plus utilisées dans les industries maritimes et aéronautiques. Ce type de structure est en général conçu pour supporter une charge de flexion. Les peaux sont principalement sollicitées en traction et en compression à cause du moment fléchissant, tandis que l'âme est soumise à des contraintes de cisaillement transverses dues à l'effort tranchant. Les objectifs de cette thèse sont de caractériser expérimentalement et numériquement les effets de l'humidité sur le comportement en flexion ainsi que les mécanismes d'endommagement des structures sandwichs en fibres de verre-balsa et en fibres de carbone-nid d'abeille sous flexion 4 points, à l'aide de l'Emission Acoustique (EA) et de la Thermographie InfraRouge (TIR).

Afin de mieux étudier le comportement en flexion des structures sandwichs par EA et TIR, tout d'abord, grâce aux essais préliminaires de Hsu-Nielsen, une nouvelle méthode de détermination rapide de la vitesse de propagation des ondes acoustiques dans toutes les directions a été proposée pour les structures sandwichs les plus couramment utilisées. Elle est basée sur des mesures de la vitesse dans la peau composite dans une seule direction. Ensuite, une nouvelle méthodologie est proposée pour prédire le module d'élasticité de la peau d'une structure sandwich humide basée sur les relations entre la teneur en humidité, la vitesse des ondes acoustiques et le module d'élasticité. Enfin, des essais de flexion statique 4 points suivis par TIR et EA ont permis de vérifier la bonne cohérence entre la réduction de la rigidité en flexion et la prédiction du module élastique du sandwich humide obtenu par la nouvelle méthode proposée. A l'aide de la technique EA, une approche de caractérisation des endommagements couplant les caractéristiques d'amplitude, de durée et de pic fréquentiel via l'algorithme K-means est également développée pour identifier l'évolution des endommagements et classer les modes d'endommagement des structures sandwiches en flexion.

Afin de prédire le comportement en flexion des composites sandwiches, les essais réalisés sont aussi modélisés numériquement avec Abaqus en introduisant la variation des propriétés mécaniques en fonction de l'humidité absorbée, telles que le module d'élasticité, la résistance et l'énergie de rupture. Il est démontré que la rigidité et la résistance en flexion, ainsi que le processus d'évolution des endommagements des structures sandwichs testées peut être correctement simulé par les modèles numériques développés. De plus, la localisation des endommagements obtenue grâce aux modèles numériques concorde bien avec les observations faites par la TIR et l'EA.

Par conséquent, la fiabilité du modèle numérique et la faisabilité de la TIR et de l'EA pour identifier les mécanismes d'endommagement des structures sandwichs ont été démontrées. Les résultats obtenus dans ce travail fournissent une base essentielle pour un futur dialogue entre l'analyse expérimentale et numérique des structures sandwichs.

Mots clés : structures sandwichs, effets de l'humidité, mécanismes d'endommagement, Emission Acoustique (EA), Thermographie InfraRouge (TIR), modèles numériques.

General Introduction

Nowadays, in the advanced aeronautical and marine industries, which require a combination of high structural rigidity and low weight, the composite structures, especially the composite sandwich structures, have been extensively applied in the major load-bearing components of the aircrafts and ships. Composite sandwich structures, which are fabricated by bonding the two thin but stiff and strength skins and the center thicker but lighter core, have been designed to allow that the skins can offer the good bending stiffness and strength, while the light core can offer the shear stiffness and strength. Finally, this three-layer structure can lead to a high specific bending stiffness and high specific bending strength, and thus it has been widely used as the primary and secondary structures in aircrafts and ships. Considering the increasing use of this kind of structure in aeronautical and marine industries, the importance of studying its bending behavior and understanding its performance in service should be highlighted.

Considering a balance between the bending behaviors and the economic cost, in the aeronautical and marine industries, the preferred constituent materials of the sandwich structures are not the same. For example, in the aeronautical field, the sandwich structures consisting of the honeycomb core and Carbon Fiber Reinforced Polymer (CFRP) skins are more popular due to the higher specific stiffness and strength, while the balsa wood core and Glass Fiber Reinforced Polymer (GFRP) skins are preferred in the marine structures due to the lower cost and environmental friendliness. Furthermore, considering the environmental influences in the service life of the sandwich structure, the ship hulls made of balsa sandwich structures are immersed in seawater for a long time, aircraft wings and fuselages composed of honeycomb sandwiches could be affected by the humidity in the air under different weather conditions. Since the constituents and skin/core interfaces of sandwich structures can be sensitive to the absorbed moisture, it pushes us to study, in this thesis, the moisture effects on the bending behaviors of the GFRP-balsa sandwich in marine structures and the CFRP-honeycomb sandwich in aircrafts, in order to better predict the damage mechanisms and stiffness/strength degradation of the sandwich structures during the whole service life.

However, because of the complicated anisotropic, heterogeneous and hygroscopic properties of the constituents, the characterization of bending behaviors of the balsa and honeycomb sandwich structures has been a great challenge, and few related references can be found, especially about the balsa sandwich. The real damage mechanisms of sandwich structures under bending load can be affected by the density and thickness of the skin and core, material property, structure geometry, loading condition, span length, environmental condition, etc. The skin damages, core damages and skin/core debonding may occur simultaneously, which makes it difficult to classify different damage

modes, and few researches have been focused on the damage mechanisms of sandwich structures which have been affected by the environmental humidity. So, it still needs further exploration about the damage initiation and evolution of the dry and wet sandwich structures under bending load. In addition, the accurate in-situ monitoring of the damage mechanisms of the aircrafts or ships is very important for ensuring the structure safety and reducing the maintenance cost. Hence, in order to help identify the damage mechanisms of the sandwich structures, Non-Destructive Testing (NDT) techniques such as Acoustic Emission (AE) and InfraRed Thermography (IRT) have attracted more and more attention recently.

AE is based on the radiation of transient stress waves in solids when a material undergoes irreversible changes in its internal structure. IRT is based on the recording of thermal radiation emitted by a surface of a specimen via an infrared camera. Temperature distribution can be measured without contact in real time when damages initiate and propagate in the structure under loading. However, each NDT technique has its own limitations, for example, AE monitoring can be affected by the acoustic wave attenuation and velocity variation in the anisotropic materials, and IRT cannot detect deep damages easily. Accordingly, it will be interesting and meaningful to couple these two techniques to know exactly more about when, where and what kinds of damages will initiate and propagate.

Over the last ten decades, the team of laboratory ICA in IUT Tarbes has been working on the coupling of IRT and AE on monitoring damages in the composite laminate and wood structures, and the group GeM-E3M in IUT Saint Nazaire has been devoted to studying foam/balsa/honeycomb sandwich structures by the traditional experimental methods. However, further investigation is needed to understand whether IRT and AE can monitor well the sandwich structures under bending loading. More importantly, the effects of the absorbed moisture on the bending behaviors of sandwich structures and the impact of the moisture absorption on the AE and IRT monitoring have not been studied very well, so it is necessary to focus on the moisture effects on the performance of sandwich structures under the monitoring of AE and IRT.

Therefore, based on the previous work of ICA and GeM-E3M, this thesis is aimed at characterizing the moisture effects on the bending behaviors and damage mechanisms of GFRP-balsa and CFRP-honeycomb sandwich structures with the help of AE and IRT techniques. Correlations of Moisture Content (MC), AE/IRT signals and mechanical properties of the two kinds of sandwiches will be firstly investigated. The feasibility of AE and IRT to monitor the damage initiation and evolution of the sandwich structures in 4-point bending tests will be demonstrated. Meantime, the numerical models will be developed for both dry and wet sandwiches to simulate bending behaviors of the two kinds of sandwich structures under 4-point bending, by introducing the moisture effects on the

variation of material parameters of the constituents, based on the preliminary active AE tests. Finally, the correlations between experimental results and numerical simulations will be discussed.

This PhD thesis is composed by four chapters as follows:

Chapter 1 presents a literature review. Firstly, the constituents, application background and fabrication process of different composite sandwich structures have been introduced. Then, the bending behaviors and common damage mechanisms of the balsa/honeycomb sandwich structures have been discussed. Considering the environmental influences on the mechanical behaviors of the constituents, moisture effects on the properties of the skins, core, skin/core interfaces have been studied, separately. Following this, the basic principles, post-processing method and applications of AE and IRT techniques on identifying and localizing damages of sandwich structures have been reviewed. Finally, the numerical models applicable to honeycomb and balsa sandwiches have been introduced to lay a foundation for our numerical models in this thesis.

In Chapter 2, the raw material properties, specimen geometries and fabrication processes of GFRP-balsa and CFRP-honeycomb sandwich specimens have been firstly presented. Preliminary characterization of AE wave propagation properties in GFRP-balsa and CFRP-honeycomb sandwiches has been studied, including acoustic wave velocity and attenuation property. Based on the measurements of velocity in only one direction in the composite skin, a new rapid model to determine AE wave velocity in any direction in the sandwich has been proposed. Based on this new method, moisture effects on AE wave propagation properties and active IRT tests have been further investigated, to lay a good foundation for the later monitoring of damages in 4-point bending tests. Finally, relationships between Moisture Content (MC), AE wave velocity and elastic modulus have been pointed out, allowing us to propose a new method to predict the elastic modulus of the skin of the wet sandwich structure. The variation of the material parameters of the wet sandwich based on this method will be introduced in the Abaqus models described in Chapter 3 and 4, to improve the prediction accuracy of numerical analysis.

In Chapter 3, the static 4-point bending behaviors of GFRP-balsa sandwich structures have been studied experimentally and numerically. Moisture effects on the bending stiffness/strength and damage mechanisms have been discussed, based on the observations by the microscope, IRT and AE. By analyzing AE data, a damage characterization approach coupling the characteristics of amplitude, peak frequency and duration via K-means clustering algorithm has been proposed to better classify different damage modes of the GFRP-balsa sandwich under 4-point bending. Herein, the 4-point bending tests have been also simulated by Progressive Damage Analysis (PDA) model in Abaqus by introducing the variation of elastic modulus, strength, and fracture energy of the skin due to moisture

absorption. It is shown that the bending stiffness, fracture load, displacement and damage evolution process of the wet sandwich can be predicted correctly. In addition, it demonstrates that the damage localizations by PDA model have a good concordance with the observations by IRT and AE.

In Chapter 4, similarly, the static 4-point bending behaviors of CFRP-honeycomb sandwich structures have been studied experimentally and numerically, but different bending responses have been found, compared to the GFRP-balsa sandwich. The non-linear buckling behavior and core damages in zone 2 of the CFRP-honeycomb sandwich have been investigated by coupling the microscope, IRT and AE observations. Furthermore, an equivalent progressive elastic-plastic damage model in Abaqus has been developed to simulate the non-linear bending behavior and core damages of the dry and wet CFRP-honeycomb sandwich. Eventually, it is shown that the damage localizations predicted by Abaqus models agree well with the microscope, AE and IRT observations.

This manuscript is closed by a general conclusion and the perspectives released by this study.

Chapter 1. Literature Review

1.1. Introduction.....11

1.2. Overviews of balsa/honeycomb sandwich structures.....11

1.2.1. Constituents of composite sandwich structures.....11

1.2.1.1. Skin materials.....13

1.2.1.2. Core materials.....13

1.2.2. Applications of balsa/honeycomb sandwich structures.....16

1.2.2.1. Applications of GFRP-balsa sandwich in marine industry.....16

1.2.2.2. Applications of CFRP-honeycomb sandwich in aeronautical industry…….....17

1.2.3. Fabrication process of balsa/honeycomb sandwich structures.....18

1.2.3.1. Fabrication process of laminated skins.....18

1.2.3.2. Fabrication process of the core.....19

1.2.3.3. Fabrication process of sandwich structures.....20

1.2.4. Challenges and perspectives of balsa/honeycomb sandwich structures.....20

1.3. Damage mechanisms of balsa/honeycomb sandwich structures under bending load…….....21

1.3.1. Theoretical sandwich theory.....21

1.3.2. Damage mechanisms of sandwich structures.....22

1.3.2.1. Damage mechanisms of balsa sandwich structures.....23

1.3.2.2. Damage mechanisms of honeycomb sandwich structures.....24

1.3.3. Moisture effects on damage mechanisms of sandwich structures.....27

1.3.3.1. Moisture effects on properties of laminated skins.....27

1.3.3.2. Moisture effects on properties of balsa/honeycomb cores.....28

1.3.3.3. Moisture effects on properties of skin/core interfaces.....30

1.3.4. Conclusions and challenges.....31

1.4. NDT techniques for monitoring damage mechanisms of sandwich structures.....32

1.4.1. Overviews of NDT techniques for composite structures 32
1.4.2. Monitoring damages by Acoustic Emission (AE).....33
1.4.2.1. Data acquisition principle of AE 33
1.4.2.2. Post-processing of AE data by clustering algorithms.....35
1.4.2.3. Damage classification of honeycomb/foam sandwiches by AE.....38
1.4.2.4. Damage initiation identification of laminates by AE 39
1.4.2.5. Damage localization by AE.....41
1.4.2.6. Conclusions 43
1.4.3. Monitoring damages by InfraRed Thermography (IRT).....44
1.4.3.1. Data acquisition principle of IRT 44
1.4.3.2. Post-processing of heat source field.....47
1.4.3.3. Moisture effects on composite structures detected by active IRT 49
1.4.3.4. Damage initiation and evolution monitored by passive IRT 51
1.4.3.5. Conclusions 52
1.4.4. Coupling of AE and IRT techniques 52
1.5. Numerical analysis of bending behaviors of balsa/honeycomb sandwich structures.....55
1.5.1. Finite Element Modeling (FEM) of balsa/honeycomb sandwich structures 55
1.5.2. Damage models for laminated skins 56
1.5.2.1. Progressive Damage Analysis (PDA) model 56
1.5.2.1.1 Damage initiation.....56
1.5.2.1.2 Damage evolution.....57
1.5.2.2. Cohesive Zone Model (CZM) for delamination.....58
1.5.3. Damage models for balsa/honeycomb cores 59
1.6. Chapter summary 62

1.1. Introduction

In the last decades, the composite sandwich structure has become more and more attractive in the industries such as the aeronautics and marine fields, due to their low weight, high bending properties and good durability. These excellent properties are owing to the combination of the Fiber Reinforced Polymer composite skins and the balsa/honeycomb core. The skins can provide the good bending loads resistance, while the core mainly resist the shear loads, due to the three-layer construction made of two kinds of materials.

On the other hand, the anisotropic, heterogeneous and hygroscopic properties of the constituent materials make it difficult to characterize the very complicated bending behaviors and damage mechanisms of the sandwich structure, because they are related to various factors such as the material property, density and thickness of the skin and core, structure geometry, loading condition, span length, environmental condition, etc. Accordingly, Non-Destructive Testing (NDT) techniques such as Acoustic Emission (AE) and InfraRed Thermography (IRT) are necessary to help identify the damage modes and localize the damage zones of the sandwich under bending load. Furthermore, the monitoring data from NDT methods can validate the accuracy of the numerical models, in order to improve the prediction accuracy of the bending behaviors and damage evolution process. All these topics studied in the literatures will be discussed in this chapter.

1.2. Overviews of balsa/honeycomb sandwich structures

1.2.1. Constituents of composite sandwich structures

A composite structure is made from two or more constituent materials with obviously different physical or chemical properties. For example, the continuous matrix and embedded reinforcement, as illustrated in Fig. 1-1 [1]. The more commonly used matrix materials are thermosetting or thermoplastic polymers with good shear properties and low densities, while reinforcements are short or long fibers with higher specific strength and stiffness, such as Carbon Fiber Reinforced Polymer (CFRP) and Glass Fiber Reinforced Polymer (GFRP) [2-3]. Normally, the mechanical properties of CFRP or GFRP composite are determined by the basic constituents. Specifically, the fibers carry majority of the external load and determine most of the stiffness/strength, while the matrices mainly provide transverse mechanical properties and protection of fibers, which finally ensure the better overall performance of composite. One kind of traditional composite structure is obtained by stacking the plies of different fiber orientation, often called the laminates [4]. Another more complicated composite structure has attracted great attentions, that is, the composite sandwich structure [5].

A sandwich structure is often fabricated by attaching two thin but stiff and strength skins/face sheets to a lightweight but thick core using the adhesive films. It is designed to bear bending load. The skins mainly resist the in-plane normal loads (similar to flanges of an I- beam) due to bending moment, one skin is under compression and the other skin is under traction. The core mainly resists the shear loads (similar to the web of an I-beam). In general, the thickness of the core should be at least 10 times as that of the skin so as to avoid the buckling of the structure under bending load [5]. Finally, this three-layer structure can lead to a high bending stiffness to weight ratio, and it can reduce the local crushing and buckling damages under bending load compared to the laminate or metal panel with the same skin thickness. Thus, it highlights the importance of studying the bending behaviors of the sandwich, as shown in Fig. 1-2 [6].

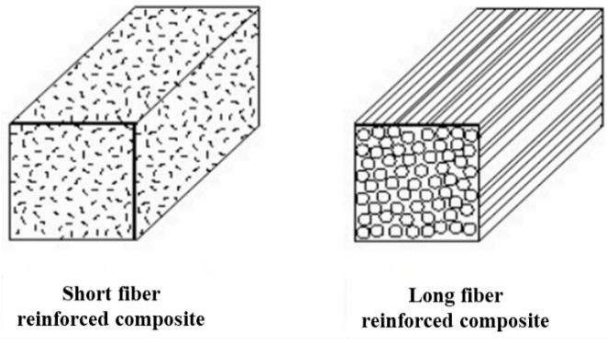

Fig. 1-1. Presentation of the short and long fiber reinforced composite [1].

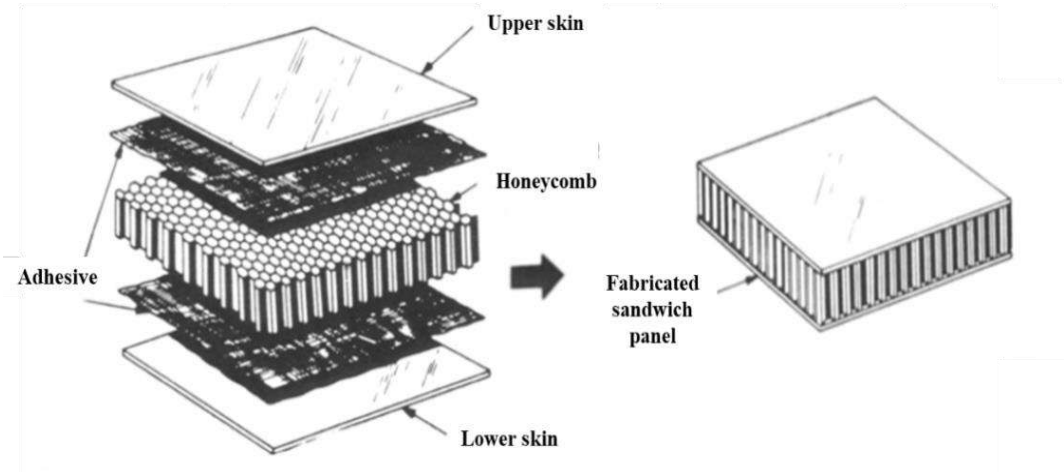

Fig. 1-2. Constituents of a typical honeycomb sandwich structure [6].

Considering the balance between the bending behaviors and the economic cost, in the aeronautical and marine sandwich structures, the GFRP and CFRP laminated skins are common due to their high specific stiffness/strength. The core is usually made from materials with relatively low strength/stiffness, such as foam, honeycomb and balsa wood, carrying transverse shear stresses and

supporting the skins against bending or buckling modes [7]. Finally, the sandwich structure can offer the higher specific bending stiffness/strength [8-9] and good durability at lower fabrication cost. To be emphasized, the skin/core interfaces are often the most vulnerable part of the sandwich, due to the shear stress gradients at interfaces [10-11]. Consequently, the bending behaviors of the sandwich structure is highly dependent on the properties of the outer skins, the skin/core interfaces and the center core [12].

1.2.1.1. Skin materials

The choice of sandwich materials depends on the function of the structure, lifetime loading, availability and cost. As the main constituents to carry bending loads, skin materials have experienced a developing process from metal to CFRP/GFRP laminated panels which have higher specific strength and stiffness. Traditional metal skins are usually coupled with metallic foam or honeycomb, to ensure the stability and homogeneity of the whole sandwich at lower cost. Generally, CFRP laminates are lighter but stiffer than GFRP [13], while GFRP has better corrosion resistance property. As a consequence, considering both mechanical properties [14] and economic cost, CFRP skins are usually bonded to aluminum or Nomex honeycomb cores, more popular in aerospace and aeronautical applications, while GFRP skins are working together with balsa or foam core in civil and marine structures [15-16].

1.2.1.2. Core materials

The most common core materials can be divided into three types: (1) solid core including foam and balsa (with continuous bonding surfaces); (2) cellular or honeycomb core (with discontinuous bonding surfaces); (3) corrugated/truss core [9].

Firstly, balsa, which is a tropical hardwood native to the Americas, particularly from Ecuador, is the lightest commercial timber and one of the preferred bio-core materials in sandwich structures, applied largely in boats, wind turbine blades, etc. The mechanical behaviors of balsa greatly depend on its various density, typically varying from 60 to 250 kg/m^3 [21-22]. The high strength-to-weight ratio provides the outstanding energy absorption [23] property of balsa, making it possible to be competitive with the hexagonal honeycomb. However, the applications of balsa cores are limited because of the high hygroscopic sensibility and anisotropy properties of the wood material [24-25]. In order to further develop the application of balsa sandwich structures, it is necessary to improve the understanding of moisture effects on the mechanical behaviors of balsa wood as a core of the sandwich structure.

The three symmetric axes of balsa are often marked by Longitudinal/Axial (L), Radial (R), and Tangential (T) direction, as seen in Fig. 1-3. (a). The anisotropic property of balsa wood mainly

results from the microscopic combination of tracheids (80–90%) in axial direction, rays (8–15%) in radial direction and sap channels (vessels, 3–9%) in axial direction, as shown in Fig. 1-3. (b) and (c) [22]. The hygroscopic property of balsa wood is mainly due to the tubular microstructure of tracheids, which are composed of cellulose, and hydrophilic polymers (hemicellulose and lignin), sensitive to moisture penetration. Axial tracheids are long prismatic cells, having a cross-section resembling hexagon honeycomb cells [26-27] (see Fig. 1-4), mainly determining the mechanical properties of balsa.

Radial rays are brick-like parenchyma cells, with a more rectangular cross-section, mainly used for storing and conducting nutrients. Axial sap channels are long tubular cells, with a larger circular cross-section and thinner wall, responsible for transporting fluids from the roots to the crown. Consequently, balsa wood is less stiff and weaker in the tangential and radial directions compared to axial direction. The two in-plane tangential and radial moduli are usually 15-40 times smaller than the axial modulus [22]. Besides, the elastic modulus and strength of balsa wood will also increase linearly with density in axial compression and bending, while in radial compression, the modulus and strength vary nonlinearly with density [21-25]. Thus, the mechanical properties of balsa wood will show great scatter due to the difference of direction, density, humidity, growing period, etc.

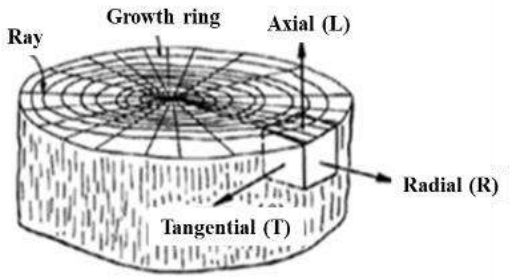

(a) Anisotropy directions of balsa wood.

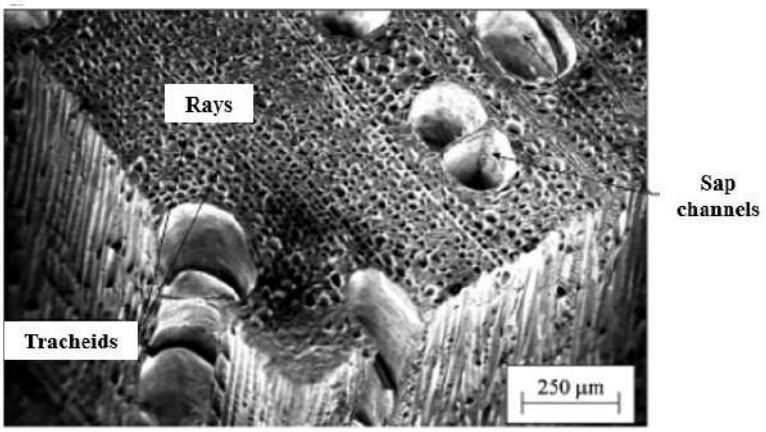

(b) Three constituents of balsa.

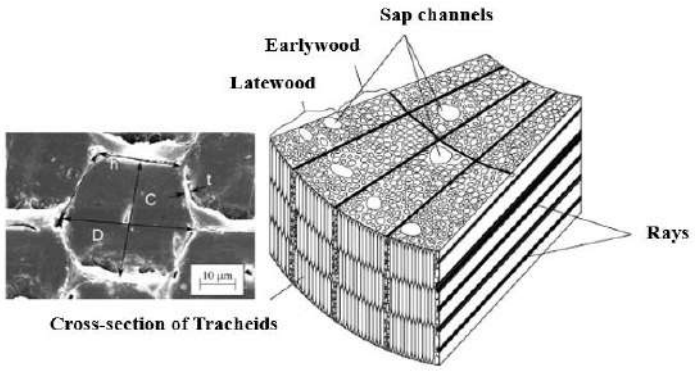

(c) Schematic of microstructure of balsa and cross-section of tracheids.

Fig. 1-3. Micrographs of balsa wood and the three types of cells [22].

Honeycomb cores also have high shear property, and Nomex (aramid paper) honeycomb [27] has become the more preferred material due to its lower density and good corrosion resistance property. Honeycomb material can be designed as diverse topologies, such as hexagon (see Fig. 1-4), rectangular and square geometry [28]. The cell geometries including cell size, cell wall thickness and core thickness, can influence the density and mechanical properties of honeycomb core. It has been demonstrated that shear strength and stiffness in L direction are usually better than those in W direction [29-30], which may result in the different crack propagation path under the same loading condition.

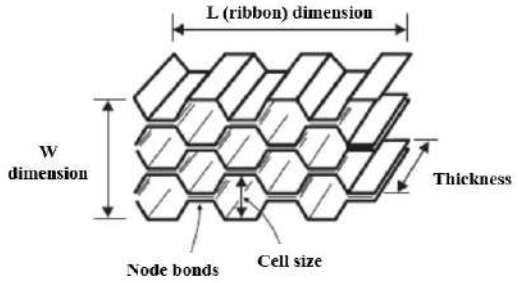

(a) Anisotropy directions of honeycomb.

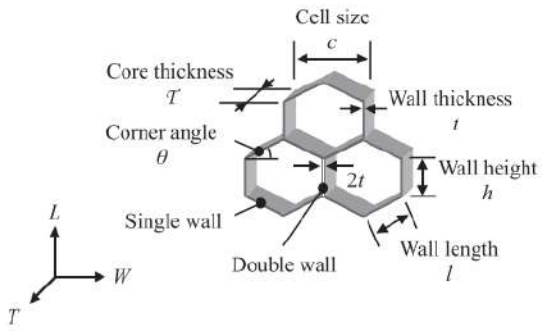

(b) Cell geometries of honeycomb.

Fig. 1-4. Hexagonal honeycomb cells in L and W directions [26-27].

In addition, foam cores can provide good thermal resistance and energy absorption properties. The closed-cell foams like Polyvinylchlorid (PVC) and Polymethalcrylimide (PMI) are the most popular due to lower water absorption rates. Mechanical behaviors of foam mainly depend on the thickness of the cell wall, density and properties of the base polymer [17-18].

Recent processing developments have now made it possible to manufacture panels where the core is reinforced by means of trusses or corrugated structures connecting the skins. Truss cores (see Fig. 1-5) are the new promising structure forms with improved strength and impact performance, due to the suppression of skin debonding. So, it has the potential to compete with honeycomb cores, but less applied due to the design complexity [19-20].

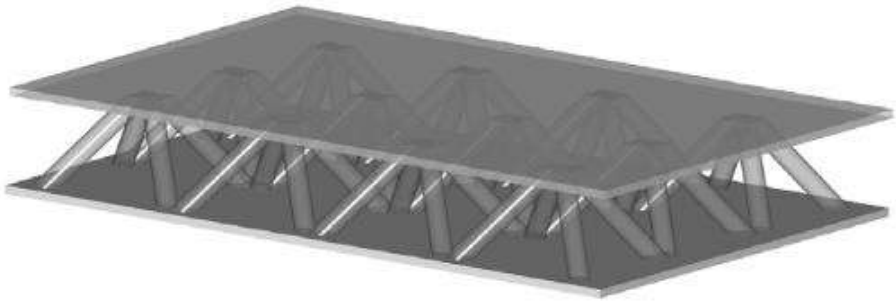

Fig. 1-5. Schematic of a pyramidal lattice truss core sandwich panel [20].

In short conclusion, the anisotropic properties of honeycomb and balsa cores are more complicated but less studied compared to foam sandwich, so it attracts our attentions.

1.2.2. Applications of balsa/honeycomb sandwich structures

Thanks to their excellent specific strength and stiffness, as well as good designability, composite sandwich structures have been widely applied in the marine, aeronautics, aerospace, transportation, construction and other industries [31-32].

1.2.2.1. Applications of GFRP-balsa sandwich in marine industry

GFRP-balsa sandwich structures have gained wide acceptance through its use in naval ship hulls [33-34] (see Fig. 1-6), wind turbine blades, due to the lighter weight and lower costs. However, in the marine industry, mechanical properties of the constituents could be highly reduced by moisture absorption during long time service [35-36]. In particular, the strength and stiffness of skin/core interfaces of sandwiches under wet environments can be also affected, and the influence may be different for foam and balsa sandwiches [37-38].

Fig. 1-6. GFRP-balsa sandwich applied in the ship hull [38].

1.2.2.2. Applications of CFRP-honeycomb sandwich in aeronautical industry

The requirements for composite sandwich structures in commercial aviation aircraft are very diverse [31, 39]. External structures such as leading-edge fairings usually face a wide range of operational temperatures and impacts due to bird strike. Floor panels in the passenger compartment must withstand transverse or discrete loads caused by passengers, and floor panels in the toilets should prevent the prolonged water ingress. To fulfill the different requirements, different material combinations could be found in the current sandwich structures in aircrafts, such as aluminum skin-aluminum honeycomb, CFRP skin-aluminum honeycomb, CFRP skin-Nomex honeycomb sandwiches, etc [40]. The pre-dominate applications are CFRP-honeycomb sandwiches, as shown in the aircraft A380 in Fig. 1-7.

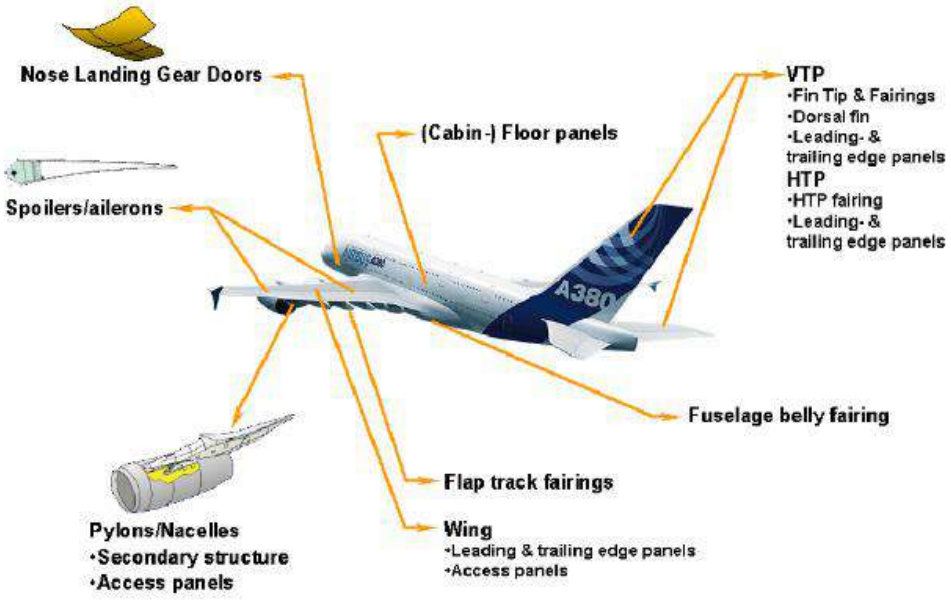

Fig. 1-7. CFRP-honeycomb sandwich applications in the aircraft A380 [39].

1.2.3. Fabrication process of balsa/honeycomb sandwich structures

Due to the complex constituents, the fabrication process of sandwich structure is also complicated, and it will have great effects on the initial structural integrity. Generally, the whole fabrication processes of balsa and honeycomb sandwich panels have some difference [41], depending on their different material properties and geometries.

1.2.3.1. Fabrication process of laminated skins

For composite laminates, the common fabrication processes include [42-45]: Compression molding, Resin Transfer Molding (RTM), Filament winding, Vacuum bag molding, Wet lay-up, etc.

Compression molding [45] is a precise and potentially rapid closed-mold process for producing high quality composite parts in a wide range of volumes due to the combination of heat and pressure. It uses matched metal molds with the application of external pressure. An engineered composite layup is placed in the open mold cavity, the mold is closed, and consolidating force is applied. The pressure remains on the mold throughout the cure cycle, which usually occurs in an oven. The system requires a high level of proficiency: placing the compound into the mold is fairly easy, but orienting the various layers of fiber correctly requires extensive training and experience.

RTM [42] is capable of consistently producing composite parts with high strength, complex geometries, tight dimensional tolerances, and part quality typically required of aerospace applications. RTM uses a closed mold commonly made of aluminum. A fiber layup is placed into the mold. The mold is closed, sealed, heated, and placed under vacuum. Heated resin is injected into the mold to impregnate the fiber layup. Having the mold heated and under vacuum, as in Vacuum Assisted Resin Transfer Molding (VARTM) assists the resin flow. The mold is then held at a temperature sufficient to cure the resin. Current RTM technology produces lightweight parts with excellent mechanical properties. But this solution is more expensive than other techniques.

Filament winding is one of the oldest composite manufacturing processes, mainly used for manufacturing open (cylinders) or closed end structures (pressure vessels or tanks), well-suited to automation. It involves winding filaments under tension over a rotating mandrel, which is fast, cost-effective and creates lightweight, high-performance structures. The controlled variables for winding are fiber type, resin content, wind angle, tow or bandwidth and thickness of the fiber bundle. The angle at which the fiber is wound has an effect on the properties of the final product, so it has high requirements for the operator's skills.

Vacuum bag molding [41, 43] is a very flexible process for consolidating fiber-reinforced polymer laminates of a wide range of shapes and sizes. The composite to be consolidated (e.g. a prepreg or

hand lay-up) is placed on a single-sided mold. The material is then covered with an impervious film (the “vacuum bag”), which is sealed around the edge of the part. By evacuating the air between the mold and the vacuum bag using a vacuum pump, the part is consolidated under atmospheric pressure. The process is often performed in an oven to assist with the curing of the resin. Vacuum bag molding is the most popular in industry because it works better for fabrication of larger curved and complex panels, producing higher fiber volume content and fewer air bubbles [44-45], so we have adopted this technique to fabricate CFRP laminated skins.

For the wet lay-up process [41], a two-component epoxy resin is mixed, and a primer layer is first applied where the composite is to be bonded. The fiber fabric is placed on top of the primer then impregnated by spreading resin over the fabric. Compaction is performed with an aluminum roller to remove excess resin and air voids. This process is repeated layer by layer, until all plies are wet infused. Vacuum bag can be placed over the lay-up to assure no air or voids during polymerization. Room temperature, heat (oven) and autoclave curing can be used for processing low, medium and high production needs. Wet lay-up is simple, low cost and open mold fabrication process, but it requires a lot of repetitive labor and not so effective for large complex structures. Woven such as plain, twill and knitted fabric laminates are often fabricated in this way, so woven GFRP laminates in this thesis will be fabricated by wet lay-up.

1.2.3.2. Fabrication process of the core

Core panels are usually offered by the suppliers, and BALTEK® SB [46] from 3A Composites Core Materials is the most widely used balsa wood from controlled cultivation cut perpendicular to the grain direction (see Fig. 1-8). Z is the axial direction of balsa wood, and the large balsa panel is bonded together by many small blocks, thus there are a lot of balsa interfaces distributed randomly in the panel [47]. Balsa has excellent laminate adhesion properties, so it could be processed with most resins and processes, including wet lay-up and vacuum bagging [48].

Fig. 1-8. BALTEK® SB balsa panels from 3A Composites Core Materials [46].

Generally, Nomex honeycomb panels are manufactured by the expansion process (see Fig. 1-9) due to good stretchability. Multiple sheets of Nomex paper are placed on top of each other and glued

together at the node locations by lines of adhesives. Then the large stack of Nomex sheets can be cut into smaller strips and expanded to the final Nomex honeycomb panel along the W direction [49-50].

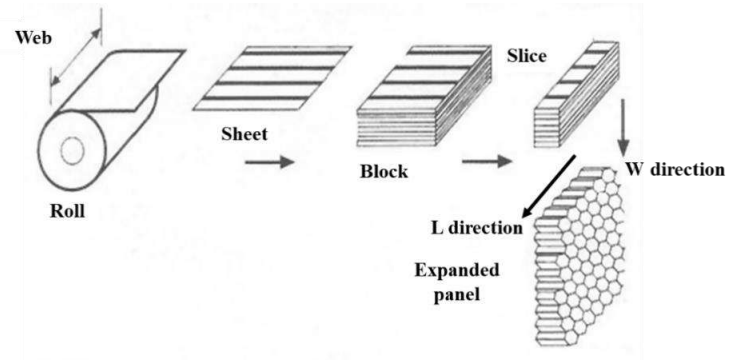

Fig. 1-9. Expansion process of the honeycomb panel [50].

1.2.3.3. Fabrication process of sandwich structures

The fabrication process of the whole sandwich panels can be classified into two types:

(1) Co-curing process:

For balsa sandwiches, the wet layup method using the liquid resin infusion process is often used. In this way, the GFRP laminated skins are laid up and co-cured with the balsa core simultaneously. During the co-curing process, the required curing temperature and duration differences between the core and skin materials shall be considered to reduce curing defects [51-52]. Sandwiches with foam cores are also formed by this method [17].

(2) Two-step curing process:

For most honeycomb sandwiches, the CFRP laminated skins are firstly fabricated by lay-up prepreg, then the skins and core are co-cured together using the adhesive film in vacuum bag at elevated temperature [7, 41].

In summary, the different curing processes of sandwiches could result in different interfacial strength, affected by the infused resin and adhesive film properties. Hence, having a good understanding of the whole fabrication process of the sandwich structure will benefit the study of its mechanical behaviors.

1.2.4. Challenges and perspectives of balsa/honeycomb sandwich structures

Due to the complicated constituents and fabrication process, it remains a great challenge to study the bending behaviors and damage mechanisms of the sandwich structures. They can be influenced by various factors [53-54] such as properties of the constituent materials, the skin/core interface strength, the structure geometries, the loading conditions, the environmental temperature and moisture, etc.

Considering the real service environment, the influence of the moisture absorption should not be ignored, because it can result in the decrease of stiffness/strength of the skin, the core and skin/core interface [36-38], and then affect the damage mechanisms of sandwich structures, especially for sandwiches with honeycomb and balsa cores [55] which are sensitive to humidity. Accordingly, moisture effects on bending behaviors and damage modes of the balsa and honeycomb sandwich structure should be further reviewed in the next part.

1.3. Damage mechanisms of balsa/honeycomb sandwich structures under bending load

1.3.1. Theoretical sandwich theory

As mentioned before, the sandwich structure is designed to allow that the skins can offer the good bending stiffness, while the light core can offer the shear stiffness. In the theoretical sandwich theory, which describes the behavior of a beam, plate, or shell consisting of three layers-two skins and one core, the linear sandwich theory [56-57] (see Fig. 1-10) is most commonly used. It assumes that the skins carry only bending stresses σ_f and the core takes only the transverse shear stresses τ_c. When the skin thickness t is much smaller than the core, the variation of bending stress through skin thickness direction can be ignored [41, 58]. These assumptions are nearly always satisfactory when the core is honeycomb or balsa wood [58-59]. Then the bending stiffness, shear stiffness, compressive stresses in the upper skin, tensile stresses in the lower skin, and core shear stresses can be calculated, either under 3-point or 4-point bending.

Bending stiffness [58-60] of a traditional sandwich beam can be expressed by Eq. (1-1):

$$D_b = b\left[\frac{E_f {h_f}^3}{6} + \frac{E_f h_f h^2}{2} + \frac{E_c {h_c}^3}{12}\right] = 2D_f + D_o + D_c \quad (1\text{-}1)$$

Where b is the width of the beam, h_f and h_c are the thicknesses of the skin and core, E_f and E_c are Young's modulus of the skin and core, and thus $h_s=2h_f+h_c$ is the sandwich thickness, $h=h_f+h_c$ is the sum of the thicknesses of the skin and the core. Thus, D_f is the bending stiffness of a skin about its own neutral axis, D_o is the stiffness of the skin associated with bending about the neutral axis of the entire sandwich, and D_c is the stiffness of the core [41, 61].

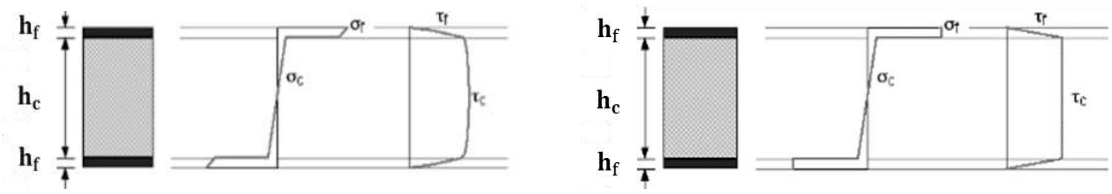

(a) Real stress distributions (b) Approximate stress distributions

Fig. 1-10. Stress distributions of bending and shear stresses in a sandwich beam [58].

Since the elastic modulus of the core is much smaller than that of the skin, it's assumed that $E_c << E_f$, in addition, the skins are thinner, so D_f and D_c can be neglected compared to D_o. Eq. (1-2) could be obtained approximately:

$$D_b \cong D_o = \frac{E_f h_f h^2}{2} b \tag{1-2}$$

Shear stiffness Q can be also given by Eq. (1-3):

$$Q = Gbh \tag{1-3}$$

Where G is the shear modulus of the core.

The skin stress can be calculated by Eq. (1-4):

$$\sigma_f = \frac{M}{I_z} \cdot \frac{h}{2} = \frac{M}{D_b/E_f} \cdot \frac{h}{2} = \frac{M}{bh_f h} \tag{1-4}$$

Where M is the bending moment of the sandwich structure, I_z is the inertia moment.

Under 3-point bending, the maximum skin stress can be calculated by Eq. (1-5) approximately:

$$\sigma_f = \frac{M}{bh_f h} = \frac{L}{4bh_f h} F \tag{1-5}$$

Where F is the applied force and L is the distance between the two supports.

Under 4-point bending, the maximum skin stress can be calculated by Eq. (1-6) approximately:

$$\sigma_f = \frac{M}{bh_f h} = \frac{L_e}{2bh_f h} F \tag{1-6}$$

Where L_e is the distance between the internal loadings and the external supports.

Under 3-point and 4-point bending, the average core shear stress can be given by Eq. (1-7) approximately:

$$\tau_c = \frac{F}{2bh} \tag{1-7}$$

Hence, it can be concluded that failure modes of sandwich structures under bending can be affected by the strength/stiffness of constituents, the skin and core thickness, specimen width, the span length between supports, the loading condition, etc.

1.3.2. Damage mechanisms of sandwich structures

Based on the sandwich theory, ASTM C393 [62] has proposed the short flexural sandwich beam to investigate core shear damages in 3-point or 4-point bending test, and ASTM D7249 [63] has proposed the long sandwich beam to study skin damages and skin/core debonding in 4-point bending test. Most bending test setup of the sandwich beam has been based on these two standards. In general, under bending load, various damage modes of sandwich structures can be generated [64-66], including:

- Core shear damages and core failure in tension/compression;
- Skin/core interface debonding;

- Skin compressive/tensile damages.

Theoretically, the upper skin of sandwich beam carries compressive stress while the lower skin takes tensile stress under bending load. Because of GFRP and CFRP fibers are often weaker in compression than in tension [13-14], compressive damages of composite skins are likely to firstly appear.

It has been demonstrated that most foam cored sandwich structures [67-68] failed due to core damages, followed by skin/core debonding and skin damages under bending loading. However, it is still unclear about the damage initiation and evolution mechanisms of balsa and honeycomb sandwich structures, especially under 4-point bending.

1.3.2.1. Damage mechanisms of balsa sandwich structures

By far, few researches [56, 69-71] have been focused on bending behaviors of balsa sandwich structures, and the existing results are mainly under 3-point bending loading. Zaharia S M et al. [56] studied the static and fatigue behaviors of CFRP-balsa sandwiches under 3-point bending, concluding that the upper skin firstly fractured, and then the crack propagated through the entire balsa core and eventually caused the lower skin/core debonding, as seen in Fig. 1-11. The fracture load is mainly determined by the strength and stiffness of the skin. Sayahlatifi S et al. [69] also found that the damage sequence of aluminum-balsa sandwiches under 3-point bending is balsa core shear cracks and skin/core debonding.

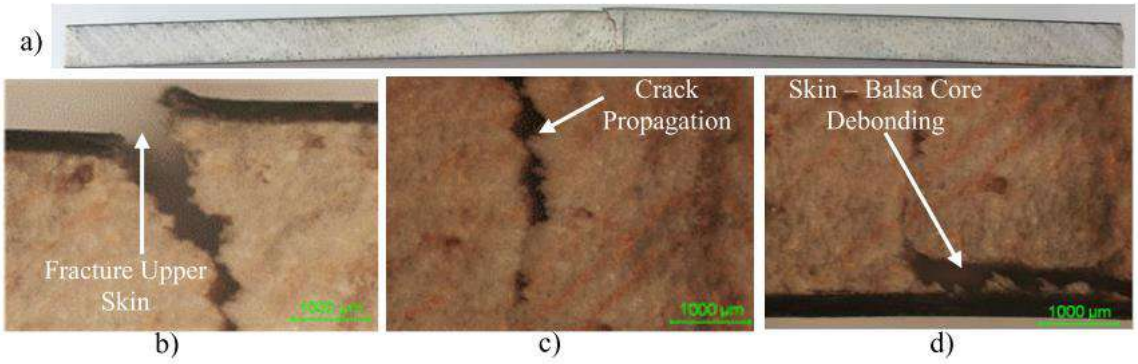

Fig. 1-11. Damage modes of CFRP-balsa sandwich under 3-point bending: a) Failure modes; Fracture area (magnification 25X): b) upper skin; c) balsa core; d) lower skin [56].

Shi H et al. [70] performed 4-point bending static and fatigue tests on GFRP-balsa sandwich beams, and revealed the significant influence of the core thickness on bending stiffness, ultimate capacity, deflection and damage modes of the sandwich. Fig. 1-12 shows that the sandwich failed due to core shear and followed by skin/core debonding. When the core thickness is doubled (TB specimens with 50.8 mm) in Fig. 1-12. (a), fracture load will increase by 56% and fewer skin/core debonding could

be found. By photographs from videos in Fig. 1-12. (b), it can be seen that as the load increased, the dominant shear crack developed and propagated rapidly in the core, followed by failure with a loud noise. Shear damages led to a secondary skin/core debonding failure. The two skins show no visible damage in these specimens.

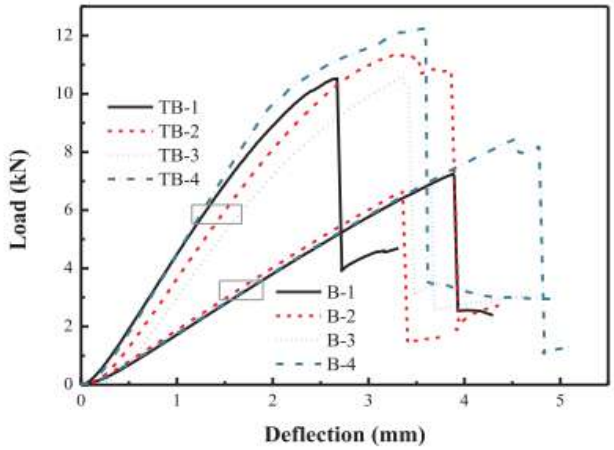

(a) Load-defection curves of GFRP-balsa sandwich with different core thicknesses.

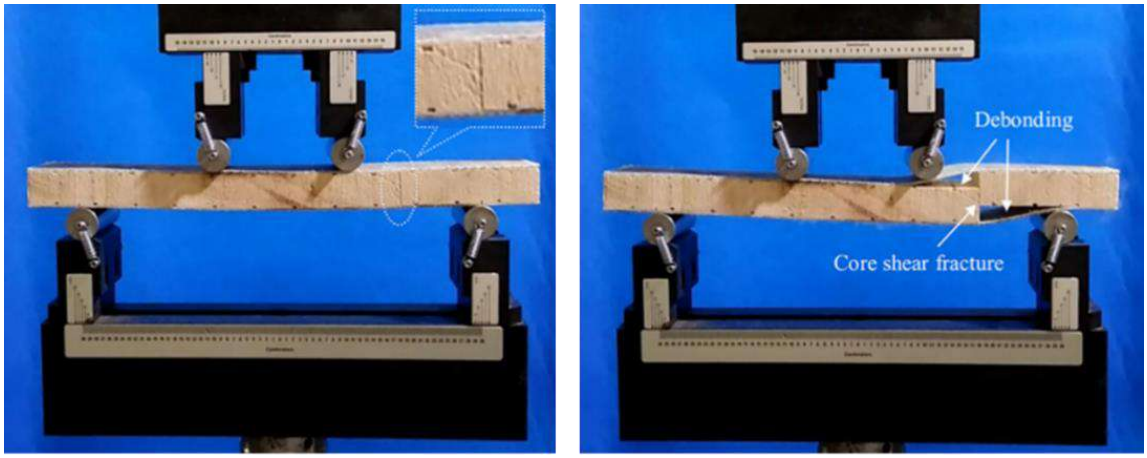

(b) Damage evolution of GFRP-balsa sandwich.

Fig. 1-12. 4-point bending behaviors and damage modes of GFRP-balsa sandwich [70].

1.3.2.2. Damage mechanisms of honeycomb sandwich structures

Honeycomb sandwich structures are prone to fail due to the core failure, including shear failure and indentation by local crushing in the vicinity of the application load [66, 72], depending on the shear and compressive/tensile stress distributions of the sandwich beam under 3-point or 4-point bending. Xie S et al. [73] have studied the static 3-point bending behaviors of an aluminum skin and Nomex honeycomb core sandwich panel (see Fig. 1-13), and concluded that the force/displacement curve can be divided into two stages by peak load: (1) Pre-buckling stage from point O to B: it indicates

linear elastic deformation, and the slope of the straight line is the stiffness of the sandwich; (2) Post-buckling stage from point B to the end: the force has a rapid drop after reaching the peak load, and then reaches a wide platform stage, where the overall bearing capacity of the sandwich decreases fast and most of the energy is absorbed in this stage.

Wu X et al. [74] also investigated the static and fatigue 3-point bending behaviors of CFRP-Nomex honeycomb sandwich panels (see Fig. 1-14), and obtained similar force/displacement curves to Fig. 1-13. They have observed that the main damage modes of honeycomb sandwich are core wrinkling, buckling, skin fracture and delamination in both static and fatigue 3-point bending tests.

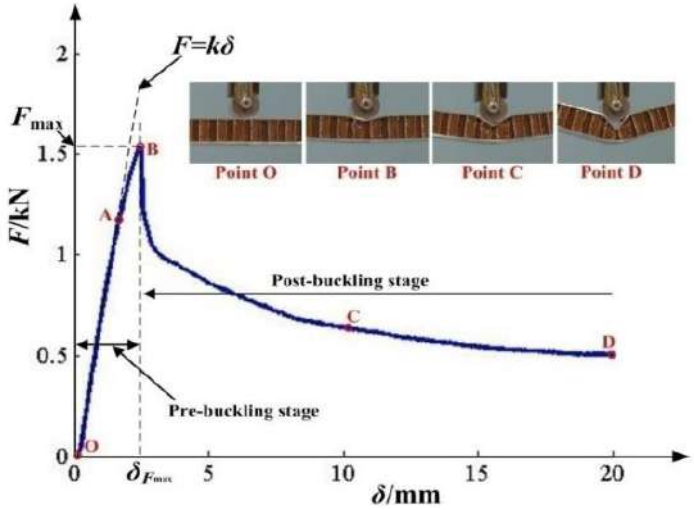

Fig. 1-13. 3-point bending force-displacement curve of Aluminum-Nomex honeycomb sandwich [73].

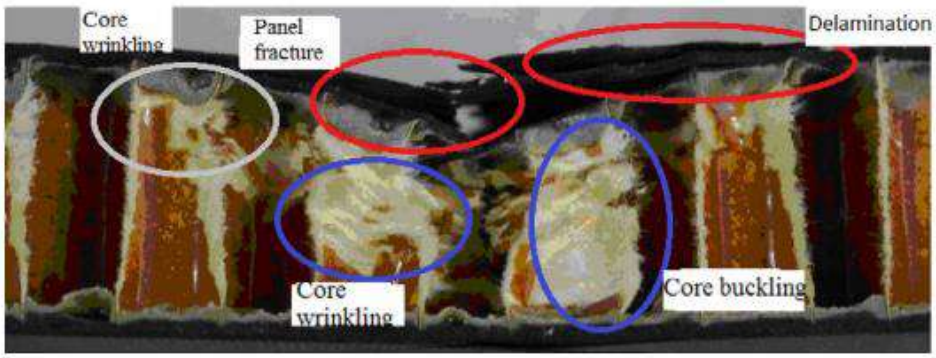

Fig. 1-14. Damage modes of CFRP-honeycomb sandwich under static 3-point loading [74].

Palomba G et al. [75] have reported that four regions can be distinguished for aluminum-Nomex honeycomb sandwiches under 4-point bending loading with a displacement rate of 2 mm/s (see Fig. 1-15): (1) the first linear elastic stage OA, where the core shear stress is uniform through thickness and only small local cell wall buckling exists; (2) the second non-linear stage AB, where core begins to yield and typical core buckling can be observed; (3) the third decreasing stage BC, where the load

shows obvious decrease and the plastic buckling of the cell wall initiates; (4) the final platform after point C, where the progressive core buckling and wrinkling dominate.

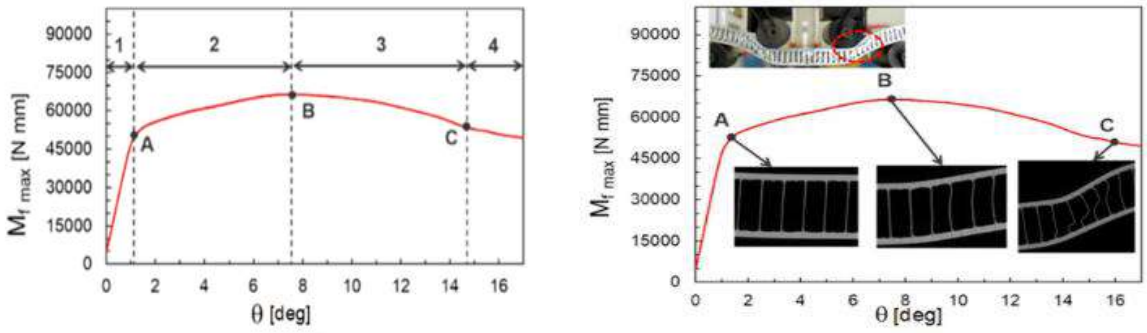

(a) 4-point bending behaviors (b) Tomographic images of the damages

Fig. 1-15. Damage modes of Aluminum-honeycomb sandwich under static 4-point loading [75].

Belouettar S et al. [76] investigated the static and fatigue 4-point bending behaviors of aluminum skin and Nomex honeycomb core sandwich structures. The visual and optical observations made on the damaged sandwiches point out that the failure modes depend essentially on the nature of the core, including material property, density, thickness, cell sizes and orientations (L or W), etc. As seen in Fig. 1-16, for W-oriented honeycomb sandwich, the failure was characterized by small cell wall buckling, small indentation of the skin in the vicinity of the loading application and a plastic deformation of the compressive skin. For L-oriented honeycomb sandwich, the failure was mainly due to a significant cell wall buckling and skin wrinkling in the vicinity of the load application zones.

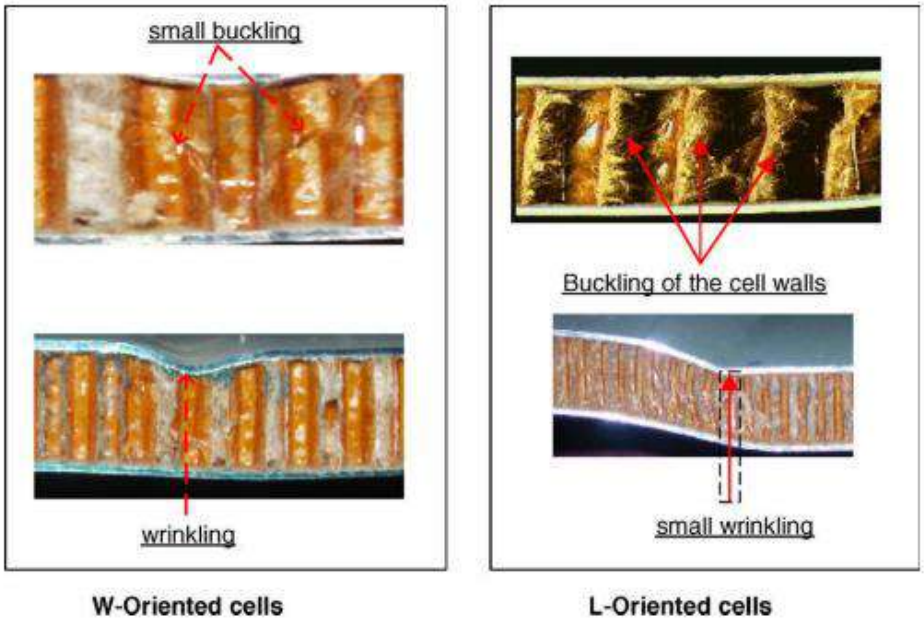

Fig. 1-16. Damage modes of Nomex honeycomb sandwich under static 4-point loading [76].

In summary, under 3-point or 4-point bending, balsa cored sandwich may show various damages, including skin fracture, balsa shear cracks and skin/core debonding, while honeycomb cored sandwich mainly shows honeycomb cell wall buckling and skin wrinkling. Thus, itis difficult to predict the damage evolution process under different experimental conditions. When the specimen has absorbed some water, the damage mechanisms can become much more complicated, due to the comprehensive moisture effects on skins, core and skin/core interfaces. This will be explained in the next part.

1.3.3. Moisture effects on damage mechanisms of sandwich structures

Moisture absorption will have great effects on the laminated skins, balsa/honeycomb cores and skin/core interfaces of sandwich structures simultaneously [36-37, 77-79]. One challenge is to discriminate the moisture effects on the different constituents of sandwiches.

1.3.3.1. Moisture effects on properties of laminated skins

Water molecules can penetrate into composite laminates by both physical diffusion and chemical decomposition [78-79]. Water molecules which are absorbed mainly through the micro voids and pores are called free water, while those dispersed in the polymer matrix and attached to the polar groups of the polymer are identified as bound water. Moisture diffusion by free water is the dominate mechanism during water immersion process, based on the capillary mechanism. Free water will penetrate into fiber-reinforced composite through micro-cracks and mainly reduce the interfacial adhesion between fiber and matrix [78], causing the swelling of fibers, matrix cracking, fiber/matrix debonding, and then the delamination (see Fig. 1-17).

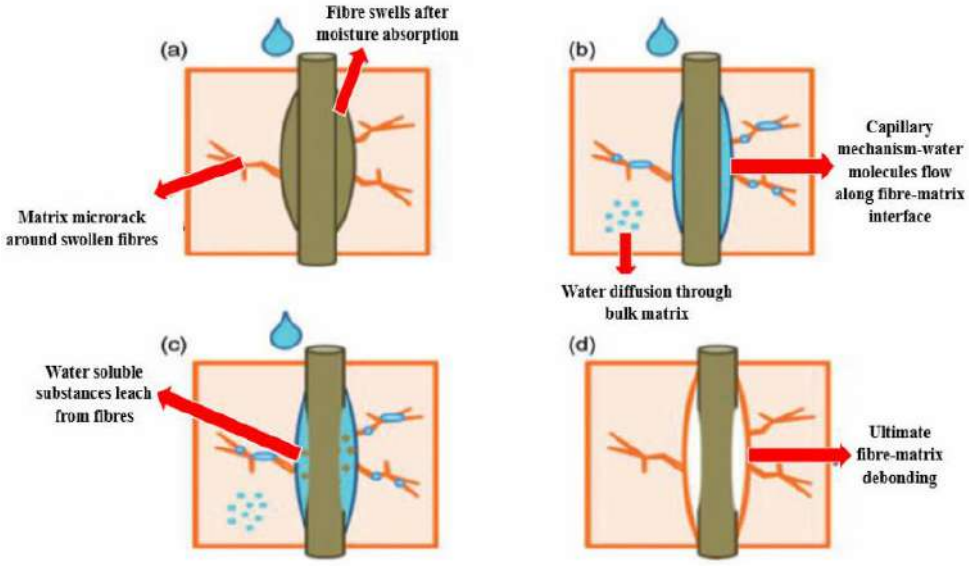

Fig. 1-17. Moisture effects on fiber/matrix interface of composite laminates [78].

1.3.3.2. Moisture effects on properties of core materials

1.3.3.2.1 Moisture effects on mechanical properties of balsa wood

The hydrophilic behavior of plant fibers, is mainly due to two factors: their composition and their specific structure. In wood material, free water is the liquid water found in cell lumens and other void spaces, while bound water comes from water molecules that penetrate the cell walls and chemically bound to cellulose molecules. Generally, one of the most important factors controlling the water diffusion phenomenon in polymeric materials is the molecular interaction occurring between the diffusing compound and the substrate [80]. In plant fibers, components have polar groups and thus are responsible for absorbing moisture are cellulose, hemicellulose, pectin and lignin.

Hence, as explained in section 1.2.1.2, due to the constituents and cellular microstructure [22, 27] of balsa wood (see Fig. 1-3), free water mainly penetrates into the porous sap channels and bound water could move into the axial tracheids containing hydrophilic polymers including cellulose, hemicellulose and lignin, which finally results in a high moisture absorption rate of balsa wood and great effects on the axial mechanical property [81].

Sadler et al. [55] have investigated that balsa wood had a significant deterioration of compressive strength/stiffness after long-term (500 days) water immersion tests (see Fig. 1-18), compared to PVC foam cores. They also verified that sea water affects more on the compression properties than the tap water.

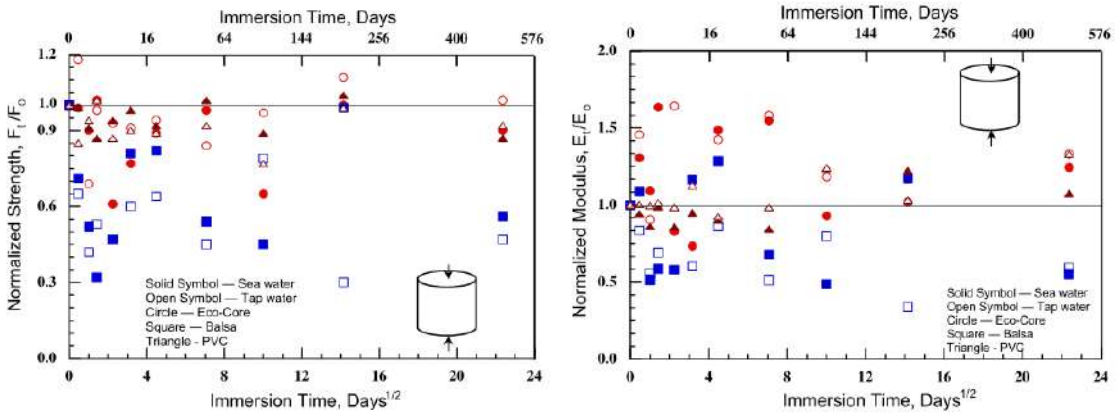

(a) Compressive strength. (b) Compressive stiffness.

Fig. 1-18. Normalized compressive property change after immersion in sea and tap water [55].

Considering moisture effects on the mechanical properties in different directions of wood, Gerhards et al. [81] have also demonstrated that moisture absorption could have the least effect on the axial tensile strength of clear wood, while the greatest effect on the axial compressive strength, after water immersion until 12% MC at about 20 ℃. It indicates that moisture effects on the compressive

property of balsa wood is more important and worth further studying, but few researches have been focused on the moisture absorption behaviors of balsa wood. Thus, it needs further investigations of moisture effects on mechanical properties of pure balsa wood and balsa core of the sandwich.

1.3.3.2.2 Moisture effects on mechanical properties of honeycomb

Since the pure honeycomb panels made of many hollow cells are usually bonded to other panels such as metal and composite to compose a useful structure, few references [82] could be found about moisture effects on mechanical properties of pure honeycomb material. Feng A et al. [82] have demonstrated that the honeycomb polyester fiber could have excellent moisture absorption and liberation ability. Its initial moisture absorption and liberation rates are much faster than those of the normal polyester fiber (see Fig. 1-19). So, it is necessary to further study the moisture absorption behavior of honeycomb panels.

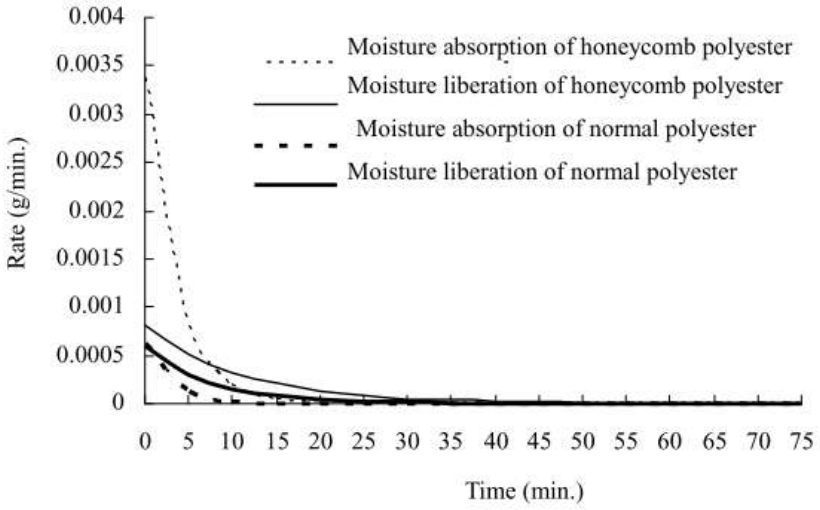

Fig. 1-19. Rate curves of moisture absorption and liberation of two fibers [82].

When honeycomb serves as the core of the sandwich, there are also few references, but some useful conclusions have been obtained by Radtke T C et al. [83]. They have studied moisture effects on the flatwise tension strength of honeycomb sandwich by direct ingress of liquid water and diffusion of humidity for 52 weeks. They have concluded that moisture can enter the sandwich via three primary means: 1) poor or damaged or degraded seals around penetrations or the edges of panels; 2) direct ingress through damaged skins; 3) diffusion of moisture through the epoxy matrix in composite skins. The specimens failed mainly due to skin/core adhesive bonding degradation and honeycomb core corrosion. Finally, it has been proven that moisture transport in the honeycomb core can be directional and biased along the ribbon direction due to the presence of adhesive node bonds. Thus, moisture absorption behavior of honeycomb panel is related to the L and W dimensions, which should be considered carefully.

1.3.3.3. Moisture effects on properties of skin/core interfaces

Skin/core interface is a very sensitive area of the sandwich structure, especially when considering the effects of moisture absorption. The internal stresses induced by moisture absorption in GFRP-balsa sandwich panels have been studied by Vincent Legrand et al. [36]. The sandwich panels (128.20*126.10**20.10 mm^3) were dried in an oven at 50°C until the weight stabilization and then immersed in distilled water at 40°C until the full water saturation for 80 days. A new analytical model for the calculation of the effective diffusivities was proposed by solving the homogenous problem. Fig. 1-20 presents the evolution of the internal hygroscopic stresses through the thickness of the sandwich panel. It shows that the compressive stresses (σ_{xx}, σ_{yy}) exist in the balsa core (thickness e is smaller than 8 mm) after different days of water immersion. These stresses could give the composite skins a role in limiting the hygroscopic expansion of the balsa core which delaminates. The skins are in traction in this case. Thus, the change of the stress state at the skin/core interface (thickness e is 8 mm) shows that the skin/core interface is an important sensible area after moisture absorption [37-38].

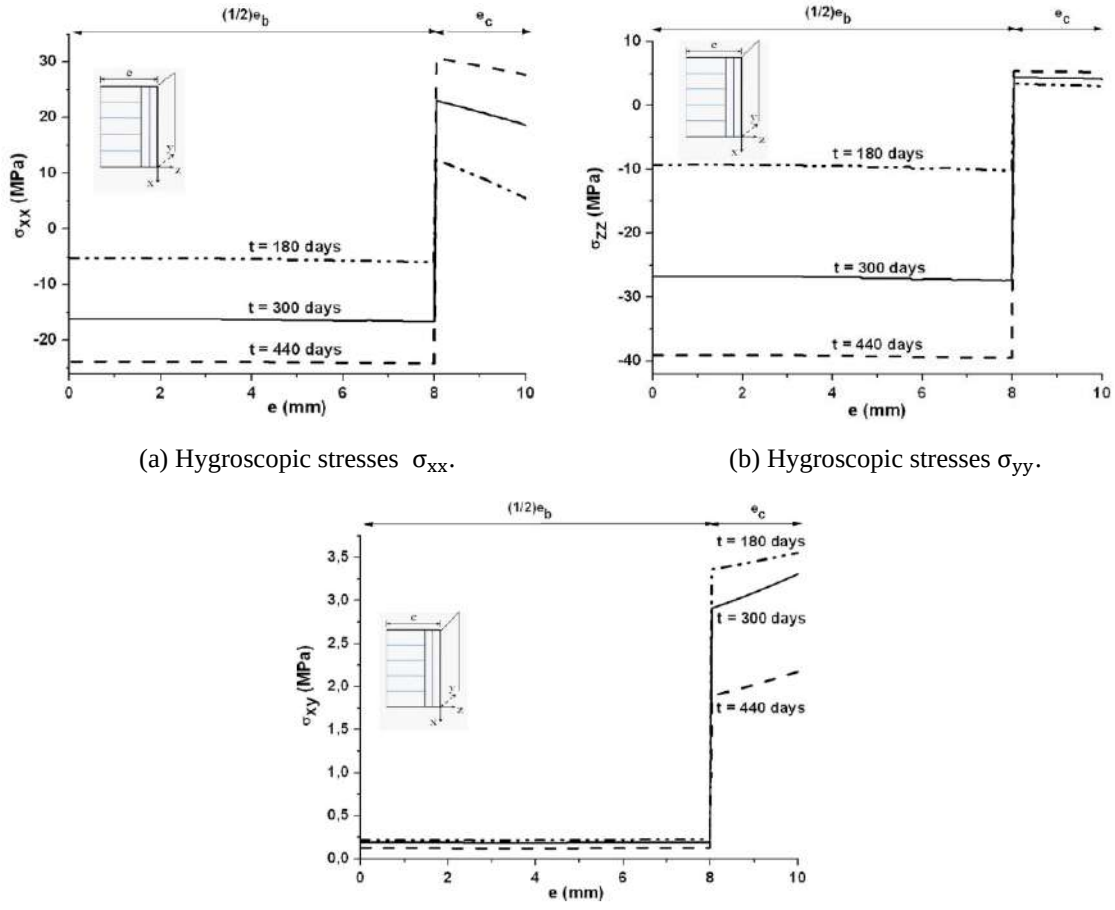

(a) Hygroscopic stresses σ_{xx}. (b) Hygroscopic stresses σ_{yy}.

(c) Hygroscopic shear stresses σ_{xy}.

Fig. 1-20. Variation of hygroscopic stresses through the thickness of the sandwich plate [36].

Veazie D R et al. [84] have investigated the hygrothermal effects on the interfacial fracture toughness of GFRP-PVC foam sandwich beams by DCB tests, reporting that the elevated temperature contributes greatest to the PVC core degradation, whereas the water immersion mostly degrades the skin/core interface. The crack paths in wet GFRP-foam sandwiches tend to stay close to the skin/core interface, while deviate into the interior of the foam core under the dry condition in DCB fracture test. Cantwell W J et al. [16, 85] have demonstrated that water immersion could result in the increase of critical interfacial fracture energies (G_C) of balsa sandwiches, while the decrease of those of honeycomb and foam sandwiches (see Fig. 1-21) by seawater immersion at 70°C until moisture saturation. The saturated MC of balsa sandwich, linear PVC foam sandwich, crosslinked foam sandwich and aluminum honeycomb sandwich is 6.25%, 5.49%, 2.5% and 1.98%, respectively. It indicates that balsa sandwich has the highest water absorption rate under the same condition.

G_C is the parameter of fracture mechanics which measures the amount of energy required to extend a crack over a unit surface area of an adhesive structural bond. So, it means that the skin/core interface debonding of the wet balsa sandwich is less prone to occur, while the skin/core interface debonding of the wet honeycomb sandwich is more likely to appear. Cantwell thought that the increase of G_C of balsa sandwich is because that the absorbed water could degrade the fiber/matrix interface, resulting in greater amounts of fiber bridging [16] and greater energy absorption after immersion. This conclusion is interesting, but the phenomenological explanation is still not clearly established and needs further investigation.

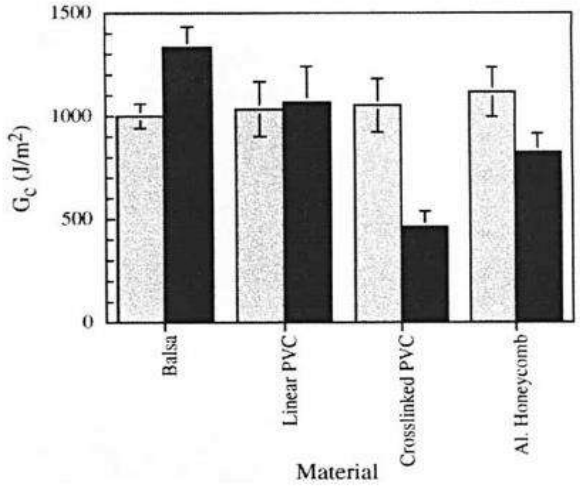

Fig. 1-21. Dry (gray) and wet (black) interfacial fracture properties of different DCB sandwich beams [85].

1.3.4. Conclusions and challenges

In conclusion, due to the complex anisotropic properties of different constituents and the loading condition, the stress distributions and bending responses of different honeycomb and balsa

sandwiches show obvious difference. The influence of moisture on the bending behaviors of the sandwich structure is also a topic that is poorly explained and requires more in-depth research. Accordingly, some new techniques shall be used to help investigate the damage initiation and evolution process of balsa and honeycomb sandwiches, for example, Non-Destructive Testing (NDT) methods [86-87].

1.4. NDT techniques for monitoring damage mechanisms of sandwich structures

1.4.1. Overviews of NDT techniques for composite structures

NDT techniques have been widely applied in aviation and other industries due to the abilities to achieve the in-situ detection of internal damages of composites without damaging the structural integrity. According to the testing situation, NDT methods could be categorized into two groups [88-92]:

- Active NDT, which can verify the composite structure integrity at any precise moment, especially for identifying the manufacturing defects and damages after loading, mainly includes active InfraRed Thermography (IRT), Ultrasonic Testing (UT), Acousto-Ultrasound (AU), Radiography Testing and Shearography Testing;
- Passive NDT, which can monitor and trace the degradation process of composite structures, especially used for Structural Health Monitoring (SHM) during the whole service life, mainly includes passive InfraRed Thermography (IRT) and Acoustic Emission (AE).

NDT techniques can also be understood based on the physical principles from the wave theory. AE is based on the stress wave, UT and AU are based on the acoustic wave, while IRT and X-Ray are based on the electromagnetic wave. The advantages and limitations of common NDT methods are shown in Table 1-1.

Table 1-1. Advantages and limitations of different NDT techniques [88-92].

NDT Techniques	**Wave propagation**	**Advantages**	**Limitations**
AE	Stress wave	Damage localization and classification; In-situ monitoring in real time;	Data process is complicated; Acoustic attenuation; High sensor sensitivity; Sensitive to environmental noise;
AU	Acoustic wave	Active AE method; Simple and rapid; High accuracy;	Acoustic attenuation; High sensor sensitivity; Sensitive to environmental noise;

UT	Acoustic wave	Precise detection (size and position); Damage depth detection; Lower costs;	Repeated scanning requiring higher skills of the operator; Local area detection; Not practical for large composite structures;
IRT	Infrared wave	Non-contact detecting; In-situ monitoring in real time; Damage detection/localization; Fast and high resolution;	Not good for deep damages and thermal insulated materials; Sensitive to room temperature and acoustic noise;
X-Ray	X rays	Non-contact detecting; Internal damage detection; Practical for almost all materials;	Expensive; Harmful to personnel health;

Most NDT methods are contact testing while non-contact techniques such as IRT and radiography have become more popular in recent years [90-92]. The abilities of different NDT methods to detect various damages of composites are different, so coupling two or three NDT methods to better detect and monitor the damages will contribute more to the study of damage mechanisms. It can raise the possibility to know exactly more about when and where what kinds of damages have initiate and propagate in the composite structures. For sandwich structures, more than three damage mechanisms may appear simultaneously under bending load, so it will be more powerful when combining two or more NDT methods to help investigate the characteristics of different damage modes.

Over the last ten decades, our team of laboratory ICA in IUT Tarbes has been working on the application of IRT and AE on monitoring damages in the composite laminate [88, 93] and wood structures [94-95], and some useful conclusions have been made. However, it still needs further exploration about what IRT and AE can further work on the sandwich structures. The coupling of these two diagnostic techniques will help understand the bending behaviors and damage mechanisms of the complicated sandwich structures.

1.4.2. Monitoring damages by Acoustic Emission (AE)

1.4.2.1. Data acquisition principle of AE

Acoustic Emission (AE) [96-97] is based on the radiation of transient stress waves in solids when a material undergoes irreversible changes in its internal structure. It is different from other NDT

techniques in two major ways, that is, listening to the energy released by the propagated damage naturally or the simulated signals such as pencil lead breakings, and monitoring the structure dynamically and continuously [98]. Sources of acoustic emission wave may come from the interface debonding, fiber fracture, plastic deformation, crack propagation, impact, friction, etc. [99]. Generally, AE monitoring could be conducted by connecting the sensors, pre-amplifiers and data acquisition system, as illustrated in Fig. 1-22 [100].

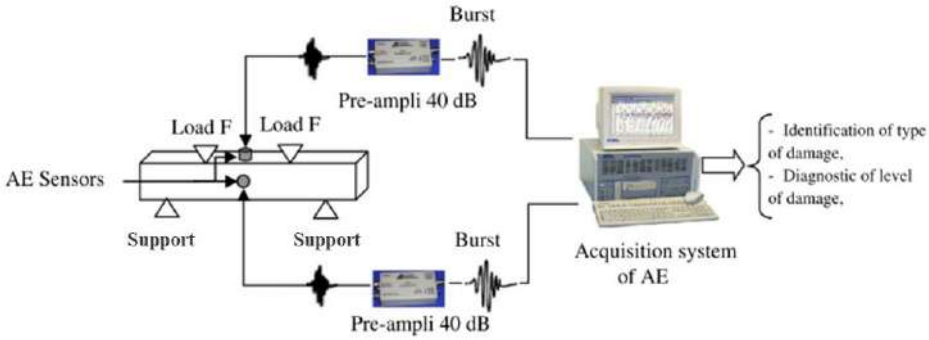

Fig. 1-22. Experimental setup of AE system under 4-point bending loading [100].

AE technique mainly depends on the sensors to convert mechanical waves into electrical voltage signals, and the output signals reflected on the computer are the combination of AE source waves, propagation properties (attenuation and wave velocity), sensor types, parameter setup, etc. For example, the level and quality of background noise determine the setup of threshold, which ensures that only useful signals from the structure can be recorded. Accordingly, the analysis of acoustic signals is very complex [101]. The conserved waveforms and their parameter characteristics are often studied to understand the recordable AE data, as shown in Fig. 1-23 [104].

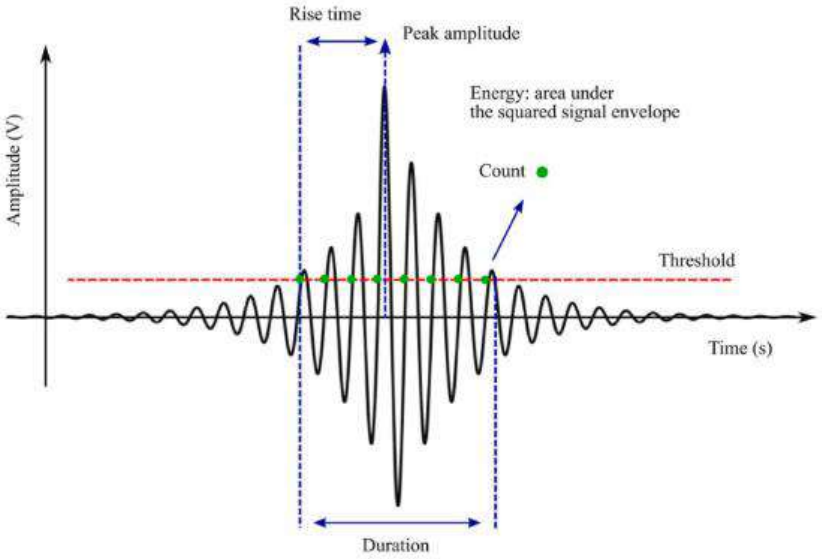

Fig. 1-23. Characteristics of one hit of acoustic emission wave [104].

The waveform analysis is to study the raw waveform of the signals in time domain, frequency domain or time-frequency domain. For example, the power spectrum of the different damage mode can correspond to the various dominant frequency range, so it can give some useful information about the identification of different damage mechanisms of the composite structures [102-103]. But the raw waveform contains too much information, and sometimes it requires too much storage space and time to process all the data. And it is difficult to remove the useless information, normally, some complicated algorithms are needed. However, the parametric analysis is a much easier and faster way to study the characteristics of the AE signals by analyzing the predominant parameters in Fig. 1-23.

These AE parameters are highly dependent on the material and geometry properties, the sensor types and the loading conditions, etc. The counts, amplitude, duration, energy, rise time and peak frequency [104-105] have been proven to be the most meaningful parameters to distinguish different damage modes of composite structures. For example, it has been proven that the low amplitude signals are corresponding to the matrix cracking of composites, the intermediate signals are delamination, and the highest amplitude signals are fiber breakage in most loading cases [104]. But one important problem is the choice of the most useful parameter, using only one parameter is not enough to classify the complicated damage modes [106-107], so coupling several parameters such as amplitude, duration and frequency have been an important topic, and this is what we want to make it clear in this work.

1.4.2.2. Post-processing of AE data by clustering algorithms

In order to find the correlations between AE parameters and different damage modes of composite structures, the clustering algorithms [109-111] are often used to improve the classification of AE signal. As seen in Fig. 1-22, the characteristics of the predominant parameters of different damage modes have some difference, the classification of the signals is to group the AE signal into several clusters with different centers, based on all the related parameters. If the expected number k of the clusters and the properties of each cluster are unknown, an Unsupervised Pattern Recognition (UPR) [106-107] method should be used. When the number of damage mechanisms and the characteristics of each cluster are known prior, a Supervised Pattern Recognition (SPR) [108] can be used. Thus, UPR method is often used firstly to train the data of a certain material and create a database of the corresponding damage mechanisms, and then SPR method can be used to classify and verify damages on the other specimens made of the same materials.

Several clustering methods belonging to UPR analysis have been built in Noesis software [112] connected to AEwin software [113], including Max-Min Distance, K-Means, Forgy, Isodata (K-Means + Forgy), etc [93, 95, 111]. Max-Min Distance is a simple algorithm suitable for identifying

extreme value data points. It can be used for selecting the initial partition points to be refined. For example, apply Max-Min Distance and use the cluster centers for initial partitioning in another algorithm [112].

K-Means is designed to identify Gaussian clusters when the number of clusters is known. It means that the clusters can be generally described to have a Gaussian distribution around their cluster center [95, 112]. It aims to partition n observations into k clusters in which each observation belongs to the cluster whose center is nearest. K-means clustering is an easy way to use the algorithm with basically a single input required: desired number of clusters.

Forgy is developed on the basis of the K-Means algorithm with additional functions which can control the minimum size and spread of the clusters. It is used for the same data categories as K-Means and offers the better control of the clustering. Heuristic procedures are implemented for the creation of new clusters, if a pattern/hit is sufficiently separated from the existing clusters, and for deleting existing small classes with fewer than the minimum requested patterns/hits.

Isodata is basically a combination of K-Means and Forgy, supplemented with a set of heuristic procedures implemented in an iterative scheme [43]. Compared with the Forgy algorithm, which is also based on K-Means, the Isodata algorithm is even more generalized and incorporates automated procedures for splitting large classes into two parts as well as for merging classes with insufficient separation. Although the Isodata algorithm offers high flexibility and can be used for a variety of data structures, it requires a great deal of experimentation for selecting suitable values for the various parameters.

In summary, K-Means is the most basic and useful algorithm which has been used by many authors [48, 101-102, 106, 110-111] in the damage characterization of composites, but few related researches can be found on honeycomb and balsa sandwiches. During the utilization of K-means method, the selection of optimum pertinent AE parameters and optimization of suitable cluster number k are the main key points to generate the robust damage classification results. Fig. 1-24 shows an example of the iteration procedure of K-Means algorithm [111].

The scenario shown in Fig. 1-24 concerns two groups of signals. The two cluster centers (red and blue points in Fig. 1-24. (b)) are defined randomly. The first iteration step is finished by calculating the Euclidean distance between each signal and the two cluster centers, and assigning the signal to the cluster which shows the smallest Euclidean distance, as seen in Fig. 1-24. (c). After the first iteration, the two cluster centers are calculated again and the new centers are obtained, as seen in Fig. 1-24. (d). Then the second iteration step is performed in the same way as the first step by using the new cluster centers, and the second clustering results are obtained, as seen in Fig. 1-24. (e). Similarly,

the third cluster centers are calculated, as seen in Fig. 1-24. (f). These iteration steps will be repeated until the cluster centers are finally stable without changing.

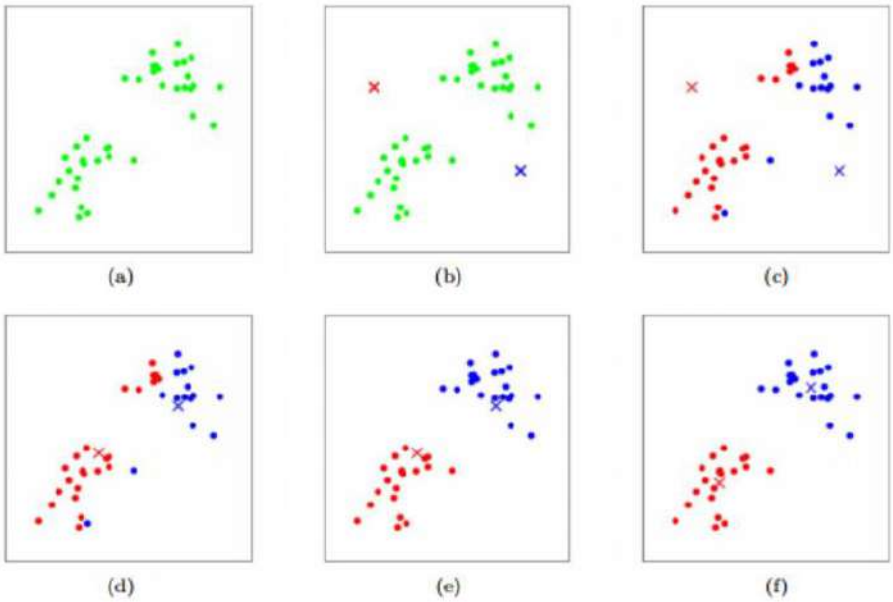

Fig. 1-24. An example of iteration procedure of K-means algorithm [112].

To study algorithms based on K-means, it is necessary to introduce a first set of descriptors on which the analysis will be based as well as to define a number of classes. According to the literatures [48, 101-102, 106, 110-111], the identification of damage mechanisms is often made from the analysis of the following eleven descriptors: energy, amplitude, duration, rise time, counts, counts to peak, average frequency, frequency centroid, peak frequency, initiation frequency and reverberation frequency.

Next, in order to determine the optimal cluster number, two criteria have been adopted to evaluate the performance of an algorithm [106, 108, 113]. Most authors [106, 108, 111] firstly analyze the coefficients R_{DB} and Tou from the view of statistics, in fact, the real physical damage modes of the structure shall be also considered to determine the cluster number k. Only by considering both the two criteria, the most convincing classification results can be obtained.

The two statistic criteria, Davis-Bouldin validity index R_{DB} and Tou, are heuristic criteria based on the ratio of average within-class distances to the distances between classes. R_{DB} criterion [108, 113] is an average measure of the ratio of within-class distances to the distances between classes, calculated using all of the different pair of classes, as Eq. 1-8 shows. The cluster result is the optimum when R_{DB} is the minimum. It could be affected by the number of AE parameters and classes.

$$R_{DB} = \frac{1}{k}\sum_{i=1}^{k} \max\left(\frac{d_i + d_j}{D_{ij}}\right) \tag{1-8}$$

Where k is the class number; d_i and d_j are the average distances within the class i and j, respectively; D_{ij} is the distance between the class i and j; i, j, k=1, 2, ……, n; $i \neq j$.

Tou criterion [113] is defined as ratio of the minimum distance between any pair of classes to the maximum of the average within-class distances, not considering the average ratio, so it is often used as the complement validation of R_{DB}, as Eq. 1-9 shows. The higher the Tou criterion is, the higher the discrimination efficiency will be.

$$\mathrm{Tou} = \frac{\min(D_{ij})}{\max(d_k)} \tag{1-9}$$

Where D_{ij} is the distance between the class i and j; d_k is the average distance within the class k; i, j, k =1, 2, ……, n.

Finally, coefficients of R_{DB} and Tou can be used to evaluate the optimum class number, but should be combined with the real damage mechanisms [114-116].

1.4.2.3. Damage classification of honeycomb/foam sandwiches by AE

Based on the post-processing analysis via clustering algorithms, correlations between AE parameters and damage mechanisms of composite sandwich structures are concluded in Table 1-2 [116-121]. Quispitupa A et al. [119] have studied AE-based tensile characteristics of CFRP-honeycomb sandwiches by static and fatigues tests, indicating that the predominant failure could be the core damage, followed by skin/core interfacial debonding, resin cracking and fiber rupture. Fotouhi M et al. [120] et Pashmforoush F et al. [109] have demonstrated that frequency domain analysis could be an efficient tool for identification and discrimination of different damages mechanisms for mode I delamination in woven GFRP-foam sandwiches in DCB tests. It was also found that core failure was followed by interfacial adhesive debonding, matrix cracking and fiber breakage.

For bending behaviors of composite sandwich structures, Tabrizi I E et al. [121] determined the failure sequence and damage classification of GFRP-honeycomb sandwiches under 3-point bending by analyzing peak frequency and duration distributions, concluding that the major damages initiate as core failure, followed by skin/core debonding, matrix cracking and fiber breakage. Masmoudi S et al. [116] compared AE amplitude and waveforms corresponding to different damage mechanisms of E-glass fiber-PVC foam sandwiches under 3-point bending, indicating that core damage was the most dominant, followed by resin cracking, interfacial debonding and fiber breakage.

While Assarar et al. [114] have reported that matrix cracking of E-glass fiber-PVC foam sandwiches appeared firstly and is the predominant damage mode, followed by fiber/matrix debonding (40-75 dB), skin/core debonding, skin delamination (50-85 dB) and fiber breakage in 3-point bending tests,

based on amplitude distributions using K-means algorithm. Ammar I B et al. [100] investigated that PVC foam density could can affect AE amplitude and counts distributions of different damage mechanisms under 4-point bending, by comparing two kinds of sandwich specimens with different PVC foam density: 60 kg/m^3 and 100 kg/m^3.

Table 1-2. Characteristics of AE parameters of composite sandwich structures [116-121].

References	Materials	Loading condition	Sensor type	AE parameters	Core damage	Skin/core debonding	Matrix cracking	Fiber breakage
Quispitupa A et al. [119]	CFRP-honeycomb	Tensile test	Two piezoelectric sensors	Amplitude (dB)	45-60	60-80	80-90	above 90
Fotouhi M et al. [120] and Pashmforoush F et al. [109]	GFRP-foam	DCB tests	Two resonance sensors (513.28 kHz)	Amplitude (dB)	40-60	60-80	75-85	85-105
				Dominant Frequency (kHz)	35-65	100-130	170-250	350-450
Tabrizi I E et al. [121]	GFRP-honeycomb	3-point bending	Two resonance sensors (550 kHz)	Duration (μs)	0-500	0-550	0-350	350-1000
				Peak Frequency (kHz)	300-500	70-250	0-70	0-120
Masmoudi S et al. [116]	E-glass fiber-PVC foam	3-point bending	Four WB sensors (100 kH-1 MHz)	Amplitude (dB)	41-60	72-93	41-78	above 92
Assarar et al. [114]	E-glass fiber-PVC foam	3-point bending	Two WB sensors (100 kH-1 MHz)	Amplitude (dB)	-	50-90	40-65	80-100
Ammar I B et al. [100]	E-glass fiber-PVC foam	4-point bending	Two WB sensors (100 kH-1 MHz)	Amplitude (dB)	30-70	80-90	60-80	above 90

In summary, most foam and honeycomb sandwich specimens under bending loading failed due to core shear damages, skin/core debonding and a few skin damages including matrix cracking, fiber/matrix debonding and fiber breakage. When concerning AE-based damage characterization of sandwich structures under 3-point or 4-point bending, more useful conclusions have been reported on foam sandwich, but few could be found on balsa or honeycomb sandwich. Furthermore, most AE parameter analysis has been based on amplitude and energy distributions. The correlations between damage mechanisms of sandwich structures and parameters such as peak frequency and duration have not been clearly demonstrated.

1.4.2.4. Damage initiation identification of laminates by AE

In addition, for composite laminates, it has been demonstrated that damage sequences identified by AE could be matrix cracking, fiber/matrix debonding, delamination and fiber breakage in most tensile [110, 115] and bending [116] tests, mainly by analyzing AE amplitude and energy distributions using clustering algorithms. To be emphasized, the cumulative counts [101-102, 104, 117] have been proven to be effective for identification of the crack front, crack opening and crack propagation path of composite laminates (see Fig. 1-25) by very few authors, while cumulative acoustic energy [118] can be used to identify the crack opening and propagation in the fiber reinforced composites, for example, the onset of delamination in mode I fracture tests. However, for damage initiation of sandwich structures, it is not clear whether the cumulative counts and energy could give useful information.

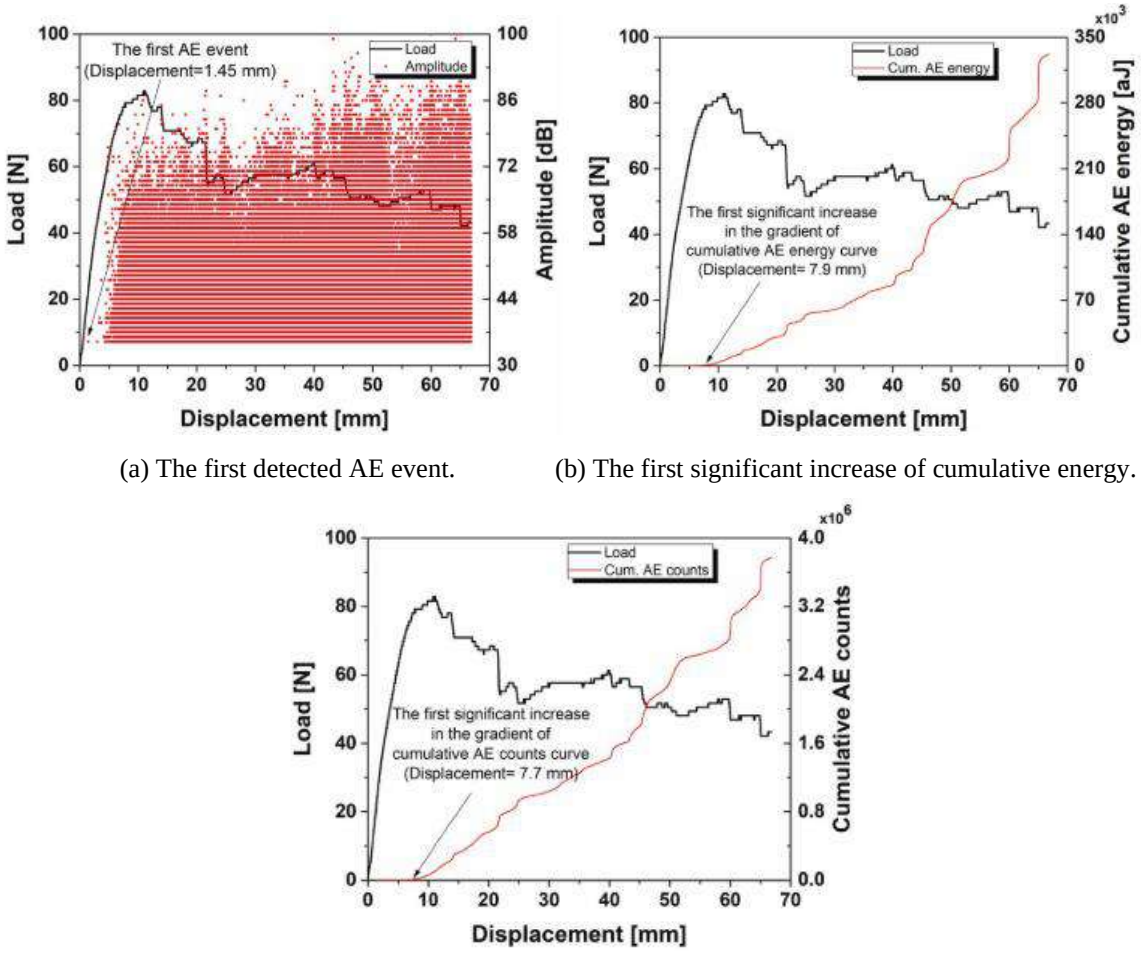

(a) The first detected AE event.

(b) The first significant increase of cumulative energy.

(c) The first significant increase of cumulative AE counts.

Fig. 1-25. Damage initiation detection in glass/epoxy DCB specimen by different AE parameters [104].

Andrew J J et al. [117] showed that AE cumulative count curve exhibits three distinct damage zones for the considered glass/epoxy laminates under quasi static compression test. The damage profile includes three stages (see Fig. 1-26):

I. AE cumulative counts initiates (Location 1) directly after the onset of first damage and the curve advances with a slope closely equal to zero up to damage progression (Location 2).

II. A gradual variation in the slope of AE cumulative count curve. This moderate increment in the AE response is accentuated by the evolution of macroscopic damage modes (Location 2) like debonding of the fiber/matrix interface and minor fibre failure.

III. A steep increase in the slope of the cumulative curve (Location 3) can be observed until up to rupture (Location 4). During final stages of mechanical loading, the counts of the AE waveform were much higher, associated predominantly with fiber failure. This subsequent accumulation of different damage hits is emphasized by an exponential growth of cumulative counts.

Consequently, four locations during the compression loading have been marked as 1, 2, 3 and 4. The four consecutive points were respectively attributed:

1. Damage initiation (microscopic damage);

2. Damage propagation (occurrence of macroscopic failure);

3. Unstable damage growth (ultimate load is reached);

4. Laminate failure (rupture).

As for the bending response and AE cumulative counts, it needs further exploration, especially when composite laminate serves as the skin of the sandwich.

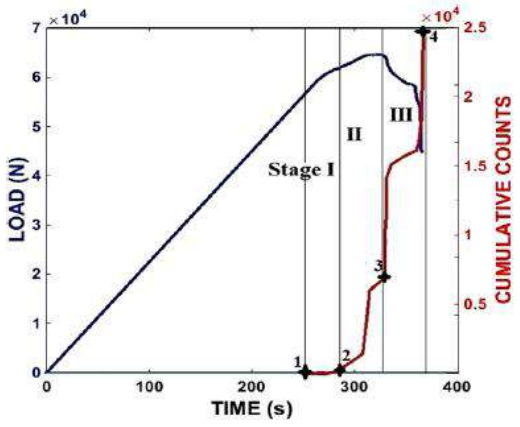

Fig. 1-26. Compression response and AE cumulative counts of glass/epoxy composite laminates [117].

1.4.2.5. Damage localization by AE

To locate the AE source, several sensors can be used to complete the linear (1D), planar (2D) or spatial (3D) location [113], allowing global monitoring [122-123]. The most common approach is based on the time of arrival (also called TOA technique). If two sensors are used (see Fig. 1-27), the

AE source is located based on the difference in the time of arrival of AE signals at the sensors and the wave velocity in the given material [124]. This approach assumes that the velocity of sound is constant in all directions and the sound is not interrupted between the AE source and the localizing sensors. However, these are not always true in strongly anisotropic composite materials, because AE wave velocity becomes direction-dependent. Wave propagation between the source and sensor may be influenced by defects, holes, moisture absorption, thickness changes, and other material and geometry factors [125].

Nevertheless, TOA location has been widely used on composite laminates. For example, Sikdar et al. [126] used TOA for AE source location in a honeycomb sandwich panel consisting of carbon fiber plates with aluminum honeycomb. Eight AE sensors were bonded to the top surface to localize three pencil lead breakage sources. The experiments were repeated with the sensor array in three different configurations: circular, rectangular and zigzag, and the zigzag has shown the best locations.

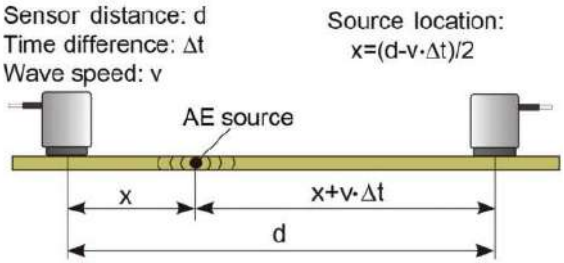

Fig. 1-27. Linear source location by two sensors [124].

Delta-T Mapping location technique relies on obtaining training time data from the structure itself, using a 2D grid with at least four AE sensors, and computing the TOAs between each pair of sensors. The arrival times of AE sources recorded from the structure can then be compared against these time maps to calculate the source locations. It was demonstrated by Abdulaziz A H et al. [125] to be more accurate at locating artificial AE sources on the honeycomb sandwich structures. However, further research needs to be devoted for optimizing the Delta-T grid to obtain a time map that is able to locate out-of-plane (3D) AE sources of sandwich structure under load.

In conclusion, for now, TOA technique has been the more popular method to localize damages of composites because it is easier to carry out and can record the data more stably. In order to locate the damage sources more accurately, AE wave propagation properties including wave velocity and attenuation, and the sensor types, number and position, have to be understood priorly to design proper damage localization strategies.

AE wave velocity [125-126] can be studied by simply generating the pencil lead breaks (Hsu-Nielsen test) on the structure surface to simulate the artificial acoustic wave source and using fixed sensors to receive the acoustic signals in any direction and position.

Theoretically, for infinite thin plates, when the wavelength is much larger than the plate thickness, Lamb wave is thought to be the dominated propagation wave. The understanding of the acoustic wave modes is usually based on the classical plate wave theory, which assumes that there exist two wave modes, the extensional/longitudinal (S_0) wave and flexural wave (A_0). Due to the Poisson effect, both modes consist of the in-plane and out-of-plane components. But the traditional extensional wave velocity equation is used to predict only the in-plane wave propagation, while the flexural wave velocity equation mainly presents the out-of-plane mode [103].

In application, wideband sensors are often located on the surface of the plate to distinguish between the two wave modes, where the extensional wave has higher velocity at lower frequency. It has been found that the delay time of the flexural mode will decrease when reducing the sensor-source distance, and the extensional wave is the predominant at the smaller pencil lead breaking angle. Consequently, using the narrowband sensor with relatively lower resonance frequency and the larger sensor-source distance can reduce the interference of the slower flexural mode on the received extensional wave signals [127].

For an isotropic plate or thin orthotropic laminate, AE wave velocity is considered as a function of in-plane Young's modulus, Poisson's ratio, and the density of the material [103]. However, it is not clear whether the traditional acoustic wave velocity formula can be applicable to thick anisotropic and heterogeneous sandwich structures. In order to apply AE technique to monitor complex damage evolution in composite sandwich structures, the further investigation and demonstration on the AE wave velocity shall be necessary and worthy. These elements will be the new construction basis of numerical and experimental models necessary for the improvement of the damage localization and the implementation of repair operations.

1.4.2.6. Conclusions

In summary, for composite sandwich structures, the major applications of AE could be classified as:

- Damage initiation identification [101-102, 117-118];
- Damage classification [116-121];
- Damage source localization [122-127];

Damage classification of composite sandwich structures has been studied a lot in different mechanical tests, while the damage initiation identification and source localization have not been

well explained because it is very difficult to consider the variation of acoustic wave propagation properties in the localization algorithms, due to the high acoustic wave attenuation and velocity variation in different directions of composite structures. In addition, most existing damage characterization work has been focused on honeycomb and foam sandwiches, for balsa sandwiches, the feasibility of AE technique is still unknown. Thus, in this work, the damage localization study in GFRP-balsa and CFRP-honeycomb sandwich structures will be firstly investigated based on the traditional linear TOA method.

1.4.3. Monitoring damages by InfraRed Thermography (IRT)

1.4.3.1. Data acquisition principle of IRT

InfraRed Thermography (IRT) is based on the recording of the thermal radiation emitted by a surface of a specimen via an infrared camera. Temperature distribution can be measured from a distance in real time without contacting the object [128-129]. Thus, IRT can be used to monitor damage initiation and evolution under load [110, 129], and detect internal defects or damaged specimens after load [129-130]. The thermal field variation is related to material properties of the structure, the thermal effusivity, diffusivity and conductivity coefficients of the constituents [128-129], as well as the stress distributions due to loading. Thus, the heat source identification of anisotropic composite under load can be complicated [130].

Based on different principles, IRT can be classified in two ways. According to the propagation directions of thermal waves, it includes:

- Reflection IRT (the heat source and IR camera are on the same side of the object);
- Transmission IRT (the heat source and IR camera are on the different sides of the object).

Based on the heat excitation pattern, IRT can be divided into passive IRT [129] and active IRT [130]:

- Passive IRT: it can monitor the structural damages without external heat excitation, for example, monitoring the crack onset and propagation during mechanical tests;
- Active IRT: it uses different kinds of heat sources to generate infrared energy on the objects, such as the halogen lamp, flash, laser, ultrasonic waves and eddy currents [130-132]. It is often used to detect the internal defects of the structure during fabrication process and service life.

Furthermore, depending on the way in which external heat supply is applied, active IRT mainly includes Pulsed Thermography (PT) [131] and Lock-in Thermography (LT) [120, 132]:

- Pulsed Thermography (PT) often uses the flash to generate pulsed signals, which can monitor a wide area very fast, but there are some difficulties in detecting deep defects of complex structures because the surface temperature can be easily affected by the environmental thermal source;
- For Lock-in Thermography (LT) (see Fig. 1-28), the surface of a specimen is periodically heated by modulated heating lamps. The excitation is defined by the magnitude and period of modulated heat, similar to sinusoid heat wave, so it is less sensitive to the environmental noise and structure surface conditions, the deep damages can be detected more easily [132].

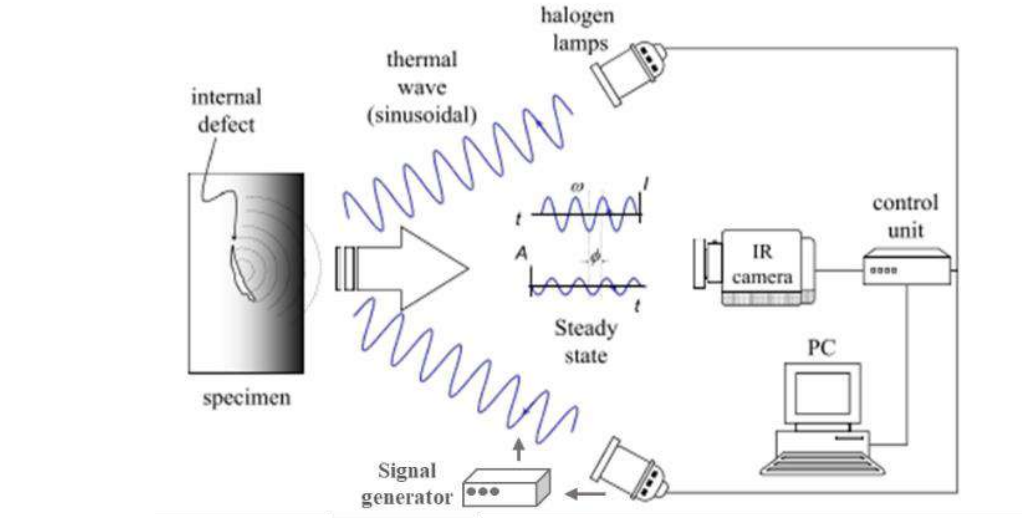

Fig. 1-28. Active Lock-in IRT system heated by halogen lamps [133].

In short conclusion, active reflection IRT is more often used to detect internal defects, while passive IRT is adopted to monitor the damage initiation and evolution of a structure due to the thermo-mechanical coupling under load [133-134]. IRT system mainly contains heat excitation instruments (only for active IRT), IR camera, and computer imaging system and processing software.

Infrared radiation is the thermal energy radiated by the surface of an object whose temperature is above zero. There are three ways in which the radiant energy striking an object may be dissipated: absorption, transmission and reflection. Three parameters are used to describe these phenomena: the spectral absorptance α_λ, which is the ratio of the spectral radiant power absorbed by the object; the spectral reflectance ρ_λ, which is the ratio of the spectral radiant power reflected by the object; the spectral transmittance τ_λ, which is the ratio of the spectral radiant power transmitted by the object [135]. The sum of these three parameters must be equal to one at any wavelength, as in Eq. (1-10):

$$\alpha_\lambda + \rho_\lambda + \tau_\lambda = 1 \tag{1-10}$$

All the three parameters depend on the considered material, surface finishing and wavelength of the incident radiation. Materials in which the transmissivity and the reflectivity are null are called

blackbodies ($\alpha_\lambda = 1$). According to Kirchhoff's law, the emissivity ε_λ and absorptivity α_λ of any material are equal at any specified temperature and wavelength [136]. This can be expressed by Eq. (1-11):

$$\varepsilon_\lambda = \alpha_\lambda \tag{1-11}$$

In fact, a real body emits only a fraction of the thermal energy emitted by a blackbody at the same temperature. Thus, the emissivity of a body is defined formally for a wavelength λ by Eq. (1-11), as the ratio of the radiant energy emitted by the body to the radiation that would be emitted by a blackbody at the same temperature.

$$\varepsilon_\lambda = W_\lambda / W_{\lambda b} \tag{1-12}$$

Where W_λ is the power emitted per unit area per unit wavelength by a real body, and $W_{\lambda b}$ is the power emitted per unit area per unit wavelength by a black body.

It is usually assumed that the emissivity can be considered as a constant ε for short wavelength intervals. Then the Stefan–Boltzmann formula can be concluded as Eq. (1-13) [137]:

$$W = \varepsilon \cdot \sigma \cdot T^4 \tag{1-13}$$

Where W is the power emitted per unit area per unit wavelength, ε is the emissivity, σ is the Stefan-Boltzmann constant and T is the temperature.

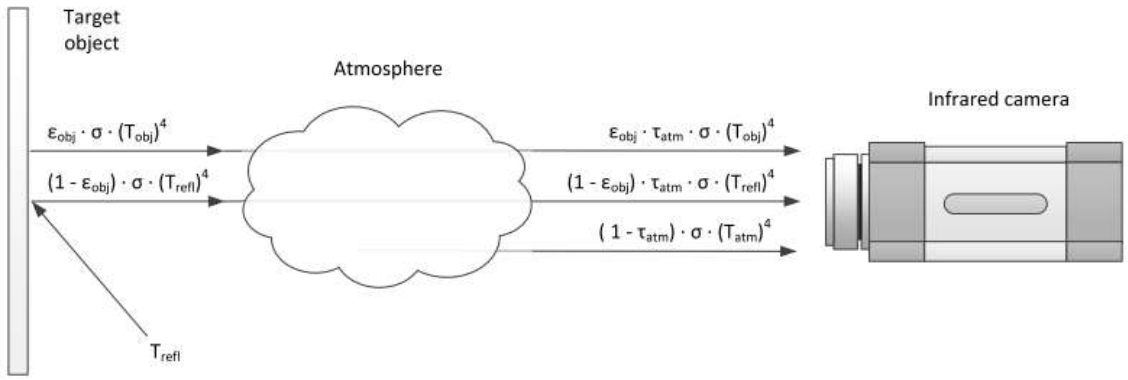

Fig. 1-29. Radiation received by the IR camera [135].

Thus, the correlation between temperature and energy released can be expressed by Eq. (1-13). It can be measured by the 2D thermal image and temperature variation data obtained by the IR camera. However, not all of the radiation received by IR camera comes from the target object (see Fig. 1-29), in order to measure temperature from the real heat source accurately, radiation from the surrounding sources must be removed. Finally, the total radiation received by the camera is from three sources, as expressed by Eq. (1-14):

$$W_{tot} = E_{obj} + E_{refl} + E_{atm} \quad (1\text{-}14a)$$

$$W_{tot} = \varepsilon_{obj} \cdot \tau_{atm} \cdot \sigma \cdot (T_{obj})^4 + (1 - \varepsilon_{obj}) \cdot \tau_{atm} \cdot \sigma \cdot (T_{refl})^4 + (1 - \tau_{atm}) \cdot \sigma \cdot (T_{atm})^4 \quad (1\text{-}14b)$$

Where E_{obj} is the emission from the target object, E_{refl} is the emission from the surroundings and reflected by the object, and E_{atm} is the emission from the atmosphere. According to Eq. (1-13), E_{obj} is coming from the emissivity of the object ε_{obj}, transmissivity of the atmosphere τ_{atm}, Stefan-Boltzmann constant σ and temperature of the object T_{obj}, as seen in Fig. 1-29. E_{refl} is decided by the emissivity ε_{obj}, transmissivity τ_{atm}, Stefan-Boltzmann constant σ and reflected temperature T_{refl}. E_{atm} is decided by the transmissivity τ_{atm}, Stefan-Boltzmann constant σ and atmosphere temperature T_{atm}.

In summary, in order to obtain the real temperature of the object Tobj, the following parameters shall be known before starting the tests: the emissivity of the object εobj, the transmissivity of the atmosphere τatm, the reflected temperature Trefl, and the atmosphere temperature (Tatm). The transmissivity of the atmosphere is generally estimated by the camera, using the distance from the object to the camera and the relative humidity. Normally, this value is very close to one ($1 - \tau atm = 0$). Thus, the emissivity εobj and the reflected temperature of the object Trefl are the most important parameters which affect the accuracy of temperature measurement [138-139].

Finally, the testing results by IRT can be affected by the heat excitation magnitude and period, IR camera resolution, environmental thermal radiation, structural surface conditions, testing direction and camera-object distance [140].

1.4.3.2. Post-processing of heat source field

In simple cases, temperature difference [135-136] can be used to evaluate the existence of material change such as voids and moisture absorption in active IRT tests, but during the loading [110, 129] of composites, the stress distribution is complicated, the temperature increase may be smaller than 1 ℃ without external heat supply, so the temperature observed by the camera can be affected by the heat loss, the environmental noise, the thermal conduction at the contact surfaces between the loading application and the specimen [141-142], etc. Hence, the temperature increase is too small to identify the real heat source coming from the induced damages, and heat diffusion equation [143] is often used to calculate the accurate heat source generated by the stress variation.

When using passive IRT method in static and fatigue tests of composites, the heat source identification is often established based on the classical principles of thermodynamics of irreversible processes, within the framework of quasi-static processes and small perturbations [93, 143]. Based on the first (energy conservation) and second (admissible evolutions) principles of thermodynamics, the following heat diffusion equation can be given:

$$\rho C\dot{T} - \mathrm{div}(\mathbf{k} \cdot \mathrm{grad}T) = s = \underbrace{d_{me} + s_{the} + s_{int}}_{s_t} + r_{ext} \tag{1-15a}$$

Where ρ is the mass density, C is the specific heat capacity and T is the absolute temperature. The term $\rho C\dot{T}$ characterizes the heat storage/absorption rate. The term $\mathrm{div}(\mathbf{k} \cdot \mathrm{grad}T)$ represents the heat conduction (heat loss) rate which is related to the overall heat source S_t produced by the material and the external heat supply r_{ext}. $\mathbf{k}$ is the thermal conductivity tensor. d_{me}, s_{the}, s_{int} and r_{ext} stand for the intrinsic (mechanical) dissipation source, thermoelastic coupling between the temperature and the strain, other thermomechanical coupling between the temperature and internal variables, and external het supply, respectively. Per unit of volume, d_1, s_{the} and s_{int} are formulized as:

$$d_{me} = \boldsymbol{\sigma} : \mathbf{D_{EU}} - \rho \frac{\partial \psi}{\partial \boldsymbol{\varepsilon}} : \dot{\boldsymbol{\varepsilon}} - \rho \frac{\partial \psi}{\partial \boldsymbol{\varepsilon}} \cdot \dot{\boldsymbol{\alpha}} \tag{1-15b}$$

$$s_{the} = \rho T \frac{\partial^2 \psi}{\partial T \, \partial \boldsymbol{\varepsilon}} : \dot{\boldsymbol{\varepsilon}} \tag{1-15c}$$

$$s_{int} = \rho T \frac{\partial^2 \psi}{\partial T \, \partial \boldsymbol{\alpha}} : \dot{\boldsymbol{\alpha}} \tag{1-15d}$$

Where $\boldsymbol{\sigma}$ is the Cauchy stress tensor, $\mathbf{D_{EU}}$ is the Eulerian strain rate tensor, ψ is the Helmholtz free energy, $\boldsymbol{\varepsilon}$ is the strain tensor**,** $\boldsymbol{\alpha_j}$ (j=2,..., n) is the components of a vector of n-1 internal variables.

To simplify Eq. (1-15a), heat source equation is often based on the following assumptions [141-143]:

1) Material thermo-physical parameters remain constant during the test, including thermal conductivity tensor $\mathbf{k}$, the mass density ρ and specific heat capacity C;

2) The temperature variation has no influence on the microstructure state; Accordingly, the coupling heat source between the temperature and internal variables, s_{ic}, is neglected;

3) The external heat supply, r_e, is time-independent;

4) The intrinsic mechanical dissipation source d_{me} and the thermoelastic heat source s_{the} are homogeneous at any time throughout the thickness of the composite structure;

Thus, a 2D heat diffusion equation (see Eq. 1-16) [110, 143] can be obtained to determine the real heat source field s during the damage evolution process under load, by considering the dependence of temperature data on time and space simultaneously.

$$\rho C\left(\frac{\partial \Delta T}{\partial t} + \frac{\Delta T + T_0 - T_{ext}}{\tau_{th}}\right) - \mathrm{div}(\mathbf{k} \cdot \mathrm{grad}\Delta T) = s_t \tag{1-16}$$

Where s_t is the real heat source, which involves the thermoelastic heat source s_{the} and intrinsic mechanical dissipation source d_{me}; T_0 is the average temperature of the first ten IRT images; T_{ext} is the room temperature; τ_{th} is the time increment which characterizes the heat convection between the

specimen and environment. $\Delta T = T - T_0$, which is the temperature difference; ρ is density; C is the specific heat; **k** is the second-order thermal conductivity tensor.

Finally, the irreversible heat source d_{me} can be obtained by Eq. (1-17):

$$d_{me} = s_t - s_{the} \tag{1-17}$$

Where $s_{the} = -\alpha T_0 \frac{\partial \boldsymbol{\sigma}}{\partial t}$. α is thermal expansion coefficient, **σ** is the stress matrix.

In addition, the Reference Area Method [129] is often used for the correction of the temporal noise. The reference area is a small portion of space contained in the field of view which is not influenced or affected by the loading during tests. The corrected signal ΔT_C could be obtained by subtracting the noise ΔT_N measured in a reference area from the raw signal ΔT_R according to Eq. (1-18):

$$\Delta T_C (i, j, t) = \Delta T_R (i, j, t) - \Delta T_N (i, j, t) \tag{1-18}$$

Where i and j indicate row and column numbers in the thermal image while t is the frame number in the sequence. The quantity ΔT_N is the mean value of ΔT evaluated in the reference area of m*n pixels for each frame in the sequence. It has been proven that the position, size and number of the reference areas can affect the measuring accuracy. So further explorations shall be developed.

Furthermore, although the above 2D heat diffusion equation has been applied to composite laminates [93, 141, 143], for the more complicated sandwich structures, it still remains great challenge to introduce the right thermal properties of the constituents, including density, specific heat capacity, thermal conductivity and expansion coefficients, which is one of the topics in this work.

1.4.3.3. Moisture effects on composite structures detected by active IRT

Sandwich structures in aviation or marine industries are easily to be exposed to wet and warm/cold environments, and the internal moisture may lead to corrosion and fracture of the structures. So, active IRT [144-146] has been proven to be effective for moisture absorption detection compared to other methods, especially for honeycomb sandwich structures applied in aircrafts.

A typical test configuration by active lock-in IRT in reflection mode is shown in Fig. 1-30 and the temperature difference is illustrated in Fig. 1-31. The wet specimen will show the smaller temperature increase rate due to the moisture absorption. It showed that the temperature increase rate of wet sandwich panel was lower than that of normal dry one. The main parameters include [147-149]:

- Temperature difference: $\Delta T = T_w - T_d$;
- Temperature contrast: $C = \Delta T / T_d$;

- Observation time: $\tau(\Delta T)$ or $\tau(C)$;

Where, T_w and T_d are the temperatures in the wet and dry specimens, respectively.

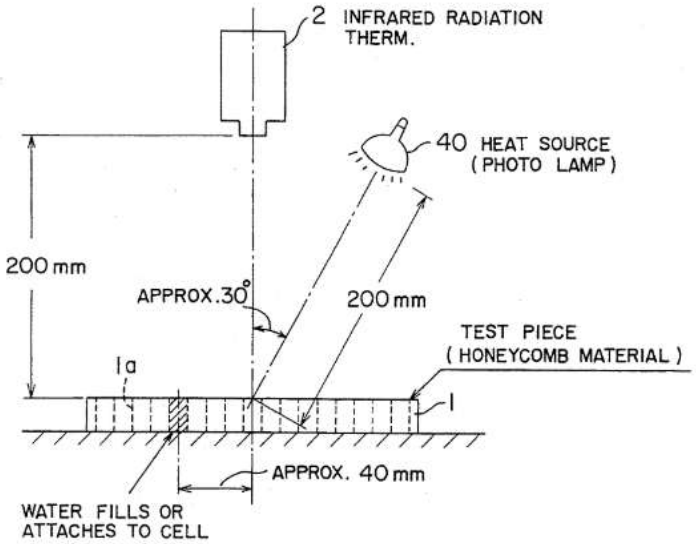

Fig. 1-30. Moisture detection setup by active IRT for honeycomb panel in reflection mode [148].

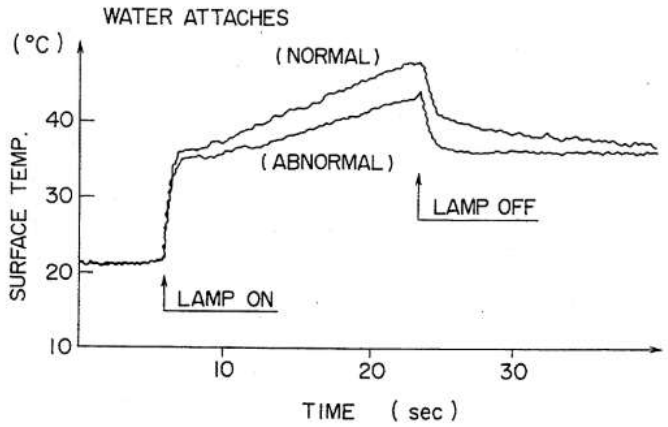

Fig. 1-31. Temperature change rates of water filled and dry honeycomb panels [148].

Vladimir Vavilov [132, 140, 144] has also studied about detecting water in honeycomb panels by active IRT for the last decades, both theoretically and experimentally: 1) possibility of quantitative evaluation of trapped water, 2) influence of honeycomb panel orientation on the efficiency of water detection [182, 183, 198], and 3) discrimination between honeycomb cells filled with water and epoxy adhesive (see Fig. 1-32). It has been proven that the bottom detection (direction ID1) showed higher temperature contrast due to effects of water gravity, the side detection (direction ID3) follows and the top detection (direction ID2) is the worst. So, the detection direction shall be considered when using IR camera to detect moisture absorption.

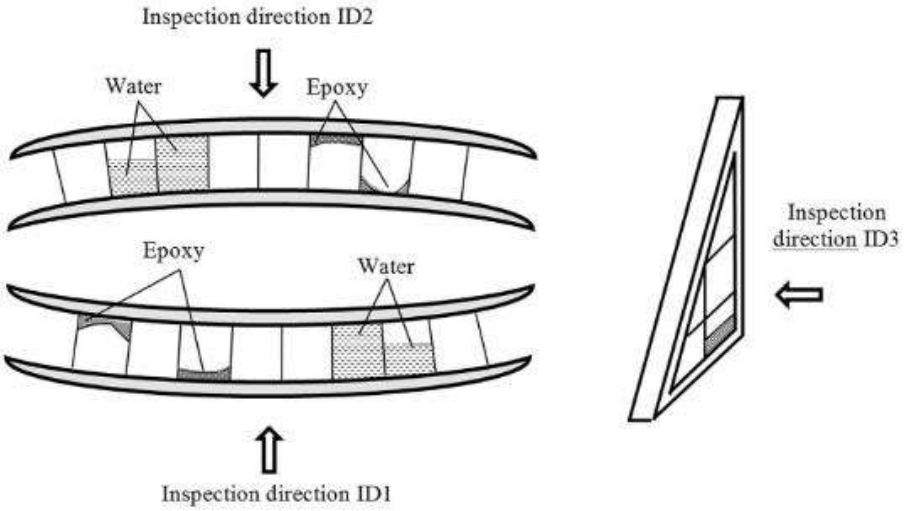

Fig. 1-32. Three moisture detection directions using active IRT method [140].

1.4.3.4. Damage initiation and evolution monitored by passive IRT

Passive IRT could be used to monitor damage evolution during mechanical tests mainly due to the non-contact advantage, especially for fatigue [150-152] and fracture crack propagation inspection. In this case, the strain energy released due to local crack initiation and propagation during the tests could be converted to thermal energy, resulting in the local temperature increase near the damage area. The loading frequency, material properties, the thermo-elastic constant and geometrical parameters like the beam length and thickness could affect the temperature variation [153-158].

Munoz V et al. [93, 143] have validated that IRT can detect damage mechanisms which release higher energy level in static tensile tests of CFRP laminates, including delamination and fiber breakage. For matrix cracking which will not greatly degrade the structure integrity [155], it is difficult to be identified by IRT. However, very few references can be found about application of IRT in bending tests, so 4-point bending tests under the monitor of infrared camera will be studied in this work.

IRT technique can also be used for obtaining the interfacial fracture toughness of sandwich structures [159-161]. An experimental approach using high speed IRT to capture the temperature evolution of GFRP-foam sandwich during the crack growth in mixed-mode bending was proposed by W. Wang et al. [161]. It has been demonstrated there is a simple linear relationship between fracture toughness and temperature, without recourse to knowledge of the applied load or displacement in a test.

R.K. Fruehmann et al. [162] have proven that IRT can not only identify the debonding region, but also relate the heating at the edge of the crack with fracture energy generated by the growth of the debonding crack. However, an evaluation of the stresses through the core thickness near the crack

tip region is required to better understand how the failure initiates. 4-point bending test setup with pre-crack in the middle of the upper interface is shown in Fig. 1-33. It shows that a decrease in the thermoelastic response in the debonding region is common to all pre-cracks. The heat generated at interfacial failure leads to an instantaneous 3 K rise in temperature at the newly formed crack surface.

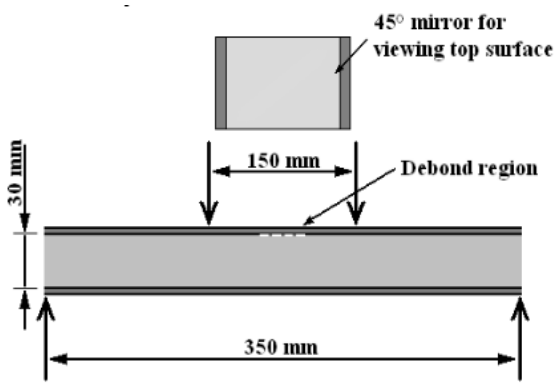

(a) 4-point bending fracture test.

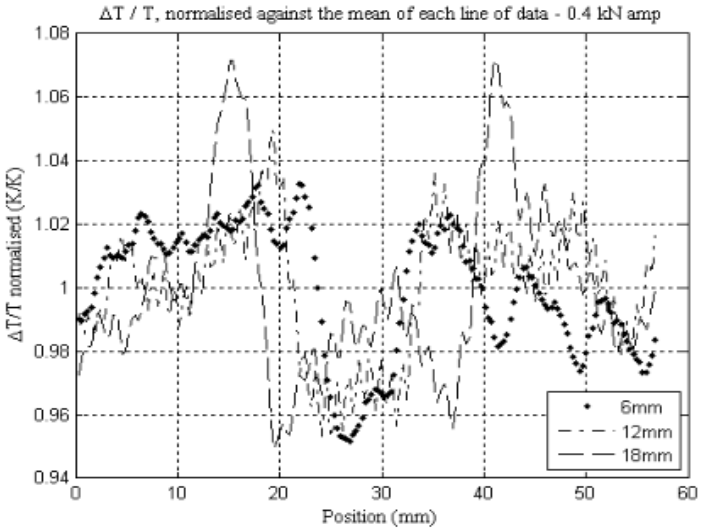

(b) Normalized temperature change with different pre-cracks.

Fig. 1-33. Experimental setup in the 4-point bending fracture test monitored by passive IRT [162].

1.4.3.5. Conclusions

In conclusion, for composite sandwich structures, active IRT using external heat excitation can be used to detect material change resulted from moisture absorption, fabrication defects and post-test damages, while passive IRT could be powerful for monitoring damage initiation and accumulation under load such as fracture and fatigue tests. But it may be limited by the detection of damage modes which could release higher energies. For microscopic damage identification, IRT shall be coupled with other techniques, such as Digital Image Correlation (DIC) or/and AE.

1.4.4. Coupling of AE and IRT techniques

As introduced above, AE is suitable for identifying, classifying and localizing the damages in sandwich structures under loading, while IRT is special due to non-contact monitoring of damage initiation and evolution, but it has difficulties in detecting deep and microscopic damages like core failure and matrix cracking. Therefore, in order to fully take advantage of AE and IRT methods, combining the acoustic and thermal signals to investigate the damage mechanisms of composites will be of great value. For example, some low energy damage modes which cannot be seen by the infrared camera, such as matrix cracking and fiber/matrix cracking, can be detected by AE, while the damage initiation and evolution localization of fiber breakage by IRT can be more accurate compared to AE. Thus, all the possible damage modes can be identified by coupling the two NDT methods, and IRT localizations can be used to verify the observations by AE.

V. Munoz et al. [43, 110] have combined AE and IRT to identify damage evolution in tensile tests of CFRP composites. It has been proven that AE activities and thermal energy released by heat sources induced by fiber/matrix debonding and fiber breakage can be well correlated. AE was the more suitable for detecting all the damages including matrix cracking and fiber breakage, but IRT could be only effective for identification and localization of fiber breakage which has released higher energy. The AE and IRT show the same localizations of the damage initiation of fiber breakage, so the two methods can be coupled to localize damages.

M. Naderi et al. [141] have also combined AE and IRT to characterize energy dissipation and degradation evolution in a woven Glass/Epoxy laminate subjected to fully reversed bending fatigue test. They have verified that similar responses of AE and IRT revealed the existence of three degradation stages, including the first initial temperature/AE cumulative counts increase stage, the second temperature/AE cumulative counts stable stage and the abrupt temperature/AE cumulative counts increase stage just before fatigue failure, as seen in Fig. 1-34. And other researches [152, 163] have shown the same evolution trends as Fig. 1-34 shows. In addition, the second stage takes up almost 70-75% of the whole fatigue life of composites, and the stable temperature change rate of this stage can be obtained without waiting for the failure of the specimen. Thus, the correlation of the stable temperature rise rate and loading stress can be calculated for rapid prediction of fatigue failure [129].

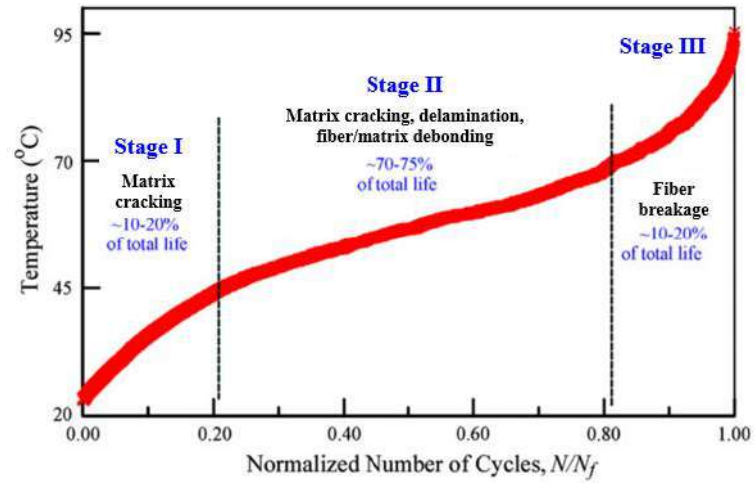

(a) Average surface temperature evolution.

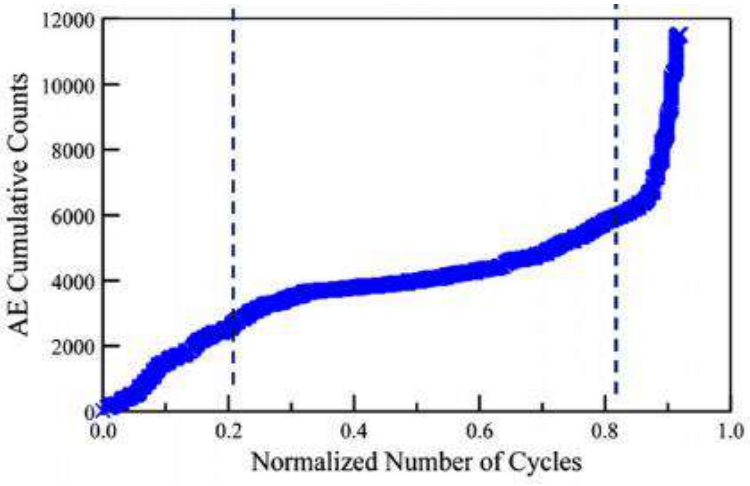

(b) AE cumulative counts accumulation.

Fig. 1-34. Three damage evolution stages of Glass/Epoxy during bending fatigue by IRT and AE [141].

However, due to the unclear complex damage mechanisms of sandwich structures, few references could be found on monitoring their damage initiation and evolution by coupling of AE and IRT, especially on balsa and honeycomb sandwich. Thus, the coupling of AE and IRT to have a complete characterization of the sandwich damages could be of great interest.

Experimental observations by AE and IRT can also be very useful to validate and improve the prediction by the numerical models. To investigate bending behaviors and damage mechanisms of sandwich structures comprehensively, numerical models intended for “virtual testing” shall be a powerful tool to predict the stiffness/strength, damage initiation and evolution process of a complicated system like sandwich structures.

1.5. Numerical analysis of bending behaviors of balsa/honeycomb sandwich structures

1.5.1. Finite Element Modeling (FEM) of balsa/honeycomb sandwich structures

The numerical analysis of composite structures can be performed by Finite Element Modeling (FEM) method by commercial software, such as Abaqus [164] and LS-Dyna [165], but most existing models have been developed on thin CFRP/GFRP laminates and foam/honeycomb sandwiches [73-74, 166], compared to very few balsa sandwich models. FEM of the composite sandwich is effective only when the following conditions are considered properly: the structure geometry, loading and boundary conditions, interaction contact between different components, material properties, as well as the mesh refinement [165]. Thus, it's difficult to simulate the bending behaviors of complex sandwiches which including the skin, core and skin/core interfaces.

For now, GFRP and CFRP laminated skins can be modelled by continuous thin shell elements based on the classical laminate theory [167-168]. In Abaqus, Composite Layup with any number of plies in any fiber orientation angle can be stacked by assuming that elastic material properties of each ply (also called lamina) are the same as the original glass or carbon fibers [164].

For thicker cores, as seen in Fig. 1-35 [73], honeycomb has very thin cell walls oriented in two directions L and W, so it is suggested to model honeycomb cores by thin shell elements [169-170]. The local material coordinates are needed to study the stress distributions of cell wall surfaces in three directions. The green cell walls are the bonding of two cell walls with the ribbon direction in 0°, while yellow cell walls have the ribbon direction in 60° or 120°.

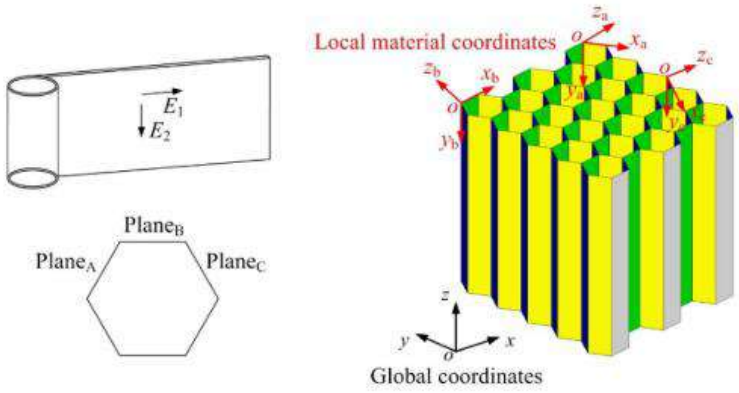

Fig. 1-35. Global and local material coordinates of honeycomb panel [73].

Balsa wood can be considered as an orthotropic material in numerical models with thick solid elements [69]. A timber wood element with its 3D stress components and the main material directions are shown in Fig. 1-36 [171], that is, parallel-to-grain (Longitudinal) and perpendicular-to-grain

(Radial and Tangential) directions. Assuming that the material properties in the radial and tangential directions are identical or sufficiently close, wood can be treated as a transversely isotropic material. Modelling of balsa wood can be the same as Fig. 1-36.

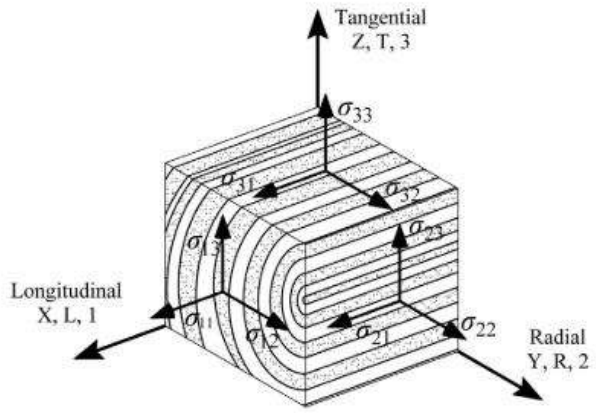

Fig. 1-36. 3D stress components and orthogonal material directions for a timber element [171].

1.5.2. Damage models for laminated skins

Creating the element models is just the first step of numerical analysis, in order to predict the fracture load and damage evolution process of thin laminates, material models considering different damage mechanisms should be introduced into the numerical models. 2D Progressive Damage Analysis (PDA) model [172-176] and Cohesive Zone Model (CZM) [177-179] are the most often used to simulate fiber/matrix damages and delamination, respectively.

1.5.2.1. Progressive Damage Analysis (PDA) model

PDA model, implemented in Abaqus to predict fiber/matrix tension/compression and shear damages, combines Hashin damage initiation criterion and damage evolution law based on fracture energy [172-175].

1.5.2.1.1 Damage initiation

In Abaqus, the damage onset of composite is determined by Hashin damage initiation criterion which considers four different damage initiation mechanisms, including fiber tension (ft), fiber compression (fc), matrix tension (mt) and matrix compression (mc).

Fiber tension ($\sigma_{11} \geq 0$) is mainly determined by the longitudinal tensile strength of the lamina, and also considering a small contribution of in-plane shear failure, as Eq. (1-19) shows:

$$F_f^t = \left(\frac{\sigma_{11}}{F_{1t}}\right)^2 + \beta\left(\frac{\sigma_{12}}{F_6}\right)^2 \quad (1\text{-}19)$$

Fiber compression ($\sigma_{11} < 0$) is controlled by the longitudinal compressive strength of the lamina, as Eq. (1-20) shows:

$$F_f^c = \left(\frac{\sigma_{11}}{F_{1c}}\right)^2 \tag{1-20}$$

Matrix tension and/or shear ($\sigma_{22} \geq 0$) is mainly determined by the transverse tensile strength and in-plane shear strength, as Eq. (1-21) shows:

$$F_m^t = \left(\frac{\sigma_{22}}{F_{2t}}\right)^2 + \left(\frac{\sigma_{12}}{F_6}\right)^2 \tag{1-21}$$

Matrix compression ($\sigma_{22} < 0$) results in the shear-compression failure of matrix, as Eq. (1-22) shows:

$$F_m^c = \left(\frac{\sigma_{22}}{2F_4}\right)^2 + \left[\left(\frac{F_{2c}}{2F_4}\right)^2 - 1\right]\frac{\sigma_{22}}{F_{2c}} + \left(\frac{\sigma_{12}}{F_6}\right)^2 \tag{1-22}$$

Where σ_{ij} are the components of the stress tensor; F_{1t}, F_{1c} are the longitudinal tensile and compressive strengths in the fiber direction; F_{2t}, F_{2c} are the transverse tensile and compressive strengths in the matrix direction; F_6, F_4 are the longitudinal and transverse shear strengths, and β describes the contribution of shear stress to the fiber failure. $F_f^t, F_f^c, F_m^t, F_m^c$ are the damage indexes. Damage initiates when any of them attains 1.

1.5.2.1.2 Damage evolution

Once any of the damage initiation criterion is satisfied, the material stiffness continues to degrade. The damage evolution is mainly characterized by the four critical energy release rate values G_i^c, where i=ft, fc, mt, mc, corresponding to the four damage mechanisms: fiber failure under tension, under compression, matrix failure under tension and compression, respectively. G_i^c corresponds to the area of the triangle OAC shown in Fig. 1-37 [172], based on the traction-separation law. And they are defined as the equivalent values, not measurable experimentally. Different from the common interlaminar fracture energy determination [33], G_i^c values input into PDA model in Abaqus are intralaminar, using a characteristic length instead of the real crack separation displacement, to calculate 1D equivalent displacement δ_{eq}. Damage variable in Abaqus is defined as d by Eq. (1-23):

$$d = \frac{\delta_{eq}^c(\delta_{eq} - \delta_{eq}^0)}{\delta_{eq}(\delta_{eq}^c - \delta_{eq}^0)} \tag{1-23}$$

Where $\delta_{eq}^c = 2G_i^c/\sigma_{eq}^0$ is the max δ_{eq} at point C in Fig. 1-37. $\delta_{eq}^0, \sigma_{eq}^0$ are the equivalent displacement and stress at point A where the damage initiates. For each damage mode, d represents the reduction of stiffness matrix and varies from zero (damage initiation point A) to one (full damage point C).

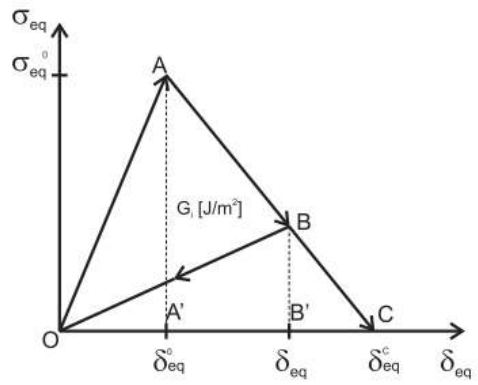

Fig. 1-37. Bilinear traction-separation law of damage evolution criterion in Abaqus [172].

Hence, besides the strength parameters, the four G_i^c values shall be introduced into Abaqus correctly to evaluate the damage evolution process of composite laminates. But it is not clear whether PDA model is also effective for the more complex sandwich structure, and few literatures about this field can be found. In addition, it is very difficult to determine the precise G_i^c due to the anisotropy of composites and the difficulty in classifying the four damage modes experimentally. For unidirectional fiber reinforced polymer by glass or carbon fibers, most engineers and researchers often assume the values as others [175-176] have done. For example, Barbero E J et al. [172] have discussed the influences of $1.5\ \mathrm{N/mm} < G_{mt}^c < 30.5\ \mathrm{N/mm}$ on simulation of longitudinal tensile damages in the $[0^\circ_2/90^\circ_4]_s$ laminates, proving that $G_{mt}^c = 12\ \mathrm{N/mm}$ was the best choice with smallest error. Lapczyk I and Hurtado J A [175] assumed that $G_{ft}^c = G_{fc}^c = 12.5\ \mathrm{N/mm}$ and $G_{mt}^c = G_{mc}^c = 1\ \mathrm{N/mm}$ can be effective for simulation of glass fiber reinforced epoxy.

However, it has been unclear whether these parameters can be applied to laminated skins of sandwich structures, so the influences of the fracture energy rate on the skin damage evolution simulation have been firstly discussed in this thesis.

1.5.2.2. Cohesive Zone Model (CZM) for delamination

When considering the delamination between different plies of composite laminates, Cohesive Zone Model (CZM) [177] has been regarded as the best numerical method. Some efforts have been made on modeling crack initiation and growth of unidirectional and multidirectional laminates with cohesive elements. In composite laminates, since the intermediate adhesive between plies is very thin as shown in Fig. 1-38. (a), the transverse shear stresses induced by membrane stretching and shear can be ignored [177]. Therefore, the constitutive model of the cohesive elements relates traction (σ) to displacement jump (Δ) at the interface where a crack may occur.

Among all the widely-used constitutive laws, the bilinear softening constitutive law [178] which assumes an initially linear elastic behavior followed by initiation and evolution of interface damage

is the most popular on account of the simplicity and straightforward physical meanings of delamination [179]. For pure mode delamination, the bilinear softening constitutive law characterized by the σ–Δ curve includes two main domains, as illustrated in Fig. 1-38. (b), similar to the bilinear traction-separation law used in PDA model in Fig. 1-37.

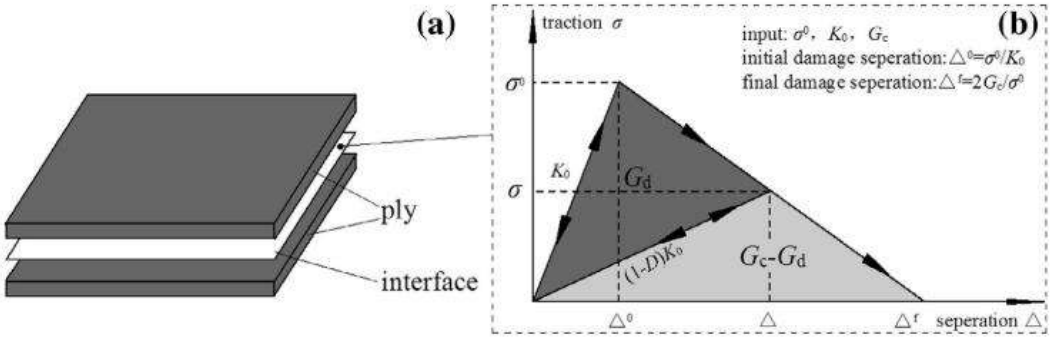

Fig. 1-38. Bilinear constitutive law of representative cohesive element [177].

However, most delamination occurs under mixed mode loading instead of pure mode loading in engineering practice [180]. For such cases, the damage onset commonly occurs at complex stress status and the crack arises before any of the energy release rate components reaches its individual critical value. For multidirectional laminates, the interlaminar fracture behaviors are complex and various factors can influence the delamination simulation, such as the residual stress, mode-mixity and curved delamination front. It has been reported that delamination initiation and propagation mostly occur in the interface between plies with different fiber orientations.

Thus, the interaction rules among the stresses for predicting the damage onset and among the energy release rates for the crack initiation and growth shall be considered for the delamination simulation under the mixed mode loading, such as the quadratic stress failure criterion [178] and power law criterion. Besides the material parameters, cohesive element sizes and viscosity also play important roles in the delamination simulation in multidirectional laminates. So, it's still difficult to accurately distinguish the mode I and mixed mode I/II delamination growth, and there are still no international agreements on suitable parameters.

When laminates serve as the skin of sandwich structures, skin delamination will be mixed with skin/core debonding, it will become much more complex. As a result, itis necessary to introduce AE and IRT observation results to help improve the numerical models.

1.5.3. Damage models for balsa/honeycomb cores

Wood is a heterogeneous and extremely anisotropic material, which is characterized as ductile in compression and brittle in shear and tension [21-22, 181]. It makes wood a challenging material to

simulate. Different approaches have been employed to simulate the mechanical behavior of wood, including fracture mechanics [182-183], multi-surface plasticity [184] and Continuum Damage Mechanics (CDM) [171].

According to fracture mechanics, there are three fracture modes depending on the loading conditions for a crack, Mode I, II and III, representing fracture induced by pure tensile stress perpendicular to the crack plane and that induced by shear stress, respectively, as shown in Fig. 1-39. (a) [182]. A mixed mode of Mode I and Mode II is the most common combination in structural applications. Owing to the three orthogonal principal directions defined as longitudinal (L), radial (R) and tangential (T) axes, wood has six crack propagation systems. A pair of letters in combination of L, R and T is used to identify a crack propagation system in Fig. 1-39. (b). The first letter indicates the direction normal to the crack surface and the second specifies the direction of crack propagation. Among all propagation systems, RL is typical in structural components.

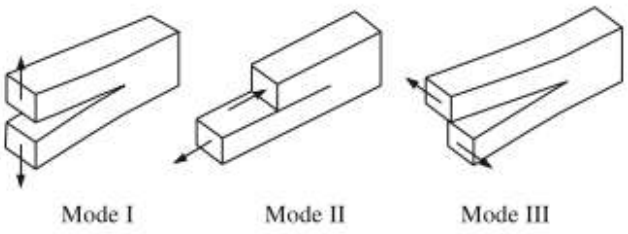

(a) Basic fracture modes.

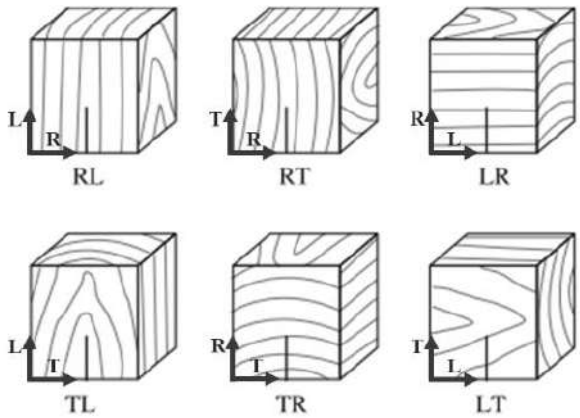

(b) Crack propagation in wood.

Fig. 1-39. Crack propagation in wood and basic fracture modes [182].

To simulate the crack propagation in wood and wood composites, the crack initiation and propagation criterion expressed by the energy release rate can be used [182-183] to identify the growth of the crack. Compact tension specimen tests and compact symmetric shear specimen tests were conducted respectively, in order to determine the critical stress intensity factors K_{IC} (mode I) and K_{IIC} (mode II).

Then the Extended Finite Element Method (XFEM) has been developed incorporating Abaqus based on the experimental results, having advantages of modeling crack growth without re-meshing, simplifying the numerical simulation.

The selected experimental data from biaxial tests with respect to distinct failure modes of spruce wood has been discussed in [184], and an orthotropic plasticity model has been developed for its mathematical description. The multi-surface plasticity model consists of four surfaces representing four basic failure modes. The first is a modified tension cut-off for the description of fiber rupture. The second is a mixed mode radial tension-shear model applied to the perpendicular-to-grain (Radial and Tangential) direction. The third is a model for compression perpendicular to grain, and the fourth surface covers the compressive failure parallel to grain.

A more powerful 3D constitutive model within the framework of CDM has also been developed to be imported to ABAQUS/Explicit via a VUMAT subroutine to simulate the balsa wood core damages in Aluminum skin-balsa sandwich [69]. CDM is a promising approach for modeling softening or even hardening behavior of wood material by incorporating a modification into the stiffness matrix. Eight stress-based failure criteria included in this model have been established in Table 1-3.

Table 1-3. Failure criteria and corresponding damage variables for wood material [69].

Failure mode	condition	Failure criterion	Damage variable
Tension parallel to fiber	$\sigma_{11} \geq 0$	$F_{t,0}(\sigma) = \frac{\sigma_{11}}{f_{t,0}} \geq 1$	$d_{t,0}$
Compression parallel to fiber	$\sigma_{11} < 0$	$F_{c,0}(\sigma) = \frac{-\sigma_{11}}{f_{c,0}} \geq 1$	$d_{c,0}$
Tension perpendicular to fiber (L-T plane splitting)	$\sigma_{22} \geq 0$	$F_{t,90R}(\sigma) = \left(\frac{\sigma_{22}}{f_{t,90}}\right)^2 + \left(\frac{\sigma_{12}}{f_v}\right)^2 + \left(\frac{\sigma_{23}}{f_{roll}}\right)^2 \geq 1$	$d_{t,90R}$ d_{vR} d_{roll}
Pure transverse compression (radial direction)	$\sigma_{22} < 0$	$F_{c,90R}(\sigma) = \frac{-\sigma_{22}}{f_{c,90}} \geq 1$	$d_{c,90R}$
Shear (under radial compression)	$\sigma_{22} < 0$	$F_{vR}(\sigma) = \left(\frac{\sigma_{12}}{f_v}\right)^2 + \left(\frac{\sigma_{23}}{f_{roll}}\right)^2 \geq 1$	d_{vR} d_{roll}
Tension perpendicular to fiber (L-R plane splitting)	$\sigma_{33} \geq 0$	$F_{t,90T}(\sigma) = \left(\frac{\sigma_{33}}{f_{t,90}}\right)^2 + \left(\frac{\sigma_{13}}{f_v}\right)^2 + \left(\frac{\sigma_{23}}{f_{roll}}\right)^2 \geq 1$	$d_{t,90T}$ d_{vT} d_{roll}
Pure transverse compression (tangential direction)	$\sigma_{33} < 0$	$F_{c,90T}(\sigma) = \frac{-\sigma_{33}}{f_{c,90}} \geq 1$	$d_{c,90T}$
Shear (under tangential compression)	$\sigma_{33} < 0$	$F_{vT}(\sigma) = \left(\frac{\sigma_{13}}{f_v}\right)^2 + \left(\frac{\sigma_{23}}{f_{roll}}\right)^2 \geq 1$	d_{vT} d_{roll}

Failure in tension and compression parallel to fiber has been defined using maximum stress criterion [69, 185]. Concerning transverse compression applied under an angle to the fiber, two failure modes

are valid to identify ductile failure in pure transverse compression and brittle failure mode owing to the shear stress components related to the compression direction. Under tension perpendicular to fiber, it is assumed that a combination of tensile and shear stresses related to the tension direction, results in tangential or radial splitting as a brittle failure mode. Once any of the failure criteria is met, although not all uniaxial strengths might be reached, all corresponding material properties (e.g. E_{22}; G_{12}; G_{23}) degrade via damage variables. Under 4-point bending of balsa sandwich, the core mainly carries shear stresses in L-T or L-R plane, so the shear failure criteria under radial and tangential compression should be the most important to be considered.

As for failure criteria of honeycomb cores, the local buckling initiates the nonlinear behavior due to shear stresses distributed on the cell walls, after pre-buckling and post-buckling periods, the collapse of cell walls induces the final degradation of shear modulus [75-76]. Nomex honeycomb can been regarded as an isotropic material [186] that presents significant plastic behavior and allows considerable strains before breaking, to simplify the numerical analysis. Elastic-plastic progressive damage model determined mainly by the yield stress and fracture toughness in Abaqus [164] can be considered in the damage evolution prediction of honeycomb cores.

1.6. Chapter summary

In summary, GFRP-balsa and CFRP-honeycomb sandwich structures, which have attracted more attentions in marine and aeronautical industries, pose a great challenge to characterize their bending behaviors and damage mechanisms, due to their complicated anisotropic, heterogeneous and hygroscopic properties. Sandwich structures are designed to better carry bending loads, mainly resulting in the in-plane compressive/tensile stresses in the thin composite skin and shear stresses in the thicker core. The complex stress distributions are related to the various factors, such as the density and thickness of the skin and core, material property, structure geometry, loading condition, span length, environmental condition, etc., thus resulting in the different damage mechanisms. The skin damages, skin/core debonding and core damages may occur simultaneously under bending loading, but the damage sequence, types of the damages and damage locations may change when any of the above influence factors changes.

Accordingly, aiming at monitoring the damage initiation and evolution process of the sandwich more clearly under 4-point bending load, InfraRed Thermography (IRT) and Acoustic Emission (AE) can be coupled to identify, classify and localize the possible skin compressive/tensile damages, core damages and skin/core debonding of GFRP-balsa and honeycomb sandwich structures. However, for now, few researches can be found about how IRT and AE can further work on the honeycomb and balsa sandwich structures under bending loading, especially on the effects of the absorbed moisture

on these structures. It will be interesting and meaningful to couple these two techniques to know exactly more about when, where and what kinds of damages will initiate and propagate in the dry and wet sandwich structures, to ensure the structure safety and save maintenance cost.

In addition, few numerical models in Abaqus for the honeycomb and balsa sandwiches have been found, the choice of the mesh modelling and the damage model depend on the complicated constituent properties, real damage mechanisms, loading and environment condition, etc., so it still needs further exploration to simulate their bending behaviors, and predict quickly and accurately when, where and how the damages initiate and propagate.

In the next chapter, the fabrication processes of the sandwich specimens and preliminary active AE and IRT tests will be firstly discussed, in order to better serve the investigations of 4-point bending behaviors of GFRP-balsa sandwich in Chapter 3 and CFRP-honeycomb sandwich in Chapter 4.

Chapter 2. Preliminary tests monitored by AE and IRT on dry and wet sandwiches

2.1. Introduction 67

2.2. Materials and specimens 67

2.2.1. Material properties 67

2.2.2. Fabrication process 68

2.2.3. Specimen cutting and geometries of specimens 71

2.2.3.1. Large panels for preliminary active AE Hsu-Nielsen tests 71

2.2.3.2. Triple dog-bone specimens for 4-point bending tests 72

2.3. Characterization of AE wave propagation properties in sandwich panels 73

2.3.1. Characterization of AE wave velocity in sandwich panels 73

2.3.1.1. Preliminary active Hsu-Nielsen test 73

2.3.1.1.1 Experimental setup of active Hsu-Nielsen test 73

2.3.1.1.2 Wave velocity determination in active Hsu-Nielsen test 75

2.3.1.2. AE wave velocity in CFRP-honeycomb sandwich panels 77

2.3.1.2.1 AE wave velocity in CFRP laminated skin 77

2.3.1.2.2 AE wave velocity in the whole sandwich 79

2.3.1.2.3 Correlation between AE wave velocity in the skin and sandwich 80

2.3.1.2.4 Validation of the proposed model using correlation ratio R 83

2.3.1.3. AE wave velocity in GFRP-balsa sandwich panels 85

2.3.1.3.1 AE wave velocity in GFRP laminated skin 85

2.3.1.3.2 AE wave velocity in the whole sandwich 86

2.3.1.3.3 Correlation between AE wave velocity in the skin and sandwich 88

2.3.1.4. Conclusions 89

2.3.2. Characterization of AE attenuation properties in sandwich panels 89

2.3.2.1. AE attenuation testing method 89
2.3.2.2. AE attenuation in CFRP-honeycomb sandwich panels 90
2.3.2.2.1 AE attenuation in CFRP laminated skin 90
2.3.2.2.2 AE attenuation in the whole sandwich 91
2.3.2.3. AE attenuation in GFRP-balsa sandwich panels 91
2.3.2.3.1 AE attenuation in GFRP laminated skin 91
2.3.2.3.2 AE attenuation in the whole sandwich 92
2.3.2.4. Conclusions 93
2.4. Moisture effects on preliminary AE and IRT signals 93
2.4.1. Moisture absorption tests monitored by active AE and IRT methods 93
2.4.1.1. Water immersion test 93
2.4.1.2. Active AE test setup on triple dog-bone sandwich specimens 93
2.4.1.3. Active IRT test setup on triple dog-bone sandwich specimens 94
2.4.2. Moisture absorption behaviors 95
2.4.2.1. Moisture absorption behavior of GFRP-balsa sandwich 96
2.4.2.2. Moisture absorption behavior of CFRP-honeycomb sandwich 97
2.4.2.3. Conclusions 98
2.4.3. Moisture effects on AE wave propagation properties 99
2.4.3.1. Moisture effects on AE wave propagation properties of GFRP-balsa sandwich 99
2.4.3.1.1 Moisture effects on AE wave velocity 99
2.4.3.1.2 A new methodology to predict elastic modulus of wet sandwich by AE wave velocity 100
2.4.3.1.3 Moisture effects on AE attenuation 101
2.4.3.2. Moisture effects on AE wave propagation properties of CFRP-honeycomb sandwich 103
2.4.3.2.1 Moisture effects on AE wave velocity 103
2.4.3.2.2 Moisture effects on AE attenuation 104

2.4.3.3. Conclusions 105
2.4.4. Moisture effects on temperature variation rate in active IRT tests..... 105
2.4.4.1. Moisture effects on IRT responses of GFRP-balsa sandwich 105
2.4.4.2. Moisture effects on IRT responses of CFRP-honeycomb sandwich 107
2.4.4.3. Conclusions 108
2.5. Chapter summary 109

2.1. Introduction

Based on the literature reviews of the GFRP-balsa sandwich applied in marine structures and the CFRP-honeycomb sandwich in aircrafts, as well as the basic principles and post-processing methods of AE and IRT techniques applied on composite structures, the preliminary experimental study of the AE wave propagation properties are firstly reported in this chapter.

Furthermore, based on the characterization of AE wave velocity and attenuation property in dry sandwich panels, moisture effects on the AE and IRT signals are investigated next by comparing the dry and wet dog-bone sandwich specimens, in order to better serve the AE and IRT monitoring of damage evolution in 4-point bending tests in Chapter 3 and 4.

2.2. Materials and specimens

2.2.1. Material properties

In this study, two kinds of sandwich structures are studied: GFRP-balsa sandwich and CFRP-honeycomb sandwich. All manufactured GFRP-balsa sandwich specimens have two identical symmetrical skins which are made of 3-layer GFRP weave balanced fabric/epoxy (Ref: Sicomin E glass fiber twill 3190 with 190 g/m^2, with 50% fiber volume fraction), and all layers are in the same direction to obtain the laminate of $[0^o]_3$. The core is made from balsa wood (Ref: BALTEK SB.100, density=148 kg/m^3), whose fiber direction is oriented in the direction of their thickness (Direction Z in Fig. 2-1. (a)). The original pure balsa panel is glued together by many small blocks, thus there are a lot of balsa/balsa interfaces distributed randomly in the core [47]. The manufactured CFRP-honeycomb sandwich specimens are composed of CFRP laminates made from three plies of unidirectional prepreg (Ref: SAFRAN Carbon fiber T800H with 300 g/m^2, with 63% fiber volume fraction) with lay-up of $[0^o/90^o/0^o]$ and Nomex/Aluminum honeycomb core. L (ribbon) direction of honeycomb, in which two cell walls are bonded, is oriented along X axis of the sandwich panel (see Fig. 2-1. (b)).

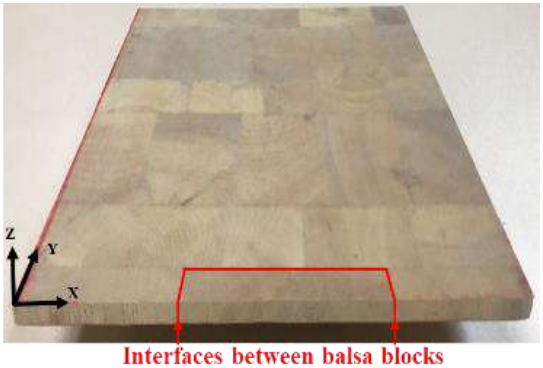

(a) GFRP-balsa sandwich panel.

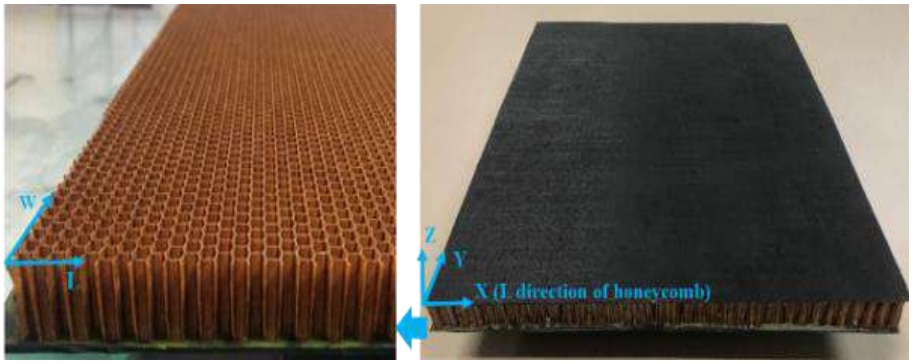

(b) CFRP-honeycomb sandwich panel.

Fig. 2-1. The two kinds of sandwich panels.

The main material parameters of glass and carbon fibers [187-188] are shown in Table 2-1. Table 2-2 and 2-3 show the equivalent material parameters of balsa [189] and honeycomb cores [190] in different directions. Nomex honeycomb sandwich is studied in both preliminary tests and 4-point bending tests, while aluminum honeycomb sandwich is only studied in AE wave velocity tests in order to validate the proposed method for velocity determination in any honeycomb material.

Table 2-1. Material parameters of glass and carbon fibers for skins.

Constituents	E_1 (GPa)	E_2 (GPa)	G_{12} (GPa)	G_{13} (GPa)	G_{23} (GPa)	ν_{12}	ρ (kg/m^3)
GFRP	20	20	2.85	2.30	2.30	0.13	1900
CFRP	152.4	9.20	4.30	2.80	2.30	0.35	1800

Table 2-2. Equivalent material parameters of balsa wood for cores.

Constituents	E_1 (GPa)	E_2 (GPa)	E_3 (GPa)	G_{12} (GPa)	G_{13} (GPa)	G_{23} (GPa)	ν_{12}	ν_{13}	ν_{23}	ρ (kg/m^3)
Balsa wood	0.092	0.092	2.5	0.003	0.1	0.1	0.6	0.01	0.01	148

Table 2-3. Equivalent material parameters of honeycomb for cores.

Constituents	E_1 (GPa)	E_2 (GPa)	G_{12} (GPa)	ν_{21}	ρ (kg/m^3)
Nomex honeycomb	0.138	0.138	0.032	0.35	48
Aluminum honeycomb	0.019	0.019	0.003	0.10	45

2.2.2. Fabrication process

As explained in Chapter 1, since GFRP laminates are made from woven glass fibers while CFRP laminates are fabricated from unidirectional carbon fiber prepregs, the fabrication processes of GFRP-balsa and CFRP-honeycomb sandwiches are different:

- For CFRP-honeycomb panels, the hand lay-up prepreg method with vacuum bag molding (see

Fig. 2-2) was applied, containing two curing steps: firstly, cure the CFRP laminated skins in the vacuum bag at 120ºC for 4 hours; next, bond the skins and honeycomb core by adhesive film (Ref: Gurit SA 70) at room temperature, and then cure them together in the vacuum bag at 70ºC for 16 hours.

- For GFRP-balsa sandwich, wet lay-up method was adopted, using the liquid epoxy resin to infuse GFRP laminated layers and balsa wood panel simultaneously at room temperature, and then co-curing them at the same time in the vacuum bag under room temperature for 7 hours, then post-cured at 45℃ for 2 hours, 60℃ for 2 hours and 80℃ for 8 hours, as the standard of the resin (Ref: EPOLAM 2017) requires.

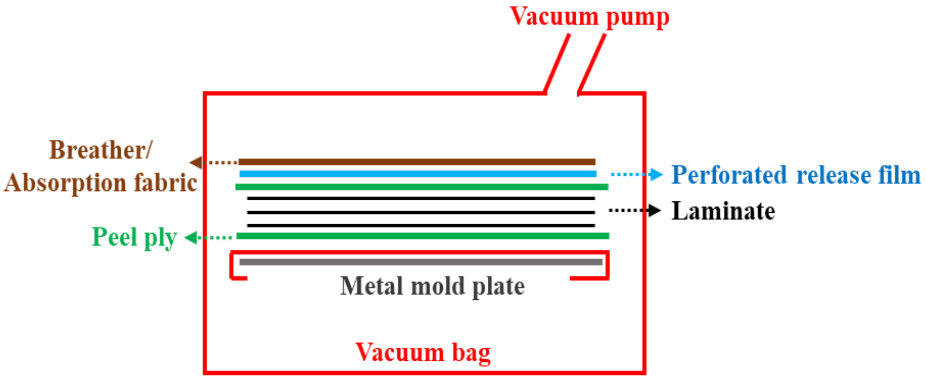

Fig. 2-2. Schematic of vacuum bag molding of composite laminates.

Fig. 2-3. (a) shows the lay-up of CFRP prepreg plies, which were cut from the prepreg roll and then stacked in the prescribed sequence of [0º/90º/0º]. Fig. 2-3. (b) show the sealed vacuum bag before being put in the oven for curing at 120ºC for 4 hours for T800H carbon fiber.

(a) Lay-up of CFRP prepreg plies.

(b) Sealed vacuum bag of CFRP laminates.

Fig. 2-3. 3-layer CFRP laminated skin before curing.

After the CFRP laminate panel (600 mm * 600 mm) was cured, it was firstly cut into smaller panels with dimension of 600 mm * 300 mm (see Fig. 2-4. (a)) using normal water jet cutting, and then the two CFRP skins were bonded to the honeycomb panel by the epoxy adhesive film (Ref: Gurit SA

70), as shown in Fig. 2-4. (b). Finally, the bonded CFRP-honeycomb sandwich panel (600 mm*300 mm) was cured in the vacuum bag in the oven at 70ºC for 16 hours considering properties of the adhesive film. Fig. 2-4. (c) show the final cured CFRP-honeycomb sandwich panel, which can be cut into smaller panels (300 mm * 300 mm) by normal water jet cutting.

(a) Cured CFRP laminates.

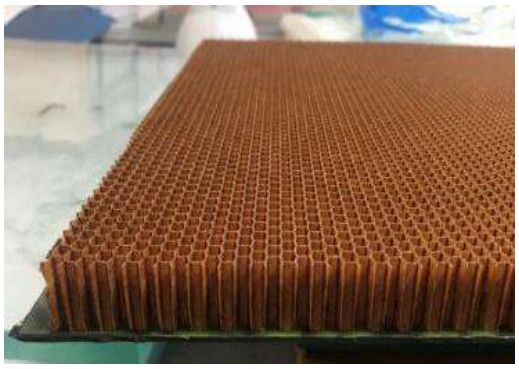

(b) Bonding of CFRP and honeycomb.

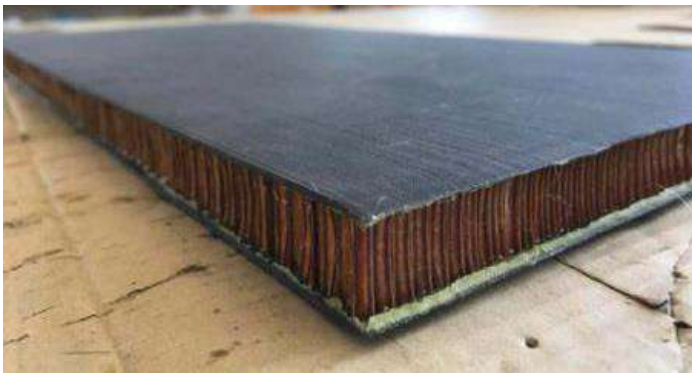

(c) Cured CFRP-honeycomb sandwich.

Fig. 2-4. Bonding of cured CFRP skin and honeycomb core.

For the wet lay-up of GFRP skins and balsa panel, the three plies of woven glass fibers were stacked by sequence (see Fig. 2-5. (a)) on a large balsa panel (1200 mm * 600 mm) from suppliers. During the liquid resin (Ref: EPOLAM 2017) infusion process, the pure balsa panel was totally infused firstly, next, the first glass fiber ply was put on the balsa panel and infused completely, as Fig. 2-5. (a) shows. And then, each ply was put on the previous one and infused by the same procedure until all the GFRP plies and balsa wood were fully wet by the resin infusion.

Afterwards, the two skins and balsa core panel were sealed in the vacuum bag (see Fig. 2-5. (b)), and co-cured firstly under room temperature for 7 hours, then post-cured at 45℃ for 2 hours, 60℃ for 2 hours and 80℃ for 8 hours as the standard of the resin requires. Finally, the cured sandwich panel can be cut into smaller one (300 mm * 300 mm) by normal water jet cutting. The selection of the cutting method will be discussed in the next part.

(a) The first fully wet GFRP ply and balsa panel.

(c) Sealed vacuum bag of GFRP-balsa sandwich.

Fig. 2-5. Co-curing process of GFRP-balsa sandwich panel.

2.2.3. Specimen cutting and geometries of specimens

Considering the different objectives of preliminary AE wave propagation tests and 4-point bending tests in this study, two kinds of sandwich specimens with different dimensions were prepared: the large panels with 300 mm * 300 mm which are needed to clearly investigate the acoustic wave propagation properties in active AE tests and the smaller triple dog-bone specimens which are prepared to better observe the different damage modes in 4-point bending tests.

2.2.3.1. Large panels for preliminary active AE Hsu-Nielsen tests

The 600 mm * 300 mm CFRP-honeycomb panel and 1200 mm * 600 mm GFRP-balsa panel can be cut into panels with dimension of 300 mm * 300 mm by normal water jet machine, so as to investigate AE wave propagation properties in active Hsu-Nielsen tests. It can be seen in Fig. 2-1 that water jet cutting will not cause the visible damages of the skin and core properties, and the microscope photos will be illustrated in Chapter 3 which shows the analysis of the 4-point bending behavior. Water jet cutting is the most simple and effective cutting technique so as to obtain this kind of panel. In order to study the influence of different honeycomb materials and thicknesses on the AE wave propagation

in sandwich, specimens with different cores have been prepared. Dimensions of the tested sandwich panels are presented in Table 2-4 and 2-5.

Table 2-4. Dimensions of GFRP-balsa sandwich panels.

Specimen	Length (mm)	Width (mm)	h_s (mm)	h_c (mm)	h_f (mm)
GFRP-balsa sandwich	300	300	10-11	9-10	0.5

Where h_s, h_c and h_f are the thickness of the sandwich, the core and the skin, respectively.

Table 2-5. Dimensions of CFRP-honeycomb sandwich panels.

Specimens	Type	Length (mm)	Width (mm)	h_s (mm)	h_c (mm)	h_f (mm)
A	CFRP-Nomex honeycomb	300	300	19.5	18	0.75
B	CFRP-aluminum honeycomb	300	300	31.5	30	0.75
C	CFRP-Nomex honeycomb	300	300	61.5	60	0.75

Where h_s, h_c and h_f are the thickness of the sandwich, the core and the skin, respectively.

2.2.3.2. Triple dog-bone specimens for 4-point bending tests

In this work, sandwich specimens with the original triple dog-bone shape [191-192] (see Fig. 2-6 and Fig. 2-7) have been designed and tested under 4-point bending. The interest of this special shape is to observe more clearly the skin damages caused by the maximum compressive stresses in the pure bending zone 1, as well as core damages in bending and shear zone 2 (see Fig. 2-6. (b) and Fig. 2-7. (b)). Another advantage of this shape is to reduce the local stress concentrations under the loading supports and ensure the stability of the tests. In order to obtain the triple dog-bone sandwich specimens, different cutting techniques have been used for GFRP-balsa sandwiches and for CFRP-honeycomb ones.

Flow Mach 2 1313b water jet is an industrial machine capable of cutting a wide variety of materials using a very high-pressure jet of a mixture of water and an abrasive substance. Flow waterjets can ensure parts very tight tolerances as close as 0.001" (0.025 mm) and cut virtually any shape in a single step with edge quality that usually requires no secondary finishing [129]. Thus, it can provide a good cut precision and edge quality (see Fig. 2-6. (b)) for GFRP-balsa sandwich which has a relatively lower specific stiffness and thickness, compared to CFRP-honeycomb sandwich.

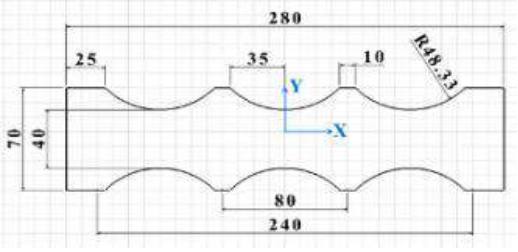

(a) Dimensions (mm) of triple dog-bone sandwich.

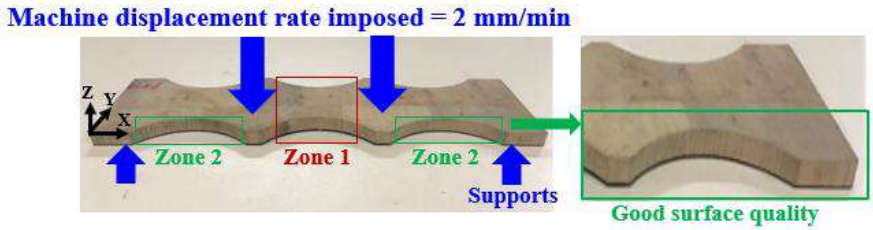

(b) Loading condition and specimen shape.

Fig. 2-6. Geometry shape of triple dog-bone GFRP-balsa sandwich specimens.

For the stiffer and thicker CFRP-honeycomb sandwich panels, it's difficult to cut them into the special triple dog-bone sandwich specimens with a good edge quality by Flow Mach 2 1313b water jet machine. So, the more power DUBUS NUM 1060 milling machine was chosen. DUBUS NUM 1060 milling is a 3-axis machine with a vertical spindle orientation. It can automatically cut and machine composite panels at different angles, so it can cut the curved edges of triple dog-bone specimens easily and quickly with a good surface quality (see Fig. 2-7. (b)).

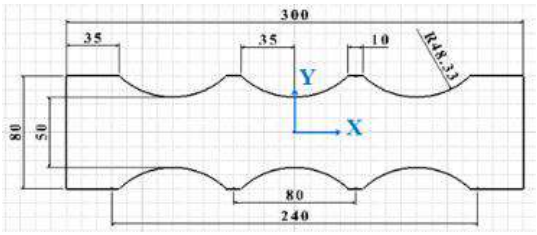

(a) Dimensions (mm) of triple dog-bone sandwich.

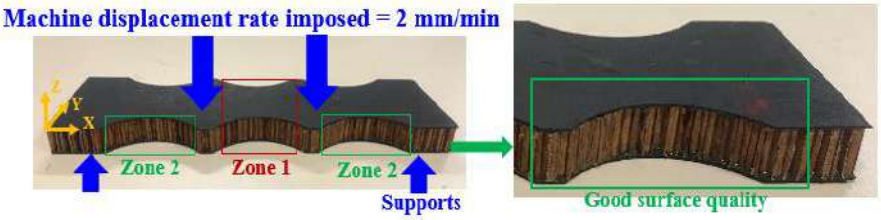

(b) Loading condition and specimen shape.

Fig. 2-7. Geometry shape of triple dog-bone CFRP-honeycomb sandwich specimens.

2.3. Characterization of AE wave propagation properties in sandwich panels

2.3.1. Characterization of AE wave velocity in sandwich panels

2.3.1.1. Preliminary active Hsu-Nielsen test

2.3.1.1.1 Experimental setup of active Hsu-Nielsen test

Active Hsu-Nielsen test (see Fig. 2-8) [93, 100] consists of breaking a 0.3-0.5 mm diameter pencil lead approximately 3 mm (± 0.5 mm) from its tip by pressing it against the surface of the object. It generates an artificial intense acoustic signal, quite similar to a natural AE source, and the sensors

detect it as a strong burst. The purpose of this test is twofold. On one hand, it ensures that the sensors are in good acoustic contact with the structure being monitored. Amplitudes higher than 95 dB should be registered more than five times by pencil lead breaks in the vicinity of the sensors, to verify the accuracy of the AE system. On the other hand, it checks the accuracy of the source location setup, which involves indirectly determining the actual value of the acoustic wave velocity in the monitored object.

Generally speaking, the typical AE system mainly includes the pencil, the sensors, the couplant, the pre-amplifier, the analogue filters, the acquisition system and software (here Mistras AEwin software with PCI-2 card). Among them, the selection of the proper sensors, threshold, pre-amplifier, analog-filter, Peak Definition Time (PDT), Hit Definition Time (HDT) and Hit Lockout Time (HLT) (see Table 2-6) are the most important factors affecting the testing sensitivity and accuracy.

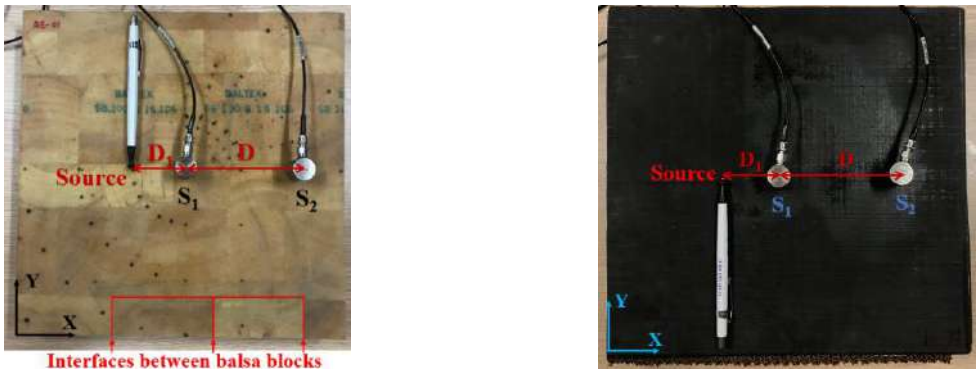

(a) GFRP-balsa sandwich panel. (b) CFRP-honeycomb sandwich panel

Fig. 2-8. Positions of the sensors and source (in 0° direction) on the tested sandwich panels.

Table 2-6. AE acquisition parameters for all sandwiches in active Hsu-Nielsen tests [113].

Threshold (dB)	Pre-amplifier (dB)	Analog Filter (MHz)	PDT (μs)	HDT (μs)	HLT (μs)	Sample Rate (MSPS)	Pre-Trigger (μs)	Hit Length
30	40	0.02-1	35	150	300	5	256	4k

First of all, concerning the choice of sensors, it has been proven that wave velocity measured by wideband sensors [193-196] is not as stable as what observed by resonance sensors, because the signals recorded by wideband sensors are more prone to be affected by the other noise sounds which have only very narrow frequency range lower than 20 kHz. Thus, in this study, a compromise has been made by using R6α sensor whose resonance frequency is 60 kHz for all the preliminary active Hsu-Nielsen tests [127], so as to produce better repeatability and give the smaller error of all measurements. The threshold, which determines the system sensitivity to the environmental noise, is set by 30 dB. The pre-amplifier is 40 dB, and the analog-filter is in the range of 20 kHz -1 MHz.

PDT, HDT and HLT are the critical parameters which can make sure that complicated AE waveforms are cut into the right number of hits (see Fig. 2-9). PDT ensures correct identification of Risetime of Peak Amplitude. HDT ensures that each AE signal from the structure is reported as one and only one hit. With proper setting of HLT, false measurements during the signal decay are avoided and data acquisition speed can be increased. For composite structures, it is suggested in AEwin user manual [113] that PDT is within 20-50 μs, HDT within 100-200 μs, and HLT be 300 μs. After repeating the Hsu-Nielsen tests for many times, finally, PDT is set by 35 μs, HDT is 150 μs, and HLT is 300 μs.

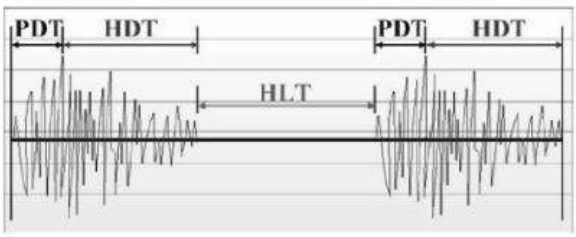

Fig. 2-9. AE timing parameters of the waveform signals [107].

Sample Rate is the rate at which the data acquisition board samples waveforms on a per second basis. A sample rate of 1 MSPS (Mega Samples Per Second) means that one waveform sample is taken every μs. A sample rate of 5 MSPS means that one waveform sample is taken every 1/5 μs., etc. After comparing the waveforms recorded by different sample rate, the max 5 MSPS was chosen for better accuracy.

Pre-Trigger tells the software how long to record (in μs.) before the trigger point (the point at which the threshold is exceeded). The minimum allowable pre-trigger value is zero. The maximum allowable pre-trigger value is calculated by dividing the hit length by the sample rate in MHz. For example, if the hit length was 4 k (1 k = 1024) and the sample rate was 5 MHz, then the maximum allowable pre-trigger would be 1024*4/5 = 820 μs. Hit Length determines the size of a waveform. At a 5 MSPS sampling rate, a hit length of 1 k will allow up to 205 μs. of data, a hit length of 4 k will allow 820 μs, and so on [113]. Thus, in this work, the max hit length 4 k was chosen, and then pre-trigger was set by 256 μs (small than 820 μs) in Hsu-Nielsen tests to ensure a proper waiting time before the trigger point.

2.3.1.1.2 Wave velocity determination in active Hsu-Nielsen test

For each panel mentioned above, in order to study the acoustic wave propagation velocity in different directions of composite structures, pencil lead breaking was conducted at least 10 times in each direction, and the tests were repeated every 15° between 0° and 90° (see Fig. 2-10) with the same D_1 (distance between the source and the first sensor), and the same D (distance between two sensors).

The velocity has been measured on the basis of the difference of the arrival times between the two sensors S_1 and S_2 mounted on top surface of the panels in Fig. 2-8, as given by Eq. (2-1):

$$v = \frac{D}{\Delta t} = \frac{D}{t_2 - t_1} \tag{2-1}$$

Where t_2 and t_1 are the arrival times at the maximum amplitude at each sensor, respectively.

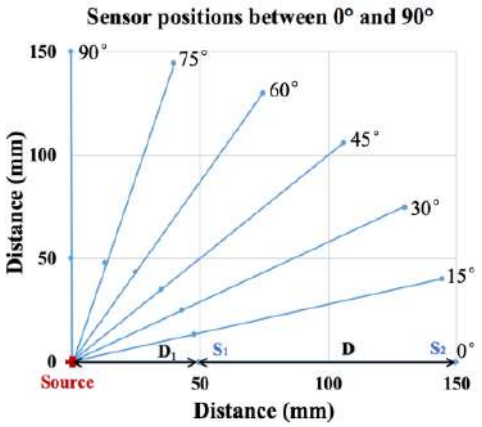

Fig. 2-10. Positions of sensors and source on the tested panel between 0° and 90°.

The influence of the sensor-source distance and sensor distance on the wave velocity measurements has been studied before finally determining these two distances for all tests. By comparing D= 100 mm and D=50 mm, it can be found that the error of measured velocity caused by the positioning of the sensors is less than 5%, and the results will be shown in the following analysis. Finally, D_1 and D are chosen as 50 mm and 100 mm for the further study to ensure that the acoustic wave has propagated a long distance in the tested panels, also to help determine the sensor distance in 4-point bending tests.

The plate wave theory [100, 197-198] is often used to analyze the acoustic wave propagation velocity when the thickness is much smaller than the other two dimensions of the plate. It is complicated to distinguish between the extensional and flexural wave modes, but the velocity measured in the standard Hsu-Nielsen test is proved to be dominated by the extensional wave [195-198]. For an infinite isotropic plate, the longitudinal wave velocity, C_L can be expressed as Eq. (2-2):

$$C_L = \sqrt{\frac{E}{\rho\,(1-\nu^2)}} \tag{2-2}$$

Where ρ is the specimen density, E is Young's modulus, ν is Poisson's ratio.

For an orthotropic composite laminated plate, C_L is thought to be related to the in-plane longitudinal elastic modulus, E_{11}. The formula is often given by Eq. (2-3) [99]:

$$C_L = \sqrt{\frac{E_{11}}{\rho\,(1-{\nu_{21}}^2)}} \tag{2-3}$$

Where E_{11} and ν_{21} denote the in-plane Young's modulus and Poisson's ratio respectively in 1 direction which is the longitudinal fiber orientation.

In this study, in order to determine the extensional wave velocity in any direction, an angle θ is defined with respect to the longitudinal X or 1 direction (see Fig. 2-7 and Fig. 2-8), and then Eq. (2-3) can be extended to Eq. (2-4) as following:

$$C_L(\theta) = \sqrt{\frac{E_x(\theta)}{\rho\,(1-\nu_{yx}(\theta)^2)}} \tag{2-4}$$

Where ρ is the density of the specimen; $E_x(\theta)$ and $\nu_{yx}(\theta)$ are Young's modulus and Poisson's ratio in the measured direction x, associated with the angle θ; recall that $\nu_{yx}(\theta)$ denotes the negative of the ratio of strain in the y direction over that in the x direction when there is stress in the x direction. Herein the composite constants $E_x(\theta)$ and $\nu_{yx}(\theta)$ in any direction can be determined easily by the classical laminate theory.

2.3.1.2. AE wave velocity in CFRP-honeycomb sandwich panels

2.3.1.2.1 AE wave velocity in CFRP laminated skin

Fig. 2-11 firstly shows that the sensor distance has little influence on the measured AE wave velocities in the thin CFRP skin of [0°/90°/0°] between 0° and 90° with a measurement step at 15°. When sensor distance D varies from 50 mm to 100 mm, the error of wave velocities is less than 5% between 0° and 90°. And the measured velocity when D=50 mm is a little higher than the values when D=100 mm.

And then, Fig. 2-12 compares the measured AE wave velocities (D=100 mm) with the calculated velocities by Eq. (2-4), to ignore the influence of sensor positions on the measured velocities. The measured velocities (red line) and analytical values (purple dotted line) show the similar variation tendency along different directions, with the highest velocity in 0° and the lowest in 60°. The maximum error between the measurements and calculated velocities by Eq. (2-4) is 15.57% in 15°, and the minimum error is 12.92% in 0°.

It is obvious that the propagation direction has a large influence on the AE wave velocity, with the max difference of 3400 m/s between 0° and 60°. The velocity in 0° with two plies of fibers is higher than that in 90° direction with only one ply of fibers. In conclusion, the farther it is away from the most fiber orientation, the lower the velocity will be. It indicates that the effects of the propagation direction on the velocity shall be considered when locating damages in the composite structures.

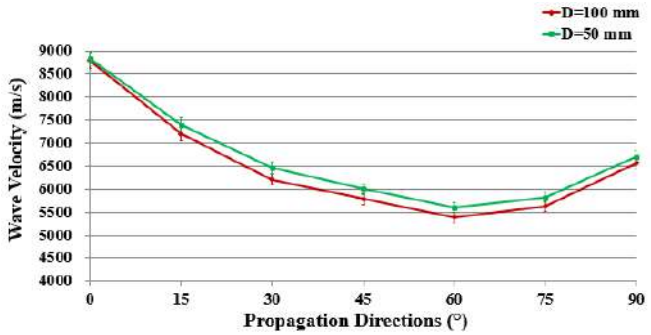

Fig. 2-11. Influence of sensor distance on measured AE wave velocities in [0°/90°/0°] CFRP panel.

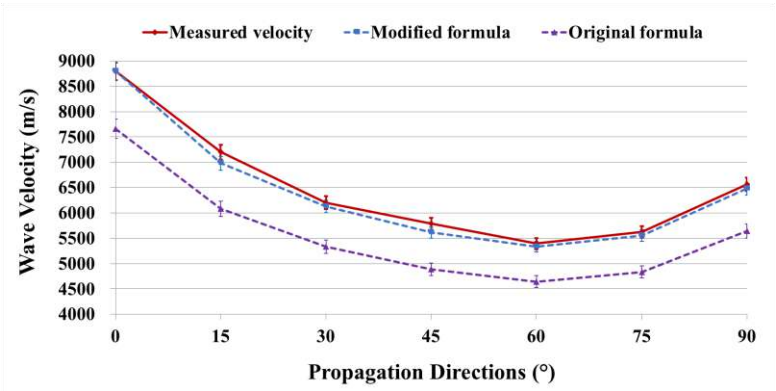

Fig. 2-12. Measured AE wave velocities and calculated values in [0°/90°/0°] CFRP panel.

According to the consistent variation tendency of measured and calculated velocity, it gives us an inspiration that only by measuring AE wave velocity in 0° direction where the error is the smallest, we can modify Eq. (2-4) to get the more precise velocity in any direction just by introducing a corrective factor, f_1. If this corrective factor is defined as the ratio of measured C_L in 0° over the C_L calculated by Eq. (2-4) in the same direction, the velocity in any direction can be determined by Eq. (2-5):

$$C_L(\theta) = f_1 \cdot \sqrt{\frac{E_x(\theta)}{\rho\,(1-\nu_{yx}(\theta)^2)}} \tag{2-5}$$

Where $f_1 = \frac{C_L{}^{\text{Measured}}(\theta=0^o)}{C_L{}^{\text{Calculated}}(\theta=0^o)} = \frac{C_L{}^{\text{Measured}}(\theta=0^o)}{\sqrt{E_x(\theta=0^o)/\rho\left(1-\nu_{yx}(\theta=0^o)^2\right)}}$.

Applying this idea to the case of the thin CFRP skin, the corrective factor f_1 can be determined by:

$$f_1 = \frac{C_L{}^{\text{Measured}}(\theta=0^o)}{C_L{}^{\text{Calculated}}(\theta=0^o)} = \frac{8796\ \text{m/s}}{7660\ \text{m/s}} = 1.148$$

The results obtained from measurements, Eq. (2-4) and Eq. (2-5) are also compared in Fig. 2-12. The max error between the measured velocity (red line) and calculated value (blue dotted line) by Eq. (2-5) is only 3.05% in 15°, which has been largely reduced, compared to 15.57% in 15° using Eq. (2-4).

In fact, the corrective factor, f_1, reflects the system error between the theoretical acoustic wave formula and the real propagated velocity in composites, such as the influence of other wave propagation modes, the sensor distance and sensitivity, as well as the test environment like sound noises. This factor is considered constant for a given composite structure, independent of the AE wave propagation direction. That's why we can reduce the prediction error of AE wave velocity by calculation using Eq. (2-5).

2.3.1.2.2 AE wave velocity in the whole sandwich

Generally, Eq. (2-4) is thought to be effective for thin laminates [193-195], but it is unclear whether the theoretical analysis could be suitable for thicker sandwich structures which consists of two different materials. Thus, to verify the effectivity of Eq. (2-4) for sandwich panels, AE wave velocity between 0° and 90° in the CFRP-honeycomb sandwich panel A (see Table 2-5) was firstly tested.

Fig. 2-13 firstly shows that the sensor distance has little influence on the measured AE wave velocities in CFRP-honeycomb sandwich A between 0° and 90° with a measurement step at 15°. When sensor distance D varies from 50 mm to 100 mm, the error of wave velocities is less than 5% between 0° and 90°. And the measured velocity when D=50 mm is a little higher than the values when D= 100 mm.

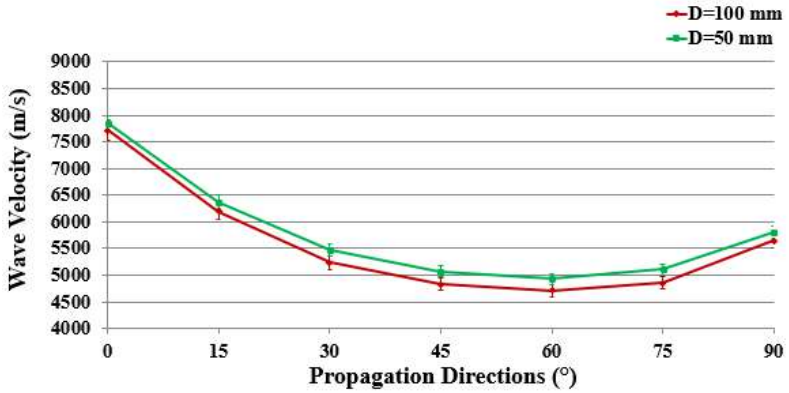

Fig. 2-13. Influence of sensor distance on measured AE wave velocities in CFRP-honeycomb sandwich A.

And then, Fig. 2-14 compares the measured AE wave velocities (D=100 mm) with the analytical results from Eq. (2-4) (purple dotted line) and modified Eq. (2-5) (blue dotted line), to ignore the influence of sensor positions on the measured velocities. Similar to the approach applied to the pure CFRP laminated skin, calculated velocities were also corrected by the modified model Eq. (2-5) (blue dotted line), where the corrective factor is determined by:

$$f_1 = \frac{C_L^{\text{Measured}}(\theta=0^o)}{C_L^{\text{Calculated}}(\theta=0^o)} = \frac{7716\ \text{m/s}}{6723\ \text{m/s}} = 1.148$$

It is observed that the test and theoretical velocities show a similar variation tendency along different directions, with the highest velocity in 0° and the lowest in 60°. The max error between test and calculation results by the modified Eq. (2-5) is largely reduced to only 3.69% in 30°, compared to the max 13.04% by Eq. (2-4). It verifies that the improved formula Eq. (2-5) can also be effective for prediction of AE wave velocity in any direction in the thick sandwich structure. In this way, plenty of time and experimental efforts can be saved.

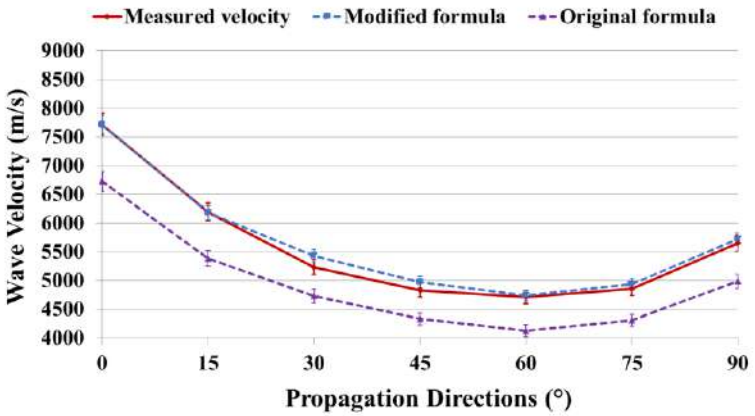

Fig. 2-14. Measured AE wave velocities and calculated values in CFRP-honeycomb sandwich A.

2.3.1.2.3 Correlation between AE wave velocity in the skin and sandwich

When analyzing Fig. 2-12 and Fig. 2-14, it is obvious there may be some relationships between the AE wave velocity in the skin and sandwich. Moreover, even the acoustic wave propagation velocity in sandwich is slower than that in pure composite skin, the corrective factor is nearly the same. Fig. 2-15 compares the measured AE wave velocities in sandwich A and those measured on the pure laminate skin of CFRP [0°/90°/0°]. It can be seen that the velocity in the skin is always higher than that in the sandwich whatever the acoustic wave propagation direction; their variation along different direction has the similar tendency with the highest velocity in 0° and lowest in 60°.

A possible explanation for this phenomenon is that the AE wave velocity in a sandwich structure is dominated by the skin property, and the existence of honeycomb core with much lower modulus and density mainly contributes to the small velocity decrease. Moreover, considering the effects of coupling of multiple wave modes [100], the out-of-plane flexural mode contributes more to the acoustic wave attenuation in thicker sandwich structure, which results in the higher velocity dispersion compared to the thinner laminate skin. In addition, the air in the hollow honeycomb core cell may cause the acoustic wave attenuation.

Considering theoretical explanations by Eq. (2-5), the similar velocity variation tendency indicates that the direction effects on the elastic modulus and Poisson's ratio can result in the variation of AE

wave velocity along different directions in both the laminate and sandwich structures. From this observation, it is now interesting to know whether it is possible to quantify the relationship between the wave propagation velocity in a composite sandwich structure and that in their composite skin.

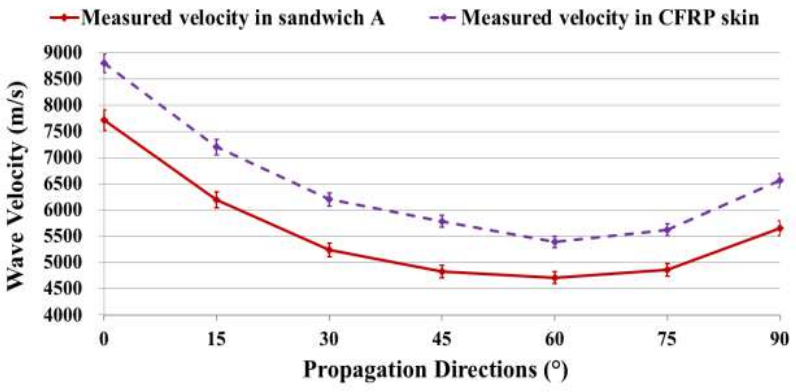

Fig. 2-15. Measured AE wave velocities in sandwich A and CFRP skin panel.

Based on multi-material beam theory [202], the equivalent in-plane modulus of sandwich structure $E_s(\theta)$ can be obtained by the combination of that of the core and that of the two skins:

$$E_s(\theta) \cdot A = E_f(\theta) \cdot \frac{2h_f}{h_s} \cdot A + E_c(\theta) \cdot \frac{h_c}{h_s} \cdot A \tag{2-6A}$$

Where A is the cross-section area of a sandwich beam; $E_f(\theta)$ and $E_c(\theta)$ are the elastic modulus of the skin and the core, respectively. h_s, h_c and h_f are the thickness of the sandwich, of the core and of the skin, respectively. Then $E_s(\theta)$ can be expressed as:

$$E_s(\theta) = E_f(\theta) \cdot \frac{2h_f}{h_s} + E_c(\theta) \cdot \frac{h_c}{h_s} \tag{2-6B}$$

Using the material parameters and panel dimensions in Table 2-1, 2-3 and 2-5, the density of sandwich can be obtained by Eq. (2-7):

$$\rho_s = \frac{2\rho_f \cdot h_f + \rho_c \cdot h_c}{h_s} \tag{2-7}$$

For the sandwich A and CFRP skin panel, $\rho_s(A) = 183\ \mathrm{kg/m^3}$.

Substituting Eq. (2-6B) and Eq. (2-7) into Eq. (2-4), AE wave velocity in a sandwich structure can be given by Eq. (2-8):

$$C_{Ls}(\theta) = \sqrt{\frac{E_x(\theta)}{\rho_s(1-\nu_{yx}(\theta)^2)}} = \sqrt{\frac{2E_f(\theta) \cdot h_f + E_c(\theta) \cdot h_c}{2\rho_f \cdot h_f + \rho_c \cdot h_c} \cdot \frac{1}{(1-\nu_{yx}(\theta)^2)}} \tag{2-8}$$

Eq. (2-8) indicates that the acoustic wave velocity in a sandwich structure is mainly determined by the elastic modulus, density and thickness of the constituent materials. For sandwich structure, E_c is

much smaller than E_f (see Tables 2-1 and 2-3). In the case of $E_c(\theta)h_c/2E_f(\theta)h_f < 5\%$, the contribution of $E_c(\theta)$ to $E_s(\theta)$ can be ignored with less than 5% error, which means $h_c < 0.1h_fE_f(\theta)/E_c(\theta)$, and then Eq. (2-6B) becomes:

$$E_s(\theta) = E_f(\theta) \cdot \frac{2h_f}{h_s} = E_f(\theta) \cdot \frac{2h_f}{2h_f+h_c} = E_f(\theta) \cdot \frac{2}{2+\frac{h_c}{h_f}} \quad (2\text{-}9)$$

This expression shows that the modulus of sandwich can be obtained from that of the skin multiplied by a geometrical coefficient: $2/(2+h_c/h_f)$. The higher the ratio of the core thickness over that of the skin is, the lower the contribution of the skin modulus will be. If the skin thickness remains the same, the thicker core will result in lower elastic modulus of sandwich structure.

According to the theoretical calculation, Poisson's ratios of the skin and the sandwich are nearly the same in the same direction for commonly used sandwiches. Hence, from the AE wave velocity formula, the correlation ratio of the wave velocity in the sandwich over that in the skin, R, is proposed by Eq. (2-10):

$$R = \frac{C_{Ls}(\theta)}{C_{Lf}(\theta)} = \sqrt{\frac{E_s(\theta)}{E_f(\theta)} \cdot \frac{\rho_f}{\rho_s}} \quad (2\text{-}10)$$

Substituting Eq. (2-7) and Eq. (2-9) into Eq. (2-10), R becomes:

$$R = \frac{C_{Ls}(\theta)}{C_{Lf}(\theta)} = \sqrt{\frac{2h_f}{2h_f+h_c} \cdot \frac{\rho_f \cdot (2h_f+h_c)}{2\rho_f \cdot h_f+\rho_c \cdot h_c}} = \sqrt{\frac{2\rho_f \cdot h_f}{2\rho_f \cdot h_f+\rho_c \cdot h_c}} = \sqrt{\frac{2}{2+\frac{\rho_c h_c}{\rho_f h_f}}} \quad (2\text{-}11)$$

Eq. (2-11) works well with a condition of $h_{c-max} < 0.1h_fE_f(\theta)/E_c(\theta)$ with less than 5% error. It signifies that the correlation between AE wave velocity in the sandwich and in their skin is mainly determined by the density and thickness of the constituent materials.

Theoretically, when h_c is 0, R becomes 1, corresponding to the pure laminate skin. If $h_c \neq 0$, $0<R<1$. Considering the application condition of Eq. (2-11), h_c has a max limitation by $h_{c-max} < 0.1h_fE_f(\theta)/E_c(\theta)$. The main problem is that the different variation tendency of elastic modulus of the core and skin along different directions makes it complex to give an accurate value of $E_f(\theta)/E_c(\theta)$. To simplify the analysis, we predict h_{c-max} by modulus of core and skin in 0^o direction which mainly determines the stiffness of the sandwich in fiber direction.

Then, for CFRP-honeycomb (Nomex) sandwiches (A and C), the h_{c-max} at $\theta = 0°$ for Eq. (2-11) is near 60 mm calculated from the material parameters. Applying Eq. (2-11) to sandwich A (h_c=18mm), R equals to 0.87. This value can be compared to the measured results in Fig. 2-16. Good agreement has been observed. The average measured ratio R in different directions is about 0.86. It demonstrates

that Eq. (2-11) can be used to predict AE wave velocity in a sandwich structure from the corresponding velocity in the skin.

Thus, there is no need to make lots of efforts to repeat Hsu-Nielsen tests to study AE propagation properties of both the skin and sandwich structure in all directions. In fact, it can save at least 4 hours of test time to obtain the precise velocities in the skin and sandwich in all directions.

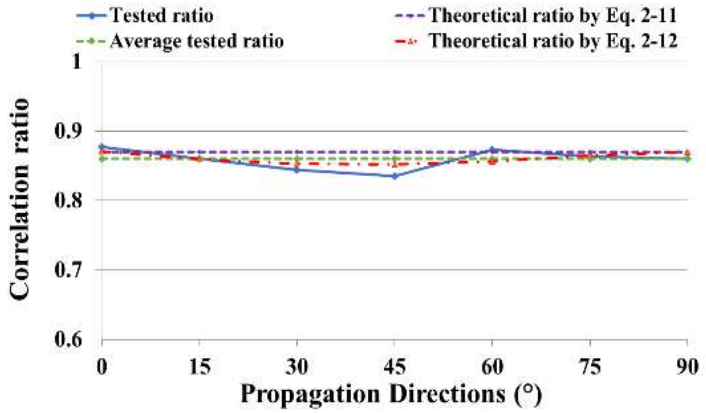

Fig. 2-16. Correlation ratio of AE wave velocity in CFRP-honeycomb sandwich A over that in the skin.

2.3.1.2.4 Validation of the proposed model using correlation ratio R

In order to validate the above proposed approach, the CFRP-honeycomb sandwich panel B (aluminum core with h_c=30 mm) and C (Nomex core with h_c=60 mm) with the same skins have been studied. AE wave velocities between 0° and 90° in sandwich B and C were measured and compared with those of sandwich A (Nomex core with h_c=18 mm) and those of the skin in Fig. 2-17.

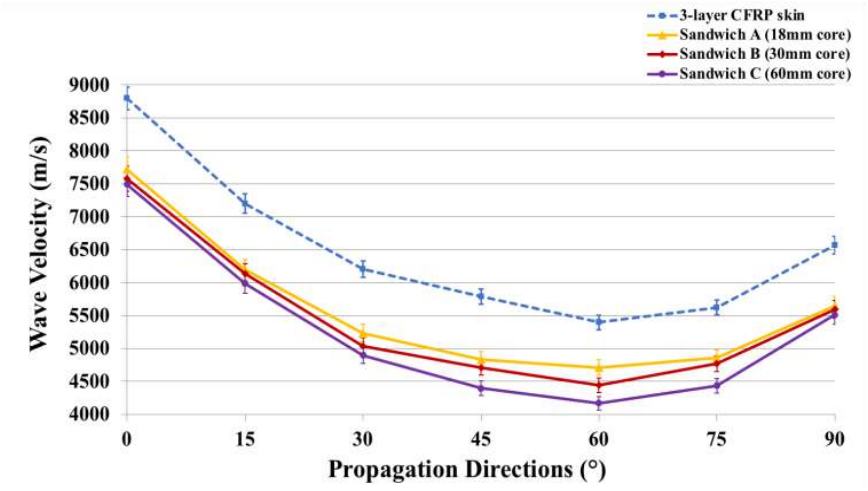

Fig. 2-17. Measured AE wave velocities in different CFRP-honeycomb sandwich panels.

The measured velocities in the skin, sandwich A, B and C show the similar variation tendency along different directions, with the highest velocity in 0° and the lowest in 60°. The thicker the core is, the

lower the wave velocity in sandwich structure will be. The farther it is away from the most fiber direction, the larger the velocity difference between the different sandwich panels will be. It means that the core thickness has larger effects on the acoustic wave velocity between 45° and 75° away from the most fiber direction.

$\boldsymbol{h_{c-max}}$ at $\boldsymbol{\theta = 0°}$ is about 60 mm for CFRP-honeycomb (Nomex) sandwiches (A and C) and 200 mm for CFRP-honeycomb (aluminum) sandwich (B). If Eq. (2-11) is also applied to sandwich B and C, the correlation ratio R of sandwich B and C can be obtained, equals to 0.82 and 0.70, respectively. Fig. 2-18 compares the theoretical and measured correlation ratio of sandwich B and C. The average tested correlation ratio of sandwich B is 0.84, and it is 0.80 for sandwich C. Obviously, the thicker the core is, the larger the error between the tested ratio and theoretical value by Eq. (2-11) will be. One explanation could be that the contribution of the Poisson's ratio of the core should not be ignored when the core thickness is much larger. Then going back to Eq. (2-8), the correlation ratio becomes:

$$\boldsymbol{R = \frac{C_{Ls}(\theta)}{C_{Lf}(\theta)} = \sqrt{\frac{2}{2+\frac{\rho_c h_c}{\rho_f h_f}} \cdot \frac{(1-\nu_f(\theta)^2)}{(1-\nu_s(\theta)^2)}}} \quad (2\text{-}12)$$

Eq. (2-12) shows that the correlation ratio can be affected by the direction via Poisson's ratio, which can be reflected by the red curves in Fig. 2-16 and Fig. 2-18. An interesting phenomenon is that correlation ratio by Eq. (2-12) shows the similar variation tendency to the tested ratio, with the highest in 0° and 90°, lowest between 30° and 60°. Theoretically, the thicker the core is, the larger the Poisson's ratio of the sandwich in 0° and 90° will be, but lower between 15° and 75°. Thus, for sandwich structure with a thicker core, the theoretical correlation ratio by Eq. (2-12) is lower than that by Eq. (2-11) between 15° and 75°. But in 0° and 90°, the correlation ratio by Eq. (2-12) is almost the same as that by Eq. (2-11) even for the 60 mm thick core.

The max error between tested ratio and value by Eq. (2-12) is 18.58% in 15° for 60 mm cored sandwich. However, the error between average tested ratio and that obtained from Eq. (2-11) is only 14.30%. Hence, the influence of Poisson's ratio of the tested sandwich structures in Eq. (2-12) can be simplified. In addition, considering the acoustic wave propagation modes, due to the Poisson effect [100], the out-of-plane flexural wave has more influences on the received signals if the core is thicker, which will result in higher acoustic wave attenuation and measurement error. This phenomenon can also explain why the tested correlation ratio is much higher than the theoretical ratio by Eq. (2-11) and Eq. (2-12) for the thicker sandwich structure.

In summary, Eq. (2-11) can be effectively used to predict AE wave velocity in most common sandwich structures from the velocity in the corresponding skin, with an acceptable error when the core thickness is smaller than 30 mm.

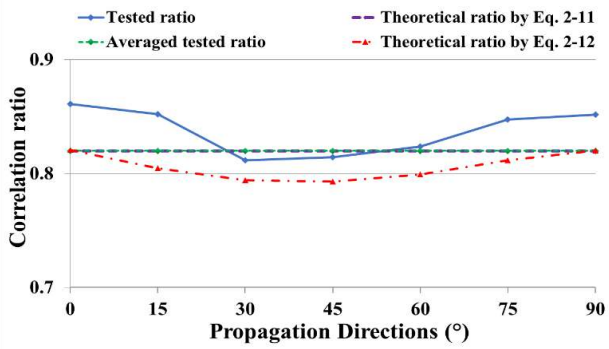

(a) Correlation ratio of sandwich B (aluminum honeycomb core h_c=30 mm).

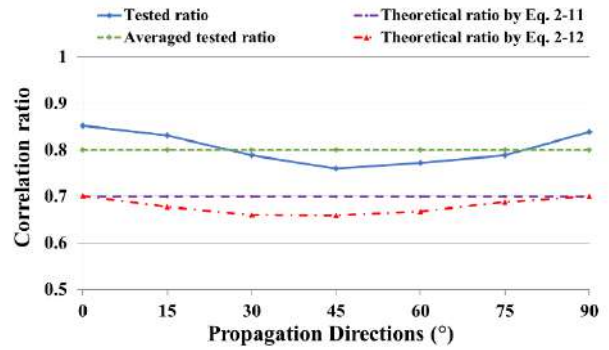

(b) Correlation ratio of sandwich C (Nomex honeycomb core h_c=60 mm).

Fig. 2-18. Correlation ratio of AE wave velocity in CFRP-honeycomb sandwiches over that in the skins.

2.3.1.3. AE wave velocity in GFRP-balsa sandwich panels

2.3.1.3.1 AE wave velocity in GFRP laminated skin

Similarly, to verify Eq. (2-5) in the 3-layer woven GFRP skin panels, AE wave velocity was also tested every 15° between 0° and 90°. Fig. 2-19 firstly shows that the sensor distance has little influence on the measured AE wave velocities in the thin 3-layer woven GFRP panel between 0° and 90° with a measurement step at 15°. When sensor distance D varies from 50 mm to 100 mm, the error of wave velocities is less than 5% between 0° and 90°. And the measured velocity when D=50 mm is a little higher than the values when D=100 mm.

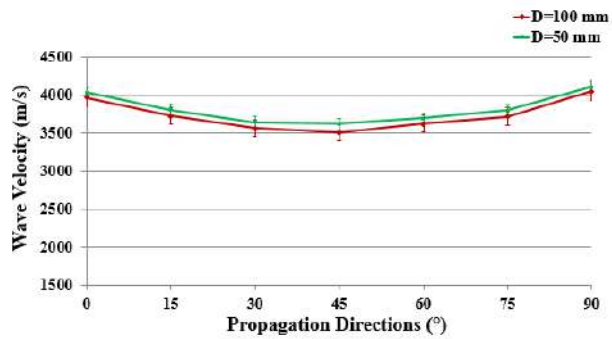

Fig. 2-19. Influence of sensor distance on measured AE wave velocities in 3-layer woven GFRP panel.

And then, Fig. 2-20 compares the measured AE wave velocities (D=100 mm) with the calculated velocities by Eq. (2-4) (purple dotted line) and modified Eq. (2-5) (blue dotted line), to ignore the influence of sensor positions on the measured velocities. In this case, by application of Eq. (2-5), the corrective factor is obtained by:

$$f_1 = \frac{C_L^{\text{Measured}}(\theta=0^o)}{C_L^{\text{Calculated}}(\theta=0^o)} = \frac{3967\ \text{m/s}}{3212\ \text{m/s}} = 1.212$$

The measured and analytical velocities show the similar variation tendency along different directions, with the highest in 90° and the lowest in 45°. The max error between the measured and calculation results by Eq. (2-4) is 22.65% in 60°, and the minimum error is 17.51% in 0°. While by using the modified formula Eq. (2-5), the max error is highly reduced, with only 6.23% in 60°.

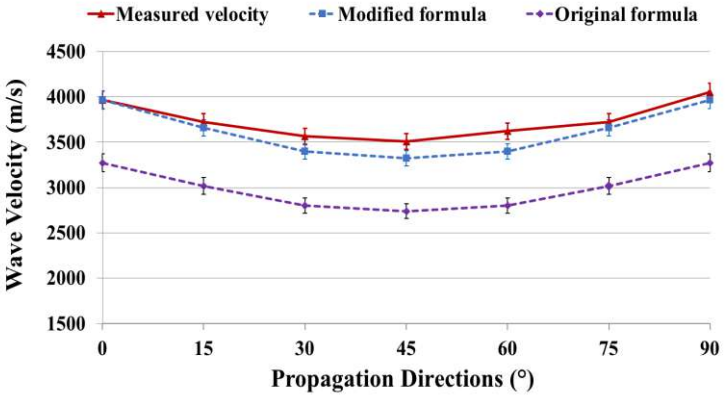

Fig. 2-20. Measured AE wave velocities and calculated values in 3-layer woven GFRP panel.

Compared to the max difference of 3400 m/s in the CFRP panel, the propagation direction has smaller effects on the velocity variation in the woven GFRP panel, with the max measured difference of only 540 m/s between 0° and 45°. It demonstrates further that the [0°/90°/0°] CFRP and the 3-layer woven GFRP laminates have the different behavior, which is mainly because the former has the most fiber oriented at 0°, while the later has the same number of fibers oriented at 0° and 90°.

2.3.1.3.2 AE wave velocity in the whole sandwich

Fig. 2-21 firstly shows that the sensor distance has little influence on the measured AE wave velocities in GFRP-balsa sandwich panel between 0° and 90° with a measurement step at 15°. When sensor distance D varies from 50 mm to 100 mm, the error of wave velocities is less than 5% between 0° and 90°. And the measured velocity when D=50 mm is a little higher than the values when D=100 mm.

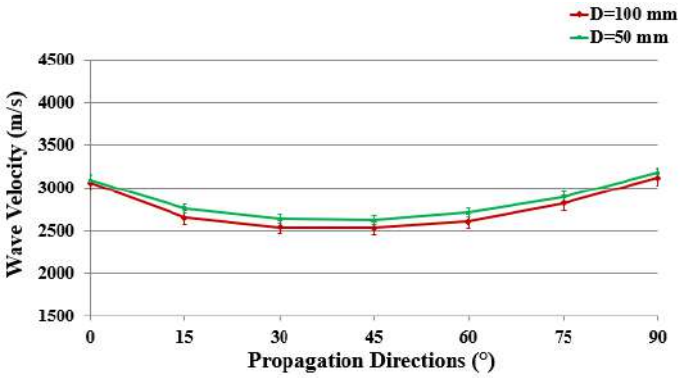

Fig. 2-21. Influence of sensor distance on measured AE wave velocities in GFRP-balsa sandwich panel.

Substituting the panel dimension and material parameters in Table 2-1, 2-2 and 2-4 into Eq. (2-7), the density of the balsa sandwich panel can be obtained by: $\rho_s(D) = 307\ \mathrm{kg/m^3}$. In the similar way, the corrective factor here equals 1.218. Fig. 2-22 compares the measured AE wave velocities (D=100 mm) with the analytical results from the original model Eq. (2-4) (purple dotted line) and modified Eq. (2-5) (blue dotted line) in GFRP-balsa sandwich, to ignore the influence of sensor positions on the measured velocities.

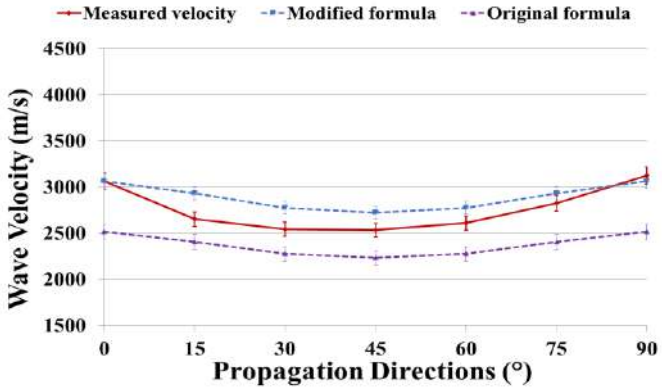

Fig. 2-22. Measured AE wave velocities and calculated values in GFRP-balsa sandwich panel.

The measured and analytical values show almost the similar variation tendency along different directions, with the highest velocity in 90° and the lowest in 45°. The max error of the results from the modified model Eq. (2-5) is reduced to 10.55% in 15°, compared to the max error 19.48% in 90° of the results from Eq. (2-4). In the most important 0° and 90°, the calculated velocities are almost the same as the tested values. So, the overall error is less reduced compared to that of the honeycomb sandwich structure, which is mainly due to the special anisotropic material property, higher acoustic attenuation and the adhesions of different balsa wood blocks in the balsa cored sandwich (see Fig. 2-8). So, it's better to verify this model on the sandwich structures made from other materials, for example, foam cored sandwich.

2.3.1.3.3 Correlation between AE wave velocity in the skin and sandwich

Fig. 2-23 compares the measured velocities in GFRP-balsa sandwich with those measured on the pure GFRP skin and balsa core. It is observed that AE wave velocity in the sandwich is always higher than that in the core but lower than that in the skin whatever the wave propagation direction is; the variation as a function of wave propagation directions in the sandwich and the skin have nearly the similar tendency, with the highest velocity in 90° and lowest in 45°.

Particularly, for pure balsa panel, the acoustic wave velocity is much lower, with lowest in 0° and within a range of 850-1000 m/s. It is interesting that the propagation direction has little effect on the acoustic wave velocity in balsa wood panel, with a very small standard deviation in each direction. This is mainly because the balsa panel is homogenized after the reconstruction of gluing small wood blocks, and it is a little different from the original anisotropic wood material. Compared to pure honeycomb core, balsa wood panel is less affected by the original material property.

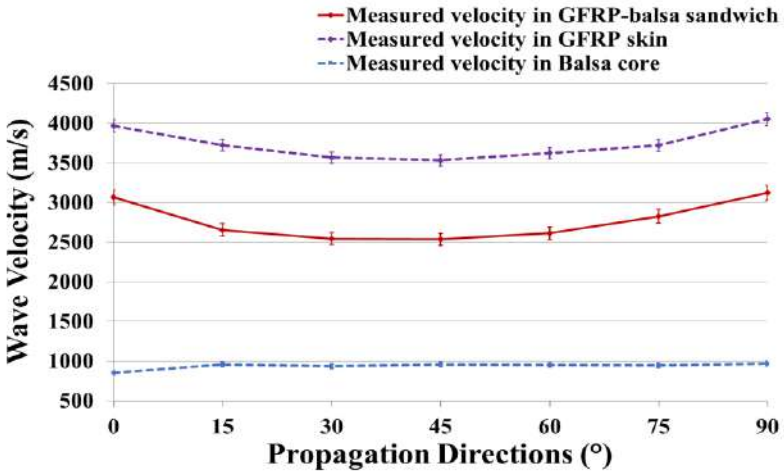

Fig. 2-23. Comparison of acoustic wave velocities in GFRP-balsa sandwich, GFRP skin and balsa core.

To apply Eq. (2-11) to GFRP-balsa sandwich, the h_{c-max} at $\theta = 0°$ is about 11 mm, so the model is acceptable for balsa core with a thickness of 9.5-10 mm in this thesis. Fig. 2-24 also shows that Eq. (2-12) gives the similar variation tendency to the tested values of correlation ratio, with the highest in 0° and 90°, and lowest between 30° and 60°. The theoretical correlation ratio by Eq. (2-12) is almost the same as that by Eq. (2-11) in 0° and 90°, but much lower between 15° and 75°. Eq. (2-11) gives the value of the correlation ratio R= 0.75, which is consistent with the average measured ratio of 0.74. It demonstrates once again that Eq. (2-11) can be used to evaluate the AE wave velocity in any direction in the common sandwich structure from the velocity in the corresponding skin when $h_c < 0.1 h_f E_f(\theta)/E_c(\theta)$, whatever the constituent materials are.

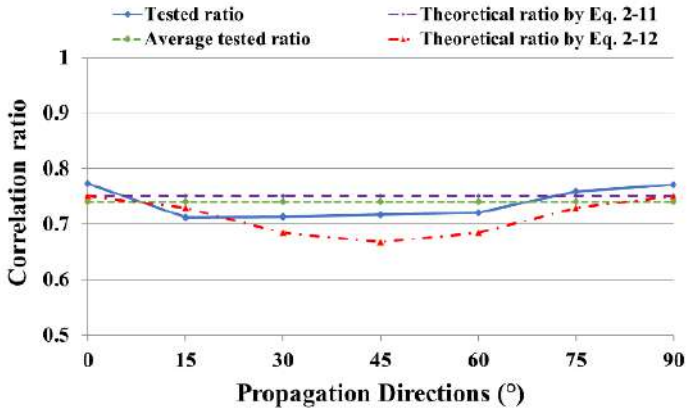

Fig. 2-24. Correlation ratio of AE wave velocity in GFRP-balsa sandwich over that in the skin.

2.3.1.4. Conclusions

Based on the experimental and theoretical analysis of AE wave velocity in composite laminated skins and sandwich panels, a new 3-step strategy of rapid determination of AE wave propagation velocity has been proposed for most usually used composite sandwich structures: 1-Measure AE wave velocity of the composite skin in one direction; 2-Calculate the corrective factor proposed in this work to determine the velocity in all directions of the composite skin by Eq. (2-5); 3-Determine the correlation ratio by Eq. (2-11), and then the velocity in any direction of a sandwich can be predicted.

To conclude, this new rapid method to determine AE wave velocity in any direction has been proven effective for both CFRP-honeycomb and GFRP-balsa sandwich panels. It can be further used as a tool to evaluate moisture effects on the stiffness degradation of composite structures before starting 4-point bending tests and modify the elastic modulus of skin of wet sandwich in the numerical models so as to improve prediction accuracy.

2.3.2. Characterization of AE attenuation properties in sandwich panels

2.3.2.1. AE attenuation testing method

When AE wave propagates in solids, the attenuation property, which is the amplitude loss of an acoustic wave with according to the propagation distance, shall not be ignored in the anisotropic composite and wood materials, in order to localize the damages more accurately. It can be caused by four factors [193, 195, 198]: 1) geometric spreading of acoustic wave; 2) internal friction; 3) dissipation of wave into adjacent media; 4) losses due to velocity dispersion. It has been proven that the geometric spreading is the dominant source of attenuation in the near field close to the source. While in the far field, attenuation is dominated by absorption or conversion of acoustic energy into heat [193]. The inhomogeneity in the structure can scatter the acoustic wave, namely the interface effects on the composite structures. The attenuation due to velocity dispersion is mainly observed in

the wideband modal AE signals, while it is usually ignored when using the narrow band sensors [195].

Thus, in our active Hsu-Nielsen tests, the attenuation property of the sandwich panels can be related to the propagation distance and directions, the materials and interface positions, etc. Similar to the wave velocity tests, pencil lead breaks were performed at least 10 times at each sensor-source distance D_1 which equals to 50 mm, 100 mm, 150 mm and 200 mm in each direction every 15° between 0° and 90° on top of panels as shown in Fig. 2-8. In this way, AE amplitude attenuation properties in different directions can be measured as a function of propagation (sensor-source) distance.

2.3.2.2. AE attenuation in CFRP-honeycomb sandwich panels

2.3.2.2.1 AE attenuation in CFRP laminated skin

AE amplitude attenuation properties in [0°/90°/0°] CFRP laminated skins along different directions between 0° and 90° were also studied by pencil lead breaks at least 10 times at each sensor-source distance which equals to 50 mm, 100 mm, 150 mm and 200 mm on the 300 mm*300 mm panels, and the average amplitude at each position was shown in Fig. 2-25. It is obvious that AE amplitude attenuates faster as the propagation direction is farther away from the most fiber orientation, with the attenuation lowest in 0° and highest in 60°.

One reason is that the reflection and refraction effects of fiber/matrix interfaces on the acoustic wave will be higher when the propagation is not along the fiber direction. When compared with AE wave velocity variations in Fig. 2-12, it is interesting to find that the attenuation is higher when the velocity is smaller in a direction between 0° and 90°. So, the higher attenuation and lower velocity in these directions shall be considered when localizing damages under loading.

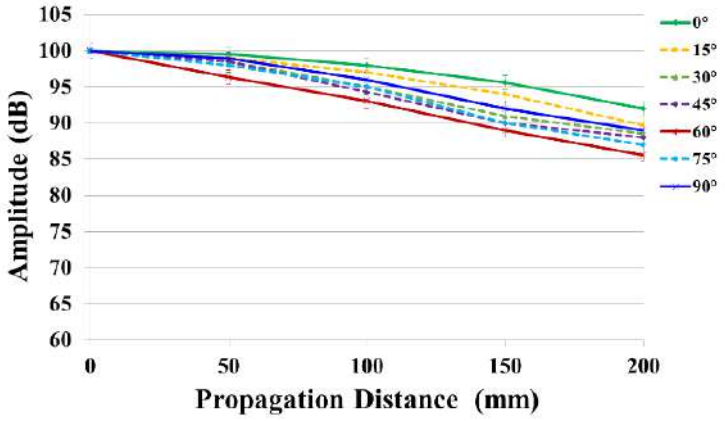

Fig. 2-25. AE attenuation properties in 3-layer CFRP skin along different directions.

2.3.2.2.2 AE attenuation in the whole sandwich

In the same way, AE attenuation properties in CFRP-honeycomb sandwich panel A along different directions between 0° and 90° were also studied in Fig. 2-26. Similar to Fig. 2-25, AE amplitude in the sandwich attenuates faster as the propagation is farther away from the most fiber orientation, slowest in 0° and fastest in 60°, which also agrees well with wave velocity variations, with the higher attenuation appearing in the direction where the lower velocity exists. This is mainly because that CFRP fibers of the skins are oriented most in 0°, and the ribbon direction L of honeycomb core is also along 0°. When the acoustic wave propagates along directions away from 0° and 90°, it will meet more interfaces of honeycomb cells and fiber/matrix, so the attenuation will become higher.

In addition, the attenuation of the sandwich is higher than that in the CFRP skin, showing that the lowest amplitude is 68 dB in 60° in sandwich at a sensor-source distance of 200 mm, while it is 85 dB in 60° in CFRP skin at the same distance. The main reason is that the air in the honeycomb cell hole will contribute to the acoustic energy dissipation. So, the higher attenuation in CFRP-honeycomb sandwich panel shall not be ignored when localizing damages under loading.

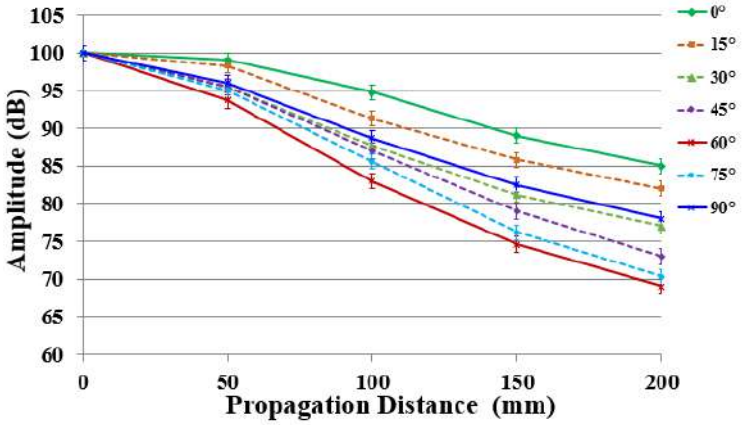

Fig. 2-26. AE attenuation properties in CFRP-honeycomb sandwich panel A along different directions.

2.3.2.3. AE attenuation in GFRP-balsa sandwich panels

2.3.2.3.1 AE attenuation in GFRP laminated skin

Similar to CFRP panels, AE attenuation properties in GFRP panels along different directions between 0° and 90° were also studied in Fig. 2-27. It verifies again that AE amplitude attenuates faster as the propagation is farther away from the most fiber orientation, lowest in 0°/90° and highest in 45°, which also agrees well with wave velocity variations, with the higher attenuation appearing in the direction where the lower velocity exists.

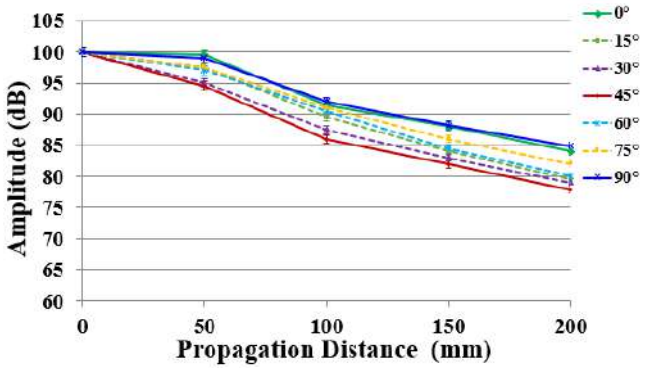

Fig. 2-27. AE attenuation properties in 3-layer GFRP panel along different directions.

2.3.2.3.2 AE attenuation in the whole sandwich

For GRRP-balsa sandwich panels, it can also be found in Fig. 2-28 that the higher attenuation appearing in the direction where the lower velocity exists, lowest in 0° and highest in 45°, which is also consistent with observations on GFRP skin panels. The different phenomenon from CFRP-honeycomb sandwich is that the attenuation in GFRP-balsa sandwich panel is lower than that in the corresponding GFRP skin. The lowest amplitude is 85 dB in 45° at a sensor-source distance of 200 mm in GFRP-balsa sandwich, while it is 77 dB in 45° at the same distance in GFRP skin in Fig. 2-27. One possible explanation is that the balsa/balsa block interfaces (see Fig. 2-8) of the thick balsa core and skin/core interfaces make it easier for acoustic waves to propagate in the solid materials than in the surrounded air.

In addition, the wave velocity (see Fig. 2-23) and attenuation in pure balsa are not highly affected by the propagation direction, which is because that balsa block interfaces are distributed randomly in all directions. The average amplitude attenuation in any direction in pure balsa panel is also plotted by black curve in Fig. 2-28. It can be seen that the amplitude at a sensor-source distance of 200 mm in pure balsa panel is 88 dB, which is close to the attenuation curves of GFRP-balsa sandwich in 15° and 75°, so it shall not be ignored when localizing damages under loading.

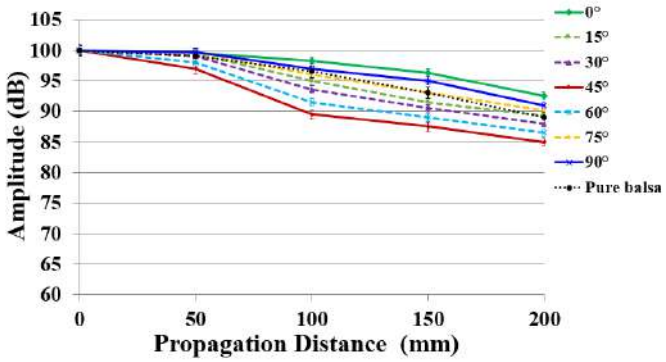

Fig. 2-28. AE attenuation properties in GFRP-balsa sandwich and pure balsa panels.

2.3.2.4. Conclusions

In conclusion, whatever the laminate material is, such as 3-layer [0°/90°/0°] CFRP and woven GFRP fibers, AE attenuation is higher as the propagation direction is farther away from the most fiber orientation, which is also the direction where the wave velocity is lower. For sandwich panels, the similar conclusions can be found. But there exists an interesting phenomenon that the attenuation in GFRP-balsa sandwich is lower than that in the corresponding GFRP skin, while the attenuation in CFRP-honeycomb sandwich is higher than that in the corresponding CFRP skin. This can be related to the fiber orientations of hollow honeycomb cells and random interface positions of balsa/balsa blocks.

2.4. Moisture effects on preliminary AE and IRT signals

2.4.1. Moisture absorption tests monitored by active AE and IRT methods

2.4.1.1. Water immersion test

According to the definitions in ISO 12571 [199] for determination of hygroscopic sorption properties of building materials and ASTM D5229 [200] for moisture absorption properties of polymer matrix composite materials, five triple dog-bone GFRP-balsa sandwich and CFRP-honeycomb sandwich specimens were firstly dried in the oven at 40℃ until the constant mass, which was reached if the change of mass between three consecutive weighing, each made every 24 h, differs by less than 0.1% of the total mass. 40℃ is below the glass transition temperature of the materials, to avoid the material damages due to high temperature. Then the specimens were immersed into water under room temperature until mass stabilization (protocol from the standard ISO 12571). On the first day, the mass was measured twice a day because water absorption rate was normally faster during the first few days. Then mass measurements were performed every 24 h later.

Finally, Moisture Content (MC) in percentage in the specimen, which is the ratio of the mass of the absorbed moisture in the structure to the oven-dried initial mass [199-200], can be defined by Eq. (2-13):

$$MC = \frac{M_i - M_0}{M_0} \times 100 \quad (2\text{-}13)$$

Where M_0 is the initial mass after drying process, M_i is the mass of wet specimen.

2.4.1.2. Active AE test setup on triple dog-bone sandwich specimens

During the whole moisture absorption period, active Hsu-Nielsen tests were performed regularly along the specimen length direction (0°, Direction X) (see Fig. 2-29) to monitor moisture effects on AE wave velocity, following Eq. (2-1) and Eq. (2-4). Distance between sensors S_1 and S_2 is 100 mm,

and the distance between sensor S_1 and the source is 50 mm. Moisture effects on AE attenuation were also investigated by measuring amplitude at different distance of 50 mm, 100 mm, 150 mm and 200 mm in 0° direction.

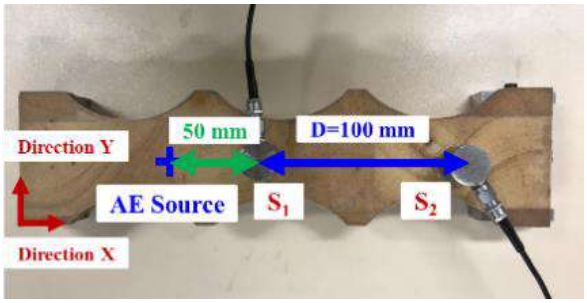

Fig. 2-29. AE Hsu-Nielsen test setup for monitoring moisture effects on sandwich structures.

2.4.1.3. Active IRT test setup on triple dog-bone sandwich specimens

As introduced in Chapter 1, a typical active IRT system (see Fig. 2-30) mainly include the IR camera (FLIR X6801sc, with a resolution of 608*312 full images at 520 frames per second), the halogen lamp (1 KW) and the acquisition computer with ResearchIR Master software. In this work, in order to study the difference between the temperature variation rate of dry and wet specimens, active reflection IRT tests were performed by using a halogen lamp to heat side surfaces of wet and dry specimens simultaneously (see Fig. 2-30. (b)). Average temperature difference of the selected surfaces (green/purple rectangular window in Fig. 2-30. (c) and Fig. 2-30. (d)) at a certain time is defined as $\Delta T=T_t-T_0$, where T_0 denotes the average temperature of the first ten images of the whole window, T_t is the average temperature of the whole window at time t. The variation of thermal field of surfaces of wet and dry specimens against time can be described by ΔT during the whole heating and cooling process [3]. The measured cooling time can reflect the heat convection between the specimen and environment.

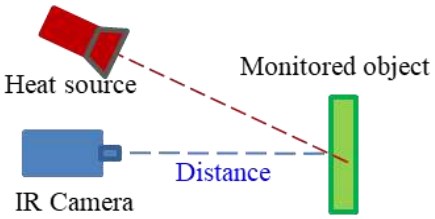

(a) Schematic of active reflection IRT tests.

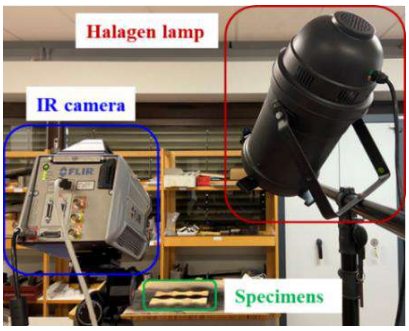

(b) Setup of active reflection IRT tests.

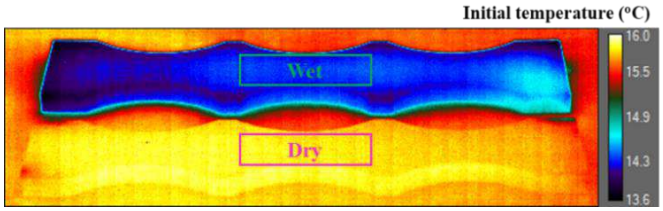

(c) Monitored surfaces of wet and dry GFRP-balsa specimens before heating.

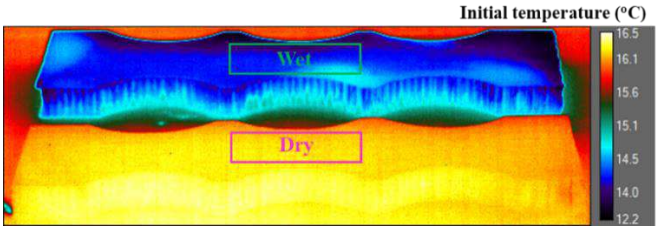

(d) Monitored surfaces of wet and dry CFRP-honeycomb specimens before heating.

Fig. 2-30. Experimental setup of active reflection IRT tests.

Before starting the tests, parameters such as distance between the camera and the monitored object, reflected temperature on the surface of the object shall be measured and input into the ResearchIR Master software correctly, as the example in Table 2-7 shows. Emissivity of composite is usually set within 0.92-0.95 according to the references [110, 129]. Frame rate shall be set properly, in this work, after some trying tests, 100 Hz is chosen to obtain the right temperature variation rate in active IRT tests.

Table 2-7. IRT acquisition parameters for dry sandwich in active reflection tests.

Emissivity	Distance (m)	Reflected Temp (°C)	Frame rate (Hz)
0.95	1.2	16.0	100

2.4.2. Moisture absorption behaviors

Fig. 2-30. (c) shows the initial temperatures of dry and wet GFRP-balsa sandwich specimens under room temperature before heating. The average temperature of the dry specimen detected by the camera is almost the same as room temperature 16 °C, while the average temperature of the wet specimen detected by the camera is only 14.5 °C, 1.5 °C lower than that of dry one/room temperature. Similarly, Fig. 2-30. (d) shows that the initial temperature of the dry CFRP-honeycomb sandwich specimen detected by the camera is 16.2 °C, which is very near to room temperature, while the average temperature of the wet CFRP-honeycomb sandwich specimen detected by the camera is only 14.0 °C, 2.2 °C lower than that of dry one. It means that the surface temperature of wet specimen has decreased due to moisture absorption, which is due to the changes in thermal and physical properties

during heat transfer. For example, the evaporation at the wet surface is an endothermic reaction, which can induce a decrease on the surface temperature [201].

2.4.2.1. Moisture absorption behavior of GFRP-balsa sandwich

Firstly, Fig. 2-31. (a) gives the Moisture Content (MC) decrease versus drying days until the final constant mass. It is shown that the average MC decreases by 1.8% (±0.03%) after 13 days. It verifies that the GFRP-balsa sandwich specimens which have been put in the environment under room temperature without absorbing moisture can be also regarded as the dry ones, with a MC about 1.8%, compared to the much higher MC of wet sandwich specimens. So, the dry GFRP-balsa sandwich specimens (with a MC about 1.8%) tested under 4-point bending load under room temperature in Chapter 3 can be further compared with the wet specimens.

Fig. 2-31. (b) shows the Moisture Content (MC) increase versus immersion days until the final constant mass, and Fig. 2-31. (c) shows the average MC versus square root of immersion days according to ASTM D5229 [200]. The average MC (orange curve) reached almost 20% (±1.39%) during the first 24 h. Then it took about 4 days to reach 40% (±2.57%) MC, 9 days to 60% (±3.59%) MC, 20 days to 80% (±2.80%) MC, 52 days to 100% (±2.81%) MC and 112 days to the constant 120% (±3.71%) MC. It indicates that GFRP-balsa sandwich is highly sensitive to humidity [55], which may have great effects on the mechanical behaviors.

In Fig. 2-31. (c), it can be seen that the average moisture absorption curve shows the first linear stage before point F (10 days with 60% MC), and then the non-linear stage begins. According to Fick's law [200], it means that the moisture diffusivity speed is constant in the first linear stage, and after point F, moisture diffusivity speed has become slower. In order to study the influence of different MC in linear and non-linear stages on the mechanical properties and damage mechanisms of GFRP-balsa sandwich, 4-point bending behaviors of 50% MC and 120% MC wet specimens will be compared in Chapter 3.

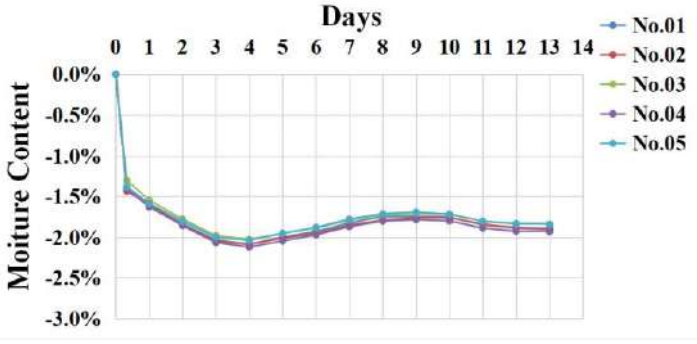

(a) Moisture Content (MC) decrease vs. drying days.

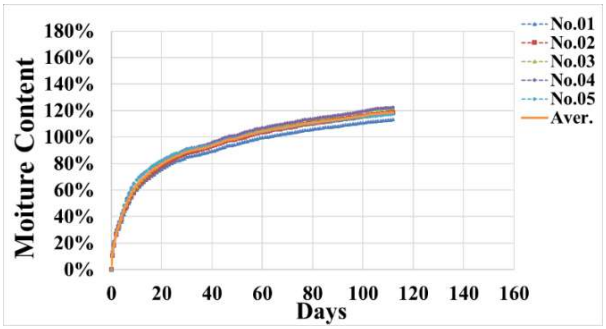

(b) Moisture Content (MC) increase vs. immersion days.

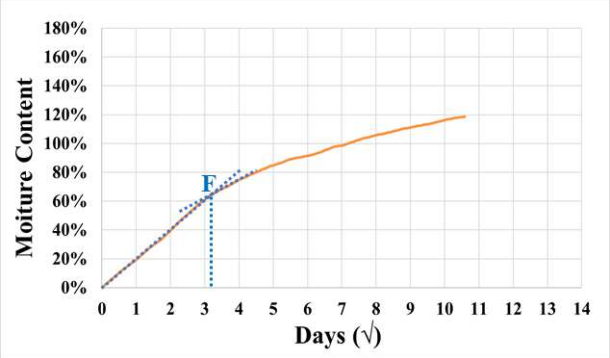

(c) Moisture Content (MC) increase vs. square root of immersion days.

Fig. 2-31. Moisture absorption behavior of GFRP-balsa sandwich specimens.

2.4.2.2. Moisture absorption behavior of CFRP-honeycomb sandwich

Firstly, Fig. 2-32. (a) gives the Moisture Content (MC) decrease versus drying days until the final constant mass. It is shown that the average MC decreases by 0.3% (±0.01%) after 6 days. It verifies that the CFRP-honeycomb sandwich specimens which have been put in the environment under room temperature without absorbing moisture can be also regarded as the dry ones, with a MC only about 0.3%, compared to the much higher MC of wet sandwich specimens. So, the dry CFRP-honeycomb sandwich specimens (with a MC only about 0.3%) tested under 4-point bending load under room temperature in Chapter 4 can be further compared with the wet specimens.

Fig. 2-232. (b) also shows the Moisture Content (MC) increase versus immersion days of CFRP-honeycomb sandwich specimens until the final constant mass, and Fig. 2-32. (c) shows the average MC versus square root of immersion days according to ASTM D5229 [200]. The average MC (orange curve) of specimens No. 01, No. 02, No. 03 and No. 05 was only 1.5% (±0.17%) during the first 24 h. Then it took 6 days to reach 3% (±0.24%) MC, 12 days to 5% (±0.42%) MC, 26 days to 6% (±0.55%) MC and 50 days to the constant 6.5% (±0.62%) MC.

Obviously, under the same environmental condition, the moisture absorption rate of CFRP-honeycomb is much smaller than that of the GFRP-balsa sandwich. And the curves of CFRP-

honeycomb sandwiches are not so smooth, which is mainly due to the hollow honeycomb cells which allows more free water to enter the structure. MC of CFRP-honeycomb sandwich specimen No. 01 is much higher than the other four specimens, which reaches about 11% MC. But no obvious difference can be found on this specimen, the higher MC may be caused by the test error and needs future validation.

In Fig. 2-32. (c), it can be seen that the average moisture absorption curve shows the first linear stage before point F (16 days with 6% MC), and then the non-linear stage begins. The mechanical behaviors of CFRP-honeycomb specimens with different MC will be further discussed in Chapter 4.

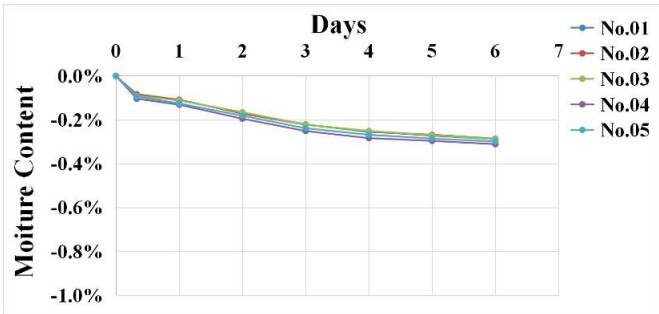

(a) Moisture Content (MC) decrease vs. drying days.

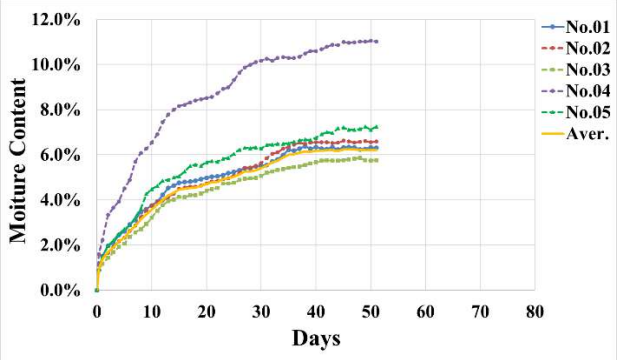

(b) Moisture Content (MC) increase vs. immersion days.

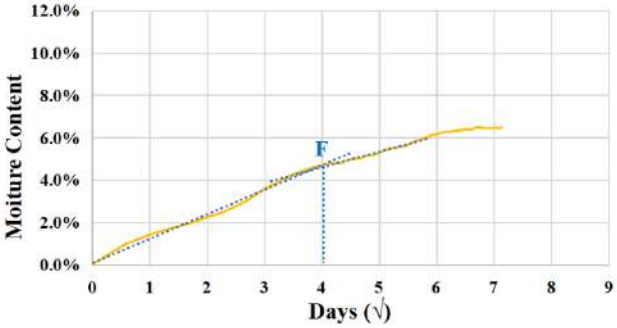

(c) Moisture Content (MC) increase vs. square root of immersion days.

Fig. 2-32. Moisture absorption behavior of CFRP-honeycomb sandwich specimens.

2.4.2.3. Conclusions

In conclusion, based on the water immersion tests, it can be observed that moisture effects on the mechanical behaviors of the GFRP-balsa sandwich shall not be ignored because of the higher moisture absorption rate, which will be investigated in Chapter 3. Although the CFRP-honeycomb sandwich shows very small moisture absorption rate with a saturation MC of 6.5% ($\pm$0.62%), but it still needs further validation in 4-point bending tests in Chapter 4, to characterize the detailed moisture effects on bending stiffness and strength of sandwich structures.

2.4.3. Moisture effects on AE wave propagation properties

2.4.3.1. Moisture effects on AE wave propagation properties of GFRP-balsa sandwich

2.4.3.1.1 Moisture effects on AE wave velocity

Based on the preliminary investigations in section 2.2.1, AE wave velocity is related to the elastic modulus of the sandwich. To further study the relationship between AE wave velocity and MC of GFRP-balsa sandwich, the average AE wave velocity of the five specimens is plotted as MC increases by every 20% (see Fig. 2-33). It shows that AE wave velocity decreases from 3120 m/s to 1870 m/s (i.e. 40%) as MC increases to 120% ($\pm$3.71%). If the curve is fitted by a polynomial equation of order 2, an empirical relationship between AE wave velocity and MC can be expressed by Eq. (2-14) which is valid when MC is 0-120% for GFRP-balsa sandwich:

$$C_{LMC}(0^{\circ}) = 444.02 \cdot MC^2 - 1609.2 \cdot MC + C_{LD}(0^{\circ}) \quad (2\text{-}14)$$

Where $C_{LMC}(0^{\circ})$ is AE wave velocity in the wet sandwich measured in specimen length direction $\theta = 0^{\circ}$; $C_{LD}(0^{\circ})$=3120 m/s is AE wave velocity in the dry specimen before water immersion, MC is the moisture content in percentage.

Based on Eq. (2-4) and Eq. (2-9), AE wave velocity of composite sandwich is mainly determined by the elastic modulus of the laminated skin, density and thickness of the constituents. For composite laminates, when moisture penetrates into the structure, it will induce some microscopic internal damages, such as matrix cracking and fiber/matrix debonding [203], due to the reduction of intralaminar strengths of fiber/matrix interfaces and interlaminar toughness of laminate plies. Thus, the stiffness of GFRP skin of the sandwich can be degraded due to moisture absorption. Fig. 2-33 signifies that stiffness of the sandwich will be reduced, and reflected by the elastic modulus and AE wave velocity decrease. It can be further demonstrated by 4-point bending tests in Chapter 3.

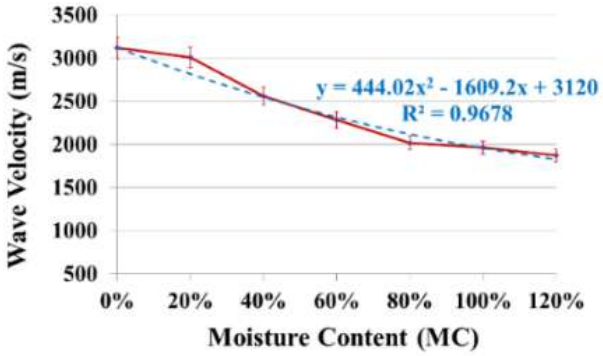

Fig. 2-33. Correlations between AE wave velocity and MC of GFRP-balsa sandwich.

2.4.3.1.2 A new methodology to predict elastic modulus of wet sandwich by AE wave velocity

In order to quantify the correlations between elastic modulus, AE wave velocity and MC, according to Eq. (2-4), elastic modulus of wet and dry sandwich in 0° can be expressed by Eq. (2-15):

$$E_{MC}(0^\circ) = \rho_{MC} \cdot \left(C_{LMC}(0^\circ)\right)^2 \cdot \left(1 - \nu_{MC}(0^\circ)^2\right) \quad (2\text{-}15a)$$

$$E_{D}(0^\circ) = \rho_{D} \cdot \left(C_{LD}(0^\circ)\right)^2 \cdot \left(1 - \nu_{D}(0^\circ)^2\right) \quad (2\text{-}15b)$$

Where ρ_{MC} and ρ_D are the density of wet and dry sandwich, $C_{LMC}(0^\circ)$ and $C_{LD}(0^\circ)$ are AE wave velocity of wet and dry sandwich in 0° direction, $\nu_{MC}(0^\circ)$ and $\nu_D(0^\circ)$ are Poisson's ratio of wet and dry sandwich in 0° direction, respectively.

Since moisture has little effect on Poisson's ratio [55, 80], $\nu_{MC}(0^\circ)$ and $\nu_D(0^\circ)$ can be regarded as the same. The volume of the sandwich shows very little difference after water immersion process, so it can be calculated that $\rho_{MC} = (1 + MC) \cdot \rho_D$. Thus, Eq. (2-16) can be obtained to predict elastic modulus $E_{MC}(0^\circ)$ of wet GFRP-balsa sandwich for a given MC if the density ρ_D and velocity $C_{LD}(0^\circ)$ of dry sandwich are known:

$$E_{MC}(0^\circ) = (1 + MC) \cdot \rho_D \cdot \left(444.02 \cdot MC^2 - 1609.2 \cdot MC + C_{LD}(0^\circ)\right)^2 \cdot \left(1 - \nu_D(0^\circ)^2\right) \quad (2\text{-}16)$$

For a sandwich made from any material which will not generate great volume and Poisson's ratio change due to moisture absorption, if AE wave velocity of wet sandwich has also been measured, $E_{MC}(0^\circ)$ of the wet sandwich can be simply predicted by Eq. (2-17b):

$$\frac{E_{MC}(0^\circ)}{E_D(0^\circ)} = \frac{\rho_{MC}}{\rho_D} \cdot \left(\frac{C_{LMC}(0^\circ)}{C_{LD}(0^\circ)}\right)^2 \quad (2\text{-}17a)$$

$$E_{MC}(0^\circ) = (1 + MC) \cdot f_2^{\,2} \cdot E_D(0^\circ) \quad (2\text{-}17b)$$

Where $f_2 = C_{LMC}(0^\circ)/C_{LD}(0^\circ)$ is the ratio of AE wave velocity in the wet sandwich over that in the dry sandwich. Eq. (2-16) and Eq. (2-17) assume that the hygroscopic expansion of the skin and the core has been ignored, so that the specimen volume is assumed to be constant.

Applying Eq. (2-17b) to specimens with 120% MC, f_2 is equal to 0.6, so it can be obtained that $E_{120\%MC}(0^\circ)$=0.80$E_D(0^\circ)$. For 50% MC specimens which will also be tested in 4-point bending tests, the average velocity was 2382 m/s, so elastic modulus of 50% MC specimens can be predicted: $E_{50\%MC}(0^\circ) = (1 + 0.5) \cdot 0.76^2 \cdot E_D(0^\circ) = 0.87E_D(0^\circ)$. According to Eq. (2-9), it signifies that elastic modulus of the skin of 50% MC and 120% MC sandwich has to be degraded in the same manner as that of sandwich, so it should be 87% and 80% of that of dry sandwich, respectively. In fact, bending stiffness of the sandwich is mainly determined by elastic modulus of the skin [127, 204], so it is logical that the degradation of elastic modulus of the skin and that of the sandwich are identical.

Consequently, a good advantage of this model is to predict the variation of elastic modulus of the skin of wet sandwich without loading, which can be time and cost saving. The knowledge of this variation can be of great interest in a numerical model, because the bending behavior of wet sandwich can be better predicted if the variation of material parameters as a function of MC has been integrated.

Consequently, Table 2-8 gives the material parameters of dry and wet skin of GFRP-balsa. Elastic modulus of wet skin of 50% MC and 120% MC sandwich can be modified as 87% and 80% of those of dry GFRP skin, and shear modulus has also been decreased as 87% and 80% of dry skin, since the reference [205] has verified that tensile and shear modulus values of carbon or glass fiber laminates will decrease by the very near percentage due to the same moisture content. Next, the proposed prediction methodology to determine elastic modulus of wet sandwich will be validated in the experimental and numerical investigations of 4-point bending behaviors of GFRP-balsa sandwich in Chapter 3.

Table 2-8. Material parameters of woven glass fiber skin of dry and wet GFRP-balsa sandwiches.

Types	E_1 (GPa)	E_2 (GPa)	G_{12} (GPa)	G_{13} (GPa)	G_{23} (GPa)	ν_{12}
Dry sandwich	20	20	2.85	2.30	2.30	0.13
50% MC sandwich	17	17	2.48	2.00	2.00	0.13
120% MC sandwich	16	16	2.28	1.84	1.84	0.13

2.4.3.1.3 Moisture effects on AE attenuation

As demonstrated in section 2.2.2, AE amplitude attenuation is higher as the propagation direction is farther away from the most fiber orientation in laminated skins and the sandwich. However, due to

the combination of anisotropic skins and core materials, moisture effects on AE attenuation properties of sandwich structures are still unclear. In this work, moisture effects on AE attenuation along 0° direction were firstly investigated during the moisture absorption process. Fig. 2-34 shows that the average AE amplitude of the five wet specimens attenuates much faster as MC increases. In particular, when MC increases from 0% to 120%, AE amplitude has an obvious decrease from 92 dB to 64 dB at a propagation distance of 200 mm. This phenomenon shall not be neglected when using AE technique to localize damages under loading. It means that the sensor distance could be reduced and more sensors could be added on the wet sandwich specimens to better localize damages, due to the higher amplitude attenuation.

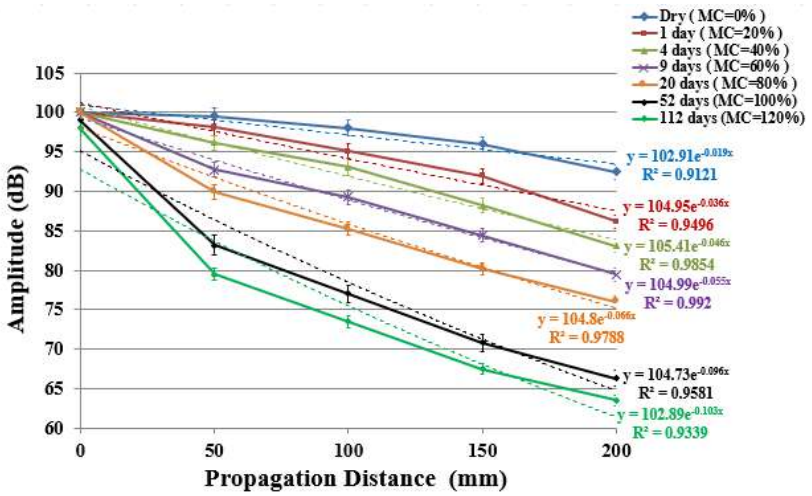

Fig. 2-34. Correlations between AE attenuation and MC of GFRP-balsa sandwich.

AE attenuation curve is as an exponential function of propagation distance [193, 198]. After fitting the curves by exponential function ($y = Ae^{-px}$), attenuation coefficient p is obtained, as shown in Fig. 32-34. Fig. 2-35 shows that the attenuation coefficient is higher as MC increases, and the curve can be fitted by a polynomial equation of order 2, then an empirical relationship between AE attenuation coefficient and MC can be expressed by Eq. (2-18) which is valid when MC is 0-120% for GFRP-balsa sandwich:

$$p_{MC}(0^{\circ}) = 0.019 \cdot MC^2 + 0.0486 \cdot MC + 0.0215 \quad (2\text{-}18)$$

Where $p_{MC}(0^{\circ})$ is the attenuation coefficient in 0°. The attenuation coefficient of 120% MC sandwich specimen is about five times as the dry one. It signifies that the great effects of moisture on AE attenuation shall be considered when monitoring damage evolution of wet specimens in mechanical tests. Eq. (2-18) can be used to predict the attenuation coefficient variation of GFRP-balsa sandwich at any MC before saturation, and then the corresponding amplitude attenuation at any distance less than 200 mm at certain MC can be evaluated.

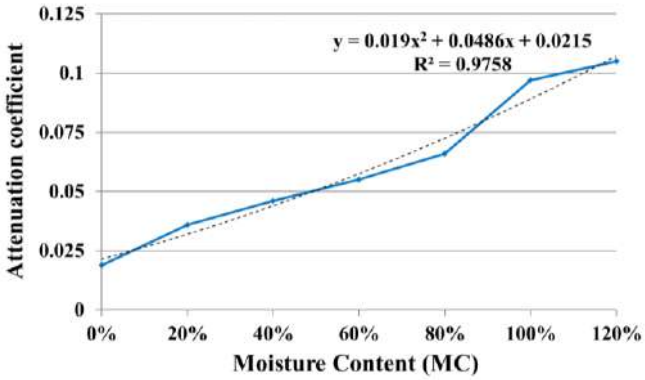

Fig. 2-35. Moisture effects on attenuation coefficient of GFRP-balsa sandwich.

2.4.3.2. Moisture effects on AE wave propagation properties of CFRP-honeycomb sandwich

In order to compare the difference between moisture effects on AE wave propagation properties of balsa and honeycomb sandwich, and verify the proposed methodology to predict elastic modulus of the sandwich structure made of any material, the same analysis method has been applied to honeycomb sandwich in the following part.

2.4.3.2.1 Moisture effects on AE wave velocity

Similarly, AE wave velocity variation of CFRP-honeycomb sandwich specimens during the moisture absorption process was also investigated. As shown in Fig. 2-36, the average velocity has a very small decrease within 300 m/s (by 4%) as MC increases to the constant 6.5%. It indicates that a very small MC absorption cannot result in the great stiffness degradation of the CFRP-honeycomb sandwich, which can be validated by 4-point bending tests in Chapter 4.

If the curve in Fig. 2-36 is also fitted by a polynomial equation of order 2, an empirical relationship between AE wave velocity and MC can be expressed by Eq. (2-19) which is valid when MC is 0-6.5% for CFRP-honeycomb sandwich:

$$C_{LMC}(0^{\circ}) = 19893 \cdot MC^2 - 6067.6 \cdot MC + C_{LD}(0^{\circ}) \quad (2\text{-}19)$$

To verify the proposed methodology to predict elastic modulus of the wet sandwich, when MC=6.5% ($\pm$0.62%), by inputting velocity test results into Eq. (2-17b), elastic modulus of 6.5% MC CFRP-honeycomb sandwich can be: $E_{MC}(0^{\circ}) = 1.065 \cdot (\frac{7450}{7782})^2 \cdot E_D(0^{\circ}) = 0.98 E_D(0^{\circ})$. It signifies that elastic modulus of the CFRP skin of wet CFRP-honeycomb sandwich is 98% of that of dry one, as shown in Table 2-9. Thus, it verifies that Eq. (2-17b) can be used to predict elastic modulus of most common sandwich structures as a function of MC and AE wave velocity.

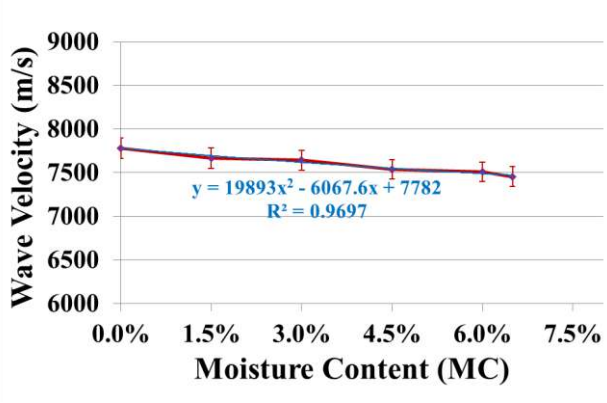

Fig. 2-36. Correlations between AE wave velocity and MC of CFRP-honeycomb sandwich.

Table 2-9. Material parameters of carbon fiber skin of dry and wet CFRP-honeycomb sandwich.

Types	E_1 (GPa)	E_2 (GPa)	G_{12} (GPa)	G_{13} (GPa)	G_{23} (GPa)	ν_{12}
Dry sandwich	152.40	9.20	4.30	2.80	2.30	0.35
6.5% MC sandwich	149.35	9.02	4.21	2.74	2.25	0.35

2.4.3.2.2 Moisture effects on AE attenuation

In the same way, moisture effects on AE attenuation along 0° direction of CFRP-honeycomb sandwich specimens were investigated. Fig. 2-37 also shows that the average AE amplitude of the five wet specimens attenuates much faster as MC increases in CFRP-honeycomb sandwiches. When MC increases from 0% to 6.5% (50 days), AE amplitude has a decrease from 85 dB to 76 dB at a propagation distance of 200 mm.

After fitting the curves by an exponential function ($y = Ae^{-px}$) in Fig. 2-37, attenuation coefficient p can be obtained as Fig. 2-38 shows. Attenuation coefficient is higher as MC increases, and the curve in Fig. 2-38 can be fitted by a polynomial equation of order 2. Then an empirical relationship between AE attenuation coefficient and MC can be expressed by Eq. (2-20) which is valid when MC is 0-6.5% for CFRP-honeycomb sandwich:

$$p_{MC}(0^{\circ}) = 4.5445 \cdot MC^2 + 0.0582 \cdot MC + 0.0416 \quad (2\text{-}20)$$

Where $p_{MC}(0^{\circ})$ is the attenuation coefficient in 0°. The attenuation coefficient of 6.5% MC CFRP-honeycomb sandwich specimen is about 1.5 times as the dry one. It signifies that the moisture has smaller effects on AE attenuation of CFRP-honeycomb sandwich, compared to GFRP-balsa sandwich. Eq. (2-20) can be used to predict the attenuation coefficient variation of CFRP-honeycomb sandwich at any MC before saturation, and then the corresponding amplitude attenuation at any distance less than 200 mm at certain MC can be evaluated.

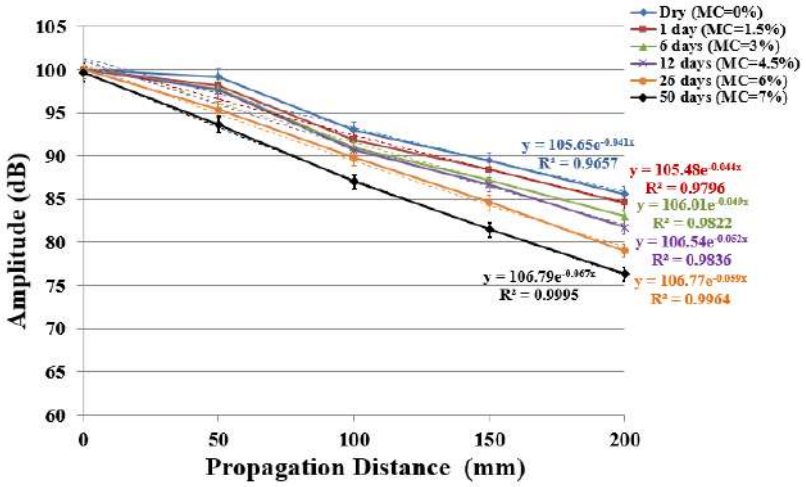

Fig. 2-37. Correlation between AE attenuation and MC of CFRP-honeycomb sandwich.

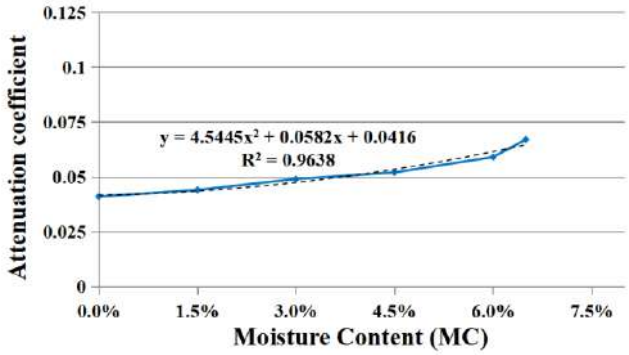

Fig. 2-38. Moisture effects on attenuation coefficient of CFRP-honeycomb sandwich.

2.4.3.3. Conclusions

As a conclusion, AE wave velocity decreases as a function of moisture content in the sandwich, and a new methodology has been proposed to predict elastic modulus variation of the wet sandwich skin, based on the wave velocity and MC measurements. The new method has been proven effective for both GFRP-balsa and CFRP-honeycomb sandwich, and the main difference is that CFRP-honeycomb sandwich has very small 6.5% saturated MC, showing only 4% velocity decrease, while GFRP-balsa sandwich has 120% MC increase, with 40% velocity decrease.

AE amplitude attenuation is much higher as MC increases for both of two different sandwich materials, and this phenomenon shall be considered when localizing damages by AE in the next mechanical tests. It means that the sensor distance could be reduced and more sensors could be added on the wet sandwich specimens to better localize damages, due to the higher amplitude attenuation.

2.4.4. Moisture effects on temperature variation rate in active IRT tests

2.4.4.1. Moisture effects on IRT responses of GFRP-balsa sandwich

As explained in Fig. 2-30, the dry and wet triple dog-bone sandwich specimens were heated by one halogen lamp and cooled to room temperature simultaneously. According to [140], temperature contrast $C_{tr} = \Delta T/T_0$ can describe the temperature variation rate more clearly by eliminating the effects of the initial temperature, compared to the simple ΔT. Considering that the detected initial temperature of the dry sandwich is higher than that of the wet one, Fig. 2-39 shows the heating and cooling curves of dry and wet specimens (120% MC) by plotting the average temperature contrast of the specimen surface versus time, in which two different heating time 30 s and 60 s are compared, to study the influence of heating time on the final cooling time until room temperature.

Whatever the heating time is, during the heating process, the average temperature contrast ($\Delta T/T_0$) of wet specimen increases always more slowly than that of dry one, which is mainly due to the higher specific heat of the absorbed water. Specific heat of the glass fiber is around 1000 J/(kg•°C) [206-207], while water is 4200 J/(kg•°C), so average specific heat of skin of wet specimen has been increased, finally resulting in the smaller temperature increase of wet skin surface.

In reference [201], it has been concluded that changes in moisture content in building components are related to changes in surface temperature which can be detected by IRT, mainly due to three physical phenomena: 1) evaporative cooling at the wet area; 2) reduced thermal resistance: the heat flow through wet materials is higher than that through dry materials, which creates a heterogeneous thermal pattern when the surface temperature over the wet material becomes higher. This effect is pushed to extremes when the wetting occurs in thermal insulation materials; The thermal conductivities [205-207] of balsa and Nomex honeycomb are 0.05 W/(m•K) and 0.02 W/(m•K), respectively, much lower than 0.6 W/(m•K) and 0.95 W/(m•K) of water and composite laminates. Thus, the thermal conductivity/resistance of wet sandwich will be more complicated due to the water absorption, affected by the coupling of skin, core and water. 3) increased heat storage capacity of the wet material: the surface temperature over a wet area responds more slowly to a change in the air temperature than the surface temperature over a dry area. Thus, when the whole surface is cooling, wet areas will cool more slowly.

But the above explanations still need further investigations. The variations of thermal coefficients and physical phenomena of heat transfer between the specimen and environment due to moisture absorption shall be considered carefully when determining the heat source filed of sandwich in later 4-point bending tests.

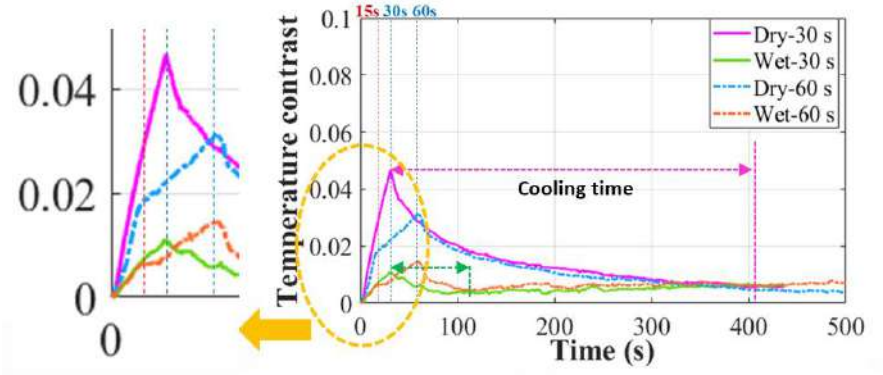

Fig. 2-39. Moisture effects on active IRT test of GFRP-balsa sandwich.

When the heating time is 30 s, the max temperature contrast ($\Delta T/T_0$) of skin of wet GFRP-balsa sandwich is 0.01 (see Fig. 2-39), almost 80% lower than 0.05 of the dry one. The average temperature contrast increase rate of the wet specimen is 0.0003/s, 80% smaller than 0.0017/s of the dry one.

When the heating time is double, the max temperature contrast ($\Delta T/T_0$) of the wet specimen is 0.01, almost 67% lower than 0.03 of the dry one. The average temperature contrast increase rates of the dry and wet specimens can be divided into two stages: the first stage before 15 s with a larger increase rate and the second stage between 15 s and 60 s with a smaller rate. Before 15 s, the average temperature contrast increase rate of the wet specimen is 0.0004/s, 64% lower than 0.0011/s of the dry one. Between 15 s and 60 s, the average temperature contrast increase rate of the wet specimen is 0.0002/s, 33% lower than 0.0003/s of the dry one.

It signifies that the heat flow has penetrated more deeply into the core material when the heating time is longer, and then the surface temperature has been affected by both the skin and the core, so the shorter heating time is a better choice to determine the cooling time of the skin material.

During the cooling process, the average temperature contrast ($\Delta T/T_0$) of the wet specimen decreases more slowly than the dry one before 110 s. After 110 s, the temperature contrast of the wet specimen remains almost stable, while that of the dry sandwich continues to decrease until the stable 0.005 near 400 s. So, the cooling time ($\tau_{th} = 355 \pm 15$ s) of the dry specimen is between 30 s/60 s and 400 s, while the cooling time ($\tau_{th} = 65 \pm 15$ s) of the wet specimen is much shorter between 30 s/60 s and 110 s. The cooling time can reflect the characteristics of heat convection between the specimen and environment [142, 143], so it shall be input into the heat source calculation in 4-point bending tests in Chapter 3. It indicates that moisture effects on the heat convection between the specimen and environment shall be considered carefully.

2.4.4.2. Moisture effects on IRT responses of CFRP-honeycomb sandwich

Similarly, Fig. 2-40 shows the heating and cooling curves of dry and wet CFRP-honeycomb sandwich specimens (6.5% MC) by plotting the average temperature contrast of the specimen surface versus time, in which two different heating time 33 s and 66 s are also compared. Similar to GFRP-balsa sandwich, whatever the heating time is, during the heating process, the average temperature contrast ($\Delta T/T_0$) of skin of wet CFRP-honeycomb sandwich increases always more slowly than that of the dry one, which is mainly due to the higher specific heat of the absorbed water.

When the heating time is 33 s, the max temperature contrast ($\Delta T/T_0$) of skin of the wet CFRP-honeycomb sandwich is 0.04, almost 69% lower than 0.13 of the dry one. The average temperature contrast increase rate of wet skin is 0.0012/s, 69% smaller than 0.0039/s of dry one.

When the heating time is double, the max temperature contrast ($\Delta T/T_0$) of wet skin is 0.04, almost 33% lower than 0.06 of the dry one. The average temperature contrast increase rate of wet skin is 0.0006/s, 67% smaller than 0.0009/s of dry one. It verifies that the heat flow has penetrated more deeply into the core material when the heating time is longer, and then the surface temperature has been affected by both the skin and the core, so it's better to heat the specimens for a shorter time to reduce the influence of the heat convection between the environment, the skin and the core.

During the cooling process, the average temperature contrast ($\Delta T/T_0$) of the wet specimen decreases more slowly than the dry one before 200 s. After 200 s, the temperature contrast of the wet specimen remains almost stable, while that of the dry sandwich continues to decrease until the stable 0.006 near 400 s. So, the cooling time ($\tau_{th} = 355 \pm 15$ s) of the dry specimen is between 33 s/66 s and 400 s, while the cooling time ($\tau_{th} = 155 \pm 15$ s) of the wet specimen is shorter between 33 s/66 s and 200 s. It can reflect the characteristics of heat convection between the specimen and environment, and it shall be input into the heat source calculation in 4-point bending tests in Chapter 4.

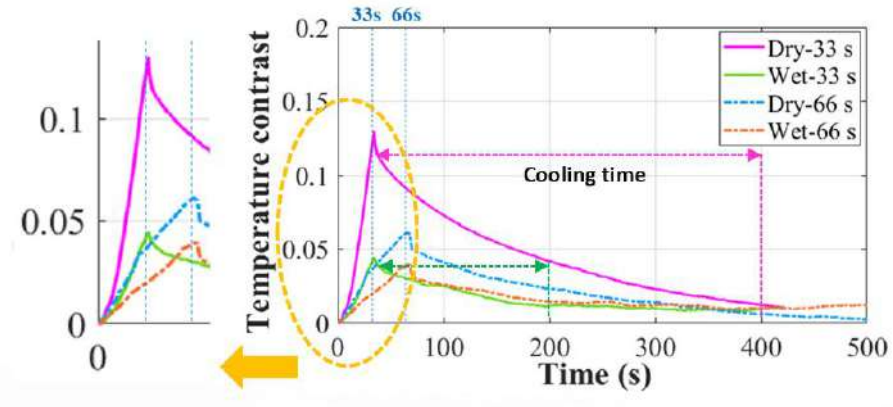

Fig. 2-40. Moisture effects on active IRT test of CFRP-honeycomb sandwich.

2.4.4.3. Conclusions

To conclude, when being heated by the same halogen lamp for nearly the same heating time (30 s), under the same environmental condition, the average temperature contrast ($\Delta T/T_0$) of the wet GFRP-balsa or CFRP-honeycomb sandwich shows smaller temperature increase rate than that of the dry sandwich. Furthermore, it is verified that the temperature contrast increase rate is mainly affected by the product of the density and specific heat of the constituent materials, and moisture absorption has caused the smaller rate mainly due to higher specific heat of water. In addition, other thermal parameters such as conductivity and diffusivity could be also affected by the existence of water, which shall be considered carefully.

To be emphasized, the cooling time can help determine the time increment which characterizes the heat convection between the specimen and the environment in the heat diffusion equation Eq. (1-16). It means that the thermal coefficient variation due to moisture absorption cannot be ignored in thermal-mechanical modeling in 4-point bending tests in Chapter 3 and 4.

2.5. Chapter summary

In summary, the preliminary characterization of AE wave velocity and amplitude attenuation properties in GFRP-balsa sandwich and CFRP-honeycomb sandwich has been carried out by active Hsu-Nielsen tests. A new rapid method has been proposed and demonstrated to quickly determine AE wave velocity in any direction in the sandwich based on the measurements of velocity only in one direction in the corresponding composite skin. It validates that the propagation direction farther away from the most fiber orientation of composite laminates and sandwiches will result in higher attenuation and lower wave velocity, which shall not be ignored when localizing damages under loading.

And then, the moisture absorption behaviors of GFRP-balsa and CFRP-honeycomb sandwiches have been studied by water immersion tests monitored by active AE and IRT techniques. Relationships between Moisture Content, AE wave velocity and elastic modulus have been pointed out to propose a new methodology to predict the variation of elastic constants of the composite skin as a function of moisture content. This method has been proven to be effective for the two kinds of sandwich materials. Furthermore, all these conclusions can be integrated into the numerical models to improve the calculation accuracy of 4-point bending behaviors of the sandwich by modifying the elastic modulus input as a function of MC in Chapter 3 and 4. In addition, it has been proven that AE amplitude attenuation will be higher and wave velocity will be lower as MC increases in the two kinds of sandwich structures, which shall be considered for the damage localization during 4-point bending tests.

Moisture effects on active IRT tests have also been studied, showing that the wet sandwiches have smaller temperature increase rate due to higher specific heat of water. The different thermal coefficients of the skin and core shall be considered carefully when determining the heat source field of sandwich in later 4-point bending tests in Chapter 3 and 4. The cooling time, τ_{th}, which characterize the heat convection between the specimen and the environment in the heat diffusion equation Eq. (1-16), shall be considered carefully in the calculation of the real heat source in 4-point bending tests.

Based on all these preliminary studies, in the next chapter, 4-point bending behaviors and damage mechanisms of dry, 50% MC and 120% MC triple dog-bone GFRP-balsa sandwich specimens will be studied experimentally and numerically, under the monitoring of passive IRT and AE techniques.

Chapter 3. Static 4-point bending behaviors of GFRP-balsa sandwich

3.1. Introduction 114

3.2. Static 4-point bending tests monitored by AE and IRT 114

3.2.1. Experimental setup 114

3.2.2. Moisture effects on bending behaviors 116

3.2.2.1. Moisture effects on bending stiffness 117

3.2.2.2. Moisture effects on fracture load 119

3.2.3. Moisture effects on damage mechanisms observed by microscope 120

3.2.4. Moisture effects on damage initiation and evolution monitored by IRT 125

3.2.5. Moisture effects on damage characterization by AE 130

3.2.5.1. Moisture effects on the cumulative hits number 130

3.2.5.2. Moisture effects on damage localizations by AE 131

3.2.5.3. Identification of balsa core damages in the first clustering process 134

3.2.5.4. Skin damage initiation detection by cumulative counts and energy 139

3.2.5.5. Classification of skin damages in the second clustering process 141

3.2.5.5.1 Damage classification based on amplitude distributions 142

3.2.5.5.2 Damage classification based on peak frequency distributions 143

3.2.5.5.3 Correlations between different AE parameters 144

3.2.5.6. Conclusions 146

3.2.6. Experimental conclusions 147

3.3. Numerical analysis of 4-point bending behaviors 147

3.3.1. Abaqus model establishment 147

3.3.2. Progressive Damage Analysis (PDA) model 149

3.3.3. Prediction of 4-point bending behaviors by PDA model 150

3.3.3.1. Influence of elastic modulus of the skin on bending stiffness 150

3.3.3.2. Influence of fracture energy of the skin on fracture load 151
3.3.3.3. Damage evolution prediction by PDA model 154
3.3.3.4. Stress distributions in numerical models 157
3.3.4. Numerical conclusions 163
3.4. Chapter summary 164

3.1. Introduction

Based on the preliminary investigations on the moisture absorption tests, AE wave propagation properties and active IRT tests described in Chapter 2, moisture effects on the static 4-point bending behaviors of GFRP-balsa sandwich are studied experimentally and numerically in this chapter. Firstly, moisture effects on the bending stiffness/strength and damage mechanisms have been discussed, based on the observations by microscopes, IRT and AE. Particularly, during the post-processing process of AE data, a damage characterization approach coupling the characteristics of AE amplitude, peak frequency and duration by applying the two clustering processes has been developed to classify different damage modes of GFRP-balsa sandwich.

Based on the experimental study, the Progressive Damage Analysis (PDA) model in Abaqus has been developed, where the variation of mechanical properties of the skin of the sandwich as a function of MC has been taken into account, to better simulate the bending stiffness, fracture load, displacement and damage evolution process of the wet sandwich.

3.2. Static 4-point bending tests monitored by AE and IRT

3.2.1. Experimental setup

Triple dog-bone GFRP-balsa sandwich specimens were tested under 4-point bending. Loading span (L) is 80 mm and support span (S) is 240 mm, as seen in Fig. 3-1. As explained in Chapter 2, the interest of this special dog-bone shape [191, 192] is to observe more clearly the skin damages caused by the maximum compressive stresses in the pure bending zone 1, as well as core damages in bending and shear zone 2 (see Fig. 2-6 and Fig. 2-7). Another advantage of this shape is to reduce the local stress concentrations under the loading supports and ensure the stability of the tests. The tests were controlled by displacement rate imposed at 2 mm/min [209-210] using the MTS machine with load cell of 100 kN, monitored by passive AE and IRT systems during the whole loading process.

AE monitoring system is composed of two wideband sensors (100 kHz-1 MHz) [94, 95], two pre-amplifiers and a PCI-2 acquisition system (Mistras AEwin software). This kind of wideband sensor was chosen so as to allow the received signals not to be limited in certain resonance frequencies in the case of a multi-material structure. The sensors were glued on the skin surface symmetrically with respect to the central axis Z (loading direction) using a couplant (silicone grease), with a distance (D) of 180 mm (see Fig. 3-1. (a)), in order to receive all possible AE hits within a large frequency range generated in zone 1 and zone 2 during 4-point bending tests.

After some preliminary tests, the threshold which determines the system sensitivity to the environmental noise, was set by 28 dB. The other AE acquisition parameters for GFRP-balsa

sandwiches under 4-point bending are given in Table 3-1. The parameters are a little different from those in Table 2-6 in active Hsu-Nielsen tests, because the loading conditions, sensors and specimen geometries are different. They are determined by some preliminary trying tests, to finally ensure fewer signals have been lost. Before starting the bending tests, AE wave velocity and attenuation tests along the specimen length have to be repeated on dog-bone specimens, as demonstrated in Chapter 2, in order to calibrate the AE acquisition parameters including velocity and attenuation properties input into AEwin software.

IRT system was set to monitor more clearly the upper skin surface in loading span (zone 1) (see Fig. 3-1. (b)), including IR camera (FLIR X6801sc, with a resolution of 608 × 312 full images at 520 frames per second) and acquisition computer with ResearchIR Master software. The IRT acquisition parameters are shown in Table 3-2.

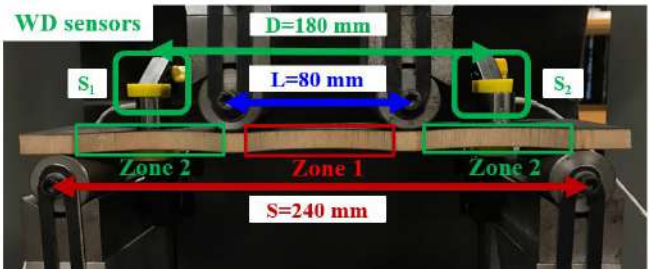

(a) Positions of AE wideband sensors.

(b) IR camera setup.

Fig. 3-1. 4-point bending test setup monitored by AE and IRT techniques.

Table 3-1. AE acquisition parameters for GFRP-balsa sandwiches under 4-point bending.

Threshold (dB)	Pre-amplifier (dB)	Analog Filter (MHz)	PDT (μs)	HDT (μs)	HLT (μs)	Sample Rate (MSPS)	Pre-Trigger (μs)	Hit Length
28	40	0.02-3	30	100	300	5	50	4k

Table 3-2. IRT acquisition parameters for GFRP-balsa sandwiches in 4-point bending tests.

Emissivity	Distance (m)	Reflected Temp (ºC)	Frame rate (Hz)
0.95	0.7	19.3	480

In order to study moisture effects on mechanical behaviors and damage mechanisms of triple dog-bone GFRP-balsa sandwich specimens, seven dry specimens, three 50% MC (with a standard deviation of 1.6% MC) wet specimens and three 120% MC (with a standard deviation of 3.7% MC) wet specimens were tested under the same 4-point bending loading condition.

3.2.2. Moisture effects on bending behaviors

Fig. 3-2 shows the force/displacement curves of all the tested dry and wet sandwich specimens. Table 3-3 gives the average bending stiffnesses and fracture loads of the dry, 50% MC and 120% MC wet specimens. Firstly, it can be seen that most specimens show the similar linear behavior before the final fracture except Wet 3 (50% MC). All the dry sandwich specimens and 120% MC wet specimens show the good repeatability. The three 50% MC wet specimens show the greater dispersion. In fact, it can be seen by the eyes that only Wet 3 shows the obvious core damages in left zone 2, while all the other specimens show the upper skin damages in center zone 1 (see Fig. 3-4).

One reason is that the dry and 120% MC wet specimens were fabricated simultaneously from the same large pure balsa panel from the supplier, while the 50% MC wet specimens were fabricated from the second large pure balsa panel and cured not at the same time as the other specimens. Thus, this fabrication process difference could cause some scatter of the bending responses.

In addition, after observing the difference of these specimens in Fig. 3-3, another interesting possible reason is that moisture absorption has penetrated into the balsa/balsa block interfaces unevenly, thus resulting in the different interfacial strength and larger scatter of the fracture load of the wet specimens. The balsa/balsa block interface locations of the 120% MC wet specimens are distributed more symmetrically, while those of the 50% MC wet specimens are not symmetrically except Wet 2, so moisture absorption will cause larger dispersion of the bending behavior of the 50% MC wet specimens.

Table 3-3. Average bending stiffness and fracture load of dry and wet GFRP-balsa sandwiches.

Specimens	Bending stiffness (N/mm)	Standard deviation (N/mm)	Fracture load (N)	Standard deviation (N)
Dry	104	4	1118	85
50% MC	84	1	1044	218
120% MC	88	3	730	37

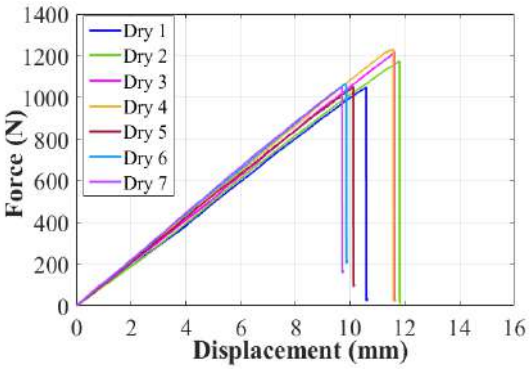

(a) Dry sandwich specimens.

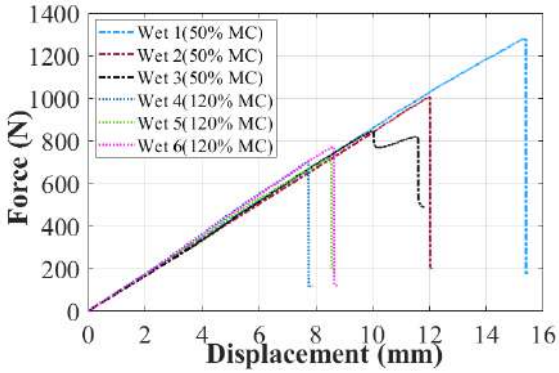

(b) Wet sandwich specimens.

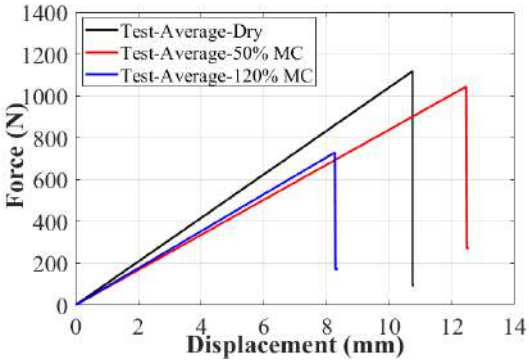

(c) Average force/displacement curves of dry and wet sandwich specimens.

Fig. 3-2. Static 4-point bending behaviors of GFRP-balsa sandwich specimens.

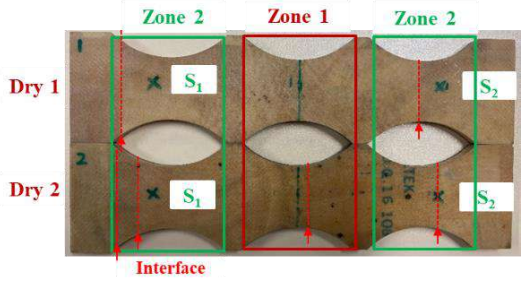

(a) Dry sandwich specimens.

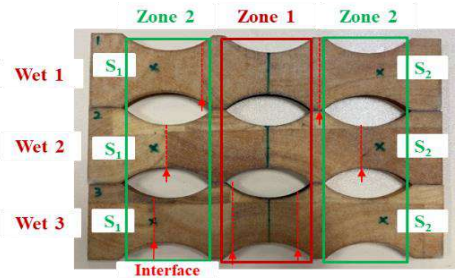

(b) Wet (50% MC) sandwich specimens.

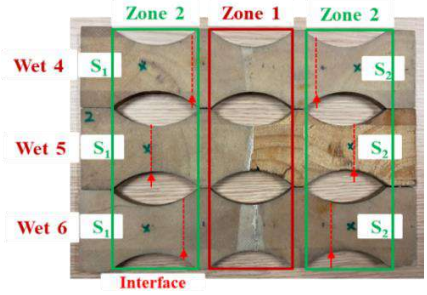

(c) Wet (120% MC) sandwich specimens (after test).

Fig. 3-3. Interfaces of balsa blocks in dry and wet GFRP-balsa sandwich specimens.

3.2.2.1. Moisture effects on bending stiffness

In Table 3-3, the average bending stiffnesses of 50% MC and 120% MC wet specimens have decreased by 19% and 15%, respectively, compared to dry specimens. It seems that during the first linear moisture absorption stage (before 60% MC) illustrated in Fig. 2-27 in Chapter 2 where the moisture absorption rate is high, the decrease of the bending stiffness of GFRP-balsa sandwich is significant, while the stiffness remains nearly stable in the non-linear moisture absorption stage (after 60% MC) where the moisture absorption rate is much smaller.

Actually, according the experimental results, the average stiffness of 50% MC specimens is a little lower than that of 120% MC specimens, which is contrary to the expected results. But it can be explained by the possible reason that moisture absorption has caused the non-uniform distribution of the mechanical properties of wet GFRP-balsa sandwich. Since the dry specimens and 120% MC specimens were fabricated from the same large pure balsa panel, while the 50% MC specimens were made from another different pure balsa panel, considering the scatter properties of balsa wood related to the density, humidity, temperature etc., this error could be acceptable. But one general conclusion is that moisture absorption can result in the decrease of bending stiffness.

In order to verify the proposed method to predict elastic modulus of the skin of the sandwich structure as a function of MC described in Chapter 2, before starting the 4-point bending tests, the average tested AE wave velocities along the specimen length directions of 50% MC and 120% MC wet dog-bone sandwich specimens have been obtained by 2382 m/s (with a standard deviation of 78 m/s) and 1870 m/s (with a standard deviation of 65 m/s) which are almost the same as those tested on the large sandwich panels (300 mm*300 mm) in Chapter 2, so elastic modulus of 50% MC and 120% MC sandwich specimens can be predicted by Eq. (2-17b) in Chapter 2 as following:

$$\mathrm{E}_{50\%\mathrm{MC}}(0^{\circ}) = (1 + 0.5) \cdot 0.76^{2} \cdot \mathrm{E}_{\mathrm{D}}(0^{\circ}) = 0.87\mathrm{E}_{\mathrm{D}}(0^{\circ})$$

$$\mathrm{E}_{120\%\mathrm{MC}}(0^{\circ}) = (1 + 1.2) \cdot 0.6^{2} \cdot \mathrm{E}_{\mathrm{D}}(0^{\circ}) = 0.80\mathrm{E}_{\mathrm{D}}(0^{\circ})$$

It indicates that bending stiffness of 50% MC and 120% MC wet specimens would be 87% and 80% of that of dry sandwich. The tested stiffnesses of 50% MC and 120% MC wet specimens are 81% and 85% of that of dry sandwich, so the errors between the predicted stiffness and 4-point bending tested values of 50% MC and 120% MC wet specimens are 7% and 7%, respectively. In conclusion, these errors can be caused by the non-uniform distributions of Moisture Content (MC) due to the special structural form of the triple dog-bone shape, the random distributions of the balsa/balsa block interfaces (see Fig. 3-3), the fabrication and cutting process of the specimens, etc. Thus, these errors less than 10% can be acceptable.

According to Eq. (2-9) which shows that the modulus of sandwich can be obtained from that of the skin multiplied by a geometrical coefficient: $2/(2+h_c/h_f)$, it also signifies that elastic modulus of the skin of 50% MC and 120% MC sandwich specimens would be 87% and 79% of that of the skin of dry sandwich, respectively. Thus, it verifies that the new method proposed in Chapter 2 is effective for the elastic modulus prediction of GFRP-balsa sandwich.

3.2.2.2. Moisture effects on fracture load

In Table 3-3, the average fracture loads of 50% MC and 120% MC wet specimens have decreased nearly by 7% and 35%, respectively. The standard deviation of fracture loads of 50% MC specimens is larger, which is mainly because that the random distributions of balsa/balsa block interfaces (see Fig. 3-3) has caused the different interfacial strength distributions in balsa core after moisture absorption.

In Fig. 3-3, when observing the difference of the specimens carefully, firstly, for the seven dry sandwich specimens, it can be seen that they can be divided into two groups: one group includes specimen Dry 1, 5, 6, 7, which show the relatively lower fracture load, and the other group includes specimen Dry 2, 3, 4 with a higher fracture load. This fracture load difference could be caused by the random distributions of the balsa/balsa block interfaces (see Fig. 3-3. (a)), the fabrication and cutting process of the specimens etc. And the fracture load scatter will be affected more when the sandwich has absorbed moisture. Since the pure balsa panel is fabricated by gluing the small balsa blocks, the different positions of these balsa/balsa bonding interfaces will cause the non-uniform moisture distributions in the balsa core, and then lead to different strength and different fracture modes of the wet sandwich structure.

As seen in Fig. 3-2. (b) and Fig. 3-3. (b), for the three 50% MC specimens, Wet 1 shows the higher strength and has only one balsa/balsa interface in left zone 2 but away from the weakened section. For Wet 2, two balsa/balsa interfaces are located quasi-symmetrically in left and in right zone 2. Concerning Wet 3, it has two balsa/balsa interfaces in zone 1 and only one interface in left zone 2 where the core shear damages can appear. That's why Wet 3 shows the final core shear damage failure in left zone 2 (see Fig. 3-4. (d)). For the three 120% MC specimens, they have very similar balsa/balsa interface distributions, that is, one interface in the left zone 2 and one in the right zone 2, so the fracture loads of the three 120% MC specimens show smaller difference.

These observations indicate that even though the fracture load of GFRP-balsa sandwich is mainly determined by the skin strength, but it will also be affected by the bonding strength between balsa blocks. The influences of theses interfaces on the fracture loads and damage mechanisms will be discussed in detail in the next parts, based on AE monitoring results. In the following work, the

microscope, IRT and AE observations of specimens Dry 1, Wet 2 (50% MC) and Wet 5 (120% MC) will be compared and discussed.

3.2.3. Moisture effects on damage mechanisms observed by microscope

Fig. 3-4 shows that only Wet 3 fails due to the core shear damages in left zone 2 in 4-point bending tests, while all the other dry and wet specimens fail mainly due to the compressive damages of the upper GFRP skin in zone 1. To further investigate the damage mechanisms, microscope VHX-7000 (100 X) was used to observe microscopic skin and core damages, as shown in Fig. 3-5-Fig. 3-7.

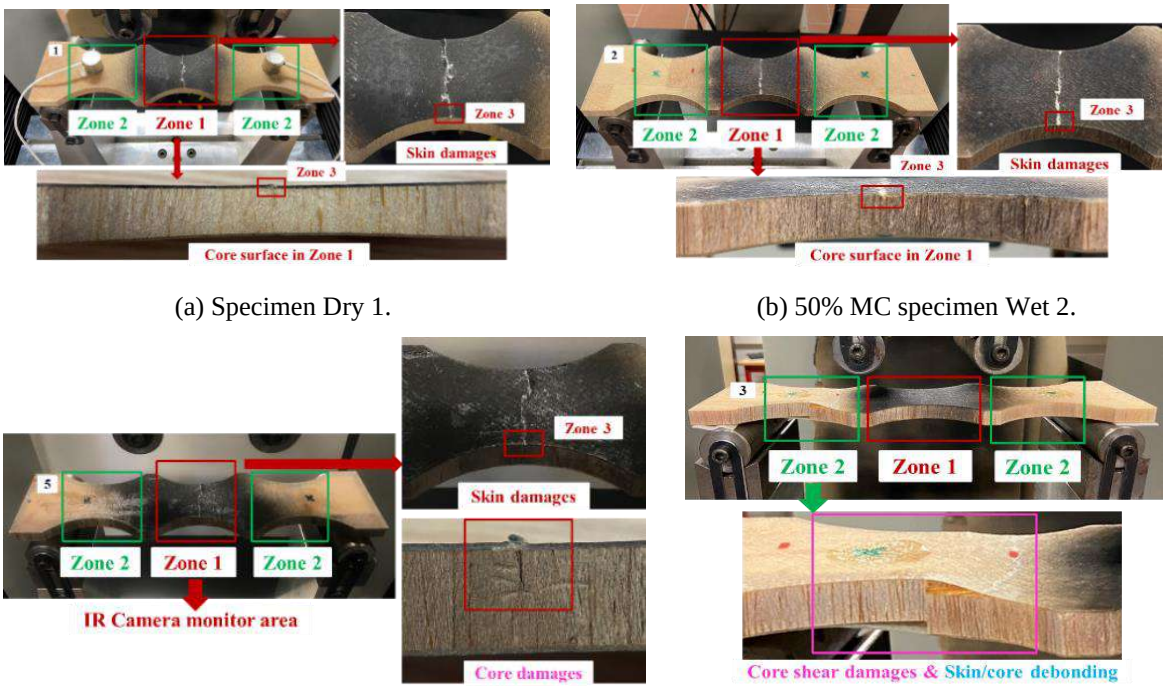

(a) Specimen Dry 1.

(b) 50% MC specimen Wet 2.

(c) 120% MC specimen Wet 5.

(d) 50% MC specimen Wet 3.

Fig. 3-4. Comparison of fracture surfaces of wet and dry GFRP-balsa sandwich specimens.

Fig. 3-5 shows an example of microscope images of skin and core surfaces in zone 1 of 50% MC specimen Wet 2 before and after water immersion tests, before 4-point bending tests. It is clear that moisture absorption has caused more matrix cracking, fiber/matrix debonding and fiber pull out of GFRP skins, that is why the stiffness and strength of the skin have been decreased, mainly due to the reduction of strengths of fiber/matrix interfaces [78-79]. Some balsa fiber pull out can also be found, but no obvious balsa core crack has been found by the microscope. It demonstrates that the moisture absorption has degraded the axial compressive strength of the fibers of balsa [80], which resulted in the decrease of strength of the skin/core interfaces and the fiber pull out.

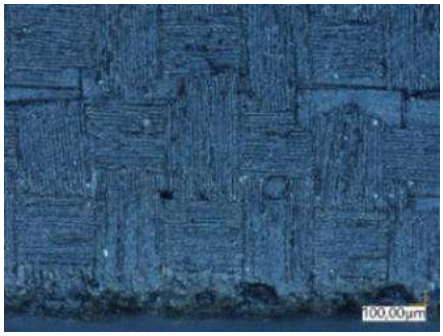

(a) Skin surface before water immersion.

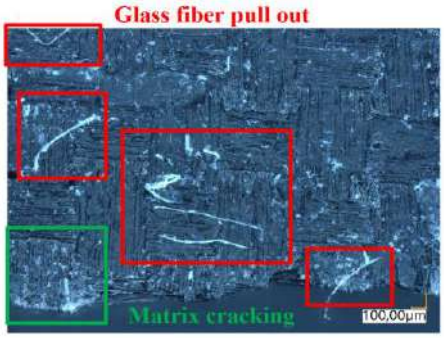

(b) Skin surface after 50% MC absorption.

(c) Skin/core side surface before water immersion.

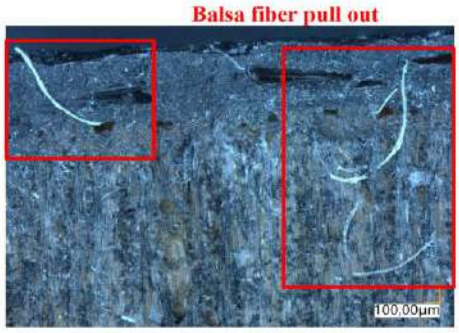

(d) Skin/core side surface after 50% MC absorption.

Fig. 3-5. Moisture effects on microscope images of 50% MC specimen Wet 2 before 4-point bending tests.

Fig. 3-6 shows the final skin damage surfaces in zone 1 of sandwich specimens Dry 1, Wet 2 and Wet 5 after 4-point bending tests, and the damages in zone 2 caused by balsa/balsa interface fracture of 50% MC specimen Wet 3. Some small extensions due to the very fast and high energy released by the glass fiber breakage [210] can only be observed on upper skin surfaces of dry specimens, meaning that fiber breakage of dry skin has released higher energy than wet specimens.

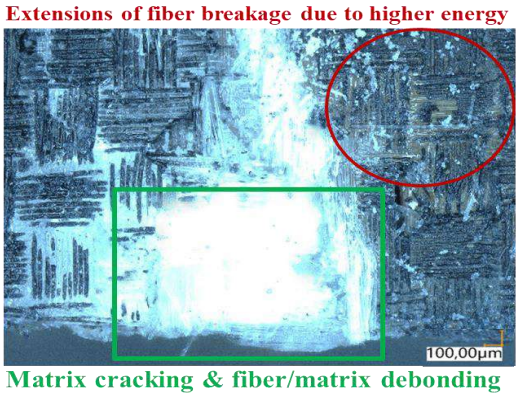

(a) Specimen Dry 1.

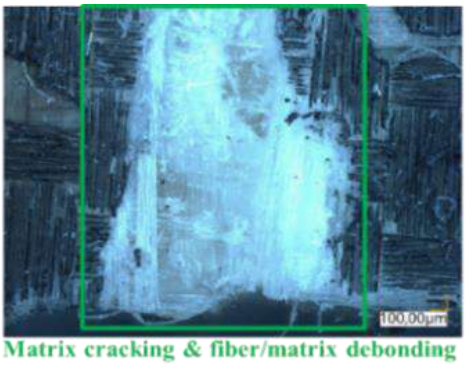

(b) 50% MC specimen Wet 2.

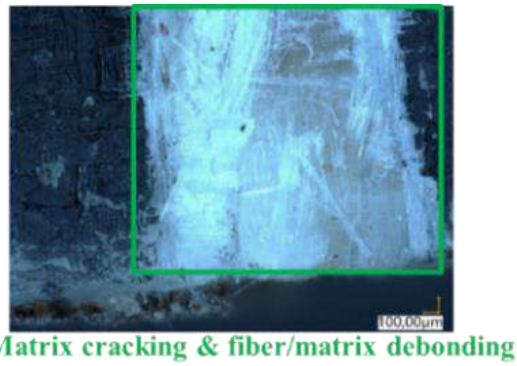

(c) 120% MC specimen Wet 5.

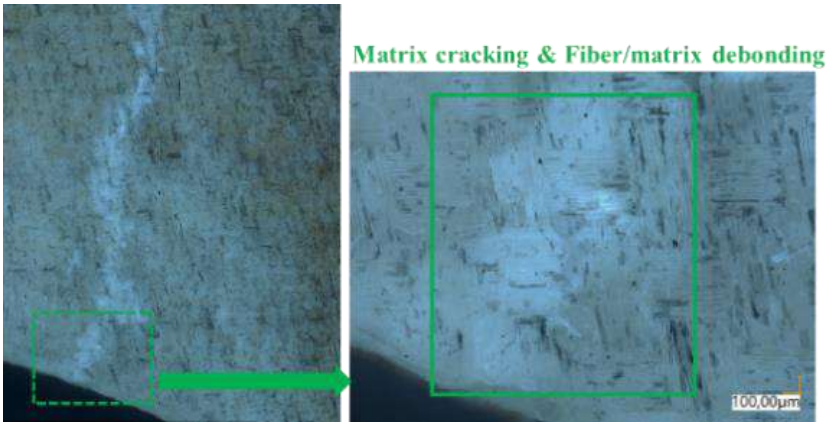

(d) 50% MC specimen Wet 3 (in zone 2).

Fig. 3-6. Upper skin damage images of dry and wet specimens after 4-point bending tests.

Fig. 3-7 expose the side view observations of GFRP skin and balsa core after bending test, mainly showing skin/core debonding and core damages. Obviously, after moisture absorption, core cracks are more obvious, skin delamination is more severe but skin/core debonding is less severe. It is interesting to note that dry specimen has the longer and wider skin/core debonding cracks, and all the dry sandwich specimens show no core damage in our tests. Skin/core debonding crack length of 50% MC (5.2 mm) and 120% MC (5 mm) specimen decrease by 7% and 11%, respectively, compared to 5.6 mm of Dry 1. It indicates that skin/core interface seems more strength in wet specimens than that in dry specimens. This observation is in good agreement with those found in the studies of Cantwell et al. [16, 84]. Herein by debonding fracture tests, it has been shown that the skin/core interfacial fracture toughness of wet GFRP-balsa sandwich can be improved.

This phenomenon is interesting, and it could be provoked by the relaxation of residual thermal stresses at the core/skin interfaces due to the curing processing of GFRP-balsa sandwich [36]. In fact, when the skin and core were co-cured at high temperature simultaneously, and then cooled at room temperature after co-curing, interlaminar shear stresses could be induced at the skin/core interfaces due to the different expansion and contraction coefficient of the two materials [55]. When the

sandwich specimen absorbs water, the thermal residual stresses existing at the skin/core interfaces of dry sandwiches due to the fabrication process can be released partially in wet sandwiches, because of the greater expansion effects of the balsa core. Finally, the skin/core interfaces of wet sandwiches seem more strength [84].

Fig. 3-7. (d) shows the typical balsa core shear damages in zone 2 of 50% MC specimen Wet 3. It can be seen that the core crack has propagated along the balsa fiber direction, followed by skin/core debonding and skin damages. This is similar to the damage sequence of GFRP-balsa sandwich in [70]. The skin/core debonding is about 14 mm, much longer than the other specimens. Based on these observations, the difference of damage mechanisms between Wet 3 and other specimens will be studied by analyzing AE signals in the following section.

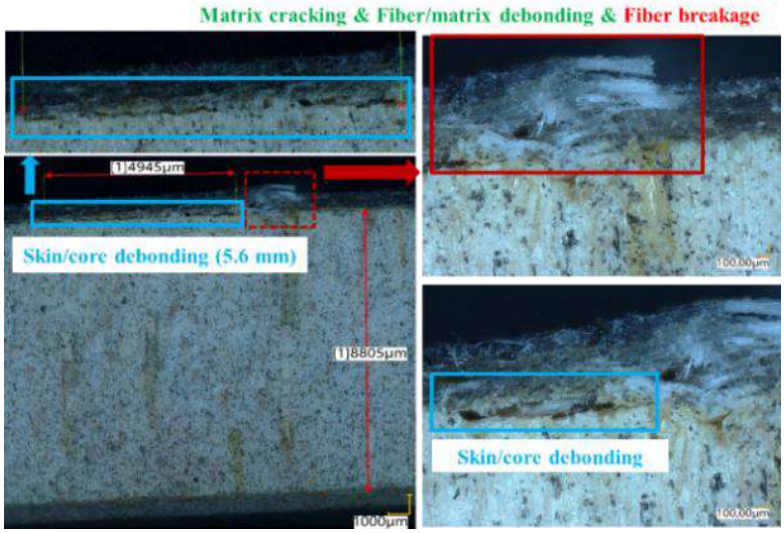

(a) Specimen Dry 1.

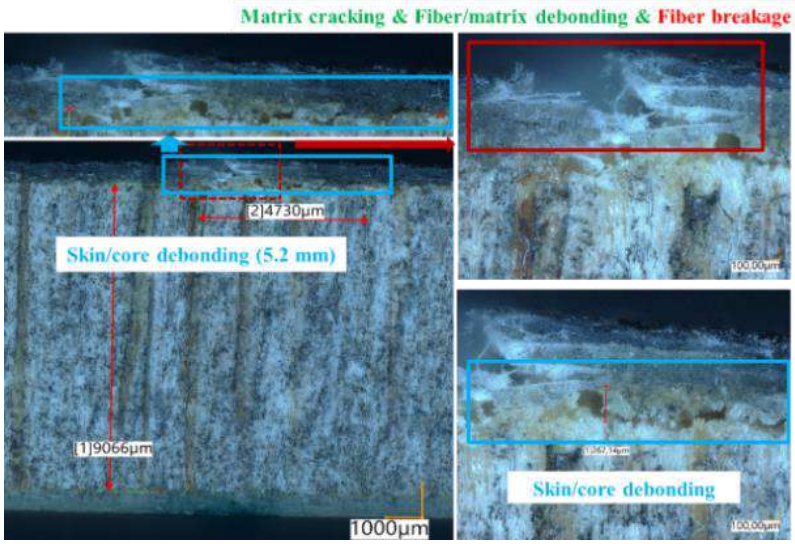

(b) 50% MC specimen Wet 2.

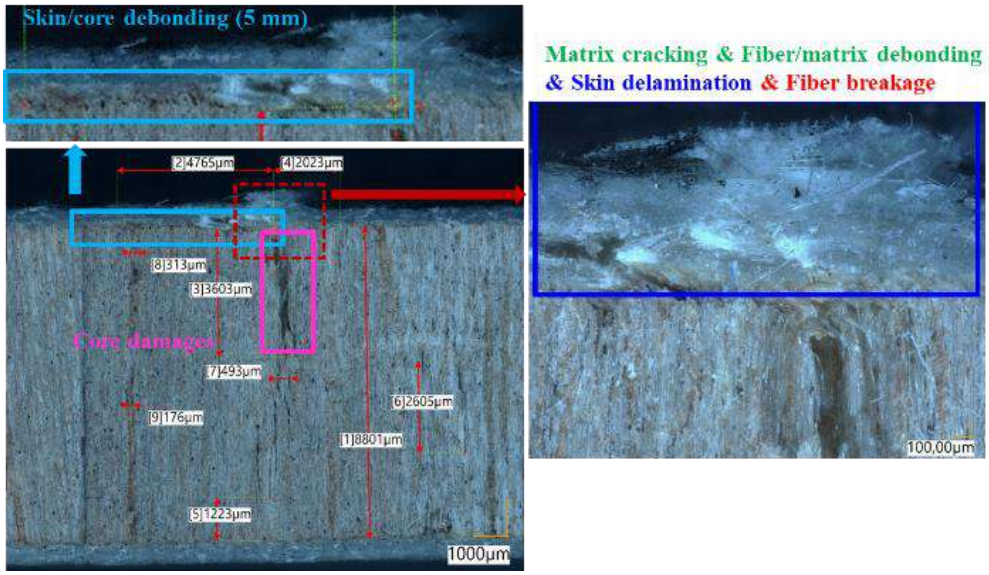

(c) 120% MC specimen Wet 5.

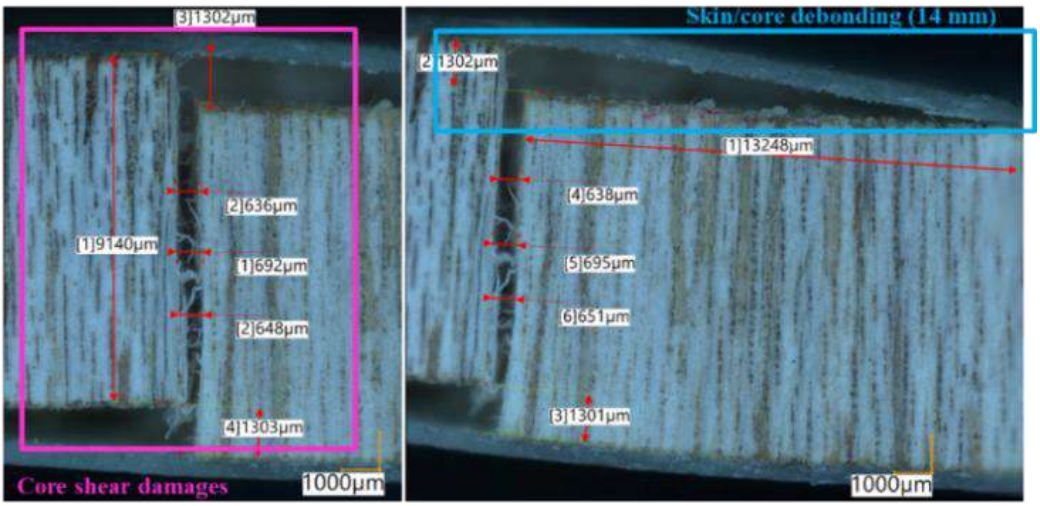

(d) 50% MC specimen Wet 3.

Fig. 3-7. Skin/core damage images of dry and wet specimens after 4-point bending tests.

It is well known that under 4-point bending loading, the upper skin of sandwich carries compressive stress while the lower skin takes tensile stress. For composite laminates, compressive strength is weaker than tensile one [67]. For wood material, Gerhards [80] has demonstrated that moisture had the least effect on parallel-to-grain tensile strength properties, while the greatest effect on compressive strength. So, when the skin damages firstly, it will be the upper compressive skin, and then the skin/core debonding occurred. Considering the most cases except Wet 3, even though moisture absorption could cause more micro balsa damages during water immersion process, the bending stiffness and strength of GFRP-balsa sandwich are mainly dominated by skin properties [127, 210].

As a preliminary conclusion, moisture absorption can result in the decrease of intralaminar strength of fiber/matrix interface and interlaminar toughness of laminate skin, but the increase of skin/core interfacial fracture toughness of GFRP-balsa sandwich. Hence, moisture absorption can result in the more severe fiber/matrix debonding, skin delamination and balsa core damages, but the less severe skin/core debonding of GFRP-balsa sandwich under 4-point bending.

3.2.4. Moisture effects on damage initiation and evolution monitored by IRT

Li H et al. [205] have proven that in-plane longitudinal and transverse thermal conductivities of woven E glass fibers are the same. The properties of balsa core can also be assumed constant in X-Y (R-T) plane [171]. Thus, in this work, thermal coefficients of GFRP and balsa are assumed identical along X and Y directions, as shown in Table 3-4 [206-208]. Based on this assumption, the general 2D heat diffusion equation (Eq. (1-16)) can be simplified to Eq. (3-1) to determine the heat source field during the damage evolution process under 4-point bending loading.

$$\rho C\left(\frac{\partial \Delta T}{\partial t}+\frac{\Delta T+T_0-T_{ext}}{\tau_{th}}\right)-k\left(\frac{\partial^2 \Delta T}{\partial x^2}+\frac{\partial^2 \Delta T}{\partial y^2}\right)=s_t \tag{3-1}$$

Where s_t is the heat source, which represents the real temperature variation rate at a certain time due to the thermoelastic source and damage dissipation; T_0 is the average temperature of the first ten IRT images; T_{ext} is the room temperature; τ_{th} is the time increment which characterizes the heat convection between the specimen and environment. $\Delta T=T-T_0$, which is the temperature difference; ρ is density; C is the specific heat; k is the thermal conductivity coefficient.

Heat source s_t is composed of the irreversible mechanical dissipation d_1 and the reversible thermoelastic coupling s_{the} between the temperature and strain [210], so the irreversible heat source can be obtained by Eq. (3-2):

$$d_{me}=s_t-s_{the} \tag{3-2}$$

Where $s_{the}=-\alpha T_0\frac{\partial \boldsymbol{\sigma}}{\partial t}$, α is thermal expansion coefficient, $\boldsymbol{\sigma}$ is the stress matrix.

Table 3-4. Moisture effects on thermal coefficients of GFRP-balsa sandwich.

Type	ρ (kg/m^3)	C (J/(kg•K))	k (W/(m•K))	α (10^{-6}/K)
Dry GFRP	1900	1000	0.95	8
Dry balsa	148	2900	0.05	35
Water	1000	4200	0.60	210
50% MC GFRP	1600	2067	0.83	75
120% MC GFRP	1409	2745	0.76	118

Since skin damages are the predominant in most of the tests, to apply 2D heat diffusion equation, heat sources are assumed homogeneous through the thickness direction since the skin is very thin. The product of density and specific heat (ρC) of GFRP skin is about four times as much as that of balsa core, k of balsa is 95% smaller than that of GFRP, and $\alpha T_0 \frac{\partial \boldsymbol{\sigma}}{\partial t}$ of the balsa core is also much lower under bending loading, because the stress in balsa core is very small. Finally, only the contributions of thermal coefficients of the GFRP skin to the sandwich specimen in Eq. (3-1) and Eq. (3-2) are considered. Moisture effects on the thermal coefficients of the skin can be obtained based on Eq. (3-3. a-d) [208]:

$$\rho_{MCF} = (\rho_{DF} + \rho_W \cdot MC)/(1 + MC) \tag{3-3a}$$

$$C_{MCF} = (C_{DF} + C_W \cdot MC)/(1 + MC) \tag{3-3b}$$

$$k_{MCF} = (k_{DF} + k_W \cdot MC)/(1 + MC) \tag{3-3c}$$

$$\alpha_{MCF} = (\alpha_{DF} + \alpha_W \cdot MC)/(1 + MC) \tag{3-3d}$$

ρ_{DF}, C_{DF}, k_{DF} and α_{DF} are the density, specific heat, thermal conductivity and expansion coefficient of the dry skin, ρ_W, C_W, k_W and α_W are the coefficients of water, ρ_{MCF}, C_{MCF}, k_{MCF} and α_{MCF} are the coefficients of the wet skin.

In Eq. (3-1), τ_{th} , which is the time increment characterizing the heat convection between the specimen and environment, is the cooling time obtained by active IRT tests in Chapter 2. It is 355 ± 15 s for the dry sandwich, and 65 ± 15 s for the wet sandwich. ∂t is 0.01 s in MATLAB program because each frame is obtained by 1s/480. So, ∂t is 10^{-4} smaller than τ_{th}. Thus, in this work, $\rho C(\frac{\Delta T + T_0 - T_{ext}}{\tau_{th}})$ can be negligible compared to $\rho C \frac{\partial \Delta T}{\partial t}$. Then Eq. (3-1) becomes Eq. (3-4):

$$\rho C \frac{\partial \Delta T}{\partial t} - k\left(\frac{\partial^2 \Delta T}{\partial x^2} + \frac{\partial^2 \Delta T}{\partial y^2}\right) = s_t \tag{3-4}$$

Cumulative irreversible damage index D_{me} can be obtained by integration of damage d_1 as Eq. (3-5):

$$D_{me} = \int_0^t d_{me}\, dt \tag{3-5}$$

Since GFRP-balsa sandwich has a max displacement of nearly 12 mm during the whole 4-point bending test, the traditional method which obtains the real temperature difference by $\Delta T = T - T_0$ without considering the displacement is no longer accurate. In order to clearly observe the damage evolution process, temperature difference at time t is firstly calculated by the superposition of the subtraction from any two adjacent frames ($\Delta T = T_1 - T_0 + T_2 - T_1 + \ldots + T_t - T_{t-1}$). Correlation between movement of the vertical pixel in IRT temperature images and true displacement of the specimen is

introduced into MATLAB program to improve the accuracy of post-processing of thermal images. Finally, a correction is introduced into ΔT in Eq. (3-4) by solving the problem of big displacement effects on temperature difference calculation accuracy.

The final accurate cumulative heat source field images are shown in Fig. 3-8-Fig. 3-10. The three yellow lines represent the edges of upper and lower skins in zone 1, as marked in Fig. 3-8-Fig. 3-10. (a-d). As seen in Fig. 3-8. (d), Fig. 3-9. (d) and Fig. 3-10. (d), at the final failure of the dry and wet specimens under 4-point bending loading, compressive damages in the middle of upper skin are the dominated damage mechanisms. Fig. 3-8. (a)-(c), Fig. 3-9. (a)-(c) and Fig. 3-10. (a)-(c) show the damage initiation point and propagation path of upper skin of dry and wet specimens. The damage locations observed by the IR camera in the tests will be correlated to the localizations predicted by PDA model in Abaqus in the later work.

IRT camera has observed that the dry skin crack propagates more quickly from the initiation point to the full specimen width, while the wet skin shows a slower and clearer propagation process. It takes about 1.03 s for dry sandwich, 1.38 s for 50% MC sandwich and 1.52 s for 120% MC one (with a frame rate of 480 Hz) to propagate from the damage initiation to the final full damage. The whole width in the center of the specimen is 40 mm, so it can be evaluated that the average crack propagation speeds of the specimen Dry 1, 50% MC specimen Wet 2 and 120% MC specimen Wet 5 observed by IRT are about 38.8 mm/s, 29.0 mm/s, and 26.3 mm/s, respectively. It demonstrates that IR camera can effectively capture the very fast GFRP skin damages at the final fracture time in static 4-point bending tests.

It is also interesting to find that some small temperature increases on the dry specimen surface have been captured by infrared camera in red circles on Fig. 3-8. (b). It should be caused by dynamic effect of higher energy released within very short time, but it is not obvious in the wet specimens. It means that moisture absorption has caused the bending strength reduction, and the final fracture in wet specimens should be more progressive. Microscope observations in Fig. 3-8. (d) can also demonstrate this phenomenon. It verifies again that dry sandwich has released higher dynamic energy than wet sandwiches at final fracture, with the max cumulative heat source field near to $4 \cdot 10^{10} \mathrm{J/m^3}$ for dry and 50% MC specimens, compared to $1 \cdot 10^{10} \mathrm{J/m^3}$ of 120% MC specimen.

In summary, it demonstrates that IRT can accurately monitor and localize the very fast skin damage evolution process of dry and wet GFRP-balsa sandwiches under 4-point bending, which in return could validate the accuracy of the numerical PDA model in Abaqus. It demonstrated that moisture absorption will result in the decrease of the strength and released energy of the skin, and then the slower crack propagation speed.

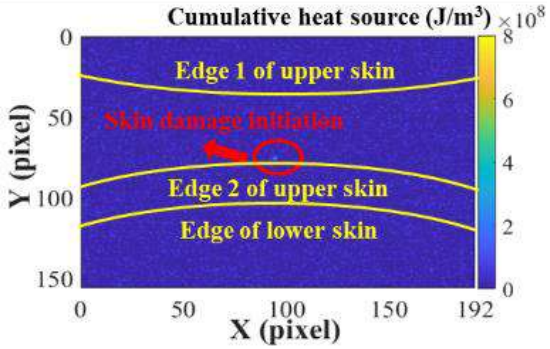

(a) t=317.40 s

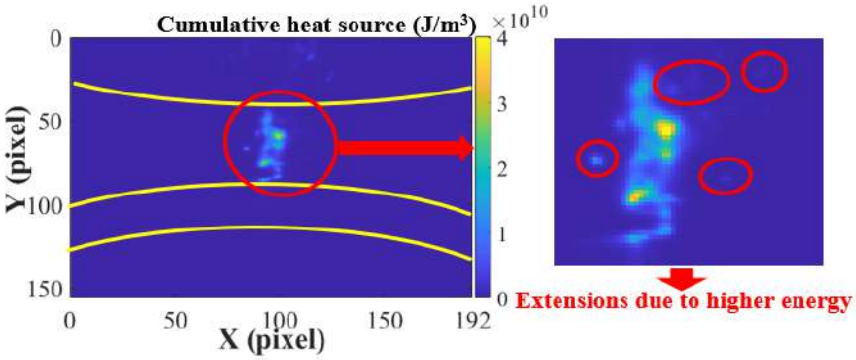

(b) t=318.40 s

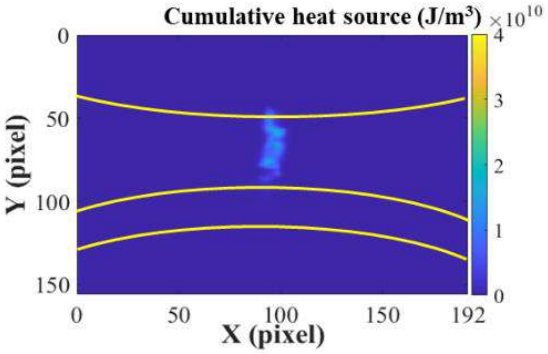

(c) t=318.43 s

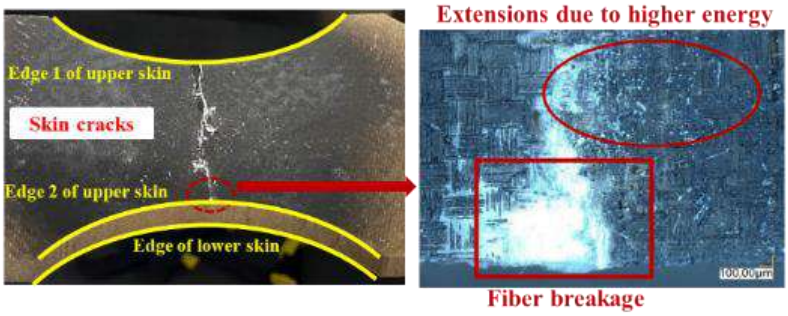

(d) Microscope images of upper skin surface

Fig. 3-8. Cumulative heat source (J/m^3) field images and damage photos of specimen Dry 1.

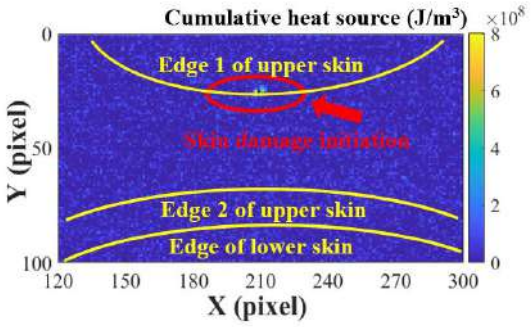

(a) t=359.60 s

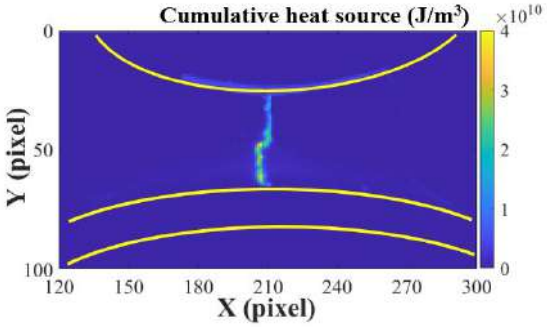

(b) t=360.96 s

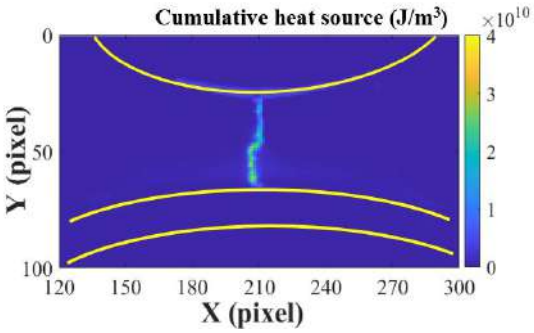

(c) t=360.98 s

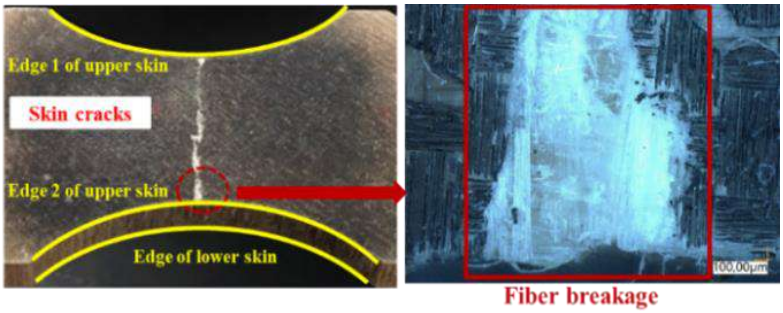

(d) Microscope images of upper skin surface in zone 2

Fig. 3-9. Cumulative heat source (J/m^3) field images and damage photos of 50% MC specimen Wet 2.

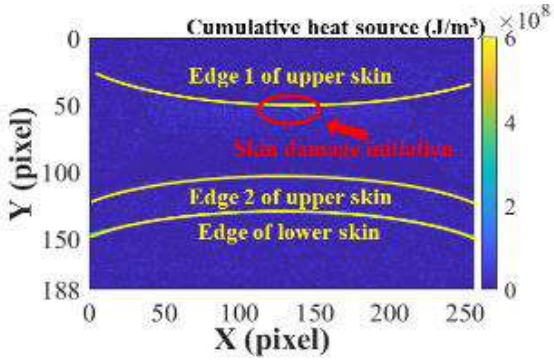

(a) t=255.43 s

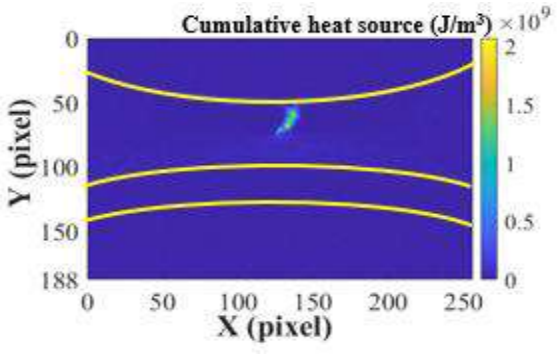

(b) t=256.94 s

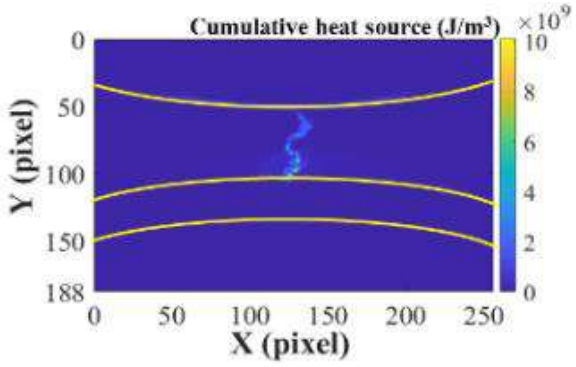

(c) t=256.95 s

(d) Microscope images of upper skin surface

Fig. 3-10. Cumulative heat source (J/m^3) field images and damage photos of 120% MC specimen Wet 5.

3.2.5. Moisture effects on damage characterization by AE

3.2.5.1. Moisture effects on the cumulative hits number

Firstly, moisture effects on the cumulative hits number of the three GFRP-balsa sandwich specimens with different MC are illustrated in Fig. 3-11. The cumulative hits number of the 50% MC specimen and 120% MC specimen has decreased by 63% and 70%, respectively, due to the moisture absorption. And it decreases faster before 60% MC at the beginning linear period of the moisture absorption curve, as shown in Fig. 2-27. (b).

One reason for this decrease is that the energy released by the wet sandwich specimen has been decreased, as verified by IRT observation. In addition, the acoustic wave attenuation is higher in the wet sandwich, as demonstrated in Chapter 2. When the acoustic wave propagates in the wet GFRP-balsa sandwich, it will meet more obstacles such as material and interface changes, because water, balsa wood and CFRP exist simultaneously in the wet sandwich. Then the acoustic wave propagation has been disturbed by these internal changes. It signifies that the monitoring results by AE on wet GFRP-balsa sandwich may be affected, especially the damage localizations, because more signals have been lost.

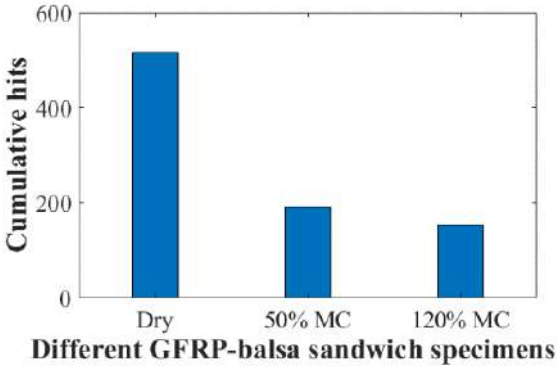

Fig. 3-11. Moisture effects on cumulative hits number of GFRP-balsa sandwich.

As for moisture effects on cumulative energy of GFRP-balsa sandwich, Fig. 3-12 shows that the final cumulative energy from dry specimen at the end of the tests is higher than that from wet ones. The cumulative energy of the 50% MC specimen and 120% MC specimen has decreased by 32% and 40%, respectively, due to the moisture absorption. It is consistent with conclusions from IRT observations which show that dry skin damages have released higher energy more quickly than that from wet skins, as shown in Fig. 3-8-Fig. 3-10.

The decrease of cumulative energy due to moisture absorption is smaller than decrease of cumulative hits in Fig. 3-11, this may be because that the fractions of hits from different damage modes such as skin damages and balsa core damages releasing different energy have changed. Thus, further classification analysis will be necessary to help understand all the damage mechanisms.

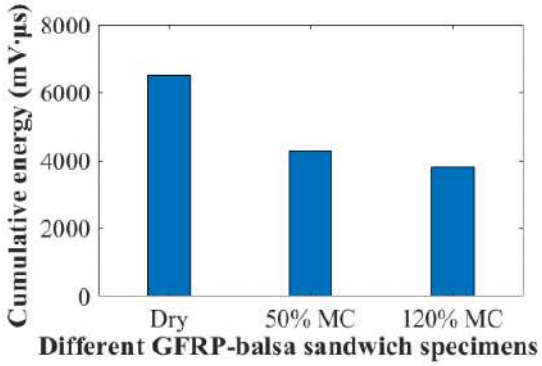

Fig. 3-12. Moisture effects on cumulative energy of GFRP-balsa sandwich.

3.2.5.2. Moisture effects on damage localizations by AE

In order to couple the damage localizations by microscope, IRT and AE observations, Fig. 3-13 shows the AE amplitude (dB) distributions between the two wideband sensors (D=0.18 m, S_1 is located at 0.06 m, and S_2 is located at 0.24 m) of the dry and wet sandwiches. The red window represents the center zone 1 within 0.115-0.185 m, and the green windows correspond to zone 2

within 0.06-0.105 m and 0.195-0.24 m. For Dry 1, Wet 2 and Wet 5, most AE signals accumulate in red zone 1, mainly after the damage onset time observed by IRT. Only very few AE signals lower than 50 dB can be found in zone 2, which may come from the microscopic core shear damages. The existence of balsa core damages will be further demonstrated in the later parts.

The locations of zone 1 in AE figures can be compared to the IRT and microscope images, which show the very clear fiber breakage in the center (X=0.15 m) of the specimen. Firstly, the highest amplitude higher than 90 dB [109, 120] should be corresponding to the final fiber breakage. In specimen Dry 1, Wet 2 and Wet 5, the highest amplitude is 97 dB, 95 dB and 92 dB, respectively. Because the amplitude attenuation property has been input into the location setup in AEwin software before the test, the attenuation due to the moisture absorption has been corrected in the 4-point bending test. Thus, the decrease of the highest amplitude indicates that the fiber breakage of the wet sandwich has released lower energy, which agrees well with IRT observations.

As demonstrated in [114], the signals within 50-80 dB just before the final fracture shall be released by skin delamination of composite laminates. It is clear that the wet sandwiches have emitted much more signals within 50-80 dB in the center of zone 1, so the skin delamination of the wet sandwiches has become more severe, which is consistent with the microscope observations in Fig. 3-7. Moreover, some signals lower than 50 dB can be observed near the center of zone 1 for both dry and wet sandwiches, according to the damage sequence of composite laminates, they should correspond to the microscopic matrix cracking [114, 116] which appear before the delamination. The damage sequence of these skin damage modes will be further explained by the amplitude versus time distributions.

It can be seen that the AE hits number of each specimen in localizations figures in Fig. 3-13 is less than the total cumulative hit in Fig. 3-11. It means that some signals have been lost due to the amplitude attenuation in the localizations of GFRP-balsa sandwich. Thus, the damage localization method for GFRP-balsa sandwich shall be improved in order to receive more useful signals. For example, the distance between the two sensors can be decreased, and three or four sensors can be used to better localize the damages. In addition, larger dog-bone sandwich specimens can be prepared to allow enough positions for more sensors.

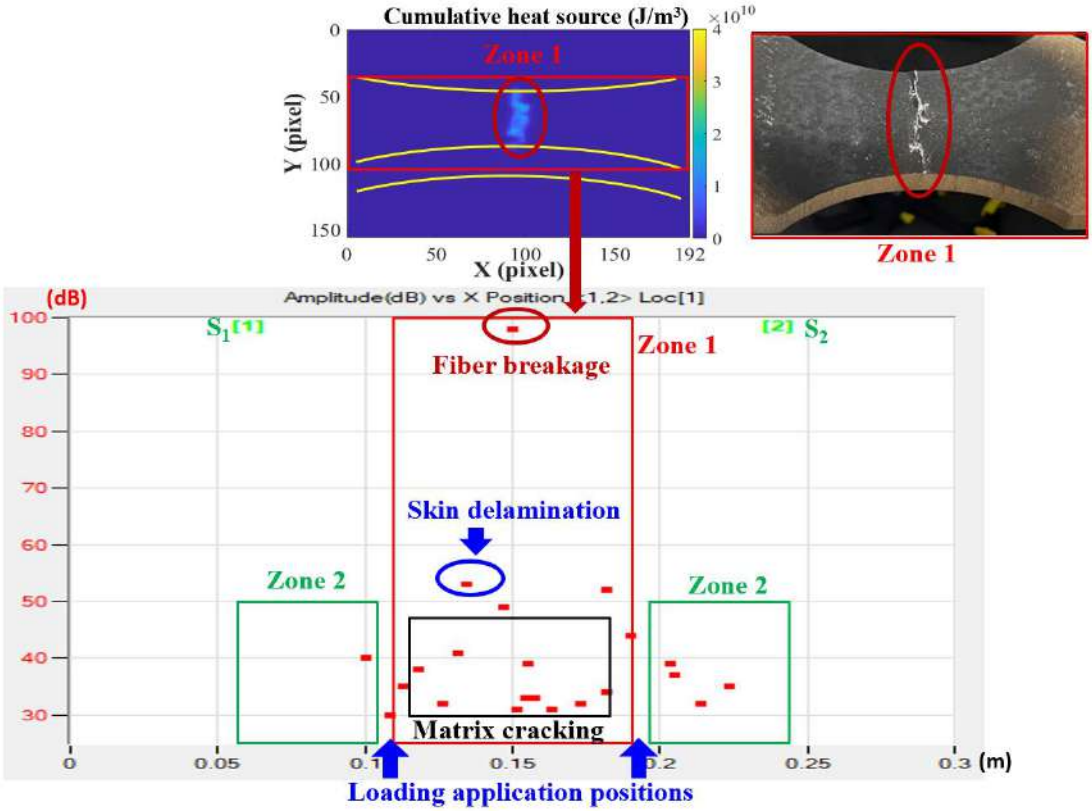

(a) Specimen Dry 1.

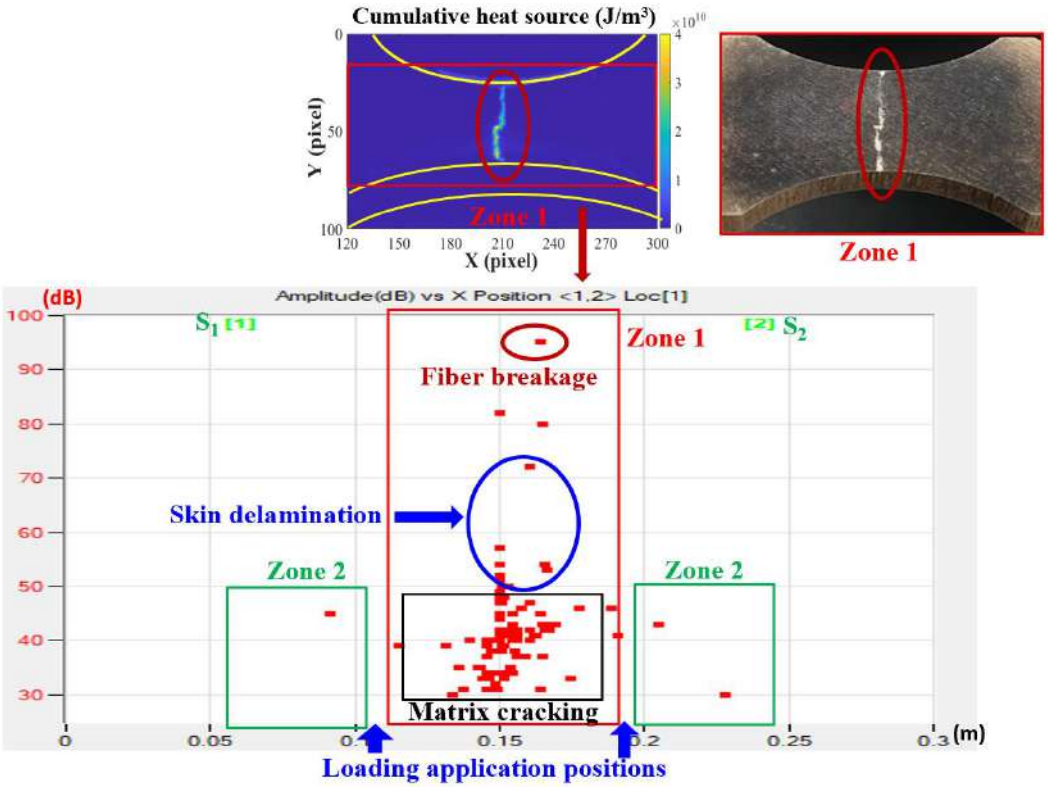

(b) 50% MC specimen Wet 2.

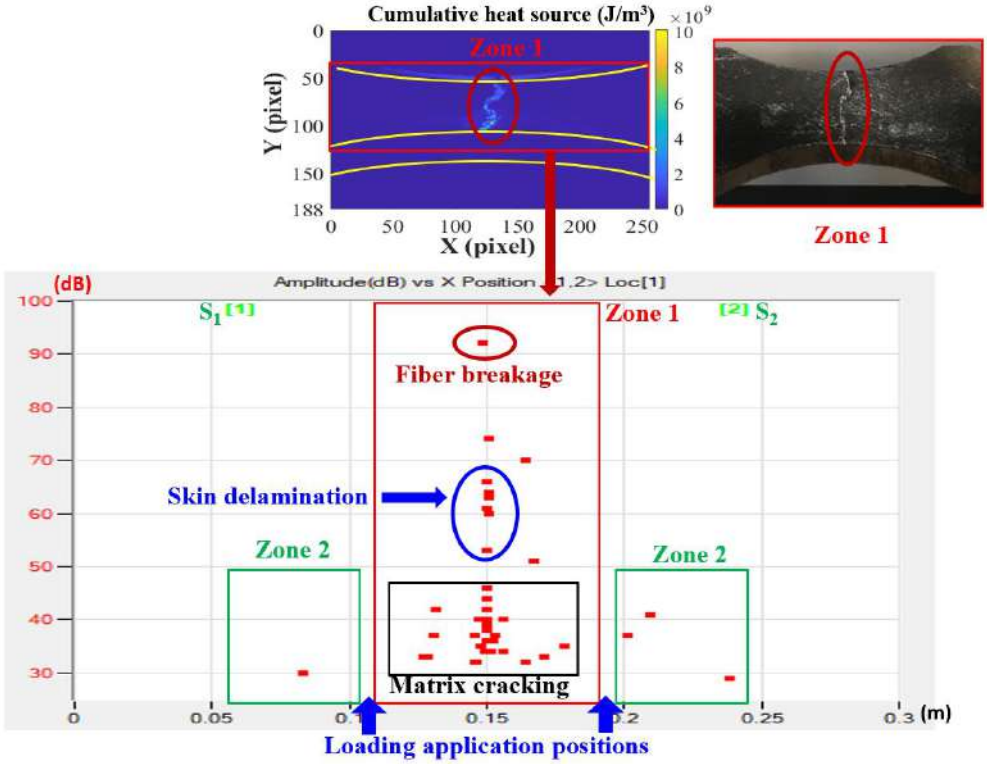

(c) 120% MC specimen Wet 5.

Fig. 3-13. Damage localizations in dry and wet GFRP-balsa sandwiches by AE.

3.2.5.3. Identification of balsa core damages in the first clustering process

In order to reduce the influence of noise signals during the tests on AE analysis, original AE signals obtained by AEwin software should be firstly filtered by the following conditions [107, 112]: remove signals whose number of counts is less than 3; remove signals whose duration is less than 1 μs; filter peak frequency by the range of 20-800 kHz, considering that most received signals are lower than 800 kHz in this work and damage mechanisms of composite sandwich structures reported in literatures (see Table 1-2) are lower than 800 kHz, and the frequency range of wideband sensors is 1 00 kHz-1 MHz.

Considering the statistical treatment of AE data, as mentioned in section 1.3.2, K-means algorithm [95, 112], which is built in NOESIS software, has been performed to classify AE hits into different cluster groups, also to find the correlations between AE parameters and different damage mechanisms of GFRP-balsa sandwich. The selection of optimum AE parameters and optimization of suitable cluster number are the key factors to generate the most robust damage classification results. Eleven most common AE parameters are chosen here to keep the most correlated AE features and improve the efficiency of the algorithm [107]: energy, amplitude, duration, rise time, counts, counts to peak, average frequency, frequency centroid, peak frequency, initiation frequency and

reverberation frequency. A normalization of the data between 0 and 1 was carried out to limit the weight of certain parameters such as the high energy values.

To determine the optimum number of cluster groups, two statistical criteria are often used: the Davies & Bouldin (DB) and Tou coefficients. The clustering result is the optimum when DB is the minimum, and DB is usually regarded as the first criterion. Tou is often used as the complement validation [95, 112], and the clustering results will be better when Tou is higher.

Thus, K-means clustering process was firstly applied to all specimens to find the best cluster number. Fig. 3-14 shows the DB and Tou Coefficients of specimen Dry 1, 50% MC specimens Wet 2 and Wet 3, and 120% MC specimen Wet 5. It can be seen that cluster number of 2 is the best choice for all specimens, showing the lowest DB and highest Tou. So, two groups of clusters have been obtained by the K-means method as the first clustering process of the received AE data.

Dry 1, Wet 2 and Wet 5 are chosen to compare the moisture effects on the AE parameters corresponding to different damage modes of GFRP-balsa sandwich. Wet 3 is chosen as a validation of the signals corresponding to the balsa core damages, because it shows the obvious core shear damages in zone 2, different from the skin damages in zone 1 of the other three specimens, as observed in Fig. 3-4.

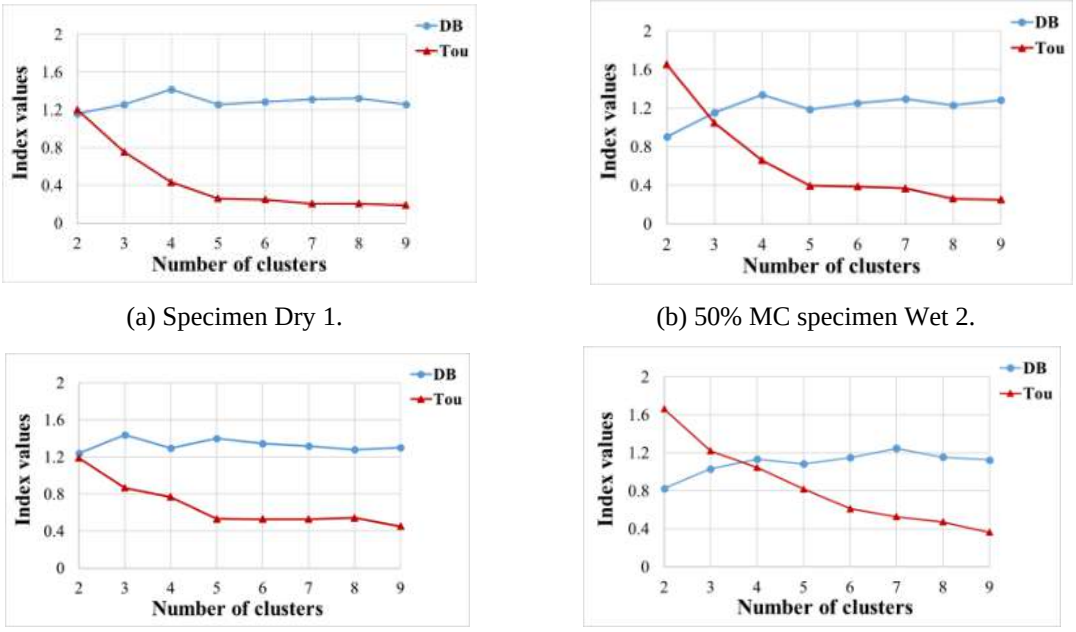

(a) Specimen Dry 1.

(b) 50% MC specimen Wet 2.

(c) 50% MC specimen Wet 3.

(d) 120% MC specimen Wet 5.

Fig. 3-14. DB and Tou coefficients of GFRP-balsa sandwiches in the first clustering process.

As mentioned above, eleven common AE parameters are chosen in the clustering analysis, however, compared with the classification characteristics based on different parameters in the references [116-

121], amplitude and peak frequency are the most meaningful in composite structures. In this thesis, in the first clustering process, in order to find the obvious difference between the two clusters, the amplitude and peak frequency distributions from sensor S_1 which has received the most signals of all the specimens are firstly compared to Force/time curves in Fig. 3-15, in which Cluster 0 is in purple and Cluster I is in green.

It can be found that AE signals higher than 60 dB accumulate intensely just at the final fracture time of Dry 1, Wet 2 and Wet 5 in Fig. 3-15. (a)-(c). For 50% MC specimen Wet 3, the obvious core shear damages and skin/core debonding appear just near sensor S_1 in the left zone 2 in Fig. 3-15. (d), so sensor S_1 of Wet 3 has received signals different from the other specimens, showing much more signals in Cluster 0 and Cluster I. It is interesting to find that most signals within Cluster 0 of all the specimens are lower than 60 dB and within a higher frequency range of 200-600 kHz, while Cluster I contains the highest amplitude above 90 dB and the peak frequency range is lower than 400 kHz.

As concluded in Table 1-2 [116-121] in Chapter 1, most signals corresponding to damages of composite laminates are lower than 400 kHz, and the honeycomb core shear damages show peak frequency higher 400 kHz, so peak frequency has become a very important parameter to distinguish the different skin and core damages. In this work, Fig. 3-15 demonstrates that Cluster I should include GFRP skin damages and skin/core debonding, and the highest amplitude signal should be fiber breakage [100, 114, 116]. Based on the possible damage mechanisms of GFRP-balsa sandwich under 4-point bending observed by the microscope in Fig. 3-6 and Fig. 3-7, Cluster I could contain more than four damage modes, including matrix cracking, fiber/matrix debonding, delamination, fiber breakage and skin/core debonding.

When observing Cluster 0, the peak frequency distributions of Dry 1, Wet 2 and Wet 5 are mainly higher than 200 kHz. The wet sandwiches have received much more signals within Cluster 0, combined with the microscope observations, it means that Cluster 0 shall correspond to the core shear damages which are more severe due to moisture absorption. Another validation for identification of Cluster 0 is that Wet 3 has received much more signals in Cluster 0 than other specimens, especially the signals within 200-600 kHz. Since Wet 3 has shown the very obvious core shear damages in zone 2, it verifies that Cluster 0 shall be from balsa core shear damages. It also indicates that it is much easier to dissociate Cluster 0 from Cluster I by peak frequency distributions, when there are obvious two different damage mechanisms, such as skin damages and core damages.

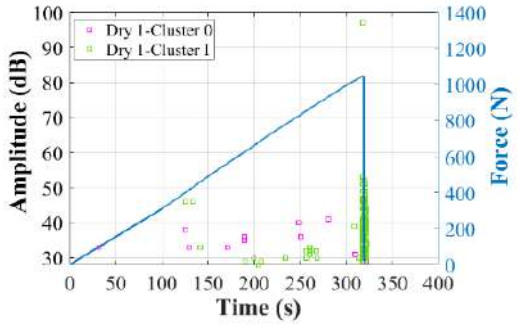

(I) Amplitude vs. Time

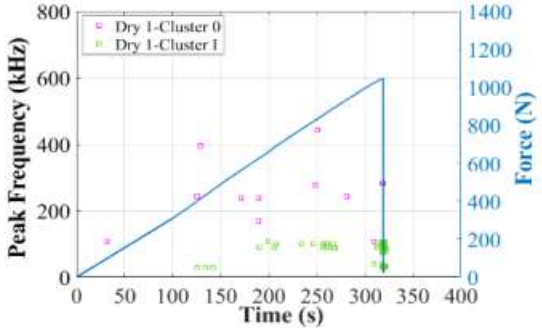

(II) Peak Frequency vs. Time

(a) Specimen Dry 1

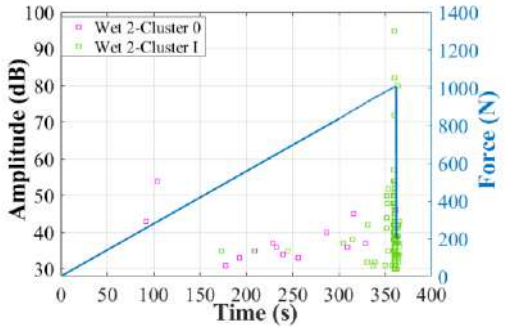

(I) Amplitude vs. Time

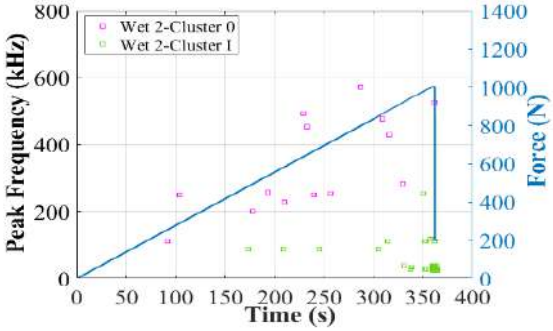

(II) Peak Frequency vs. Time

(b) 50% MC specimen Wet 2.

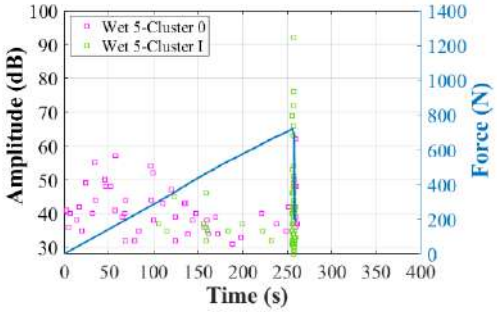

(I) Amplitude vs. Time

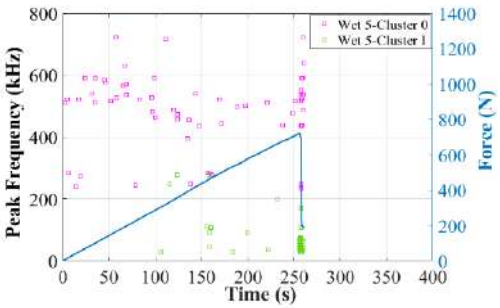

(II) Peak Frequency vs. Time

(c) 120% MC specimen Wet 5.

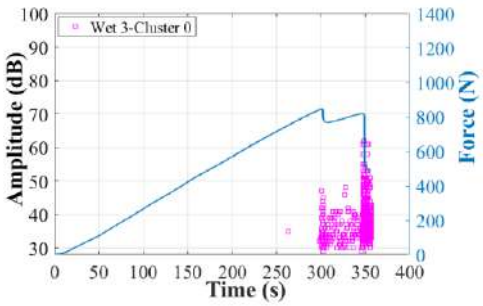

(I) Amplitude vs. Time of Cluster 0

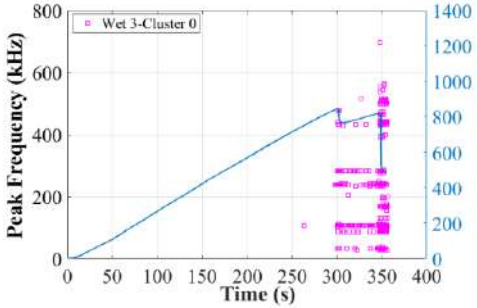

(II) Peak Frequency vs. Time of Cluster 0

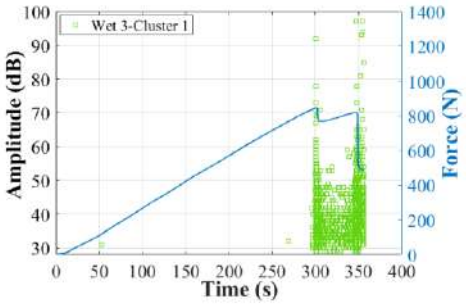

(III) Amplitude vs. Time of Cluster 1

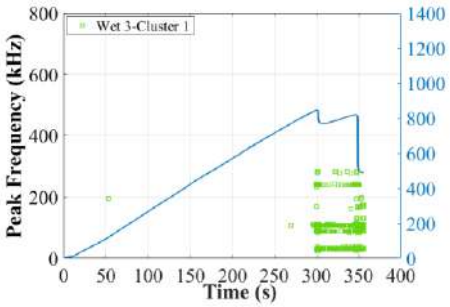

(IV) Peak Frequency vs. Time of Cluster 1

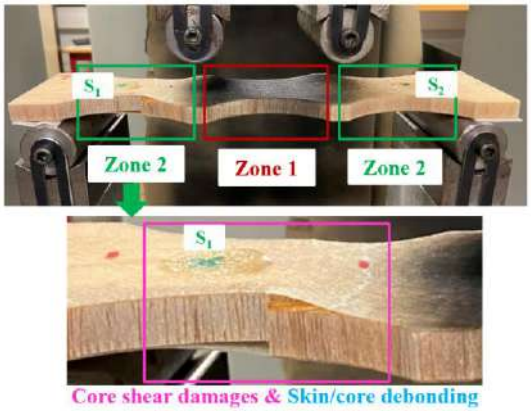

(V) Sensor positions and damage locations in zone 2.

(d) 50% MC specimen Wet 3.

Fig. 3-15. Two clusters after first clustering process of dry and wet GFRP-balsa sandwiches.

As explained in [121], duration could be also a useful parameter to explain different damage mechanisms of the sandwich structure, but it has not been studied a lot. In order to identify the further validate the damage mechanism corresponding to Cluster 0 in this work, Fig. 3-16 and Fig. 3-17 add the correlations between amplitude, peak frequency and duration of all the specimens. Some interesting conclusions can be made, it is more obvious that peak frequency of Cluster 0 is lower than 600 kHz and amplitude is lower than 60 dB. It is interesting to find that duration of Cluster 0 is always lower than 400 μs for all the specimens. The duration of Cluster 0 will be compared to those of Cluster I in the next part.

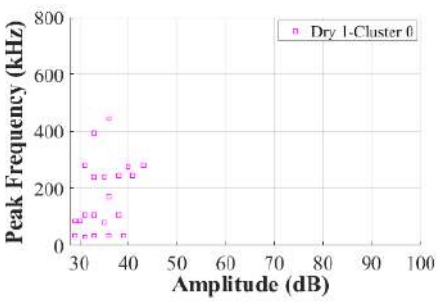

(a) Specimen Dry 1.

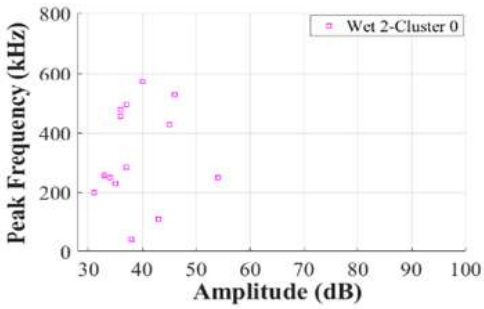

(b) 50% MC specimen Wet 2.

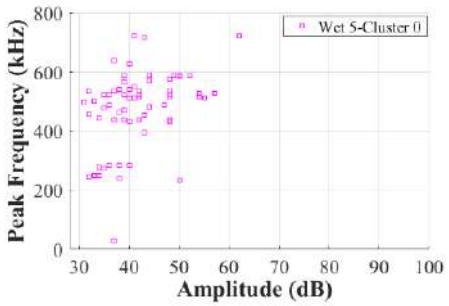

(c) 120% MC specimen Wet 5.

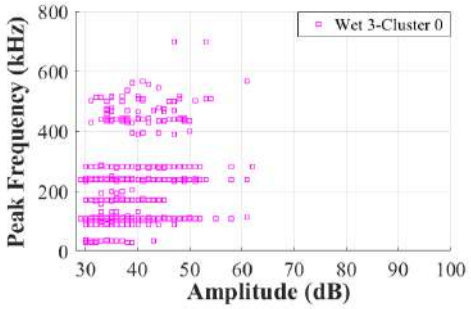

(d) 50% MC specimen Wet 3.

Fig. 3-16. Peak frequency vs. Amplitude of Cluster 0 of dry and wet GFRP-balsa sandwiches.

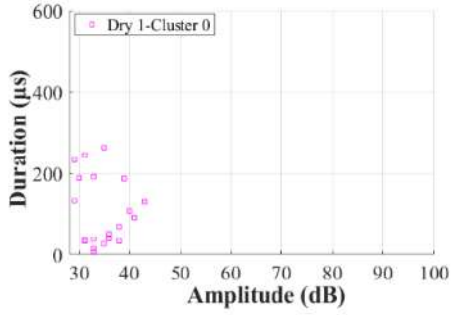

(a) Specimen Dry 1.

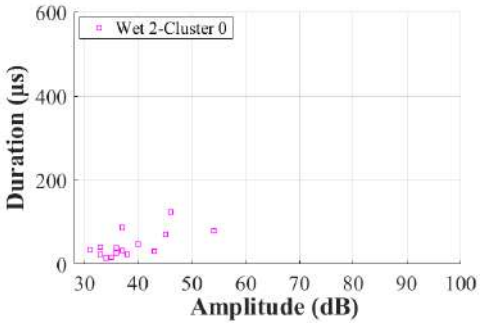

(b) 50% MC specimen Wet 2.

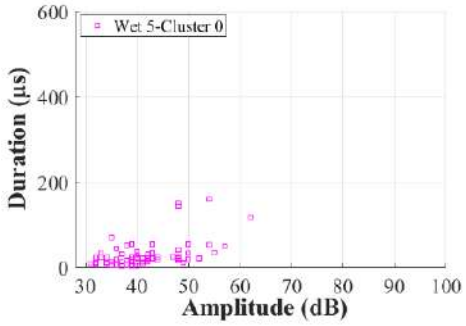

(c) 120% MC specimen Wet 5.

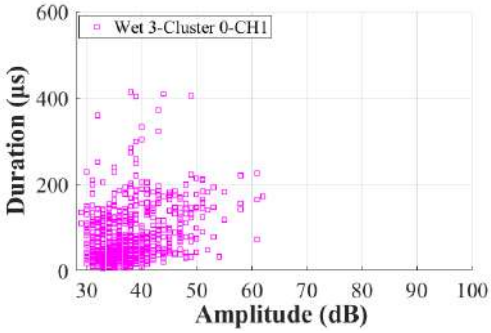

(d) 50% MC specimen Wet 3.

Fig. 3-17. Duration vs. Amplitude of Cluster 0 of dry and wet GFRP-balsa sandwiches.

In conclusion, when more than two kinds of different damage mechanisms exist in the composite sandwich structures, such as the skin damages, the skin/core debonding and core damages, the clustering process can be firstly finished by obtaining two groups of clusters: Cluster 0 which corresponds to the balsa core shear damages and Cluster I which contains the composite skin damages. In the following analysis, the second clustering process will be done to classify the different damages in Cluster I.

3.2.5.4. Skin damage initiation detection by cumulative counts and energy

The first damage characterization work of the skin is to find the initiation moment. Cumulative counts [102, 104, 117] (see Fig. 1-25 and Fig. 1-26) have been proven to be effective for identification of the crack front, crack opening and crack propagation path of composite laminates, while cumulative acoustic energy can be used to identify the crack opening and propagation in the fiber reinforced composites. In this work, combined with IRT observations which have detected clearly the damage initiation time of higher energy damage modes including skin delamination and fiber breakage just at the final fracture moment, cumulative counts accumulation of Cluster I of dry and wet sandwiches are investigated to identify the damage initiation of all possible skin damages, as seen in Fig. 3-18.

Firstly, it is obvious that all the curves of the three specimens with different MC show the similar variation tendency. The cumulative counts have the most obvious increase just at the final fracture time. Before the final failure time, cumulative counts begin to increase at point A and have a small increase at point B. Combined with the damage mechanisms of composites identified by cumulative counts in references [104, 117], point A should be the damage initiation of microscopic matrix cracking before which there is no irreversible damage [117], and the specimen still shows the linear response. Although no obvious non-linear behavior can be seen by the force/displacement curve, Point B should be the initiation moment of macroscopic damages [104, 117], for example, delamination, and Point C should be the start of delamination and final fiber breakage [117, 118]. Point B of Wet 5 has appeared much earlier compared to the specimens Dry 1 and Wet 2, which means that the macroscopic damages of the wet sandwiches have been advanced. It verifies that AE cumulative counts can be a useful parameter to identify the initiation of microscopic and macroscopic damages of composite laminates under bending load.

Next, the initiation and evolution time of these different microscopic and macroscopic damage modes will be further demonstrated based on the AE parameter distributions versus time.

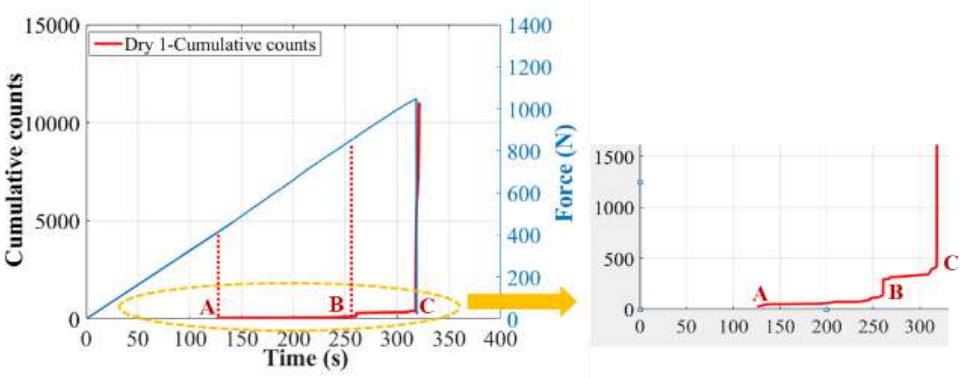

(a) Specimen Dry 1.

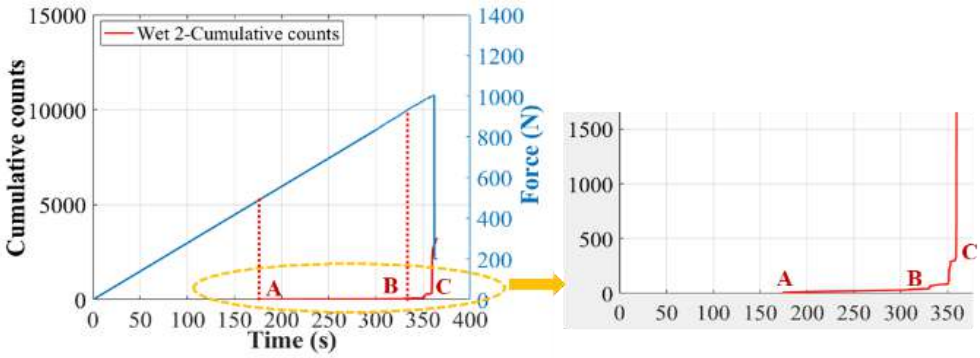

(b) 50% MC specimen Wet 2.

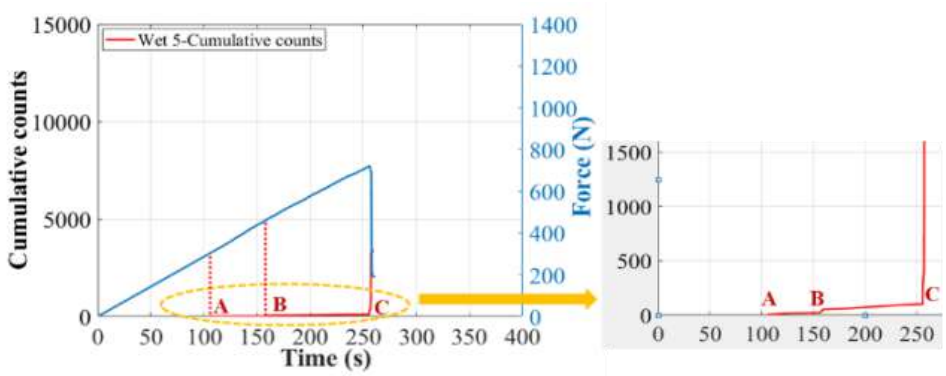

(c) 120% MC specimen Wet 5.

Fig. 3-18. Cumulative counts of Cluster I vs. time of dry and wet GFRP-balsa sandwiches.

3.2.5.5. Classification of skin damages in the second clustering process

After identifying Cluster 0 corresponding to balsa core damages, the second clustering process was done on Cluster I [94-95], in order to further classify skin/core debonding and different skin damages. Fig. 3-19 exposes that cluster number of four is the optimum choice because it has lowest DB. R_{DB}(DB) [108, 113] is an average measure of the ratio of within-class distances to the distances between classes, but Tou [113] is a ratio of the minimum distance between any pair of classes to the maximum of the average within-class distances, not considering the average ratio. So, DB is often used as the first criterion to determine the optimum cluster number, while Tou is used as the complement criterion. In this work, when DB is lowest, Tou is much higher than those when cluster number is larger than four. Tou values show the better agreement with DB for wet sandwiches, which means that more obvious damage difference of different damage modes (clusters) exist in wet sandwiches.

Finally, the four clusters decomposed from Cluster I will be named as Cluster 1, 2, 3 and 4 and discussed in the following discussions.

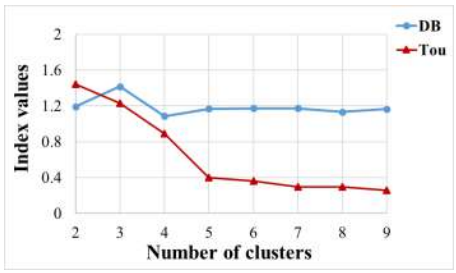

(a) Specimen Dry 1.

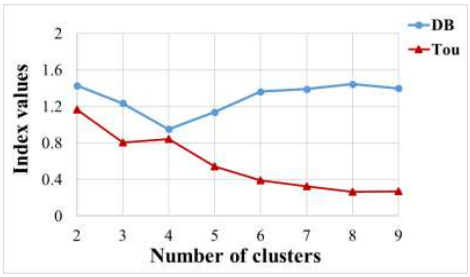

(b) 50% MC specimen Wet 2.

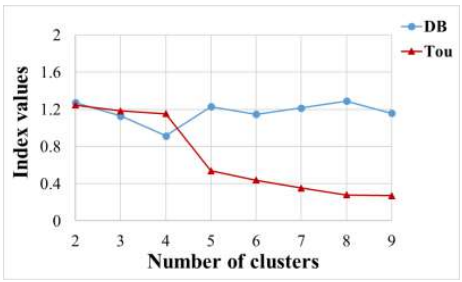

(c) 120% MC specimen Wet 5.

Fig. 3-19. DB and Tou coefficients of GFRP-balsa sandwiches in the second clustering process.

3.2.5.5.1 Damage classification based on amplitude distributions

Generally, AE amplitude [116-121] is the first important parameter to help identify the damage mechanisms of the composite structures. The AE amplitude distributions of Cluster 1-4 are compared to Force/time curves in Fig. 3-20, based on the second clustering process. As identified by cumulative counts in Fig. 3-17, points A, B and C are also marked in Fig. 3-20. It can be noted that Cluster 1 and Cluster 4, lower than 50 dB, are the predominant during the stage AB. Although several signals of Cluster 2 also appear during stage AB, the signals of Cluster 2 are accumulated mainly after point B. Cluster 3 mainly appears at point C. The highest amplitude of Cluster 3 is above 90 dB, so it should correspond to the final fiber breakage which only appears at point C. Cluster 2, which appears just before fiber breakage with the intermediate amplitude range of 40-80 dB, should be GFRP skin delamination [114].

Then, the existing problem is to distinguish the damage mechanisms of Cluster 1 and Cluster 4 which have similar amplitude range and continue to be accumulated in stage BC. Considering the hits number of these specimens, Cluster 4 should be skin/core debonding which is more severe in Wet 3. But it needs further validation from other AE parameters to identify them. In addition, matrix cracking and fiber/matrix debonding should be included in Cluster 1 which has lowest amplitude and appears much earlier. Combined with the curves of cumulative counts in Fig. 3-17, it verifies that point A should be the onset of matrix cracking (in Cluster 1), point B and C should be the important

indicators of irreversible damages including fiber/matrix debonding (in Cluster 1), delamination (Cluster 2) and fiber breakage (Cluster 3).

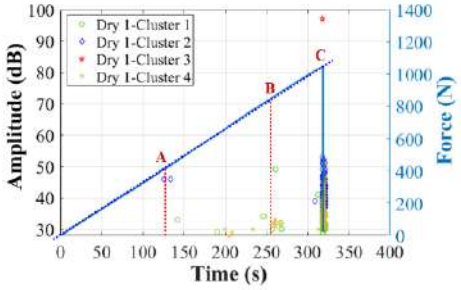

(a) Specimen Dry 1.

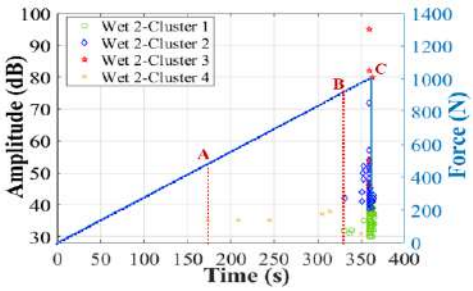

(b) 50% MC specimen Wet 2.

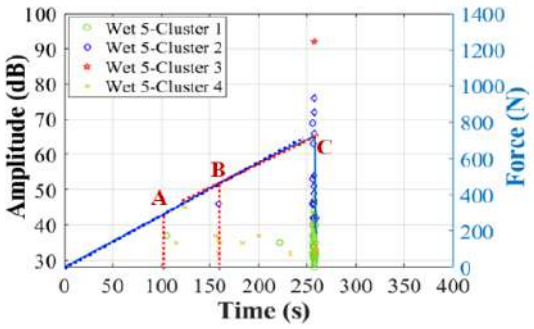

(c) 120% MC specimen Wet 5.

Fig. 3-20. AE amplitude distributions of dry and wet GFRP-balsa sandwiches.

3.2.5.5.2 Damage classification based on peak frequency distributions

As introduced in the identification of balsa core damages, peak frequency is a very important parameter to help classify different damage modes. Fig. 3-21 compares peak frequency distributions of Cluster 1-4 of dry and wet sandwich specimens. Firstly, it is obvious that most of the signals in Cluster 1, 2 and 3 have the frequency range lower than 200 kHz, while Cluster 4 has more signals higher than 200 kHz, and signals of Cluster 4 increase greatly mainly after point B. In addition, the hits number of Cluster 4 in the wet sandwiches is fewer than that of the dry sandwich. Combined with microscope observations, one of the main damage differences between dry and wet sandwiches is the more obvious skin/core debonding in the dry sandwich and the more severe delamination in the wet sandwiches. In reference [121], it has been found that skin/core debonding of GFRP-honeycomb sandwich is within 70-250 kHz under monitoring of wideband sensors in 3-point bending tests. Although the loading condition and material are not totally same as ours, it indicates that Cluster 4 does correspond to skin/core debonding.

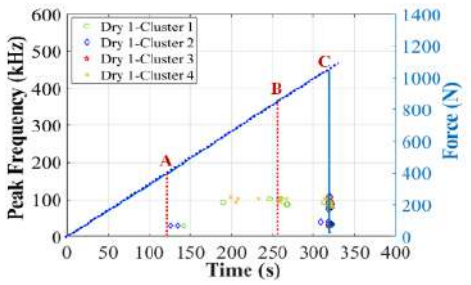

(a) Specimen Dry 1.

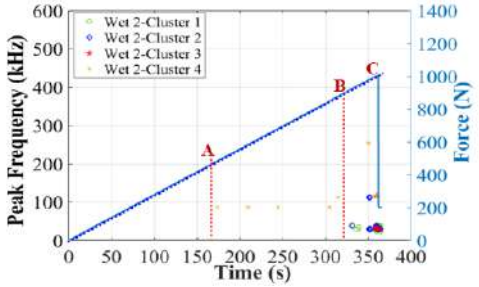

(b) 50% MC specimen Wet 2.

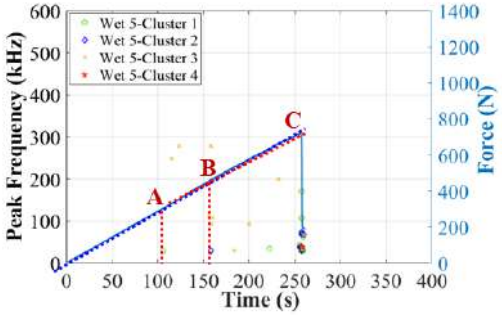

(c) 120% MC specimen Wet 5.

Fig. 3-21. AE peak frequency distributions of dry and wet GFRP-balsa sandwiches.

3.2.5.5.3 Correlations between different AE parameters

Similar to the analysis of Cluster 0 corresponding to the core shear damages, in Fig. 3-22 and Fig. 3-23, correlations between amplitude, duration and peak frequency from Cluster 1-4 of dry and wet sandwiches have been further illustrated. In Fig. 3-22, it can be seen very clearly that all the specimens show the similar distributions. Cluster 3 has the highest amplitude and lowest peak frequency. Cluster 2 has the low peak frequency within 40-80 dB. Cluster 1 also has low peak frequency, lower than 50 dB. Cluster 4 has the low amplitude and higher peak frequency than Clusters 1-3. It indicates that Cluster 4 shall come from the very different damage modes from Cluster 1-3, that is, skin/core debonding.

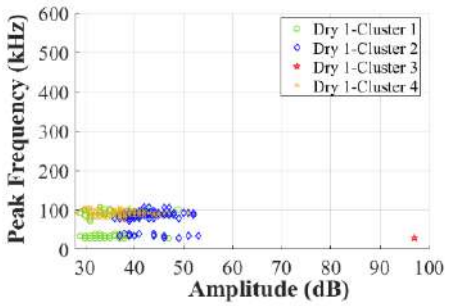

(a) Specimen Dry 1.

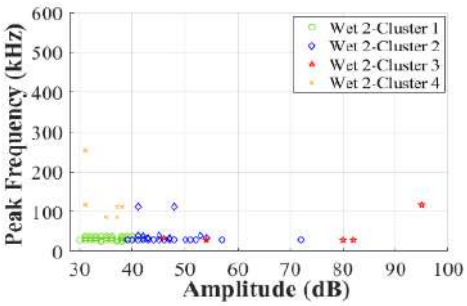

(b) 50% MC specimen Wet 2.

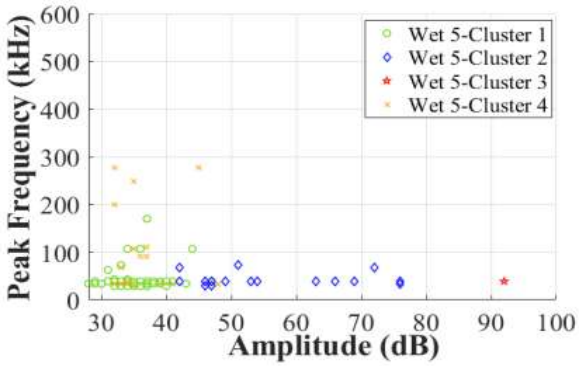

(c) 120% MC specimen Wet 5.

Fig. 3-22. Peak frequency vs. Amplitude of dry and wet GFRP-balsa sandwiches.

Fig. 3-23 shows clearly that Cluster 1-3 have the longer duration than Cluster 4, and Cluster 4 has the shortest duration less than 500 μs. Considering that the duration of balsa core damages (Cluster 0) is less than 400 μs, it indicates that the skin/core debonding and core shear damages due to shear stresses have the shorter duration than the skin damages. The physical reason of this phenomenon shall be further studied in the future.

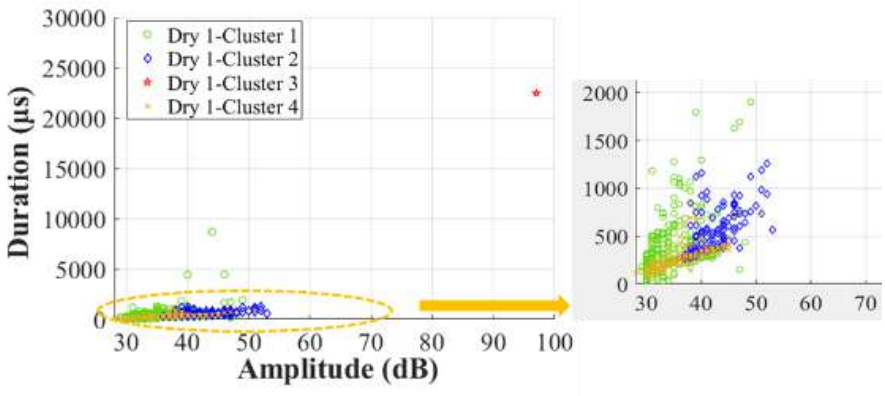

(a) Specimen Dry 1.

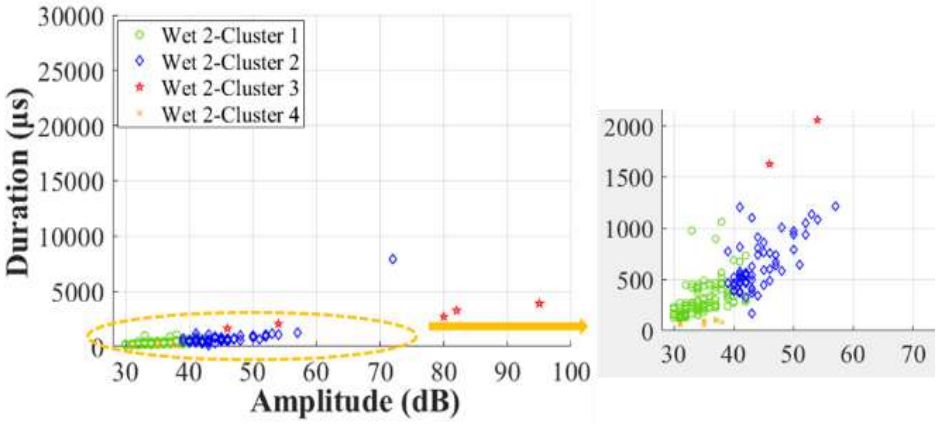

(b) 50% MC specimen Wet 2.

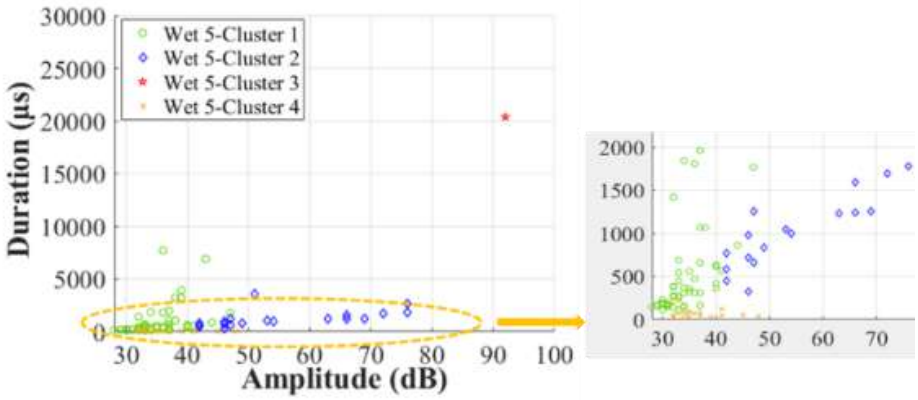

(c) 120% MC specimen Wet 5.

Fig. 3-23. Duration vs. Amplitude of dry and wet GFRP-balsa sandwiches.

In conclusion, it demonstrates again that duration and peak frequency can be very important to distinguish skin/core debonding (Cluster 4) which shows higher peak frequency within 80-400 kHz and shorter duration less than 500 μs, from skin damages including fiber breakage (Cluster 3), skin delamination (Cluster 2), fiber/matrix debonding and matrix cracking (Cluster 1).

3.2.5.6. Conclusions

Based on the above analysis from cumulative counts, clustering results coupling amplitude, duration and peak frequency distributions, compared with microscope observations, some conclusions could be made in Table 3-5. However, it shall be noticed that these characteristics could be affected by the sensor types, loading condition and laminate stacking sequence and so on.

Table 3-5. AE characteristics of dry GFRP-balsa sandwiches under 4-point bending.

	Cluster 0	**Cluster 1**	**Cluster 2**	**Cluster 3**	**Cluster 4**
AE parameters	**Microscopic balsa core cracks & Interfacial debonding**	**Matrix cracking & Fiber/matrix debonding**	**Skin delamination**	**Fiber breakage**	**Skin/core debonding**
Amplitude (dB)	<60	<50	40-80	>80	<50
Duration (μs)	<400	<5000	<2000	2000-25000	<500
Peak Frequency (kHz)	20-800	20-200	20-200	20-200	80-400

Table 3-6 compares the dominance of Clusters 1-4 with Cluster 0 from balsa core damages based on cumulative hits number. It is obvious that more hits have been captured by Dry 1. But Cluster 0 of Wet 5 receive much more signals corresponding to microscopic balsa core damages due to higher moisture content absorption. When the MC increases to 50% and 120%, the fractions of cumulative

hits of Wet 2 and Wet 5 have decreased by 90% and 915%. It means that more microscopic balsa core cracks appear in wet GFRP-balsa sandwich specimens. It needs further investigation about the classification of balsa damage mechanisms in the future work.

Among Cluster 1-4, the fraction of Cluster 4 of Dry 1 are higher than that of wet sandwiches, combined with microscope observations, it verifies that Cluster 4 should be skin/core debonding which is less severe in wet GFRP-balsa sandwich [84]. While Cluster 1 is more important for Wet 2 and Wet 5 among all the skin damages including Cluster 1, 2 and 3, which verifies that moisture absorption has mainly degraded the fiber/matrix interface strength (see Fig. 1-17) [78].

Table 3-6. Dominance of different damage mechanisms of GFRP-balsa sandwiches under 4-point bending.

Specimen	Total	Cluster 0 Microscopic balsa core cracks & Interfacial debonding	Cluster 1 Matrix cracking & Fiber/matrix debonding	Cluster 2 Skin delamination	Cluster 3 Fiber breakage	Cluster 4 Skin/core debonding
Dry 1	%:100	4.1	42.9	20.8	0.2	32.0
	Hits:515	21	221	107	1	165
Wet 2 (50% MC)	%:100	7.8	54.4	31.1	2.6	4.1
	Hits:193	15	105	60	5	8
Wet 5 (120% MC)	%:100	41.6	33.8	12.3	0.6	11.7
	Hits:154	64	52	19	1	18

3.2.6. Experimental conclusions

In conclusion, by microscope observations, IRT and AE observations, comparing dry, 50% MC and 120% MC specimens, it can be seen that moisture absorption can result in the decrease of intralaminar strength of fiber/matrix interface and interlaminar toughness of laminate skin, but the increase of skin/core interfacial fracture toughness. Consequently, moisture absorption can accelerate balsa core damages, matrix cracking, fiber/matrix debonding and skin delamination, but slow down skin/core debonding of GFRP-balsa sandwich under 4-point bending. These observations will be considered in numerical models.

3.3. Numerical analysis of 4-point bending behaviors

3.3.1. Abaqus model establishment

In this part, the bending tests on GFRP-sandwich structure were simulated by implicit analysis in Abaqus/Standard 2019 to investigate their bending behaviors. FEA model of composite sandwich is

effective only when the following conditions are set properly: the structure geometry, loading and boundary conditions, interaction contact between different components, material properties, as well as the mesh refinement. The geometry and loading condition are shown in Fig. 3-24. (a). Considering that the average failure displacement of dry sandwich in the tests was a little smaller than 12 mm, the max vertical displacement of 12 mm, which determines the end moment of the simulation, was applied to all the dry and wet models to ensure the fracture displacement can be reached. The two lower supports are fixed to eliminate all freedom. For the interaction between skins and loading/support surfaces, surface-to-surface contact was chosen to ensure the convergence of the models, and the friction coefficient is given by 0.15 [41] to allow enough slippage between the surfaces. Based on damage observations described above, upper skin damages are predominant, so skin-core interfaces are tied in the model without considering skin-core debonding.

Based on the classical laminate theory, 3-layer GFRP skins are modelled by continuous thin shell element S4R (without thickness definition), while the thicker balsa core is created by solid element C3D8R for meshing (see Fig. 3-24. (b)). In the models, the longitudinal fiber direction of balsa wood is along the thickness direction Z. As demonstrated in [171], elastic modulus and strength of balsa wood are considered constant in Radial-Transverse (R-T) plane, and elastic modulus in this plane is much lower than that in the Longitudinal-Radial (L-R) and Longitudinal-Transverse (L-T) planes (see Table 2-2).

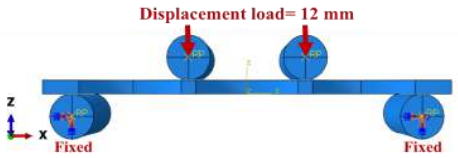

(a) Loading and boundary conditions.

(b) Thin shell elements S4R of GFRP skin.

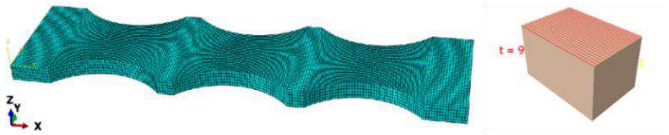

(c) Thick solid elements C3D8R of balsa core.

Fig. 3-24. Abaqus model of GFRP-balsa sandwich under 4-point bending.

As well known, the mesh density in FEA models will highly affect the calculation convergence and accuracy. The smaller mesh size means more accurate results, but the computing time gets significant as well. Stress singularities may also appear in the model where the stress increases permanently as the mesh size decreases, which may result in the bigger computation error [164]. Therefore, a balance between computing time and accuracy shall be found by using mesh cells which are small enough. Dependency of calculation accuracy on the mesh size was studied by using different cell size of 3 mm, 2.5 mm, 2 mm and 1.5 mm for both skin and core elements. It was found that the much bigger mesh size of 3 mm and smaller size of 1.5 mm will cause the non-convergence problem. To compromise between computational efficiency and accuracy, the mesh element is finally chosen as 2 mm for the thin skins in X-Y plane and core cells both in X-Y plane and thickness direction Z.

Finally, the remaining problem is to determine correct material parameters of sandwich constituents. Sadler R L et al. [55] and Gerhards C C [80] have proven that moisture had the greatest effect on compressive properties along fiber direction of wood, but less effect in Radial-Transverse plane. It means that moisture could not affect greatly the core compressive properties in R-T (X-Y) plane under 4-point bending. Actually, when we tried to reduce the elastic modulus of balsa core in Table 2-2, it has been found that it almost has no influence on the final simulation result of the bending behavior of the sandwich. Therefore, one hypothesis adopted here is that material properties of the core will not be changed when simulating bending behavior of wet sandwich.

It has been demonstrated that water molecules could penetrate into composite laminates by both physical diffusion and chemical decomposition, and then result in both reversible and irreversible hygroscopic damages [69]. Moisture diffusion is the dominate reason, mainly inducing irreversible fiber/matrix interface debonding by capillarity mechanism and reversible matrix plasticization. Because most of the wet and dry balsa cores show very little damage during bending tests, only Wet 3 has obvious core shear damages, in this work, the simulation of wet sandwich is firstly discussed by only modifying elastic modulus of GFRP skins (see Table 2-8) using the proposed stiffness prediction method presented in Chapter 2.

3.3.2. Progressive Damage Analysis (PDA) model

As introduced in Chapter 1, PDA model, which combines Hashin damage initiation criterion and damage evolution law based on fracture energy [172-175], can be used to predict fiber/matrix tension, compression and shear damages of thin laminates. This model is based on the bilinear traction-separation law as shown in Fig. 1-35. The damage onset is determined by Hashin damage initiation criterion which considers four different damage initiation mechanisms, including fiber tension (ft), fiber compression (fc), matrix tension (mt) and matrix compression (mc). In this work, fiber

compression criterion is firstly considered because the upper skin is damaged due to compressive stresses in the 4-point bending tests.

Fiber compression ($\sigma_{11} < 0$) is controlled by the longitudinal compressive strength of the lamina, as Eq. (3-6) shows:

$$F_f^c = \left(\frac{\sigma_{11}}{F_{1c}}\right)^2 \tag{3-6}$$

Where σ_{11} is (longitudinal) normal stress in specimen length direction; F_{1c} is longitudinal compressive strength in fiber direction. F_f^c is the damage index. Damage initiates when it attains 1.

Once any of the damage initiation criterion is satisfied, the material stiffness continues to degrade. The damage evolution can be characterized by the critical fracture energy release rate values G_{fc}^c, corresponding to fiber compression damage, based on the traction-separation law.

In Abaqus, besides the strength parameters, the fracture energy release rate G_i^c (i=fc, ft, mc and mt, where f: fiber; m: matrix; t: traction; c: compression) shall be also introduced correctly to evaluate the damage initiation and evolution process of composite laminates. But it is not clear whether PDA model is also effective for the more complex sandwich structure, and few literatures about this field could be found. In addition, it is very difficult to determine the precise G_i^c, because the physical sense of these parameters is not clear, in the meantime, the anisotropy of composites and the difficulty in classifying the four skin damage modes make it more complicated. Actually, for the polymer reinforced by unidirectional glass or carbon fibers, most engineers and researchers just assume the values [172, 173, 175, 176]. Barbero E J et al. [172] have discussed the influences of $1.5\ \mathrm{N/mm} < G_{mt}^c < 30.5\ \mathrm{N/mm}$ on simulation of longitudinal tensile damages in the $[0^\circ_2/90^\circ_4]_s$ laminates, proving that $G_{mt}^c = 12\ \mathrm{N/mm}$ was the best choice with smallest error. Lapczyk I and Hurtado J A [175] assumed that $G_{ft}^c = G_{fc}^c = 12.5\ \mathrm{N/mm}$ and $G_{mt}^c = G_{mc}^c = 1\ \mathrm{N/mm}$ for glass fiber reinforced epoxy.

In this work, woven glass fiber-reinforced epoxy laminates were used, the fracture energy release rate in longitudinal direction should be the same as the transverse one, so the experiences in unidirectional fibers shall be reconsidered. Influences of G_i^c on the prediction of fracture load and damage evolution process of GFRP-balsa sandwich will be discussed next by adjusting G_i^c in different groups between 1 N/mm and 36 N/mm.

3.3.3. Prediction of 4-point bending behaviors by PDA model

3.3.3.1. Influence of elastic modulus of the skin on bending stiffness

As mentioned above, the variation of elastic constants of the composite skins as a function of MC (see Table 2-8) has been considered in the simulation of 4-point bending tests. The numerical force/displacement curves obtained are compared to experimental results in Fig. 3-25. In fact, bending stiffness obtained by simulation is only affected by the input elastic constants, not affected by strengths and fracture energies in the material models [210], so only one (with smallest error) of the numerical groups corresponding to dry, 50% MC specimen and 120% MC specimen are compared to the average experimental Force/Displacement curves in Fig. 3-25. The influence of strengths and fracture energies on the final damage initiation and evolution prediction will be discussed in the next part.

Fig. 3-25 shows that Force/Displacement curves predicted by numerical models have the similar linear behaviors up to failure for both dry and wet specimens. It is interesting to note that numerical bending stiffnesses of 50% MC (91 N/mm) and 120% MC (85 N/mm) wet specimens decrease by 13% and 19% of that of dry one (105 N/mm). Compared to the average experimental bending stiffnesses, the simulations give the relative errors of 1.0%, 8.3% and 3.4% for dry, 50% MC and 120% MC wet specimens, respectively. Recalling that the decrease of bending stiffness in 50% MC and 120% MC wet sandwich measured experimentally is about 19% and 15%, the reduction of the skin modulus of wet sandwich predicted by Eq. (2-18b) used in the numerical simulations, gives a good concordance with the experimental measurements. Thus, the proposed methodology described in Chapter 2 should be practical and valuable to predict the variation of elastic constants of wet sandwich skin by measuring AE wave velocity.

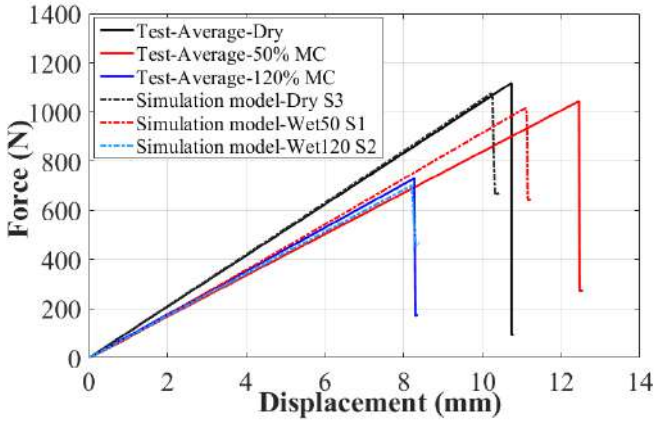

Fig. 3-25. Comparison of bending stiffness of simulation and test results of GFRP-balsa sandwich.

3.3.3.2. Influence of fracture energy of the skin on fracture load

For GFRP-balsa sandwich structure under 4-point bending, the final upper skin damages are controlled mainly by compressive strength [211]. So, the accuracy of this material parameter is critical for determining correctly the damage initiation by Abaqus model. Strengths of woven E glass

epoxy composites are chosen as the average values in literatures [212-213], as Table 3-7 shows. Moisture effects on strengths of 50% MC and 120% MC wet sandwiches [205] have been considered by decreasing all the parameters of dry sandwich by 7% and 35%, based on 4-point bending test results in Fig. 3-2.

Table 3-7. Strength values of dry and wet woven GFRP skin [212-213].

Group	Longitudinal tensile strength (MPa)	Longitudinal compressive strength (MPa)	Transverse tensile strength (MPa)	Transverse compressive strength (MPa)	In-plane shear strength (MPa)
Dry	400	260	400	260	55
50% MC	372	242	242	242	51
120% MC	260	169	260	169	36

For a sandwich structure under bending loading, the compressive strength, compressive fracture energy values are the determined parameters for damage evolution prediction of the upper skin. Normally, tensile fracture energy shall be a little higher than compressive energy [211], but tensile energy almost has little influence on the final damage evolution in our cases. In this work, considering assumptions in [172, 175] and the same characteristics in longitudinal and transverse directions of woven GFRP laminates, tensile and compressive energies are assumed the same, so $G_{ft}^{c} = G_{fc}^{c} = G_{mt}^{c} = G_{mc}^{c}$. In fact, we have found that when the compressive fracture energy is constant, the influence of the variation of tensile fracture energy is small enough to be negligible.

Table 3-8. Fracture energy values of PDA models of dry and wet woven GFRP skin in Abaqus.

Groups		Compressive strength (MPa)	Longitudinal tensile fracture energy (N/mm)	Longitudinal compressive fracture energy (N/mm)	Transverse tensile fracture energy (N/mm)	Transverse compressive fracture energy (N/mm)
Dry	Dry S1	260	36	36	36	36
	Dry S2		24	24	24	24
	Dry S3		12	12	12	12
	Dry S4		1	1	1	1
50% MC	W50 S1	234	12	12	12	12
	W50 S2		10.8	10.8	10.8	10.8
	W50 S3		6	6	6	6
120% MC	W120 S1	169	12	12	12	12
	W120 S2		9.6	9.6	9.6	9.6
	W120 S3		6	6	6	6

In Table 3-8, Groups Dry S1, S2, S3 and S4 denote the simulation models using different fracture energy values by 36, 24, 12 and 1 N/mm, respectively, while W50 S1, S2 and S3 stand for the

simulation models using 12, 10.8 (90% of 12) and 6 N/mm (50% of 12) for 50% MC wet sandwich, W120 S4, S5 and S6 for the simulation models using 12, 9.6 (80% of 12) and 6 N/mm (50% of 12) for 120% MC wet sandwich, respectively.

The bending behaviors predicted by numerical models are compared with the average experimental curve in Fig. 3-26. For the dry sandwich (see Fig. 3-26. (a)), the fracture load increases with the fracture energy imposed. The difference between the models Dry S1 (1228 N), Dry S2 (1178 N), Dry S3 (1078 N), Dry S1 (1022 N) and the average experimental fracture load (1118 N), is 9.8%, 5.4% higher, 3.6% and 8.6% lower, respectively. In the range of the variation of the fracture energy rate from 36 to 1 (N/mm), the maximum relative error of fracture load between the simulation and the experiment is about 10%. The Force/Displacement curves of Dry S3 which assumes the fracture energy rate G^c=12 N/mm give the fracture load and fracture displacement nearer to the average experimental one.

Fig. 3-26. (b) compares the simulation results of three models with the average experimental curve of 50% MC wet specimens. It can be seen that the fracture load obtained by the model W50 S1 (1015 N), W50 S2 (992 N), W50 S3 (907 N) is 2.8%, 5.0% and 13.1% lower than that of experimental one (1044 N), respectively. Fig. 3-26. (c) compares the simulation results of three models with the average experimental curve for 120% MC wet specimens. It can be seen that the fracture load obtained by the model W120 S1 (761 N), W120 S2 (701 N), W120 S3 (673 N) is 4.2%, 4.0% and 7.8% lower than that of experimental one (730 N), respectively. It is obvious that the accuracy of fracture load prediction of all these three models can be accepted, but the models W50 S1 (G^c=12 N/mm) and W120 S2 (G^c=9.6 N/mm) give the fracture displacements closest to the average experimental values. Herein, it indicates that it is better to consider the reduction of the fracture energy due to the moisture effects to improve the fracture displacement prediction by PDA model, as the moisture content increases.

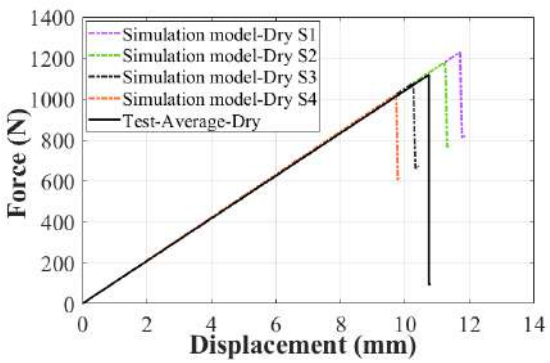

(a) Dry sandwich.

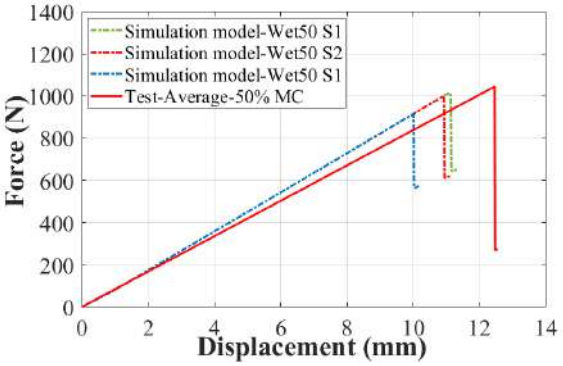

(b) 50% MC wet sandwich.

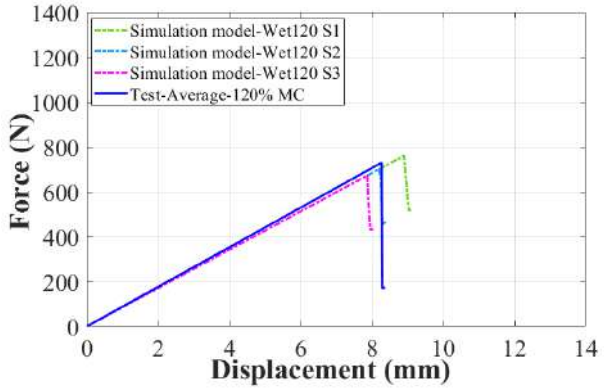

(b) 120% MC wet sandwich.

Fig. 3-26. Numerical Force/Displacement curves and experimental curves of GFRP-balsa sandwich under 4-point bending.

In a conclusion, for dry GFRP-balsa sandwich, the fracture load prediction using fracture energy rate within 1 N/mm-36 N/mm could be acceptable with almost less than 10% relative error. Considering both fracture load and displacement, evaluated by combining the elastic modulus and strength reduction, the reasonable fracture energy rate of wet sandwich can be estimated approximately as following:

$$G_i^c(\,\mathrm{MC}) = (1 - \mathrm{MC}/6) \cdot G_i^c(\,\mathrm{dry}) \tag{3-7}$$

Thus, for the wet GFRP/balsa sandwich, if $G_i^c(\,\mathrm{dry}) = 12\ \mathrm{N/mm}$, $G_i^c(\,50\%\ \mathrm{MC}) \approx 11\ \mathrm{N/mm}$ and $G_i^c(\,120\%\ \mathrm{MC}) \approx 9.6\ \mathrm{N/mm}$. These conclusions need to be validated with more experimental and numerical results, but they lay crucial foundations for the future simulation study on woven glass fiber laminates and composite sandwich structures with variable MC.

3.3.3.3. Damage evolution prediction by PDA model

In this part, only the results from model Dry S3, W50 S1 and W120 S2 will be discussed. Their damage initiation and evolution images are shown in Fig. 3-27 - Fig. 3-29, respectively. In Fig. 3-27. (a) - Fig. 3-29. (a), only the GFRP skin is displayed since the damage initiation predicted is in the center of zone 1. Herein, the damage indexes in term of (DAMAGEFC) represent compression mechanism, and damage initiates when DAMAGEFC exceeds 0, full damage of the elements occurs only when DAMAGEFC equals 1 (red color). It is clear that the most full damaged areas (red mesh cells) are located at the center of upper skin where there are the highest longitudinal compressive stresses. Around the maximum red damaged area in the center (DAMAGEFC=1), the stress concentration appears with DAMAGEFC=0.3-0.6, it should be caused by the redistribution of the stresses due to full damage of the elements at the center of the specimen.

Fig. 3-27. (b)-(d) - Fig. 3-29. (b)-(d) show the damage evolution of dry and wet sandwich with the increase of applying displacement (Dis.) or force (F). Fig. 3-27. (b) - Fig. 3-29. (b) show the skin damages at the failure load. Fig. 3-27. (c) - Fig. 3-29. (c) correspond to the time when each crack has propagated about 1/4 of the specimen width. Fig. 3-27. (d) and Fig. 3-29. (d) show the final complete fracture of the whole specimen width. In both dry and wet sandwiches, the damage propagates always from the edges to the center in the width direction as the displacement increases up to final failure.

In fact, the propagation of the damage is very rapid. From the damage at maximum load to final fracture, it can be evaluated by simulation that just about 1.5 seconds are required for a dry specimen, 1.8 seconds for a 50% MC wet one, and 2.1 seconds for a 120% MC wet one with the loading rate at 2 mm/min. So, the average crack propagation velocities of the dry, 50% MC and 120% MC specimens are 27 mm/s, 22 mm/s and 19 mm/s, respectively. Compared to 38.8 mm/s, 29.0 mm/s, and 26.3 mm/s of the dry, 50% MC and 120% MC specimens observed by the IRT camera, it means that skin cracks of dry sandwich propagate much faster than the wet one from damage onset point to the full fracture.

Moreover, according to the size of red area in the center of zone 1 (Fig. 3-27. (d) - Fig. 3-29. (d)), it can be concluded that damages of dry sandwich are more severe than those of wet one. These results can be confirmed by microscope observations in Fig. 3-6 and IRT images in Fig. 3-8- Fig. 3-10.

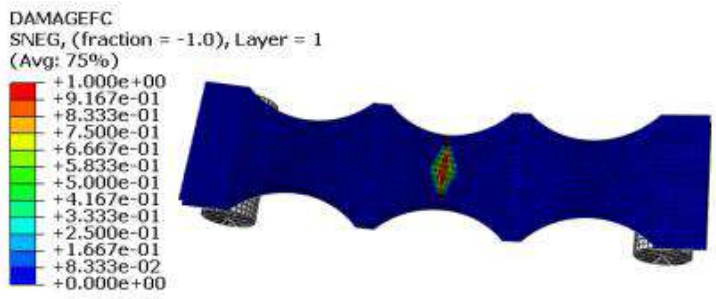

(a) Final damage localization by PDA model.

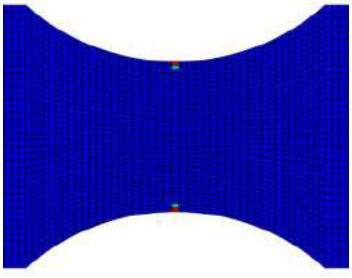

(b) Dis.=10.25 mm, F=1078 N.

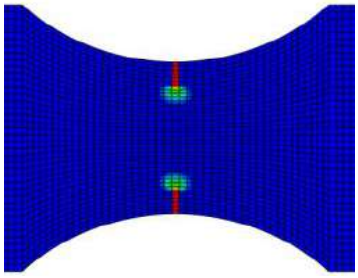

(c) Dis.=10.28 mm, F=987 N.

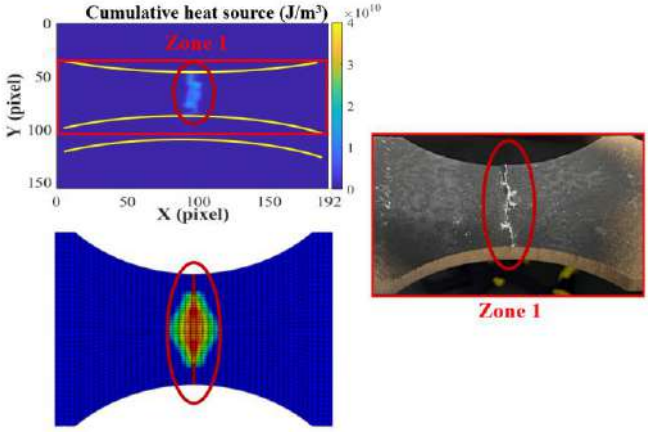

(d) Dis.=10.30 mm, F=726 N.

Fig. 3-27. Damage evolution prediction of dry sandwich by Abaqus simulation model Dry S2.

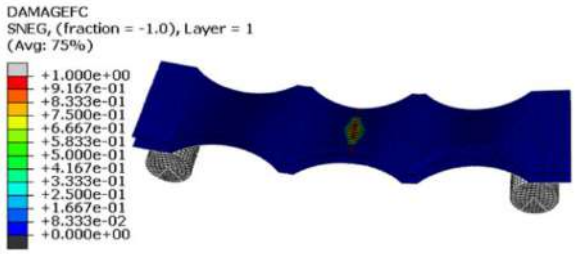

(a) The final damage localization by PDA model.

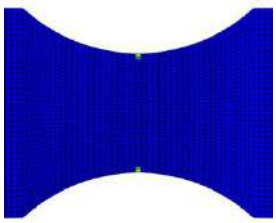

(b) Dis.=10.88 mm, F=996 N.

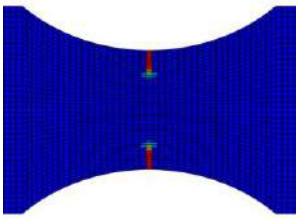

(c) Dis.=10.92 mm, F=954 N.

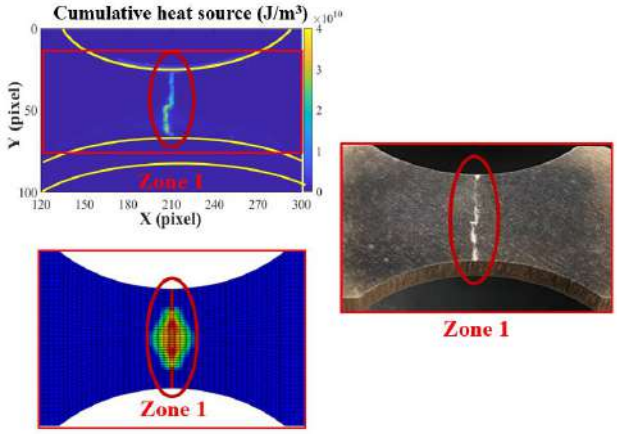

(d) Dis.=10.94 mm, F=734 N.

Fig. 3-28. Damage evolution prediction of 50% MC wet sandwich by Abaqus model W50 S2.

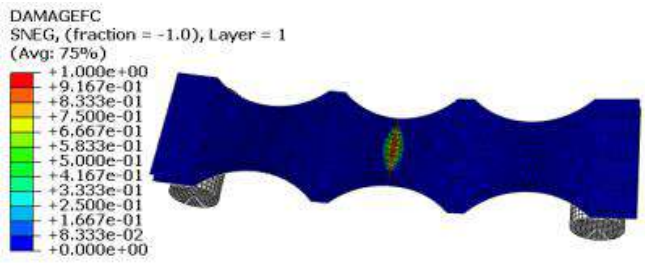

(a) The final damage localization by PDA model.

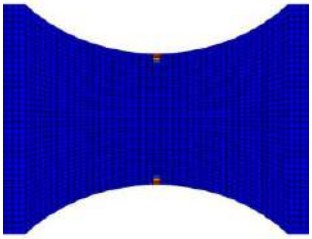

(b) Dis.=8.20 mm, F=701 N.

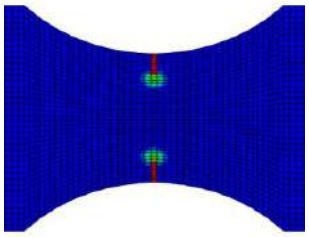

(c) Dis.=8.24 mm, F=678 N.

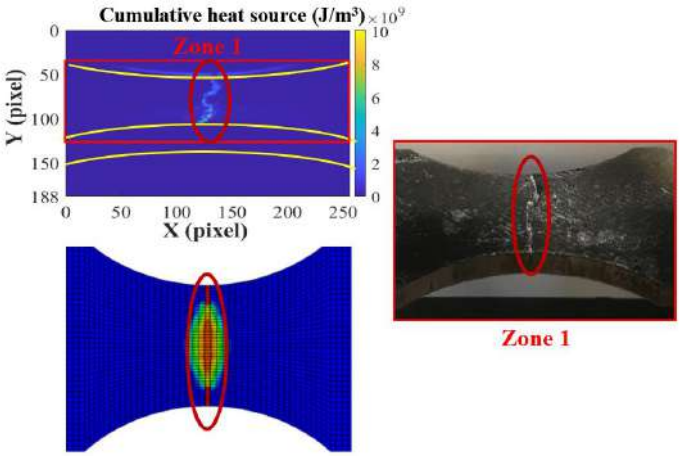

(d) Dis.=8.27 mm, F=635 N.

Fig. 3-29. Damage evolution prediction of 120% MC wet sandwich by Abaqus model W120 S2.

3.3.3.4. Stress distributions in numerical models

In order to explain the reasons of the upper skin damages, the stress distributions in zone 1 and zone 2 of dry and wet sandwiches corresponding to the moment of damage initiation and evolution are further discussed. Fig. 3-30. (a) - Fig. 3-32. (a) correspond to the moment when the skin damage initiation appears at the failure load. Fig. 3-30. (b) - Fig. 3-30. (b) correspond to the time when each crack has propagated about 1/4 of the specimen width. Fig. 3-30. (c) and Fig. 3-30. (c) show the final complete fracture of the whole specimen width.

Firstly, it is obvious that the normal stress S11 along the specimen length direction in zone 1 of the upper skin in compression (blue elements) shows the distribution agreeing well with the damage

evolution locations in Fig. 3-27-Fig. 3-29. The stresses in zone 2 are relatively small compared with those in zone 1, so the stress distribution in zone 1 is the predominant in the damage evolution process.

When the damage begins to initiate, S11 is max in the center of the two edges of the upper skin in zone 1, about 237 MPa for dry sandwich, 214 MPa for 50% MC wet sandwich, 154 MPa for 120% MC wet sandwich. S11 of 50% MC wet sandwich and 120% MC wet sandwich has decreased by 9.7% and 35%, respectively. The normal stress S22 along the specimen width direction in zone 1 is also maximum but very small in the center of zone 1, about 15 MPa for dry sandwich, 14 MPa for 50% MC wet sandwich, 9.7 MPa for 120% MC wet sandwich. The max shear stress S12 is also small, about 40 MPa for dry sandwich, 37 MPa for 50% MC wet sandwich, 22 MPa for 120% MC wet sandwich near the two edges of the upper skin in zone 1.

When the damage propagates about ¼ of the specimen width, S11 is max about ¼ of the specimen width in the center of zone 1, about 270 MPa for dry sandwich, 251 MPa for 50% MC wet sandwich, 177 MPa for 120% MC wet sandwich. S11 of 50% MC wet sandwich and 120% MC wet sandwich has decreased by 7.0% and 34.4%, respectively. S22 is also max in the center of zone 1, about 68 MPa for dry sandwich, 64 MPa for 50% MC wet sandwich, 32 MPa for 120% MC wet sandwich. The max S12 has increased to about 40 MPa for dry sandwich, 37 MPa for 50% MC wet sandwich, 22 MPa for 120% MC wet sandwich in center zone 1.

When it reaches the final complete fracture time, S11 is max in the center of zone 1, about 294 MPa for dry sandwich, 260 MPa for 50% MC wet sandwich, 181 MPa for 120% MC wet sandwich. S11 of 50% MC wet sandwich and 120% MC wet sandwich has decreased by 11.6% and 38.4%, respectively. S22 is also max in the center of zone 1, about 81 MPa for dry sandwich, 64 MPa for 50% MC wet sandwich, 27 MPa for 120% MC wet sandwich. The max S12 has increased to about 39 MPa for dry sandwich, 27 MPa for 50% MC wet sandwich, 21 MPa for 120% MC wet sandwich in center zone 1.

In conclusion, the final upper skin damage is dominated by the compressive stress S11 (blue elements) along the specimen length direction in zone 1. And S11 has decreased after the moisture absorption, which can cause the skin damages releasing lower energy, agreeing well with IRT observations.

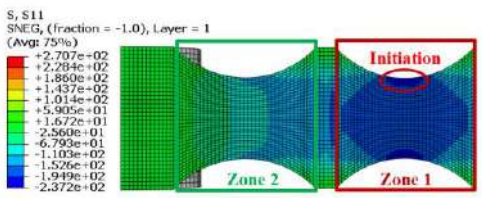

(I) Normal stress S11.

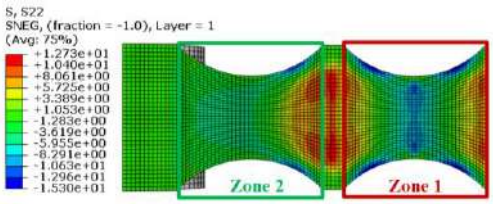

(II) Normal stress S22.

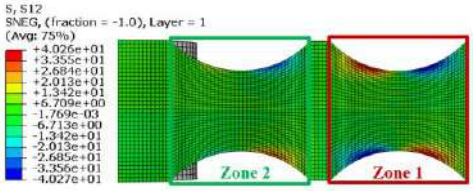

(III) Shear stress S12.

(a) Dis.=10.25 mm, F=1078 N.

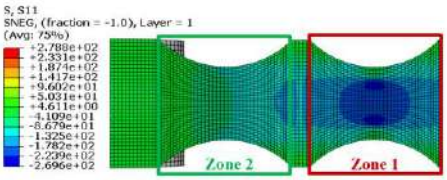

(I) Normal stress S11.

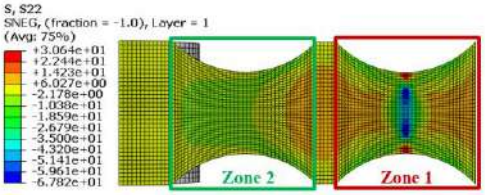

(II) Normal stress S22.

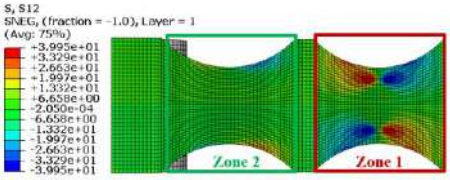

(III) Shear stress S12.

(b) Dis.=10.28 mm, F=987 N.

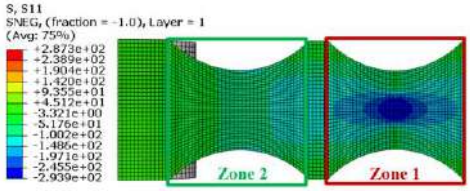

(I) Normal stress S11.

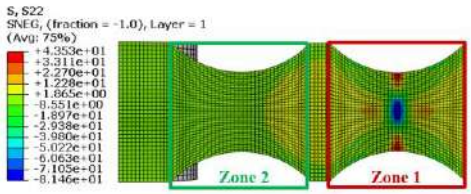

(II) Normal stress S22.

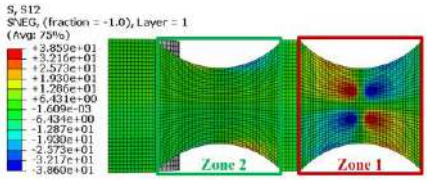

(III) Shear stress S12.

(c) Dis.=10.30 mm, F=726 N.

Fig. 3-30. Stress distributions of dry sandwich by Abaqus model Dry S2.

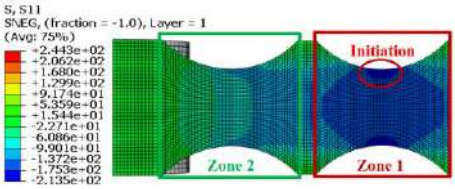

(I) Normal stress S11.

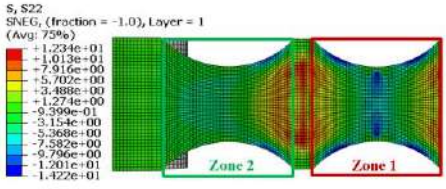

(II) Normal stress S22.

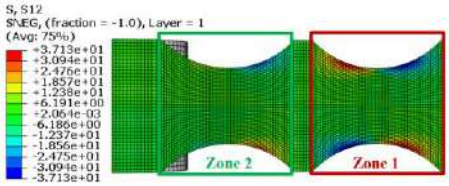

(III) Shear stress S12.

(a) Dis.=10.88 mm, F=996 N.

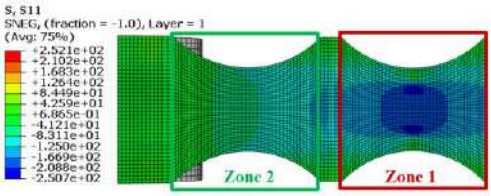

(I) Normal stress S11.

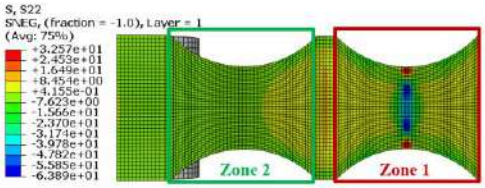

(II) Normal stress S22.

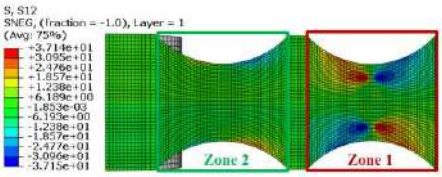

(III) Shear stress S12.

(b) Dis.=10.92 mm, F=954 N.

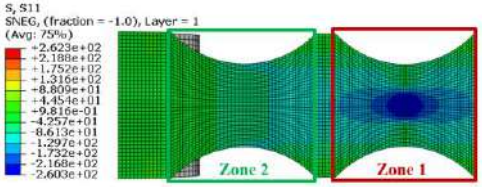

(I) Normal stress S11.

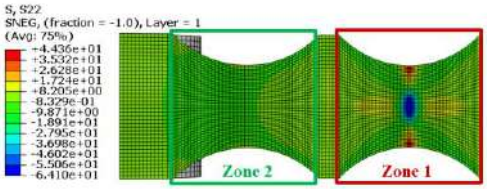

(II) Normal stress S22.

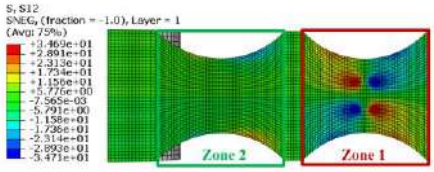

(III) Shear stress S12.

(c) Dis.=10.94 mm, F=734 N.

Fig. 3-31. Stress distributions of 50% MC wet sandwich by Abaqus model W50 S2.

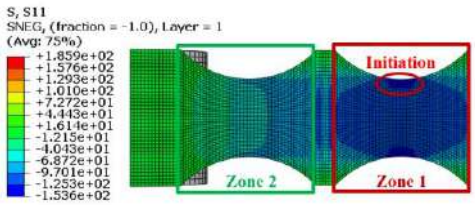

(I) Normal stress S11.

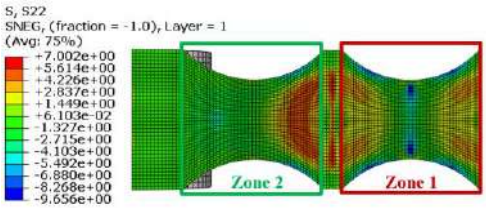

(II) Normal stress S22.

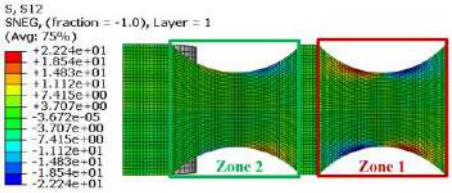

(III) Shear stress S12.

(a) Dis.=8.20 mm, F=701 N.

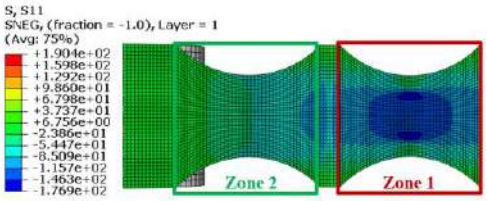

(I) Normal stress S11.

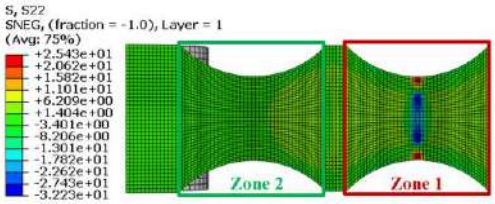

(II) Normal stress S22.

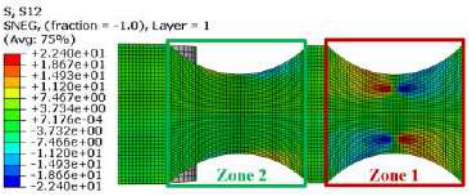

(III) Shear stress S12.

(b) Dis.=8.24 mm, F=678 N.

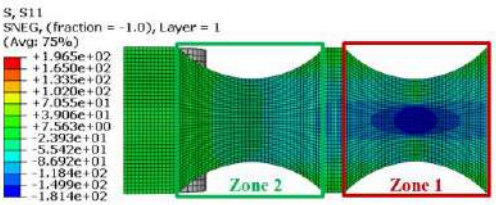

(I) Normal stress S11.

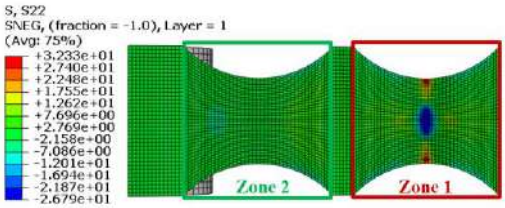

(II) Normal stress S22.

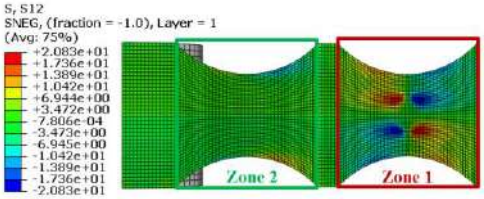

(III) Shear stress S12.

(c) Dis.=8.27 mm, F=635 N.

Fig. 3-32. Stress distributions of 120% MC wet sandwich by Abaqus model W120 S2.

In addition, Fig. 3-33 also shows the stress distributions of the lower skin of the dry and wet sandwich models at the final fracture moment of the upper compressive skin. It is obvious that S11 is max in the center of zone 1 of lower skin, about 322 MPa for dry sandwich, 262 MPa for 50% MC wet sandwich, 197 MPa for 120% MC wet sandwich. S11 of 50% MC wet sandwich and 120% MC wet

sandwich has decreased by 18.6% and 38.8%, respectively. S22 is also max near the center of zone 1, about 46 MPa for dry sandwich, 35 MPa for 50% MC wet sandwich, 22 MPa for 120% MC wet sandwich. The max S12 is about 42 MPa for dry sandwich, 35 MPa for 50% MC wet sandwich, 21 MPa for 120% MC wet sandwich in center zone 1 of lower skin.

In conclusion, it means that S11 in lower skin under tension stress is lower than the tensile strength of woven glass fiber, and thus the tensile lower skin is not damaged finally.

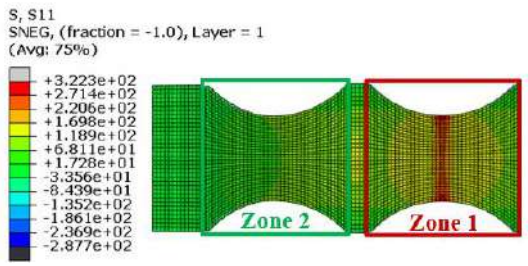

(I) Normal stress S11.

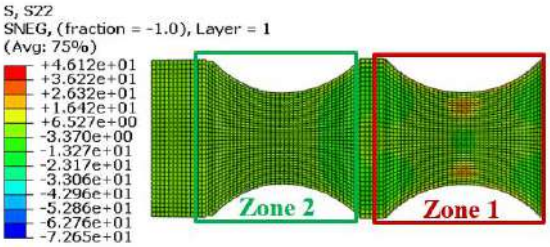

(II) Normal stress S22.

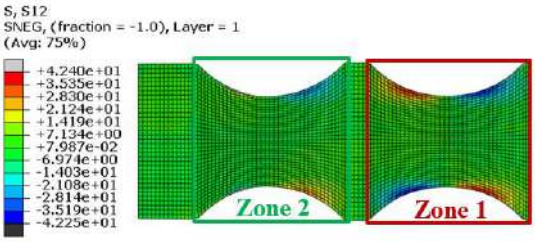

(III) Shear stress S12.

(a) Lower skin in Abaqus model Dry S2.

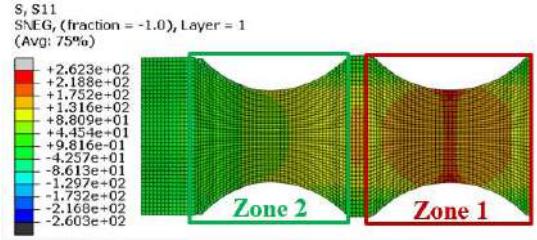

(I) Normal stress S11.

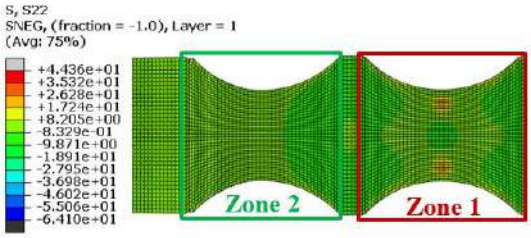

(II) Normal stress S22.

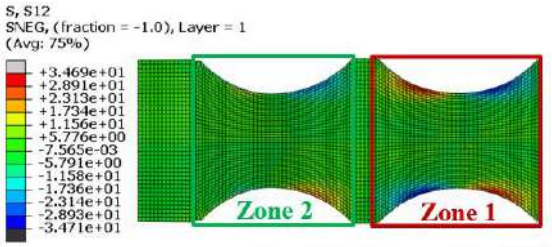

(III) Shear stress S12.

(b) Lower skin in Abaqus model W50 S2.

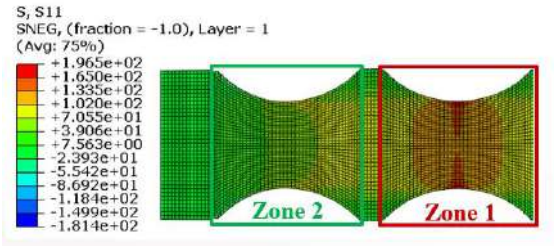

(I) Normal stress S11.

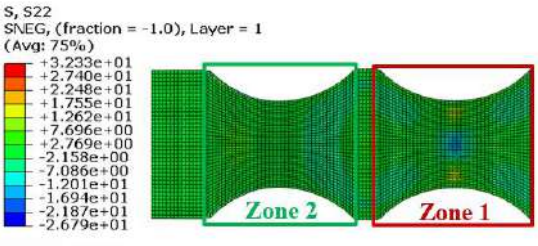

(II) Normal stress S22.

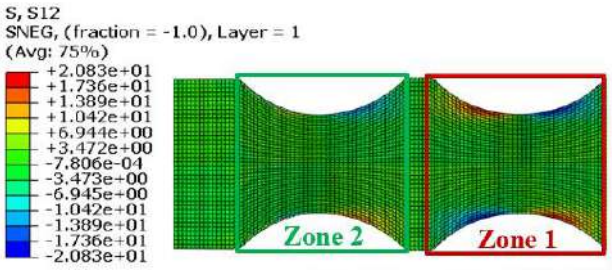

(III) Shear stress S12.

(c) Lower skin in Abaqus model W120 S2.

Fig. 3-33. Stress distributions of lower skins of dry and wet sandwich models at the final fracture moment.

3.3.4. Numerical conclusions

In summary, in order to predict the 4-point bending behaviors of GFRP-balsa sandwich, the PDA model proposed for laminates in Abaqus was firstly applied to the bonded sandwich structure to simulate the damage initiation and evolution process of the compressive upper skin, as well as the fracture load/displacement. Based on the proposed new methodology to evaluate elastic modulus variation due to moisture absorption by AE wave velocity in Chapter 2, moisture effects on elastic modulus, strength, and fracture energy of woven GFRP skin are introduced into PDA models to improve the prediction accuracy of wet sandwich. It has been found that longitudinal/transverse fracture energy of woven glass epoxy laminates should be within 1 N/mm -36 N/mm for better prediction of fracture load/displacement and damage evolution process. For wet sandwich, it's better to reduce the fracture energy of dry sandwich

In addition, damage localizations and propagation paths predicted by PDA model agree well with IRT observations, since IRT and PDA model have shown similarly that the upper skin of dry sandwich fully fractures much faster and releases higher energy in the center of zone 1. And the skin crack of dry sandwich is wider than that of wet sandwich specimen. But the future model considering delamination and skin/core debonding using Cohesive Zone Model shall be developed to simulate all the existing damage mechanisms according to the experimental observations, to improve the prediction accuracy.

3.4. Chapter summary

In summary, in this chapter, moisture effects on the bending stiffness/strength and damage mechanisms of GFRP-balsa sandwich under 4-point bending have been discussed experimentally and numerically, coupling the observations by the microscope, IRT and AE.

Firstly, by microscope observations, comparing dry, 50% MC and 120% MC specimens, it can be seen that moisture absorption can result in the decrease of intralaminar strength of fiber/matrix interface and interlaminar toughness of laminate skin, but the increase of skin/core interfacial fracture toughness. Consequently, moisture absorption could accelerate matrix cracking, fiber/matrix debonding and skin delamination, but slow down skin/core debonding of GFRP-balsa sandwich under 4-point bending.

By infrared thermography, it is verified that skin damages of wet sandwich have released lower energy and propagates more slowly. By AE, it is also demonstrated by cumulative energy that wet woven GFRP skin damages have released lower energy. In addition, cumulative counts have been proven to be very useful for the identification of the initiation of microscopic and macroscopic composite skin damages, showing three obvious transition points corresponding to the beginning of matrix cracking, fiber/matrix debonding and fiber breakage.

Most importantly, a comprehensive damage characterization approach coupling the characteristics of AE amplitude, peak frequency and duration via K-means clustering algorithm has been proposed, to classify damage modes of GFRP-balsa sandwich structures. When there are two obvious different damage mechanisms, such as skin damages and core damages, based on the physical damage mechanisms and statistical criteria, two steps are suggested to deal with the huge number of AE data:

Step 1- the first clustering process of the original filtered signals: based on statistical criteria, Davies & Bouldin (DB) and Tou coefficients, combined with real damage mechanisms, to identify balsa core damages which show higher peak frequency and shorter duration; Step 2- the second clustering process on Cluster I containing skin damages: to distinguish skin/core debonding from laminate skin damages mainly by peak frequency and duration distributions, and to classify different damage modes in composite skin.

Thus, it is concluded that the damage modes of GFRP-balsa sandwich under 4-point bending may occur at different levels including in balsa core: balsa/balsa interfacial debonding between balsa blocks, microcracking; at composite skin/core interface: skin/core debonding; in upper composite skin: matrix cracking, fiber/matrix debonding, delamination and fiber breakage. The last four skin damage mechanisms are the predominant.

Finally, PDA model verifies that the new proposed method in Chapter 2 can be effective for prediction of bending stiffness of wet sandwich by measuring AE wave velocity. For the damage localizations of GFRP-balsa sandwich, PDA model agree well with IRT observations.

However, future work shall be done to improve the damage localization accuracy by AE, considering the higher AE wave attenuation in wet sandwiches. For example, the distance between the two sensors can be decreased, and three or four sensors can be used to better localize the damages. Considering the numerical study, the further model considering skin delamination and skin/core debonding using Cohesive Zone Model shall be developed to simulate all the existing damage mechanisms according to the experimental observations, to improve the prediction accuracy.

Chapter 4. Static 4-point bending behaviors of CFRP-honeycomb sandwich

4.1. Introduction 169

4.2. Static 4-point bending tests monitored by AE and IRT 169

4.2.1. Experimental setup 169

4.2.2. Moisture effects on bending behaviors 170

4.2.2.1. Moisture effects on bending stiffness 172

4.2.2.2. Moisture effects on bending strength 172

4.2.3. Damage mechanisms observed by microscope 172

4.2.4. Damage localizations by IRT and AE 175

4.2.4.1. Core damages monitored by IRT 175

4.2.4.2. Coupling of damage localizations by IRT and AE 179

4.2.4.3. Validation of damage localizations by peak frequency and duration 184

4.2.5. Moisture effects on damage initiation identification by AE 188

4.2.5.1. Moisture effects on cumulative hits 189

4.2.5.2. Moisture effects on cumulative energy 189

4.2.5.3. Moisture effects on cumulative counts 190

4.2.6. Experimental conclusions 191

4.3. Numerical analysis of 4-point bending behaviors 191

4.3.1. Abaqus model establishment 191

4.3.2. Equivalent elastic-plastic and shear damage model 193

4.3.3. Prediction of 4-point bending behaviors 195

4.3.3.1. Prediction of bending stiffness and strength 195

4.3.3.2. Damage localizations by numerical models 197

4.3.3.3. Stress distributions in honeycomb core 200

4.3.4. Numerical conclusions 205

4.4. Chapter summary 205

4.1. Introduction

The 4-point bending behaviors of the CFRP-honeycomb sandwich are different from those of the GFRP-balsa sandwich mainly due to the good compression and shear resistance properties of the honeycomb core [26-27]. In reality, the final failure is dominated by the non-linear core buckling behavior [74-75]. In the first part of this chapter, the static 4-point bending behaviors of the CFRP-honeycomb sandwich have been investigated with the help of the microscope, IRT and AE observations. The time and locations of the damage initiation and evolution of dry and wet CFRP-honeycomb sandwich specimens have been compared by coupling the three observation techniques.

In the second part, the progressive core shear damage model in Abaqus has been introduced to simulate the 4-point bending tests of GFRP-honeycomb sandwich, and the damage localizations by Abaqus model has been demonstrated to agree well with the microscope and IRT observations.

4.2. Static 4-point bending tests monitored by AE and IRT

4.2.1. Experimental setup

The triple dog-bone CFRP-honeycomb sandwich specimens (see Fig. 2-7) were also tested under 4-point bending. Loading span (L) is 80 mm and support span (S) is 240 mm, as seen in Fig. 4-1. (a). The tests were also controlled by displacement rate imposed at 2 mm/min [209-210] using the MTS machine with load cell of 100 kN, monitored by passive AE and IRT systems during the whole loading process (see Fig. 4-1 (b)).

Similar to the 4-point bending tests on GFRP-balsa sandwiches, AE monitoring was conducted by two wideband sensors (with frequency range of 100 kHz-1 MHz) with a distance (D) of 180 mm, the pre-amplifier, the analogue filters and the PCI-2 acquisition system (with Mistras AEwin software), as seen in Fig. 4-1. (a). This kind of wideband sensor was chosen so as to allow the received signals not to be limited in certain resonance frequencies in the case of a multi-material structure. According to preliminary study, the threshold which determines the system sensitivity to the environmental noise, was set by 30 dB. AE wave velocity and attenuation tests have to be repeated on dog-bone specimens before starting the bending tests, so as to calibrate AE setup input into AEwin software. The other AE acquisition parameters under 4-point bending are given in Table 4-1.

Different from GFRP-balsa sandwiches, IRT system was set to monitor more clearly the honeycomb core surface in zone 1 and zone 2 from the side view (see Fig. 4-1. (b)), because core damages firstly appear in CFRP-honeycomb sandwich under 4-point bending. IRT acquisition parameters are shown in Table 5-2. For these tests, we have chosen a frame rate of 100 Hz (compared to 480 Hz on GFRP-balsa sandwich) because it can capture enough information during the relatively longer static tests

which take about 600 s, this choice may be questioned for future tests in order to promote the recording of as much information as possible.

In order to study moisture effects on mechanical behaviors and damage mechanisms of triple dog-bone CFRP-honeycomb sandwich specimens, three dry specimens and three wet specimens (average MC: 6.5%) were tested under the same 4-point bending loading condition.

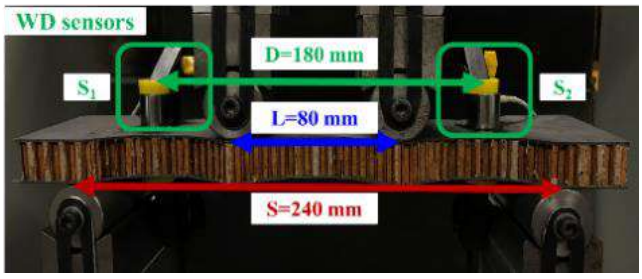

(a) Positions of AE wideband sensors.

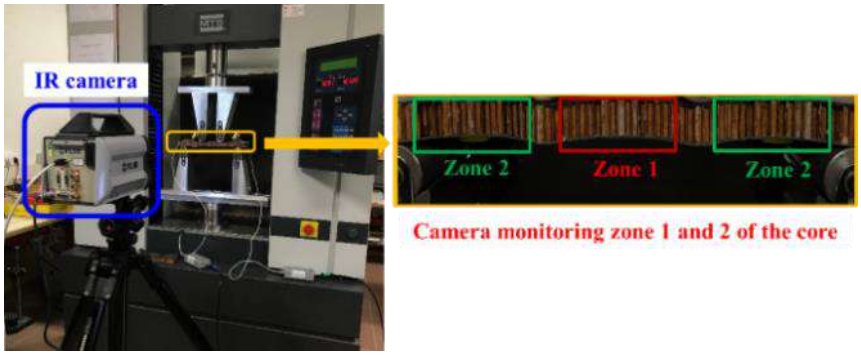

(b) IR camera setup.

Fig. 4-1. 4-point bending test setup monitored by AE and IRT for CFRP-honeycomb sandwich.

Table 4-1. AE acquisition parameters for CFRP-honeycomb sandwiches under 4-point bending.

Threshold (dB)	Pre-amplifier (dB)	Analog Filter (MHz)	PDT (µs)	HDT (µs)	HLT (µs)	Sample Rate (MSPS)	Pre-Trigger (µs)	Hit Length
30	40	0.02-3	35	150	300	5	50	4k

Table 4-2. IRT acquisition parameters for CFRP-honeycomb sandwiches under 4-point bending.

Emissivity	Distance (m)	Reflected Temp (°C)	Frame rate (Hz)
0.95	0.7	19.3	100

4.2.2. Moisture effects on bending behaviors

Force/Displacement curves of dry and wet CFRP-honeycomb sandwich specimens under 4-point bending loading are compared in Fig. 4-2. Firstly, it is obvious that the dry and wet sandwich

specimens show the similar elastic-plastic behavior. As seen in Fig. 4-2. (b), the 4-point bending behavior of the CFRP-honeycomb sandwich can be divided into four stages: the first linear stage before point A, the second non-linear stage before the maximum load B, the decreasing stage before point C and the platform after point C. This behavior is different from the linear behavior of the GFRP-balsa sandwich, mainly due to the honeycomb core buckling behavior [75].

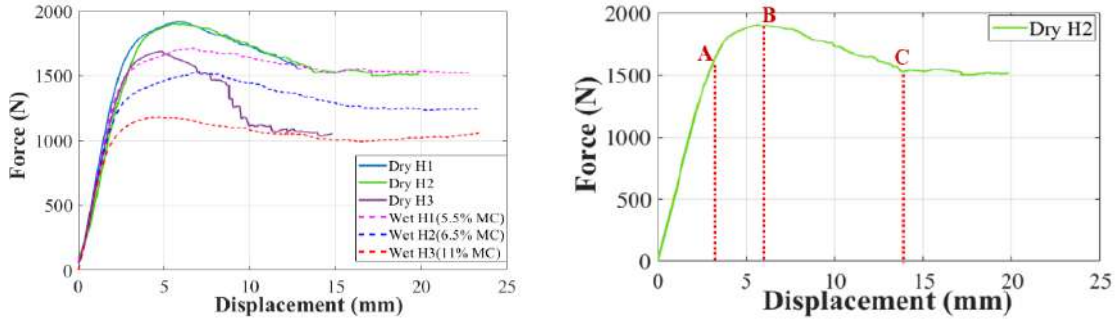

(a) Force/Displacement curves of dry and wet sandwiches. (b) Example of four stages.

Fig. 4-2. Static 4-point bending behaviors of CFRP-honeycomb sandwich specimens.

In literatures [73-75], it has been explained that the typical force/displacement curves of honeycomb sandwich under 4-point bending can be divided into four stages, which agree well with Fig. 4-2. (b). The four stages can be explained as following as demonstrated in [75]: (1) the first linear elastic stage before point A, where only small local core cell wall buckling exists; (2) the second non-linear stage AB, where core begins to yield and typical core buckling can be observed; (3) the third decreasing stage BC, where the load shows obvious decrease and the plastic buckling of honeycomb cell walls initiates; (4) finally, the final platform after point C, where the propagation of core buckling can collapse to a higher number of honeycomb cells, together with core wrinkling or called indentation intensification.

The first two stages can be also considered as the pre-buckling period, which is mainly related to the elastic response of the sandwich. After point B, it's also called post-buckling period, where the typical plastic buckling initiates and propagates. Thus, the honeycomb core buckling plays a very important role in the bending behavior of honeycomb sandwich structures. However, the definitions of the honeycomb core buckling and wrinkling in the literatures are still not clear. In this work, the different honeycomb core damage modes in the four stages will be demonstrated based on microscope, IRT and AE observations.

Considering moisture effects on the 4-point bending behavior of CFRP-honeycomb sandwich, it is obvious that the fractions of different stages have changed after moisture absorption. Point A of the wet sandwich appears much earlier, meaning that the yield stress of the wet honeycomb has been decreased, which shall be considered in numerical models. Point C of the wet sandwich appear later,

so the stage AC is longer for wet sandwich. Moreover, the decrease rate in stage 3 of wet sandwich specimens seems much smaller than that of dry ones. All these observations can be correlated to the next investigations with the help of the microscope, IRT and AE.

4.2.2.1. Moisture effects on bending stiffness

In Fig. 4-2, the average bending stiffnesses of dry and wet CFRP-honeycomb sandwich specimens in initial elastic linear stages are 605 N/mm (±78 N/mm) and 596 N/mm (±58 N/mm), respectively. The variation is only 1.5%, so it indicates that the moisture effects on the bending stiffness of CFRP-honeycomb sandwich is not significant. In Chapter 2, it has been predicted by the proposed new method that the elastic modulus of the saturated wet CFRP-honeycomb sandwich specimen (average MC: 6.5%) can be decreased by 2% of that of the dry one. Thus, it verifies again that the proposed method to predict stiffness variation of skin of wet sandwich structure by AE wave velocity measurements can also be effective for honeycomb cored sandwich.

4.2.2.2. Moisture effects on bending strength

However, Fig. 4-2 shows that moisture absorption greatly affects the bending strength of CFRP-honeycomb sandwich. The average maximum force of dry sandwich is 1837 N (±127 N), while those of wet specimens (Wet H1 (5.5% MC), Wet H2 (6.5% MC) and Wet H3 (11% MC)) are 1712 N, 1529 N and 1183 N, decreasing by 7%, 17% and 36%, respectively. Considering that Wet H1 (5.5% MC) and Wet H2 (6.5% MC) have the MC much nearer to the average 6.5% MC in Chapter 2, the average maximum force of these two specimens is 1621 N (±129 N), decreasing by 12%, compared to that of the dry sandwich. So, it indicates that moisture effects on the bending strength of CFRP-honeycomb sandwich shall be considered carefully. These conclusions will be further demonstrated by microscope, IRT and AE observations, as well as numerical simulations.

4.2.3. Damage mechanisms observed by microscope

For all dry and wet CFRP-honeycomb sandwich specimens, the honeycomb core damages in zone 2 are the predominant, caused by the combination of shear and compression stresses (see Fig. 4-3) under 4-point bending loading [75]. No visible skin damage can be seen. So, the microscope is needed to further inspect the skin surface. Fig. 4-3. (a) shows that the honeycomb core buckling is more obvious on dry sandwich specimen, because the very clear core shear crack bands propagating along about 45° of the honeycomb cell walls in zone 2 can be seen, with a length of 25 mm.

According to the reference [75], the similar core damage mechanisms were also observed on the dry sandwich. However, no study has been found in the literature about the damage modes of wet CFRP-honeycomb sandwich. Comparing Fig. 4-3. (a) and Fig. 4-3. (b), for the wet sandwich, the core

wrinkling near the lower skin and loading application region is more obvious on honeycomb cell wall surfaces, while the core shear crack bands are less obvious after the same 4-point bending.

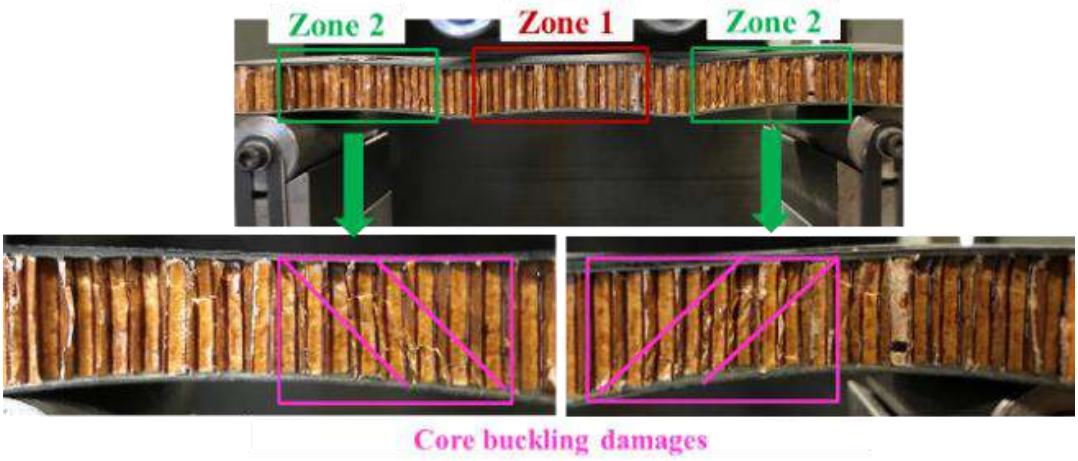

(a) Specimen Dry H2.

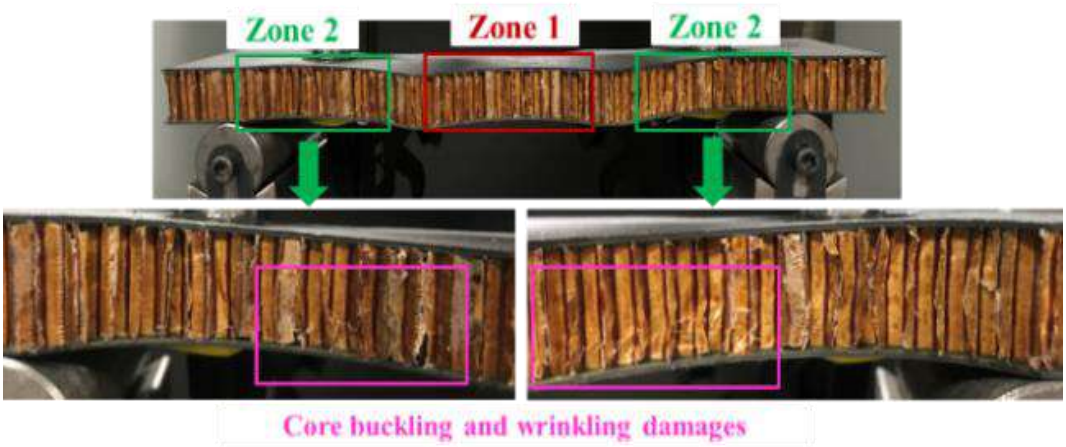

(b) 5.5% MC specimen Wet H1.

Fig. 4-3. Honeycomb cell wall surfaces of dry and wet CFRP-honeycomb sandwich under bending.

The core and skin damage images observed by microscope VHX-700 (100 X) are further shown in Fig. 4-4 and Fig. 4-5. Firstly, it's obvious in Fig. 4-4 that the skin/core debonding in zone 2 is wider and more severe at the lower skin/core interface of the wet CFRP-honeycomb sandwich than that of dry sandwich. The length of the skin/core debonding crack is 4.8 mm in the wet sandwich, while that in the dry sandwich is only 2 mm, decreasing by 58%. In addition, the core shear crack on one honeycomb cell surface is more obvious with a length of 5 mm, while that of wet honeycomb is 3.5 mm, decreasing by 30%.

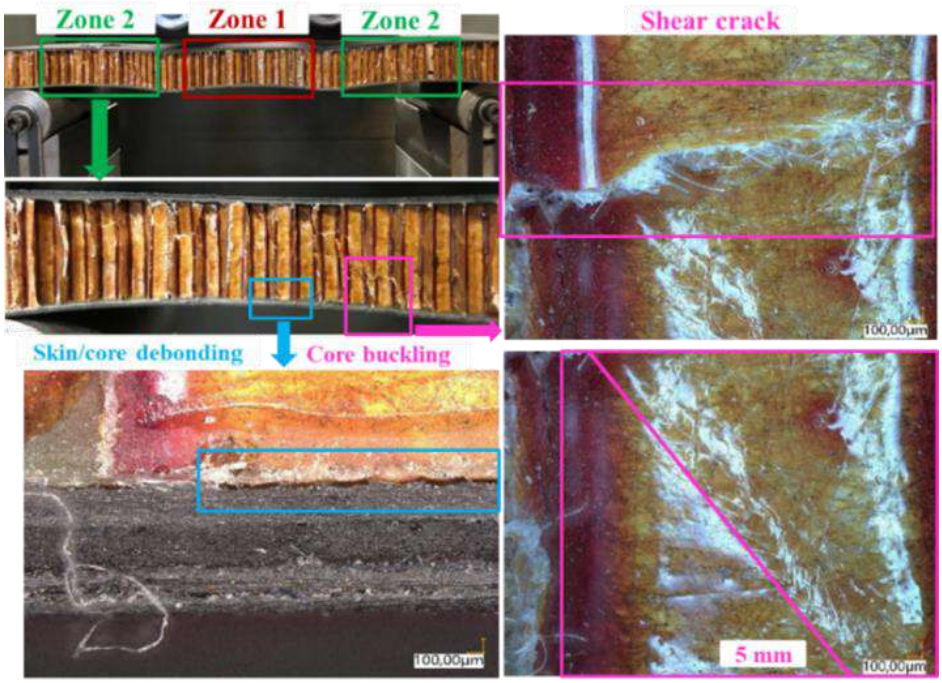

(a) Zone 2 of specimen Dry H2.

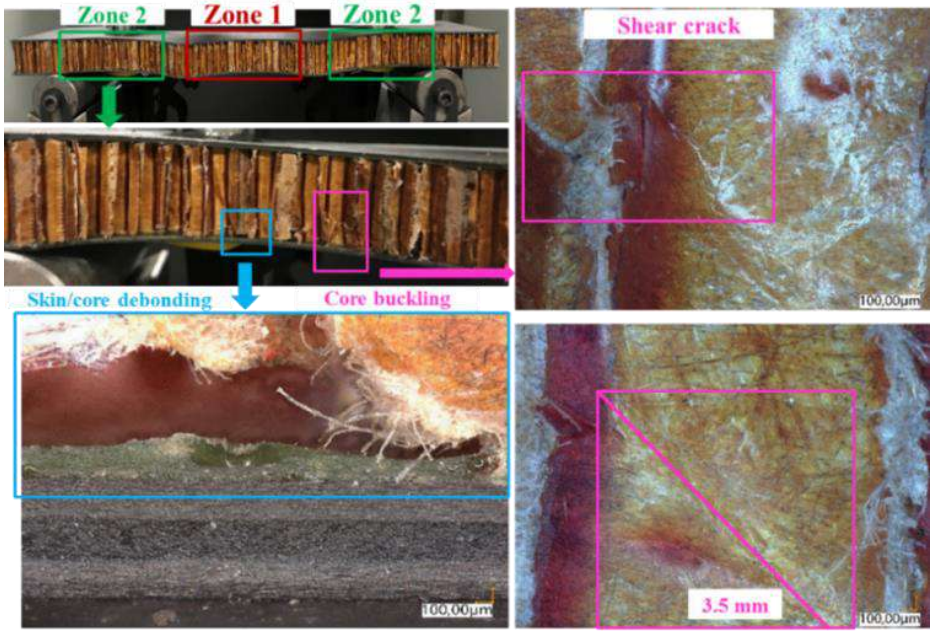

(b) Zone 2 of 5.5% MC specimen Wet H1.

Fig. 4-4. Core damage images of dry and wet CFRP-honeycomb sandwich after 4-point bending tests.

Fig. 4-5 shows the upper skin surface images of dry and wet CFRP-honeycomb sandwich in zone 1 and zone 2 after 4-point bending tests. In zone 1, matrix cracking of upper CFRP skin of dry sandwich is more obvious, while in zone 2, it's more obvious in wet sandwich.

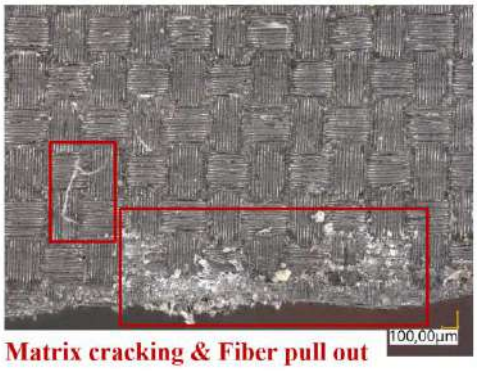

(a) Zone 1 of specimen Dry H2.

(b) Zone 2 of specimen Dry H2.

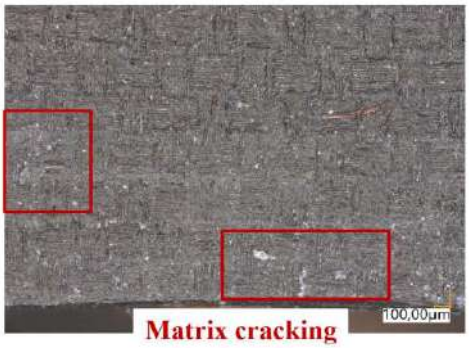

(c) Zone 1 of 5.5% MC specimen Wet H1.

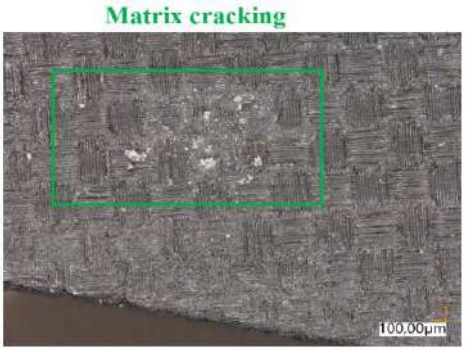

(d) Zone 2 of 5.5% MC specimen Wet H1.

Fig. 4-5. Skin images of dry and wet CFRP-honeycomb sandwich after 4-point bending tests.

Therefore, by microscope, it can be observed that moisture absorption has caused the more severe skin/core debonding, core wrinkling and matrix cracking of the CFRP skin in zone 2, but less obvious honeycomb core buckling in zone 2. Next, IRT and AE monitoring results will be discussed to better understand the damage mechanisms of CFRP-honeycomb sandwich under 4-point bending.

4.2.4. Damage localizations by IRT and AE

4.2.4.1. Core damages monitored by IRT

Since CFRP-honeycomb sandwich has a max displacement of about 20 mm during the whole 4-point bending test, the traditional method which obtains the real temperature difference by $\Delta T = T - T_0$ without considering the displacement is no longer accurate. Similar to GFRP-balsa sandwich, correlation between movement of the vertical pixel in IRT temperature images and true displacement of the specimen is introduced into MATLAB program to improve the accuracy of post-processing of thermal images. In reality, the temperature variation at time t is calculated by the superposition of the subtraction from any two adjacent frames ($\Delta T=T_1-T_0 + T_2-T_1+\ldots+ T_t-T_{t-1}$).

The temperature variation images of Dry H2 and Wet H1 (5.5% MC) between the two wideband AE sensors (D=0.18 m) during the four stages of 4-point bending tests are shown in Fig. 4-6 and Fig. 4-

7. Firstly, it can be observed that thermal images of wet sandwich specimen show much higher non-homogenous temperature increase under the 4-point bending loading. This phenomenon [201] is mainly because that an evaporation reaction on the wet surface and an increase in the energy storage capacity exist simultaneously, and the water distribution is not uniform in wet sandwich due to the hollow honeycomb cells and special dog-bone shape. It has been explained in Chapter 2 that the initial average temperature of the wet specimen is about 2.2 ^{o}C lower than that of the dry one before the 4-point bending tests, due to the water absorption.

Finally, temperature increase in wet sandwich during bending load may be caused by the damage accumulation, as well as the heat conduction between the loading rolls and the specimen surface. But for now, no definite explanation can be given, further experiments shall be added to verify the reasons of this phenomenon. However, it is interesting to find that thermal images of dry sandwich show good agreements with microscope observations.

Fig. 4-6. (a)-(d) show the temperature variation images of Dry H2 at 100 s in linear stage before point A, at 180 s in pre-buckling stage AB, at 350 s in post-buckling stage BC and at 600 s in post-buckling platform stage after point C, respectively. Fig. 4-6. (e) shows that the real image of the monitored zone (in purple window) by IRT during the test, which is also the zone between the two wideband sensors, so as to better couple the localization results by IRT and AE in the following analysis. The obvious honeycomb core shear crack bands in zone 2 can be seen in Fig. 4-6. (d) and (e), propagating near 45^{o} from the upper skin/core interface in the center of zone 2 to the lower skin/core interface near the loading applications. In fact, the core buckling is dominated by the shear stress in the thin honeycomb cell wall plane, while the core wrinkling is mainly resulted from the normal stress in the honeycomb cell wall plane [73-74]. This can be further demonstrated by the numerical simulations.

Fig. 4-6. (a)-(d) shows clearly the honeycomb core damage initiation and evolution during the four stages in Fig. 4-2. The obvious honeycomb core buckling in zone 2 can be seen from stage AB, and then the more obvious plastic buckling initiates in stage BC and propagates in stage after point C. The max temperature keeps increasing during the four stages. After point B, some small core wrinkling can be seen near the lower skin/core interface and near the loading applications. In zone 1, especially near the loading applications, some very small temperature increase (yellow points about 1 ^{o}C) can be also seen after point B in post-buckling stage, which can be caused by the honeycomb cell wall wrinkling due to compressive stresses from contact between loading rolls and the specimen.

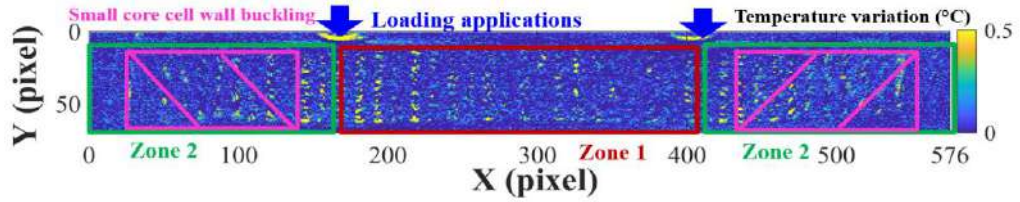

(a) t=100 s in linear stage before point A.

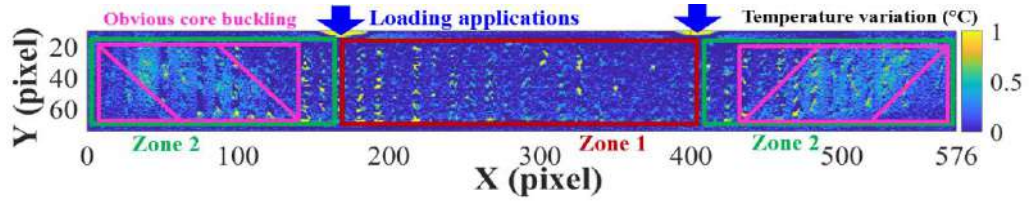

(b) t=180 s in pre-buckling stage AB.

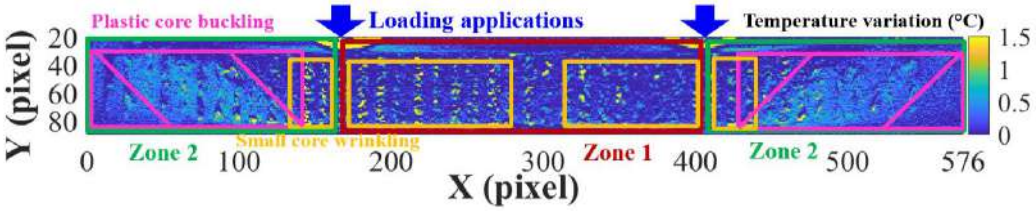

(c) t=350 s in post-buckling stage BC.

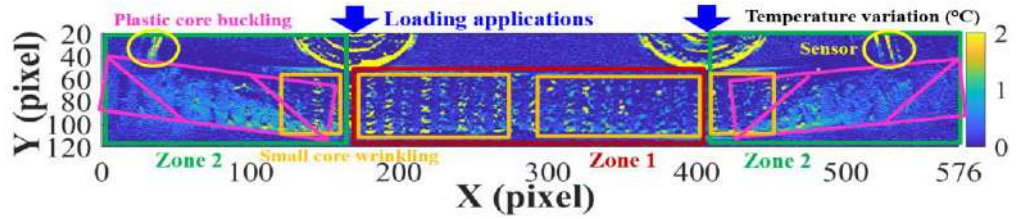

(d) t=600 s in post-buckling stage after point C.

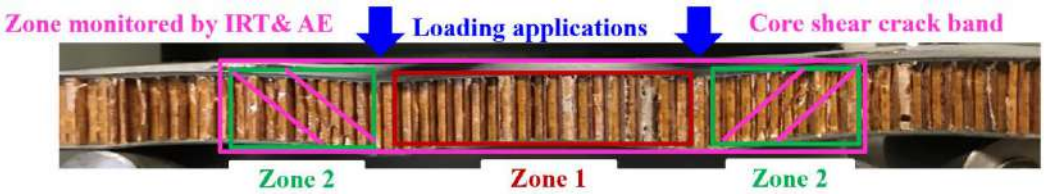

(e) The real damage surfaces of the honeycomb core after the test.

Fig. 4-6. Temperature variation (°C) images in CFRP-honeycomb sandwich specimen Dry H2.

Fig. 4-7. (a)-(d) shows the honeycomb core damage initiation and evolution of specimen Wet H1 (5.5% MC) during the four stages. Firstly, one interesting thing is that the honeycomb core buckling of the wet sandwich is less obvious than that of the dry sandwich, because the obvious shear bands in zone 2 cannot be seen in the wet sandwich. But core wrinkling (see Fig. 4-7. (e)) is more obvious in the wet sandwich, which is mainly due to compressive stresses caused by the contact between the loading rolls and the honeycomb sandwich surface. The core wrinkling in the wet sandwich appears

much earlier before point B near the lower skin/core interface and loading application regions, while that in dry sandwich appear mainly after point B. This can be validated by the further stress distributions in numerical simulations.

In conclusion, IRT conclusions agree well with the microscope observations, showing the damage difference between dry and wet sandwich. Core buckling (shear crack band) is more obvious in dry sandwich; however, core wrinkling is predominant in wet sandwich. Thermal images of wet sandwich show much higher temperature increase. It may be related to the very complicated physical and mechanical phenomena. Higher energy may be released by damage modes in wet sandwiches, and the moisture in wet specimens has changed the physical mechanisms of heat transfer inside the material and heat exchange with the outside environment. So, further investigation is needed to identify the correlations between the real thermal field change, the damage evolution and moisture content variation.

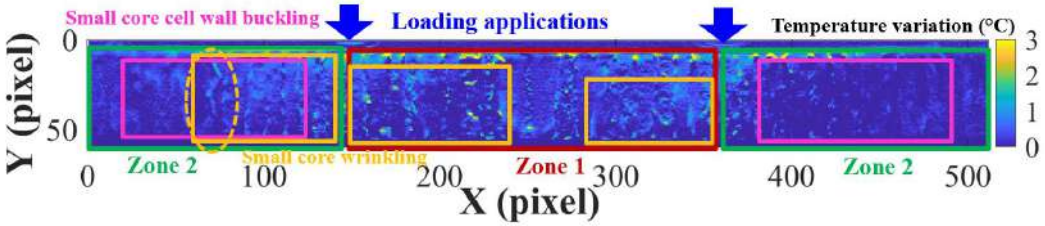

(a) t=100 s in linear stage before point A.

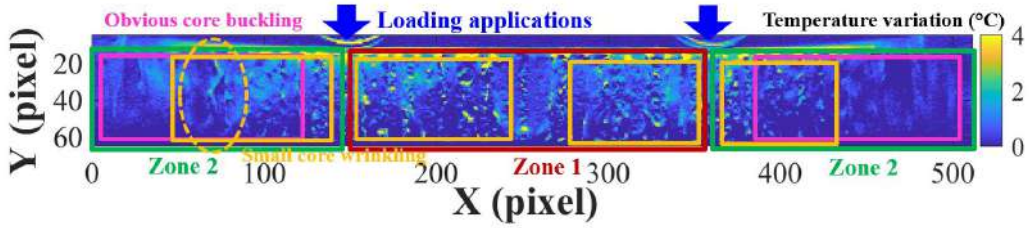

(b) t=180 s in pre-buckling stage AB.

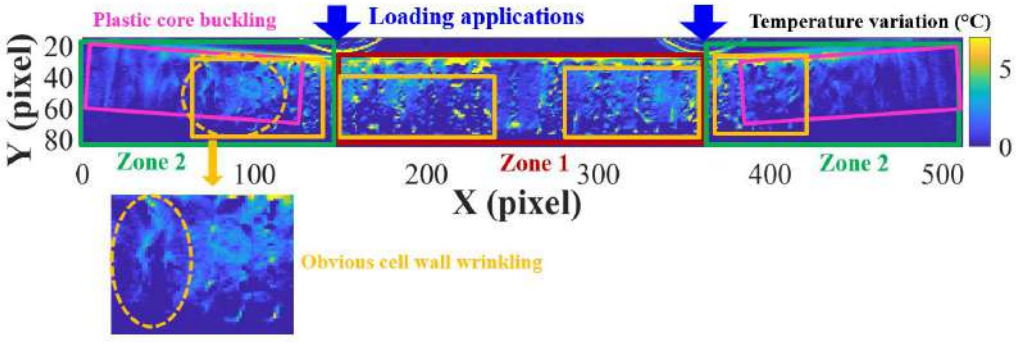

(c) t=350 s in post-buckling stage BC.

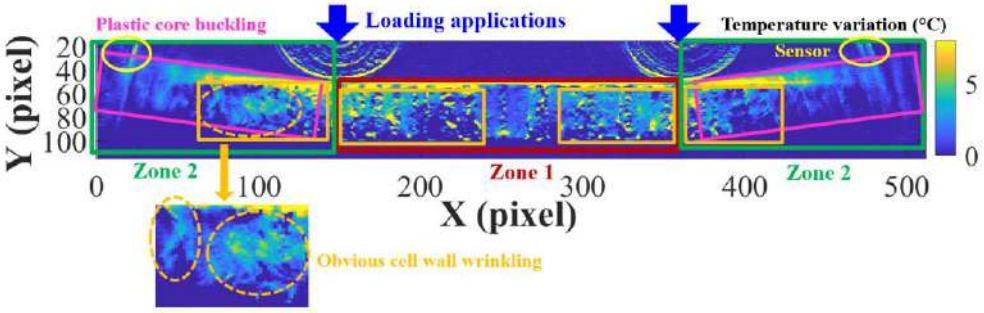

(d) t=600 s in post-buckling stage after point C.

(e) The real damage surfaces of the honeycomb core after the test.

Fig. 4-7. Temperature variation (°C) images in CFRP-honeycomb sandwich specimen Wet H1 (5.5% MC).

4.2.4.2. Coupling of damage localizations by IRT and AE

Based on the damage localization images by IRT, AE localization results are coupled with IRT images, as shown in Fig. 4-8 and Fig. 4-9. Firstly, Amplitude (dB) distributions between the two wideband sensors (D=0.18 m) of dry and wet sandwiches during the four stages of 4-point bending tests are illustrated. In Fig. 4-8, the red window represents the center zone 1 within 0.115-0.185 m, and the green window corresponds to zone 2 within 0.060-0.105 m and 0.195-0.240 m near the two sensors.

Compared to the GFRP-balsa sandwich, localization figures of CFRP-honeycomb sandwich have received much more signals, it may be because that the damages of the CFRP-honeycomb sandwich have released higher energy and moisture has less effect on the acoustic wave attenuation in CFRP-honeycomb sandwich, as seen in Fig. 2-34 and Fig. 2-37.

In Fig. 4-8. (a), in the first linear stage before point A, for dry CFRP-honeycomb sandwich, most AE signals appear in zone 2, showing amplitude within 40-80 dB. Combined with IRT image in zone 2, Fig. 4-8. (a) verifies that AE signals in zone 2 could come from local honeycomb cell wall buckling. Very few signals appear in center zone 1 in this stage, showing amplitude within 30-50 dB. Similar to the analysis of skin damages of GFRP laminates in zone 1 in Chapter 3, these signals in zone 1 of CFRP-honeycomb sandwich may come from matrix cracking in the composite skin [114-116], as observed in Fig. 4-5 by microscope, but they cannot be detected by IRT because of the lower energy released.

In the second non-linear pre-buckling stage AB in Fig. 4-8. (b), much more AE signals within 30-90 dB accumulate in zone 2, compared with the IRT image, they could come from the more obvious honeycomb core buckling. It is interesting to note that more AE signals higher than 70 dB accumulate nearer to the two sensors which are located just near the narrowest region in zone 2, where the core shear stress is the maximum. In zone 1, more signals lower than 80 dB appear in stage AB, combined with zone 1 in the IRT image, they may come from the skin damages and small core wrinkling near the loading application regions. This shall be combined with the later clustering analysis to make the most robust conclusions.

In post-buckling stage BC in Fig. 4-8. (c), a large number of AE hits accumulate both in zone 1 and zone 2. In zone 2, honeycomb core buckling signals within 30-100 dB continue to increase, which could correspond to the very obvious shear crack band detected by IRT image. More signals within 30-80 dB corresponding to honeycomb core wrinkling (see Fig. 4-4 and Fig. 4-6) have accumulated in this stage near the loading applications in zone 1 and zone 2. In zone 1, signals lower than 50 dB shall come from matrix cracking and fiber/matrix debonding in composite skin [114-116].

In post-buckling platform stage after point C in Fig. 4-8. (d), AE amplitude distributions are similar to those in stage BC. More AE signals within 30-50 dB accumulate in zone 1, which shall come from the skin [114-116]. Combined with IRT images, more signals higher than 50 dB accumulate near the loading applications in zone 2, coming from core wrinkling. Signals within 30-100 dB in zone 2 continues to accumulate, coming from the plastic core buckling accompanied by local core cracking.

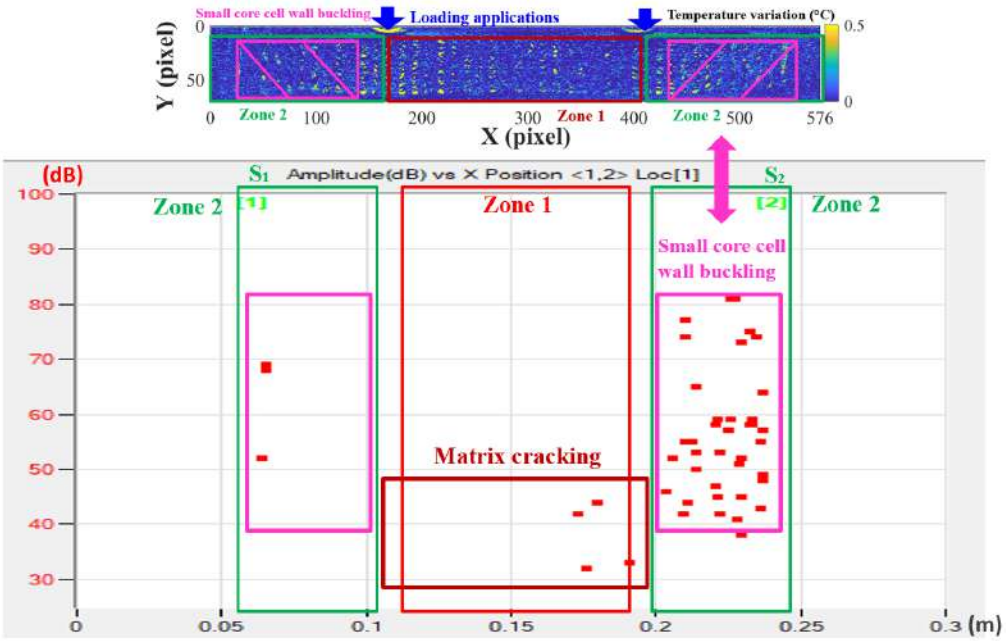

(a) t=100 s in linear stage before point A.

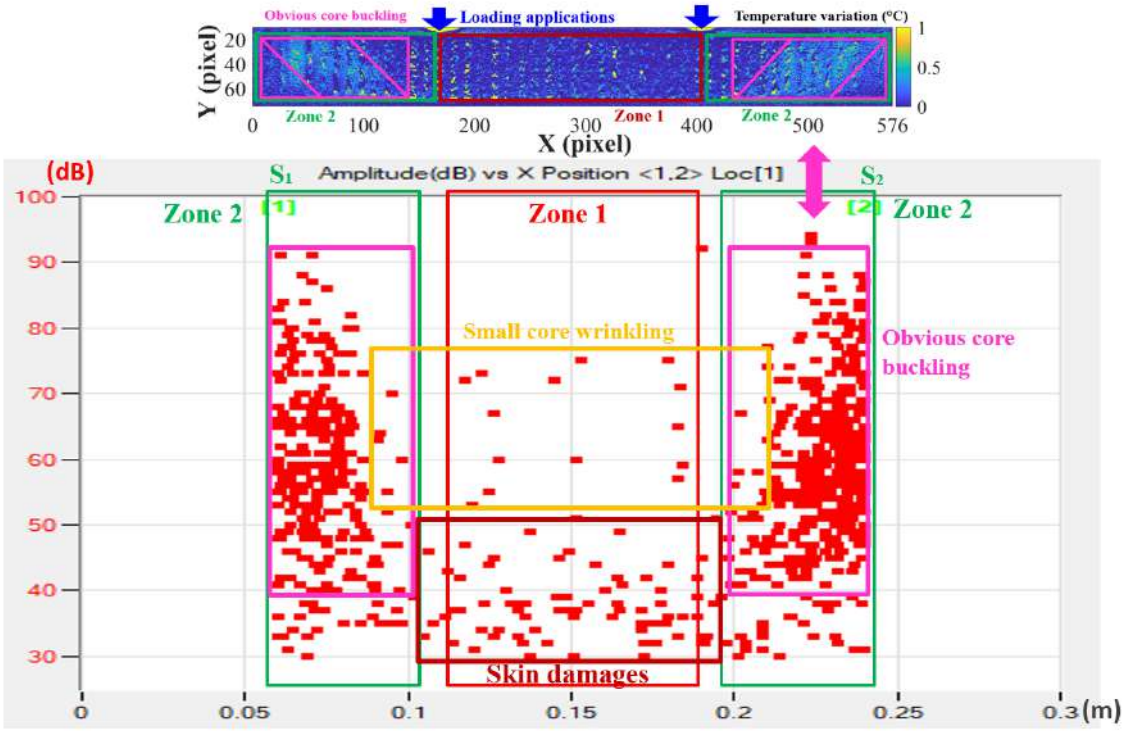

(b) t=180 s in pre-buckling stage AB.

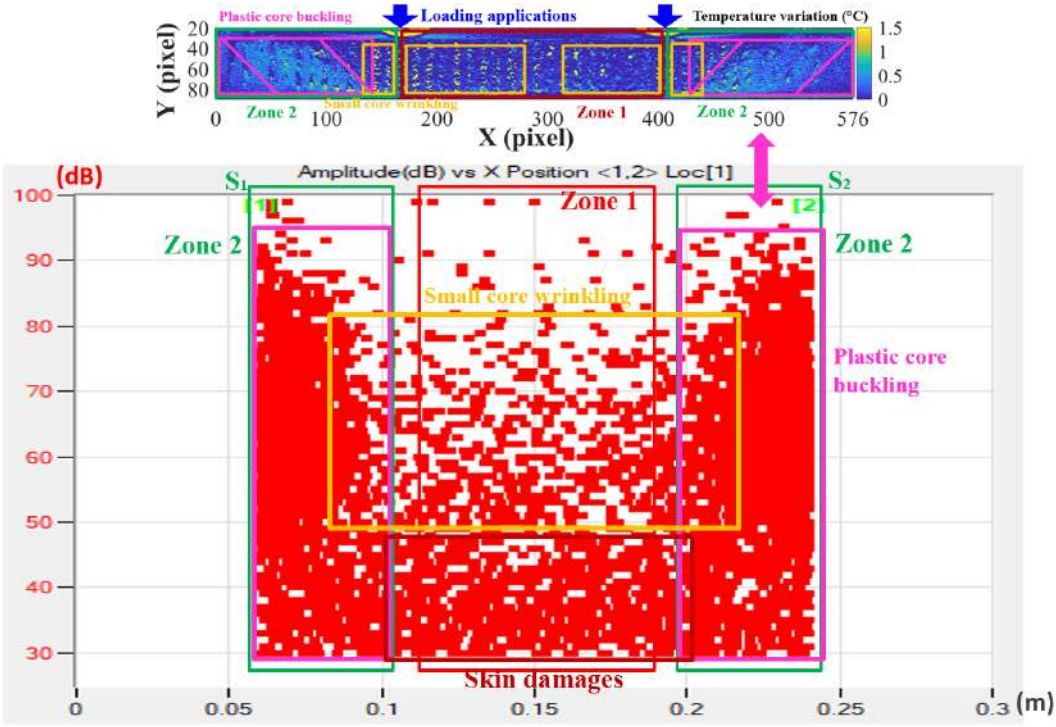

(c) t=350 s in post-buckling stage BC.

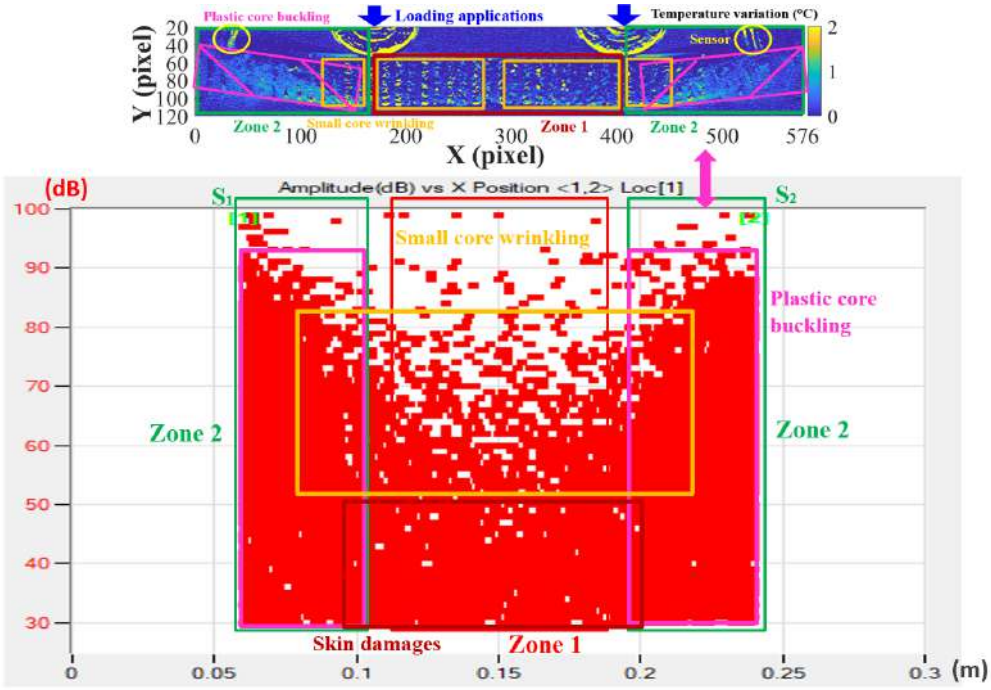

(d) t=600 s in post-buckling stage after point C.

Fig. 4-8. Damage localizations of specimen Dry H2 by AE amplitude and IRT.

In the localization figures of wet sandwich specimen 5.5% MC in Fig. 4-9, similar AE amplitude distributions can be found. In the first linear stage before point A in Fig. 4-9. (a), most signals within 40-80 dB also appear in zone 2. The typical difference between wet and dry sandwich in this stage is that fewer signals within 30-50 dB appear in zone 1.

In the second non-linear pre-buckling stage AB in Fig. 4-9. (b), compared to the dry sandwich, fewer honeycomb core buckling signals lower than 50 dB accumulate in zone 2. In zone 1, there are also fewer signals lower than 80 dB. Combined with IRT image, the honeycomb core buckling in zone 2 of the wet sandwich is less obvious from this stage, so AE localizations agree well with the IRT images.

In post-buckling stages BC in Fig. 4-9. (c) and in Fig. 4-9. (d) after point C, similar to the dry sandwich, a large number of AE hits accumulate in zone 2 and near the loading application region. In zone 2, honeycomb core buckling signals within 30-100 dB continue to accumulate intensely. But in zone 1, there are fewer signals, compared to the dry sandwich. More signals within 50-80 dB accumulate near the loading application regions in zone 2 in the wet sandwich, which indicates that the core wrinkling in zone 2 has become more severe, which agrees well with the IRT images. While the AE signals coming from the core buckling have become less important in the wet sandwich., showing fewer signals within 30-50 dB in zone 2. It is also obvious that the core buckling signal

distributions are no longer symmetric to the center of zone 1, which could be affected by the non-uniform moisture absorption in the wet sandwich.

In summary, at 600 s, compared to the dry sandwich, there are fewer signals within 30-50 dB in zone 1 and zone 2 in wet sandwich. Between zone 1 and zone 2, near X=0.1 m and X=0.2 m, where the loading application regions locate, AE signals within 50-80 dB play a more important role in wet sandwich, corresponding to core wrinkling due to indentation of cell walls. Thus, moisture absorption has resulted in the more obvious honeycomb core wrinkling near the loading application regions in zone 2, but less severe core buckling in zone 2.

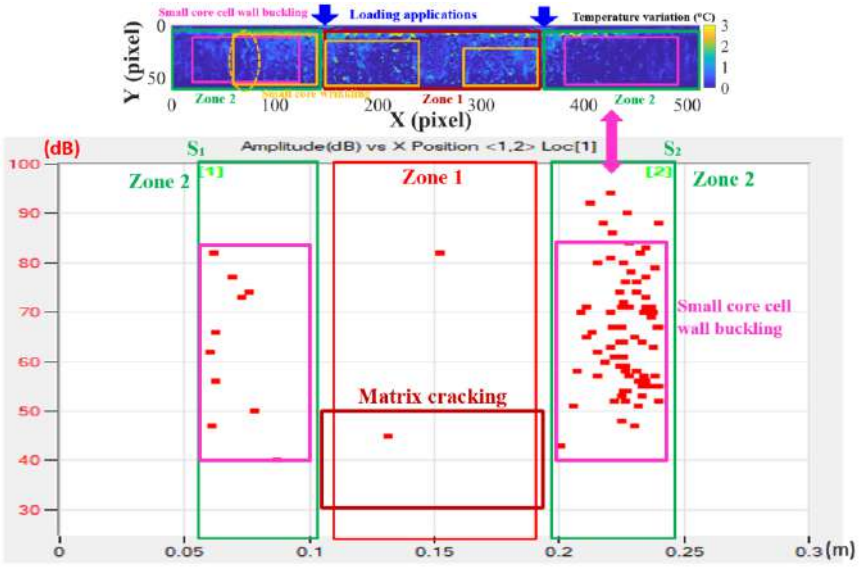

(a) t=100 s in linear stage before point A.

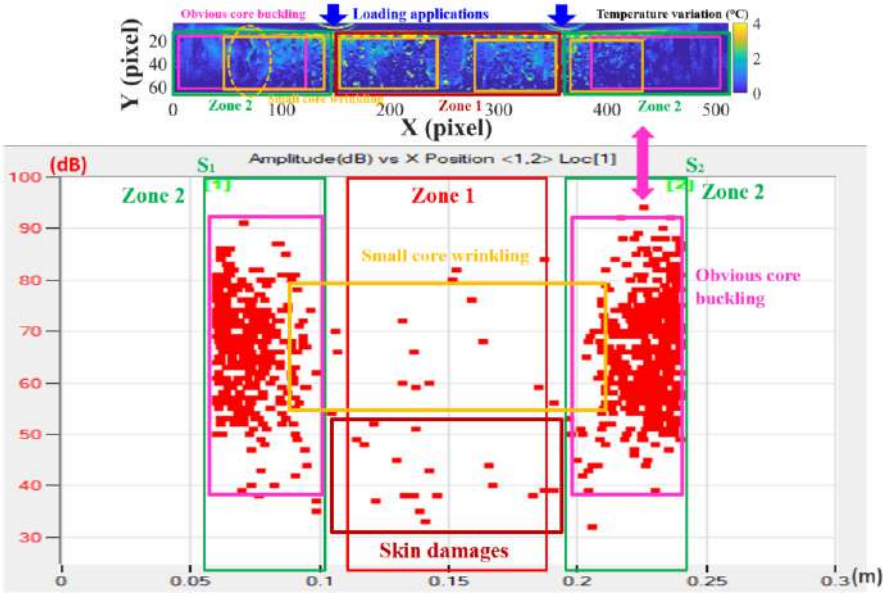

(b) t=180 s in pre-buckling stage AB.

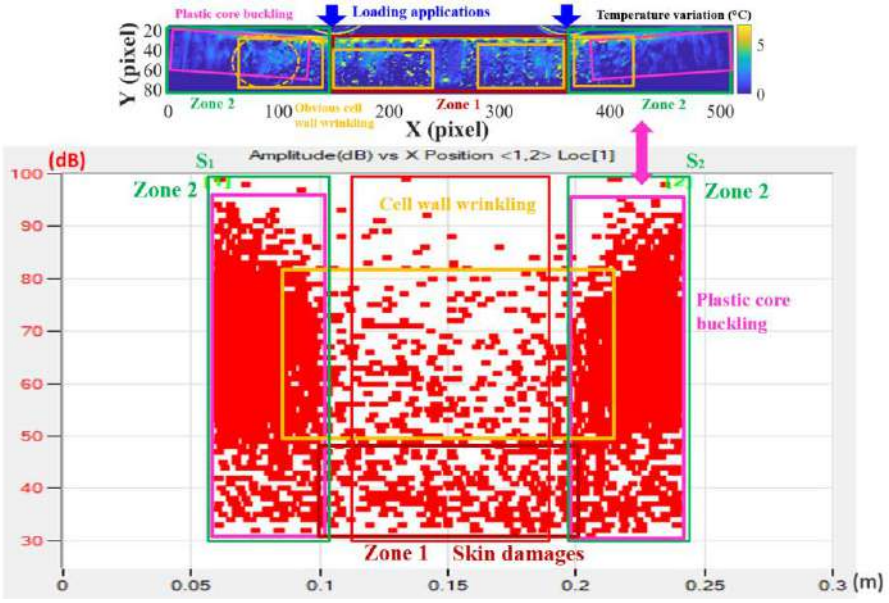

(c) t=350 s in post-buckling stage BC.

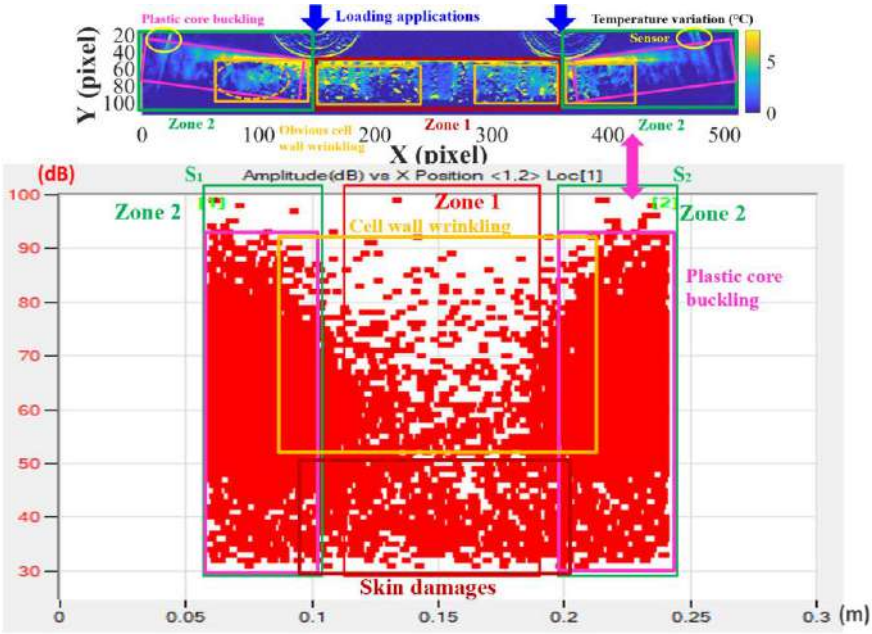

(d) t=600 s in post-buckling stage after point C.

Fig. 4-9. Damage localizations of specimen Wet H1 (5.5% MC) by AE amplitude and IRT.

Finally, it can be concluded that amplitude in zone 1 is mainly within 30-70 dB, corresponding to matrix cracking and fiber/matrix debonding in the composite skin [116-121], which is similar to those observed on GFRP skin damages in Chapter 3. While amplitude in zone 2 is mainly within 30-90 dB, corresponding to honeycomb core buckling and wrinkling [121]. The damage difference between dry and wet specimens needs further validations.

4.2.4.3. Validation of damage localizations by peak frequency and duration

As demonstrated in Chapter 3, peak frequency and duration [121] are the two important parameters to identify the damage modes of sandwich structures. Based on the above localization results by AE amplitude and IRT, Fig. 4-10 show the peak frequency and duration distributions to help identify the characteristics of the different damage modes.

In Fig. 4-10, for dry CFRP-honeycomb sandwich, in the first linear stage before point A, most signals appear in zone 2, showing peak frequency lower than 600 kHz and duration less than 2000 μs. Very few signals appear in center zone 1, showing peak frequency within 100-200 kHz and duration less than 1000 μs.

In the second non-linear pre-buckling stage AB, much more honeycomb core buckling signals accumulate in zone 2, showing peak frequency lower than 600 kHz and duration less than 4000 μs. In zone 1, more signals lower than 300 kHz appear. According to the demonstrated peak frequency range [114-116] of composite skins in Chapter 3, these signals shall come from matrix cracking and fiber/matrix debonding in the composite skin, but they cannot be observed by IRT. In zone 1, some signals within 300-600 kHz also appear, which shall come from the core wrinkling mainly near the loading applications. It has been demonstrated that the peak frequency range of the honeycomb core damage shall be within 200-800 kHz [121], so the high frequency signals in zone 1 shall also come from the core damages, not from the skin.

In post-buckling stage BC, in zone 2, honeycomb core buckling signals continue to accumulate, with peak frequency lower than 600 kHz and duration less than 10000 μs. In zone 1, skin damage signals within 20-300 kHz and core wrinkling signals within 300-600 kHz also accumulate more. In post-buckling stage after point C, AE signal distributions are similar to stage BC, the main difference is that more signals within 400-600 kHz accumulate in zone 1 and zone 2, which shall be core wrinkling and core cracking due to buckling.

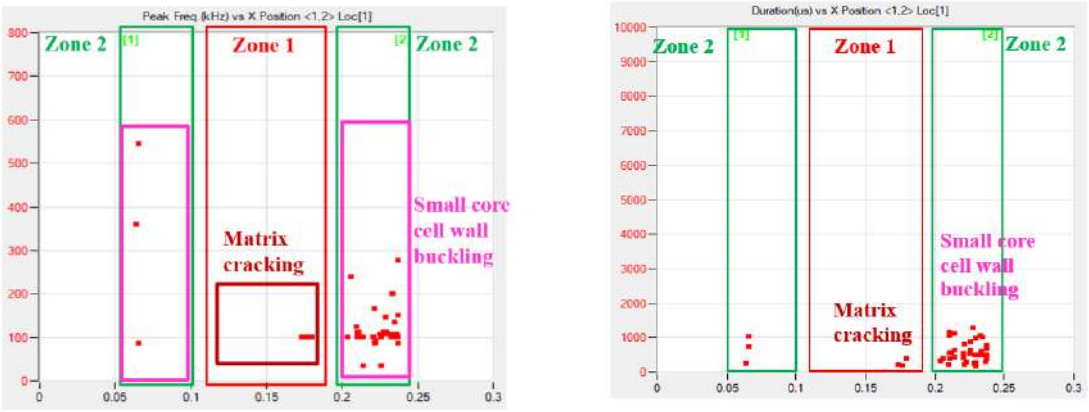

(I) Peak Frequency. (II) Duration.

(a) t=100 s in linear stage before point A.

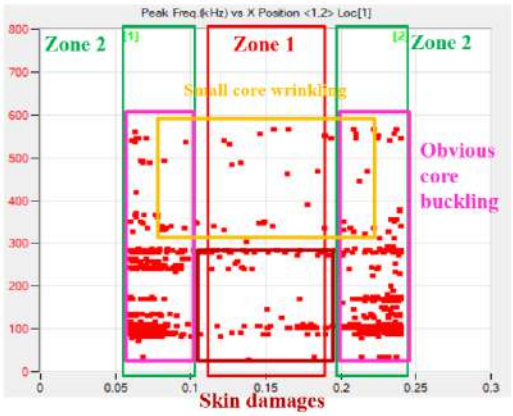

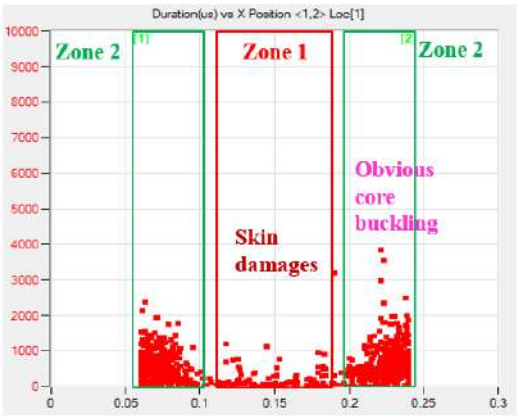

(I) Peak Frequency. (II) Duration.

(b) t=180 s in pre-buckling stage AB.

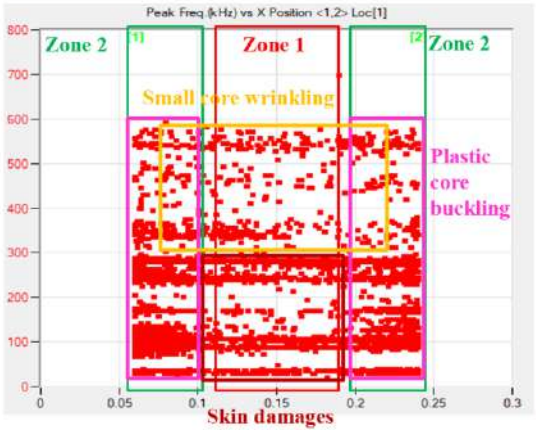

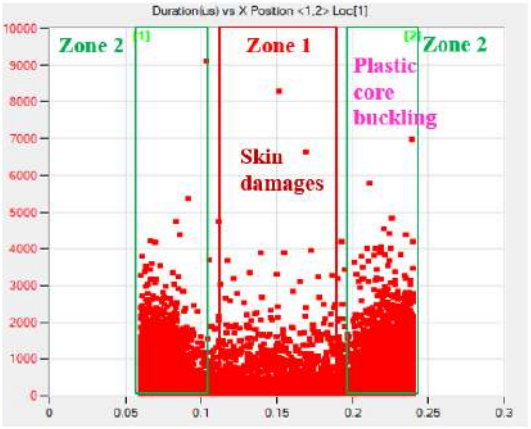

(I) Peak Frequency. (II) Duration.

(c) t=350 s in post-buckling stage BC.

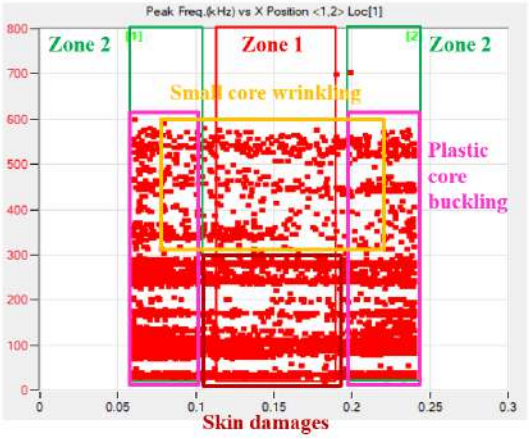

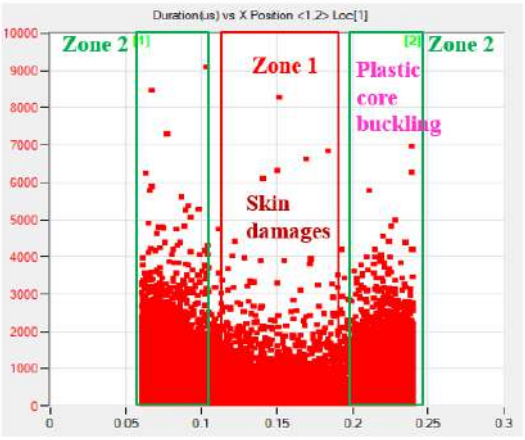

(I) Peak Frequency. (II) Duration.

(d) t=600 s in post-buckling stage after point C.

Fig. 4-10. Damage localizations (Unit of X position: m) of specimen Dry H2 by AE.

In localization results of wet sandwich specimens in Fig. 4-11, similar AE peak frequency and duration distributions can be found. In the first linear stage before point A in Fig. 4-11. (a), most signals within 100-400 kHz appear in zone 2, with duration less than 3000 μs. Very few signals within 100-300 kHz appear in zone 1, with duration less than 2000 μs.

In the second non-linear pre-buckling stage AB in Fig. 4-11. (b), compared to the dry sandwich, fewer honeycomb core buckling signals within 300-600 kHz [121] accumulate in zone 2. Combined with the IRT image, the honeycomb core buckling in zone 2 in the wet sandwich is less obvious, so AE localizations agree well with the IRT image. In zone 1, there are also fewer signals lower than 300 kHz. Signals in zone 2 have duration less than 4000 μs, and those in zone 1 have duration less than 2000 μs.

In post-buckling stages BC in Fig. 4-11. (c) and in Fig. 4-11. (d) after point C, it's obvious that the number of signals within 300-600 kHz has decreased a lot in zone 2, which demonstrates that the honeycomb core buckling of the wet sandwich has become less severe. Signals in zone 1 and 2 have duration less than 10000 μs.

Finally, it can be concluded that the peak frequency is a very useful parameter to identify the skin damages (lower than 300 kHz), core buckling and cracking (lower than 600 kHz), and core wrinkling (300-600 kHz), combined with the damage localizations by IRT and microscopes. But it is difficult to find the difference of the duration of different damage modes according to the localization figures. Thus, peak frequency shall be investigated detailly to identify damages of CFRP-honeycomb sandwich in the future.

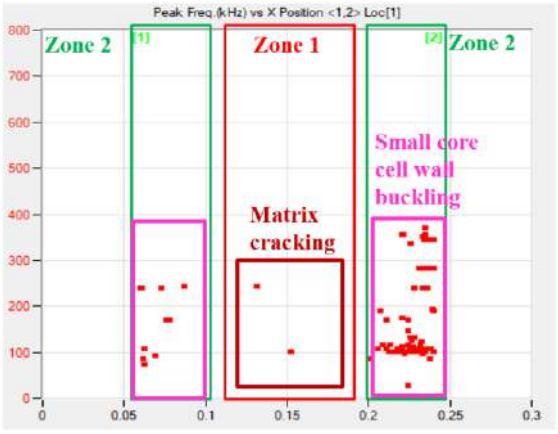

(I) Peak Frequency.

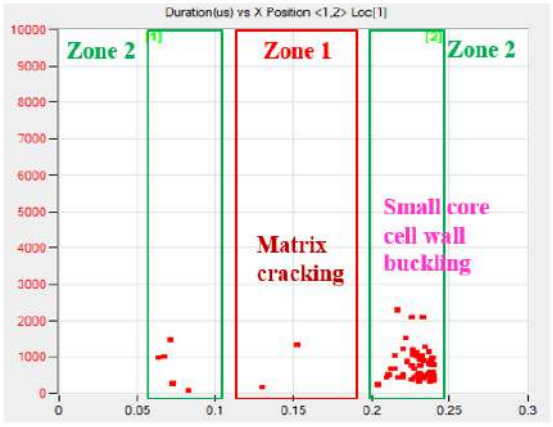

(II) Duration.

(a) t=100 s in linear stage before point A.

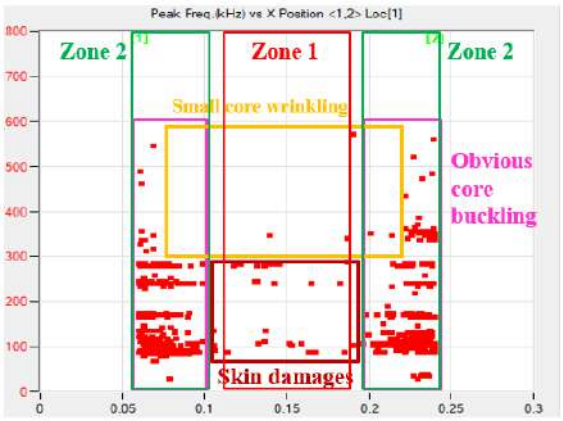

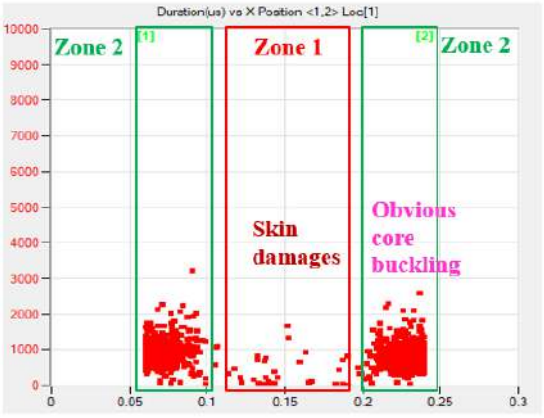

(I) Peak Frequency. (II) Duration.

(b) t=180 s in pre-buckling stage AB.

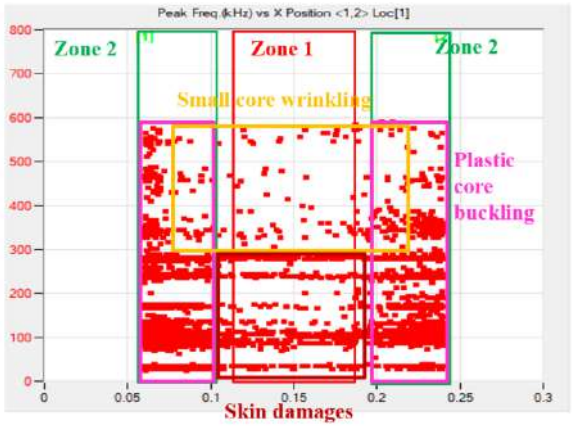

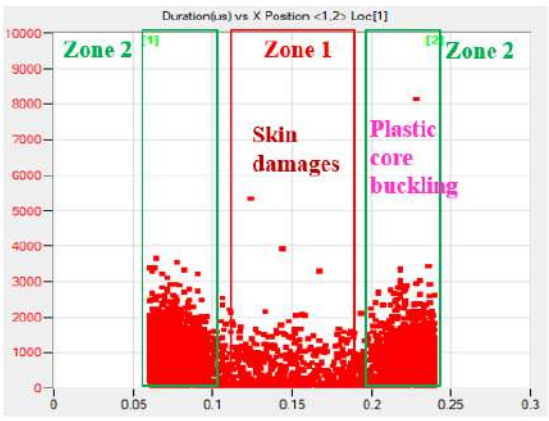

(I) Peak Frequency. (II) Duration.

(c) t=350 s in post-buckling stage BC.

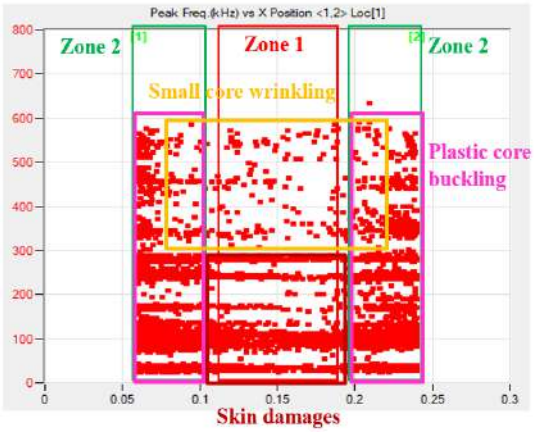

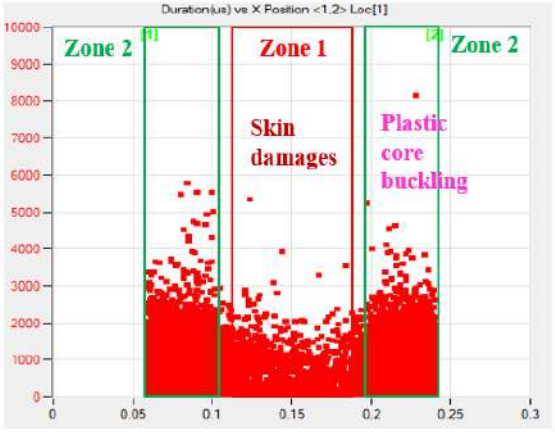

(I) Peak Frequency. (II) Duration.

(d) t=600 s in post-buckling stage after point C.

Fig. 4-11. Damage localizations (Unit of X position: m) of 5.5% MC specimen Wet H1 by AE.

4.2.5. Moisture effects on damage initiation identification by AE

4.2.5.1. Moisture effects on cumulative hits

Although the damage localization results of wet CFRP-honeycomb sandwich by IRT is not accurate enough, which cannot be compared with localization results by AE. Moisture effects on the cumulative AE hits number of the three CFRP-honeycomb sandwich specimens with different MC are illustrated in Fig. 4-12, to show the preliminary analysis of AE signals. It can be seen that the cumulative hits number of the 5.5% MC specimen and 11% MC specimen has decreased by 28% and 31%, respectively, due to the moisture absorption. One reason for this decrease is that the energy released by the wet sandwich specimen has been decreased, in addition, the acoustic wave attenuation is higher due to moisture absorption, as demonstrated in Chapter 2. When the acoustic wave propagates in the wet CFRP-honeycomb sandwich, it will meet more obstacles such as material and interface changes, because water, air, honeycomb and CFRP exist simultaneously in the wet sandwich. Then the acoustic wave propagation has been disturbed by these internal changes.

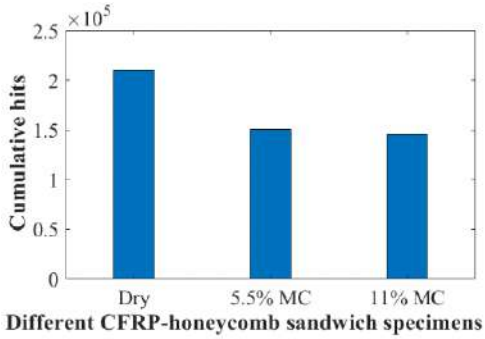

Fig. 4-12. Cumulative hits number of dry and wet CFRP-honeycomb sandwiches.

4.2.5.2. Moisture effects on cumulative energy

Moisture effects on cumulative energy of CFRP-honeycomb sandwich are also shown in Fig. 4-13. It shows that the final cumulative energy at the end of the tests has been decreased as MC increases. The cumulative energy of the 5.5% MC specimen and 11% MC specimen has decreased by 23% and 31%, respectively. Considering the damages observed by IRT and microscope, it means that the damages of wet sandwiches have released lower energy, which can be related to the less severe core buckling due to moisture absorption. Because the honeycomb core mainly carries the shear stresses in a sandwich structure, the core buckling damage shall be the dominated, so AE observations have verified that the predominant core buckling has released lower energy in the wet sandwiches.

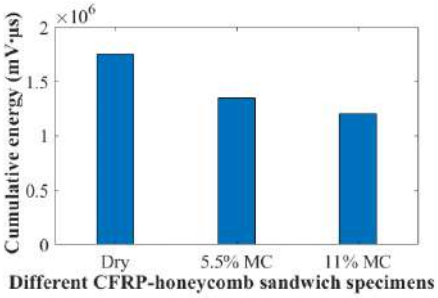

Fig. 4-13. Cumulative energy of dry and wet CFRP-honeycomb sandwiches.

4.2.5.3. Moisture effects on cumulative counts

Similar to the analysis method of GFRP-balsa sandwich, in order to identify the damage onset moment of CFRP-honeycomb sandwich, cumulative counts accumulation is firstly investigated in Fig. 4-14. It's interesting to find the four stages of CFRP-honeycomb sandwich under 4-point bending can be reflected by the slope of cumulative counts curves, almost divided by point A, B and C. For all dry and wet specimens, cumulative counts have an obvious increase just after point A, where the obvious pre-buckling of honeycomb core begins. After point B, the slope of cumulative counts curve increases, and after point C, the slope has a small decrease again. It means that the cumulative counts accumulate more intensely in stage BC, and the plastic core buckling mainly initiates and propagates in this period. Wet sandwiches have the smaller number of cumulative counts within longer period AB and BC, which indicates that the honeycomb core buckling is less severe.

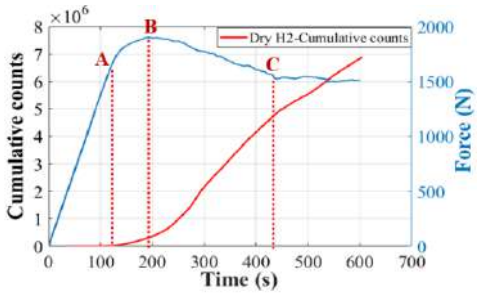

(a) Specimen Dry H2.

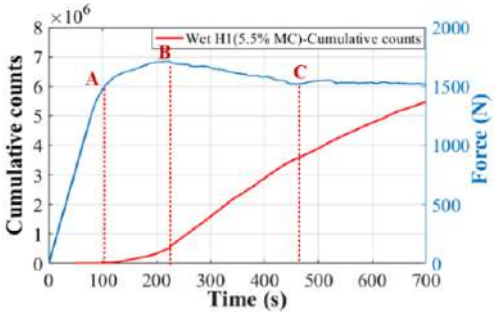

(c) 5.5% MC specimen Wet H1.

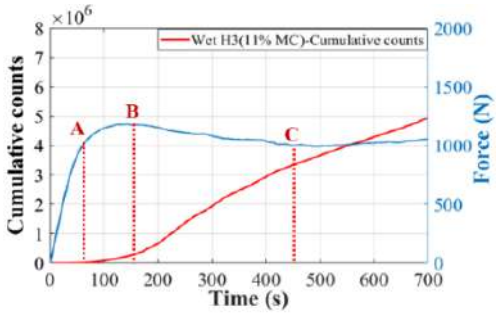

(d) 11% MC specimen Wet H3.

Fig. 4-14. Cumulative counts of dry and wet CFRP-honeycomb sandwiches.

4.2.6. Experimental conclusions

In conclusion, by microscope, IRT and AE observations, it can be found that moisture absorption can result in the more obvious honeycomb cell wall wrinkling mainly due to compression stresses near the loading applications in zone 1 and zone 2, but less severe core buckling in zone 2. The damage localizations by IRT and AE show good consistency. It can be further simulated by Abaqus models.

4.3. Numerical analysis of 4-point bending behaviors

4.3.1. Abaqus model establishment

Different from numerical simulations of GFRP-balsa sandwich, the non-linear 4-point bending behavior of CFRP-honeycomb sandwich was simulated by dynamic explicit analysis in Abaqus/Standard 2019. In explicit analysis of Abaqus, time period is firstly given by 0.08 s in the step settings. Considering that the final displacement in tests is about 20 mm, in all the models, the max vertical displacement is set by 20 mm (see Fig. 4-15. (a)) for dry sandwich and 25 mm for wet sandwich considering the real displacement in 4-point bending tests, which determines the end moment of the simulation. The two lower supports are fixed to eliminate all degrees of freedom. For the interaction between skins and loading/support surfaces, surface-to-surface contact was chosen to ensure the convergence of the models, and friction coefficient is given by 0.05 [41] to allow some slippage between the surfaces and stability after testing different values of friction coefficient. Based on damage observations in tests, honeycomb core damages are predominant, so skin/core interfaces are tied in the models without considering skin/core debonding.

Based on the classical laminate theory, 3-layer CFRP skins (see Fig. 4-15. (b)) are modelled by continuous thin shell element S4R (without thickness definition). Considering that the core is composed of the thin honeycomb cell walls (with a thickness of 0.065 mm), which is much smaller than the diameter of the honeycomb cell (4.8 mm), the honeycomb core is also created by continuous thin shell element S4R (see Fig. 4-15. (c)).

As seen in Fig. 4-15. (d), one honeycomb cell is composed of six cell walls along three directions: 0^o which is along the specimen length direction, 60^o and 120^o which have a certain angle relative to the 0^o direction. So, the local material orientations of these three kinds of cell walls are different, as shown by the three green honeycomb shell elements. The 1-axis of the honeycomb shell element along 0^o is the same as the specimen length direction, the 2-axis is along the height of the wall (the thickness direction of the sandwich), and the 3-axis is normal to the shell element plane. The 1-axis of the honeycomb shell element along 60^o is also along 60^o, and 1-axis of the honeycomb shell

element along 120° is also along 120°. While 2-axis of all the honeycomb shell elements is along the sandwich thickness direction, and 3-axis is normal to the corresponding shell element plane.

Dependency of calculation accuracy on the mesh size was studied by using different cell size of 3 mm, 2.5 mm and 2 mm for both skin and core elements. Finally, in order to compromise between computational efficiency and accuracy, the mesh element is chosen as 2.5 mm for both the skins and honeycomb cells.

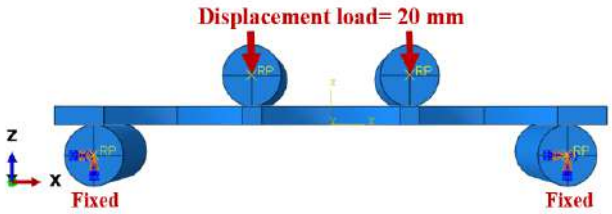

(a) Loading and boundary conditions.

(b) Thin shell elements of CFRP skin.

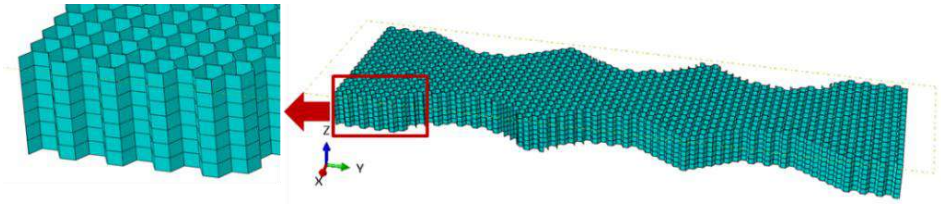

(c) Thin shell elements of honeycomb core.

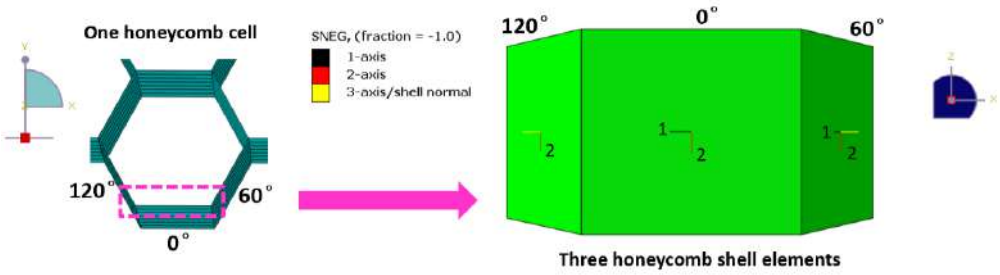

(d) Local material orientations of honeycomb shell elements.

Fig. 4-15. Abaqus model of CFRP-honeycomb sandwich under 4-point bending.

Finally, the most important problem is to determine accurate material parameters of sandwich constituents. Since bending stiffness of sandwich is mainly determined by elastic modulus of the skin, similar to the analysis of GFRP skins in Chapter 3, the degradation of elastic modulus of CFRP

skin of wet sandwich has been considered based on the proposed method by AE wave velocity measurements, as seen in Table 2-9. For Nomex honeycomb paper, it has been demonstrated that isotropic material model can be accurate enough [186], so elastic modulus of honeycomb core is given by 4000 MPa and Poisson's ratio is 0.35.

4.3.2. Equivalent elastic-plastic and shear damage model

Since 4-point bending behavior of honeycomb sandwich is mainly determined by honeycomb core buckling properties, the progressive damage model considering the elastic-plastic behavior and shear damage criterion of the honeycomb core is developed in this work. Fig. 4-16 [214] explains the stress-strain relation employed in Abaqus/Explicit for ductile metals up to complete failure. In this work, according to the simulations in [165, 186], the honeycomb core is assumed as the isotropic material, and thus the elastic-plastic progressive damage model for ductile isotropic material in Abaqus can be applied on it, to simulate the core buckling behavior equivalently.

As shown in Fig. 4-16, the typical linear elastic response appears firstly, followed by the non-linear plastic behavior. Yield point A is determined by the yield stress of the material. A damage model variable *D* is introduced and it equals 0 at damage initiation point B. The equivalent plastic strain at the onset of damage is denoted as $\bar{\varepsilon}_0^{\mathrm{pl}}$, and it can be a function of stress ratio, strain rate, temperature, etc. Subsequently, the yield stress softens and elastic modulus degrades until the strain reaches $\bar{\varepsilon}_{\mathrm{f}}^{\mathrm{pl}}$, or the equivalent strain at complete failure. Finally, elements representing failed material points are removed from the model.

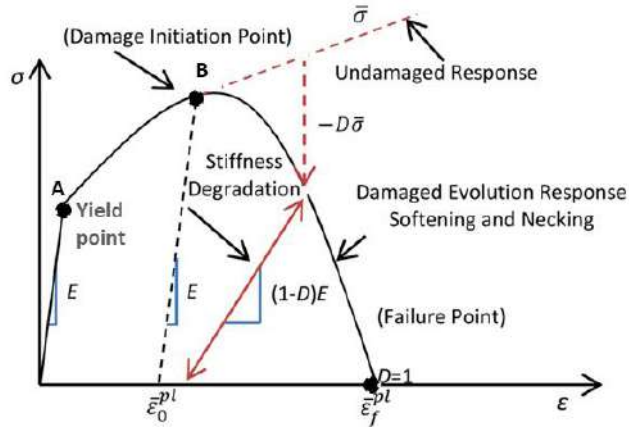

Fig. 4-16. Schematic diagram of elastic-plastic material with progressive damage [214].

When the damage behavior described in Fig. 4-16 is applied to the honeycomb core to simulate the honeycomb buckling damage, the four stages of Force/Displacement curves of CFRP-honeycomb sandwich in Fig. 4-2 could be considered. In this study, the yield stress point in Fig. 4-16 shall be point A in Fig. 4-2 which is the transition from elastic linear behavior to non-linear behavior.

According to [165, 186], the von Mises yield stress of the Nomex honeycomb is about 100 MPa, because the average strength of wet sandwich has decreased by 12% in Fig. 4-2, the yield stress of the wet honeycomb is set by 88 MPa, to simulate the elastic behavior before point A.

Next, in order to determine the damage initiation and evolution process after point A, the shear damage criterion [164, 186] is introduced into Fig. 4-16, since the shear damage criterion can be used in conjunction with the Von Mises, Johnson-Cook, Hill, and Drucker-Prager plasticity models. Firstly, the shear damage initiation criterion is used for predicting the onset of damage mainly due to shear band localization. It assumes that the equivalent plastic strain $\bar{\varepsilon}_0^{pl}$ at the damage onset is a function of the shear stress ratio and strain rate. The shear stress ratio in Abaqus is defined as $\theta_s=(q+k_sp)/\tau_{max}$, where q is the Von Mises equivalent stress, p is the pressure stress, and τ_{max} is the maximum shear stress. k_s is the material parameter which can be calculated according to the other parameters.

In order to simulate the core shear damage initiation, the equivalent plastic (fracture) strain, the shear stress ratio and the strain rate shall be input into Abaqus to get the more accurate simulation results. Shear stress ratio is given by a common value 1.6 [164, 186], and the simulation results can display this value to help us to determine whether it is set accurately. The equivalent plastic strain rate of the honeycomb material is 0.01-250 s^{-1} according to [186] and almost has no influence on the simulation results, so it is set by 0.01 s^{-1} in this work. Fracture strain $\bar{\varepsilon}_0^{pl}$ determines the damage initiation point B in Fig. 4-16 and max force in Fig. 4-2, referred to [186], the shear fracture strain of Nomex honeycomb is between 0.04 and 0.08, so the influence of these fracture strain values will be discussed in this work.

Next, in order to simulate the core shear damage evolution after point B, the damage evolution criterion shall be introduced, which is also based on the fracture energy rate [164]. Similar to the analysis of GFRP-balsa sandwich, there is no clear test standards to determine this parameter of Nomex honeycomb. Referred to [165], it has been pointed out that fracture energy for the longitudinal tensile/compressive failure of fiber of aramid-epoxy laminates is between 20 N/mm and 50/mm, so different groups with various fracture energy values will be compared in the simulations. When simulating the damage evolution, the two kinds of the damage degradation law as a function of plastic displacement can be considered: a) linear; b) exponential, as seen in Fig. 4-17 where d is the damage variable and $\bar{u}^{pl}$ is the equivalent plastic displacement. Considering the decreasing tendency of force in Fig. 4-2, the exponential type is finally chosen in our simulation.

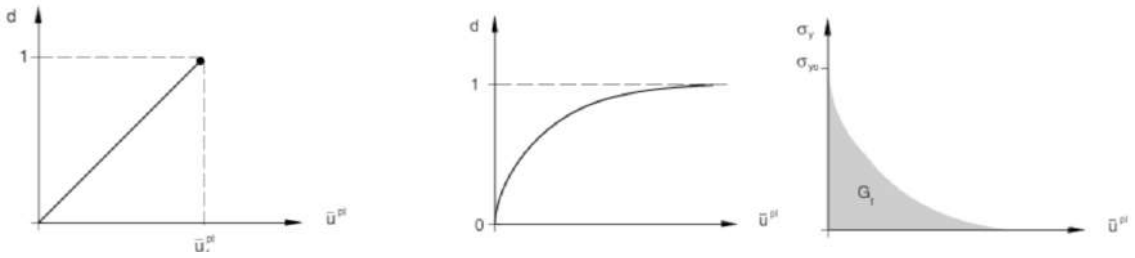

(a) Linear displacement. (b) Exponential displacement and the corresponding fracture energy.

Fig. 4-17. Damage degradation law as a function of plastic displacement in damage evolution model [164].

Finally, the importance of fracture strain and fracture energy on the honeycomb plastic and shear damage initiation and evolution will be discussed in the following work.

4.3.3. Prediction of 4-point bending behaviors

4.3.3.1. Prediction of bending stiffness and strength

Table 4-3 and 4-4 show different groups with different fracture strain and energy values used in the simulation of dry CFRP-honeycomb sandwich, while Table 4-5 show those of the wet sandwich. Firstly, as demonstrated before, bending stiffness of sandwich in simulation is mainly affected by the values of elastic modulus of the laminated skin. Fig. 4-17 compares Force/Displacement curves predicted by numerical models and those in the tests for both dry and wet specimens. It is interesting to note that numerical bending stiffnesses of all groups are very near to those of the tests in the first linear stage before point A. The calculated bending stiffnesses of dry and wet CFRP-honeycomb sandwich specimens in initial elastic linear stages are 517 N/mm and 502 N/mm. Compared to the average tested bending stiffnesses of dry (605 N/mm) and wet (596 N/mm) CFRP-honeycomb sandwich specimens, their relative error is about 15% and 16% for dry and wet specimen, respectively. These results could be acceptable. Consequently, the variation of elastic constants of wet CFRP/honeycomb sandwich skin as a function of MC predicted by the proposed methodology to modify elastic modulus by AE wave velocity can be effective to predict the bending stiffness of the wet sandwich.

Table 4-3. Groups of different fracture strain of dry honeycomb in Abaqus.

Group	Dry HS1	Dry HS2	Dry HS3	Dry HS4
Fracture strain	0.08	0.07	0.06	0.05
Fracture energy (N/mm)	50	50	50	50

Table 4-4. Groups of different fracture energy of dry honeycomb in Abaqus.

Group	Dry HS1	Dry HS5	Dry HS6	Dry HS7
Fracture strain	0.08	0.08	0.08	0.08
Fracture energy (N/mm)	50	60	40	30

Table 4-5. Different groups of fracture energy of wet honeycomb in Abaqus.

Group	Wet HS1	Wet HS2	Wet HS3	Wet HS4
Fracture strain	0.08	0.09	0.10	0.10
Fracture energy (N/mm)	50	50	50	40

Fig. 4-18. (a) shows that the damage initiation point B and damage stabilization point C appear a little later as the fracture strain increases from 0.04 to 0.08 when the fracture energy is 50 N/mm. Considering both the max force and the corresponding displacement at which point B appears, the curve of simulation Dry HS1 (in green) is nearest to the experimental results. The error between max force (1721 N at Dis.=6.2 mm) of simulation Dry HS1 and that (1901 N at Dis.=5.7 mm) of the test is 9.5%.

Fig. 4-18. (b) also shows that the damage initiation point B and damage stabilization point C appear later as the fracture energy increases from 30 N/mm to 60 N/mm when the fracture strain is 0.08. It can be seen that the curve of simulation Dry HS5 (in green) shows the nearest max force and corresponding displacement. In summary, the fracture strain mainly affects the damage initiation moment B, and the fracture energy has greater influence on the final damage stabilization point C.

Based on the simulation results of dry sandwiches, Fig. 4-18. (c) shows the results obtained for different groups of wet sandwiches. It shows that simulation Wet HS3 (in blue) is nearest to the average test curve, when the fracture strain is 0.10 and fracture energy is 50 N/mm. The error between the max force (1454 N at Dis.=7.1 mm) of simulation Wet HS3 and that (1529 N at Dis.=7.0 mm) of the test is only 4.9%. Moreover, the decrease rate in stage BC of simulation curves of wet sandwich seems much smaller than that of dry ones. It also demonstrates that this equivalent elastic-plastic damage model is suitable for both dry and wet honeycomb sandwiches, to predict the bending behavior quickly and accurately.

To be mentioned, in stage AB, the simulation of wet sandwich is much closer to the experimental curve, while the numerical curve of dry sandwich is a little different from the experimental curve. This is because of the elastoplastic behavior with isotropic hardening phenomenon. In the models in this work, the hardening after the yield point is not considered, so the models are more accurate when the material has absorbed water and become softer. It also indicates that the damage models for dry sandwich can be improved by adding the hardening criterion of the Nomex honeycomb material.

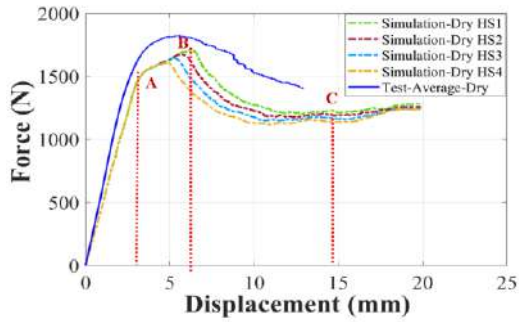

(a) Different fracture strain of dry sandwich.

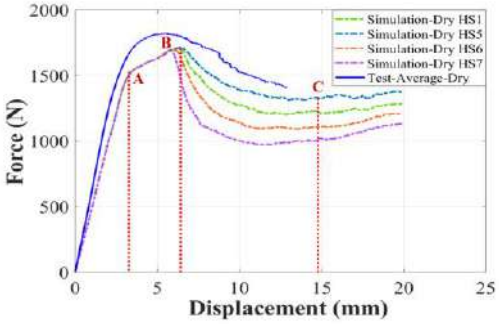

(b) Different fracture energy of dry sandwich.

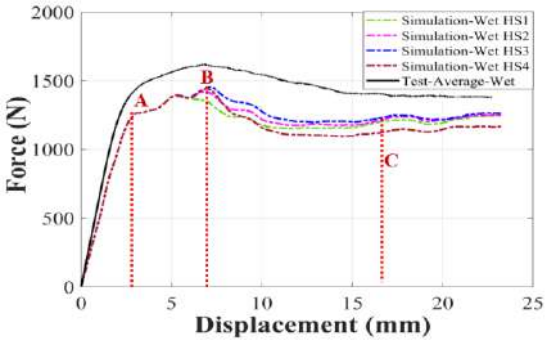

c) Different groups of wet sandwich (6.5% MC).

Fig. 4-18. Comparison of simulation and test results of dry and wet CFRP-honeycomb sandwich.

4.3.3.2. Damage localizations by numerical models

In this part, only the results from Simulation Dry HS1 and Wet HS3 will be discussed. Their damage initiation and evolution images are shown in Fig. 4-19 and Fig. 4-20, respectively.

In Fig. 4-19. (a) and Fig. 4-20. (a), only honeycomb core damages in zone 2 appear in Abaqus models. In the ideal case, in zone 1, there is no shear stress, so no damage occurs in the center. Herein, the damage indexes (SHRCRT) represent the shear damage criterion. The damage initiates when SHRCRT exceeds 0. The full damage of the element occurs only when SHRCRT equals 1. The fully failed elements will be removed finally.

It is clear that the most damaged regions (red mesh cells) are located near the center of zone 2 of honeycomb core where there is the highest shear stress, and near the loading application regions. It can be noted that the distributions of red elements are similar to observations by IRT. Near the loading application regions and supports regions, contact stresses are superimposed with the shear stress, where the damage has been perturbed. This can be demonstrated by the next stress distributions. Around the loading application regions, the full damaged elements (red elements) have moved to the traction zone due to the bending moment, which also agrees well with microscope, IRT and AE observations.

Fig. 4-19. (b)-(e) and Fig. 4-20. (b)-(e) show the damage initiation and evolution of the dry and wet sandwich with the increase of applying displacement (Dis.) or force (F) in the four stages divided by point A, B and C, compared with the damage localizations by IRT images.

Fig. 4-19. (b) and Fig. 4-20. (b) show that the small honeycomb core buckling initiates in the center of zone 2 where the max shear stress exists before point A. Fig. 4-19. (c) and Fig. 4-20. (c) correspond to point B when the max force exists, and the red elements appear in center of zone 2, which agrees well with the obvious core buckling localized by the IRT image. Fig. 4-19. (d) and Fig. 4-20. (d) show the obvious plastic core buckling elements in the traction region in zone 2 at point C after which the final platform follows the post-buckling stage BC. Obvious core shear crack band can be seen on the dry honeycomb. Fig. 4-19. (e) and Fig. 4-20. (e) shows that some fully failed red elements in the traction region near the center of zone 2 have been removed after point C, which shall be the fully damaged honeycomb cells. The locations of these elements agree well with those observed by the IRT image.

Furthermore, comparing the simulation results of the dry and wet sandwich, it can be seen that more red elements near the loading application regions appear in zone 2 of the wet sandwich after point B, which can explain the higher temperature increase of wet sandwich because higher damage energy has been accumulated. But fewer elements have been removed near the center of zone 2 in the wet sandwich, which means that core shear cracks of the wet sandwich have become less severe. Therefore, it verifies that the honeycomb core compressive strength plays a more important role in wet sandwich, compared to the shear strength. This will be further demonstrated by the stress distributions.

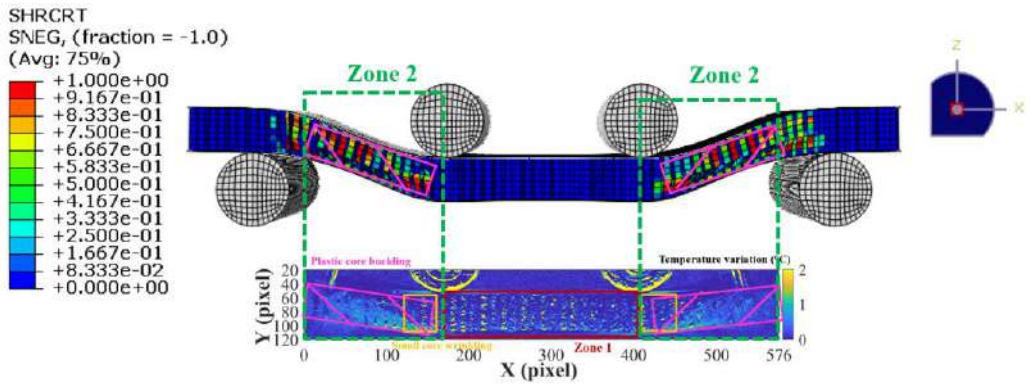

(a) Damage localization by the shear damage model and IRT.

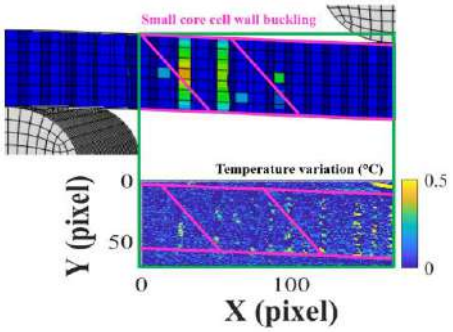

(b) Point A: Dis.=3.4 mm, F=1520 N.

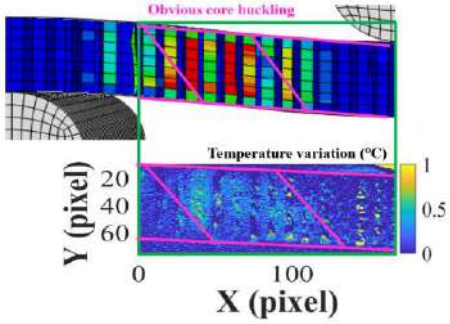

(c) Point B: Dis.=6.2 mm, F=1721 N.

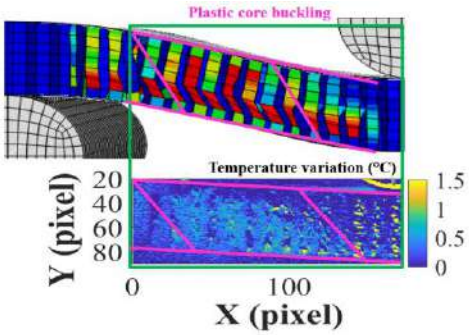

(d) Point C: Dis.=14.0 mm, F=1221 N.

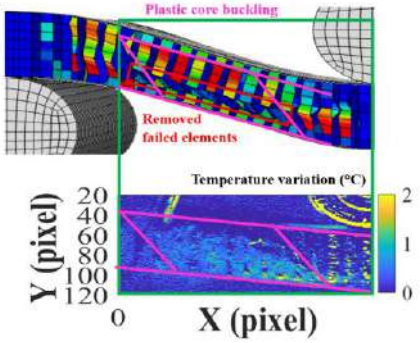

(e) After C: Dis.=20 mm, F=1311 N.

Fig. 4-19. Damage evolution prediction of dry sandwich by Abaqus simulation model Dry HS1.

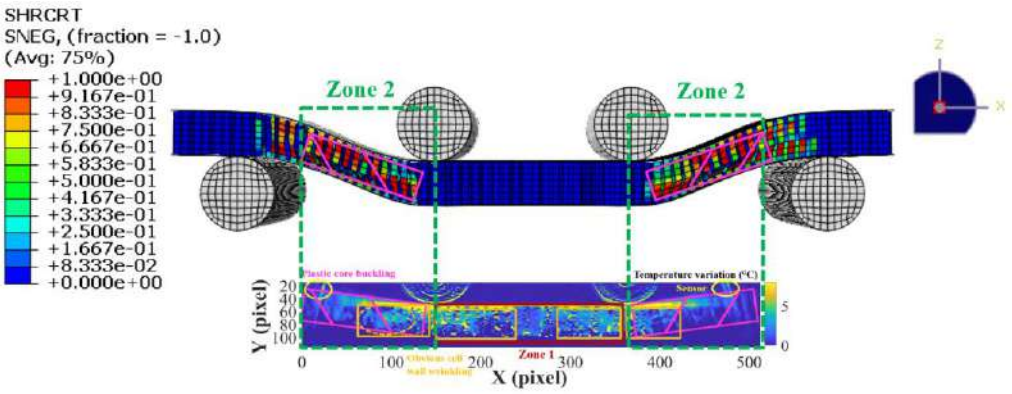

(a) Damage localization by the shear damage model and IRT.

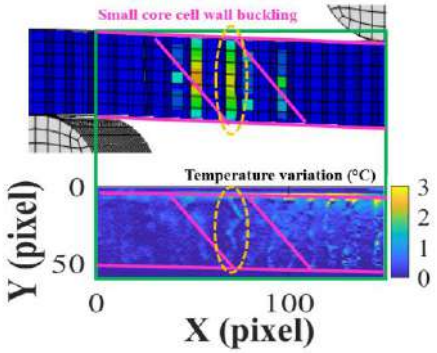

(b) Point A: Dis.=2.6 mm, F=1202 N.

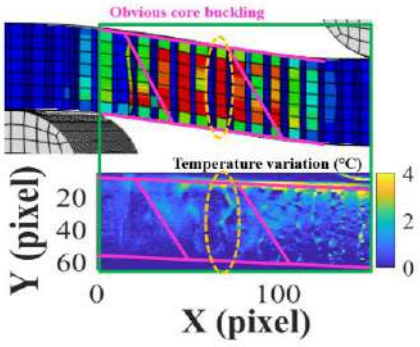

(c) Point B: Dis.=7.1 mm, F=1454 N.

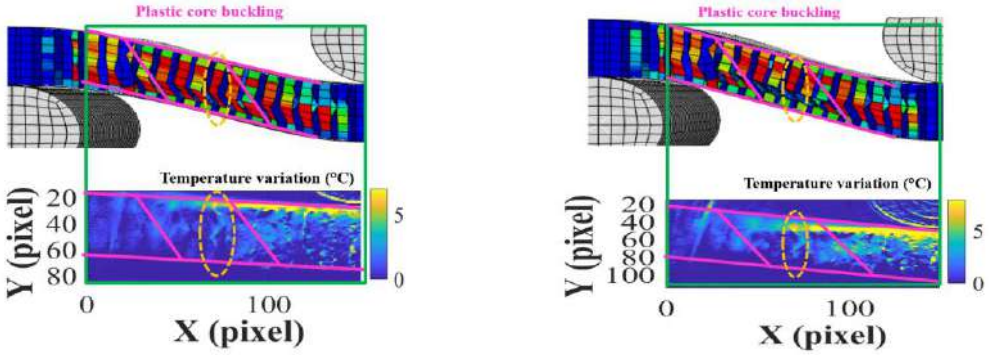

(a) Point C: Dis.=17.0 mm, F=1253 N. (e) After C: Dis.=20 mm, F=1215 N.

Fig. 4-20. Damage evolution prediction of wet sandwich by Abaqus simulation model Wet HS3.

4.3.3.3. Stress distributions in honeycomb core

In order to understand the honeycomb core damage modes, the stress distributions in zone 2 of dry and wet sandwich corresponding to the moment of point A, B, C and the final platform are further discussed in Fig. 4-21 and Fig. 4-22. Since the honeycomb cells are created by thin shell elements, the local material orientation of each wall of a honeycomb cell is different, as explained in Fig. 4-15. (d) . So, the local material axes on each wall are different from the global coordinates. As seen in Fig. 4-21. (a) and Fig. 4-22. (a), a typical honeycomb shell element along 0^o which is along the specimen length direction is chosen to understand the max stress variation. For element 1 and element 2, 1-axis is along the sandwich length direction, 2-axis is along height of a wall (the thickness direction of the sandwich), and the 3-axis is normal to the cell wall plane. Normal stress components S11, S22 and shear stress S12 are shown in Fig. 4-21. (b)-(e) and Fig. 4-22. (b)-(e).

It can be seen that in dry and wet sandwiches, the shear stress (S12) distribution remains almost even and stable in stage AB, as seen in Fig. 4-21. (b)-(c) and 4-22. (b)-(c). But the max shear stress (red elements) distribution in dry sandwich is along about 45^o in zone 2 after point C in Fig. 4-21. (d) and (e), which matches well with microscope and IRT observations. However, in wet sandwich Fig. 4-22. (d) and (e), the core shear crack band along 45^o in zone 2 is not obvious. Concerning normal stress (S22) in the direction of the height of the honeycomb cell walls, in dry or wet sandwiches, it remains much smaller than the shear stress S12 in most honeycomb elements in center of zone 2. But the stresses S22 of honeycomb elements near the loading applications and supports keep increasing from point A. The blue elements show that the normal stresses (S22) in compression near the loading application regions are more important in the wet sandwich, which may cause the indentation due to contact stresses

These stress variation and distributions verify that the honeycomb core damages in this work in zone 2 is caused by the combination of shear stress S12 and normal stresses S11 and S22. The

predominant damage mode is core buckling due to shear stress S12. And some core wrinkling (indentation) caused by normal stresses S11 and S22 near the loading applications can be found after point B. It indicates that moisture absorption could result in the less obvious honeycomb core shear cracks due to the decrease of shear stress.

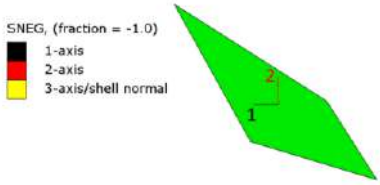

(a) Local material orientations on deformed element 1 along 0° in zone 2 at point C.

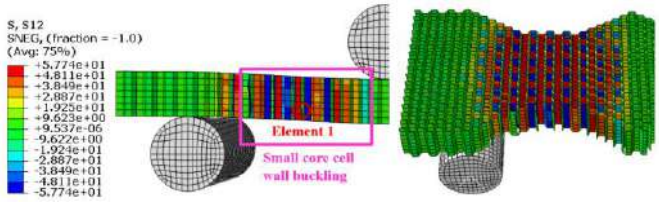

(I) Shear stress S12.

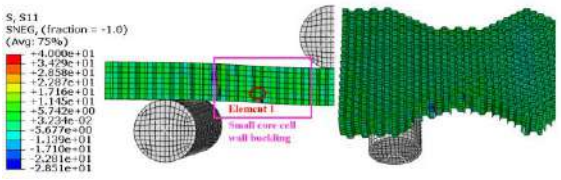

(II) Normal stress S11.

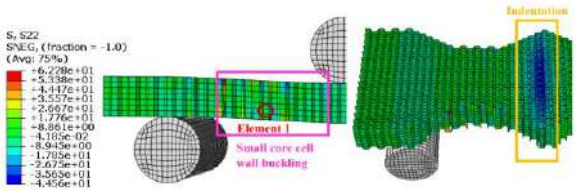

(III) Normal stress S22.

(b) Point A: Dis.=3.4 mm, F=1520 N.

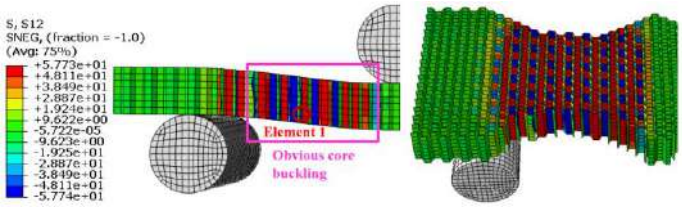

(I) Shear stress S12.

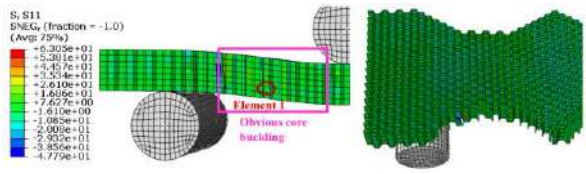

(II) Normal stress S11.

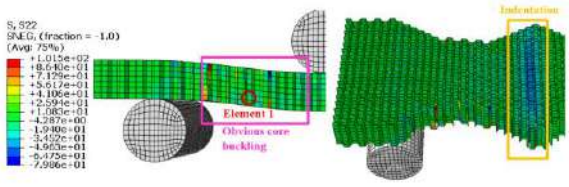

(III) Normal stress S22.

(c) Point B: Dis.=6.2 mm, F=1721 N.

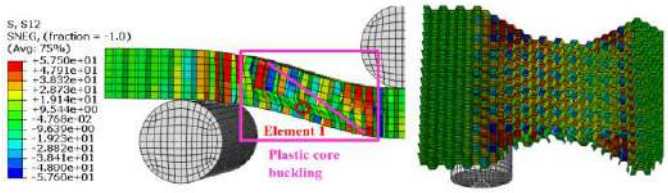

(I) Shear stress S12.

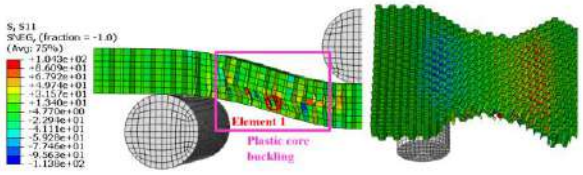

(II) Normal stress S11.

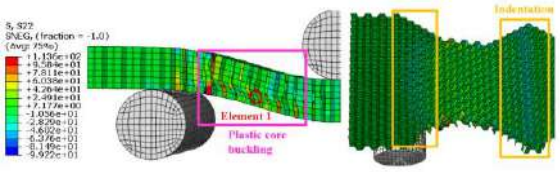

(III) Normal stress S22.

(d) Point C: Dis.=14.0 mm, F=1221 N.

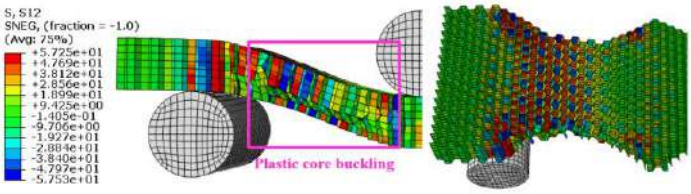

(I) Shear stress S12.

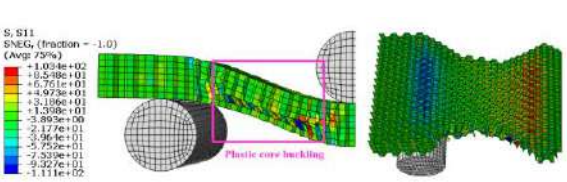

(II) Normal stress S11.

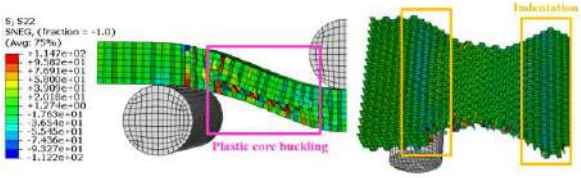

(III) Normal stress S22.

(e) After C: Dis.=20 mm, F=1311 N.

Fig. 4-21. Stress distributions in zone 2 of dry sandwich by Abaqus simulation model Dry HS1.

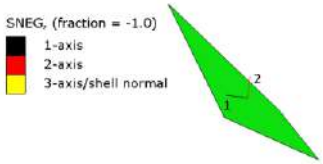

(a) Local material orientations on deformed element 2 along 0° in zone 2 at point C.

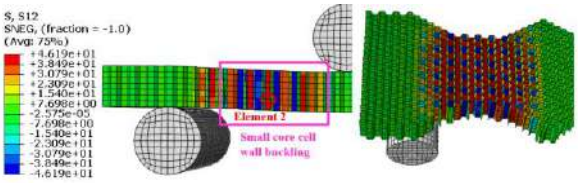

(I) Shear stress S12.

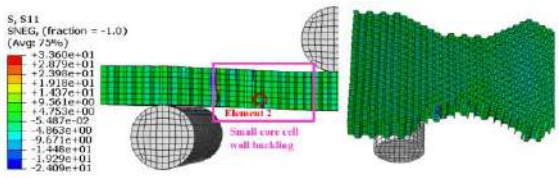

(II) Normal stress S11.

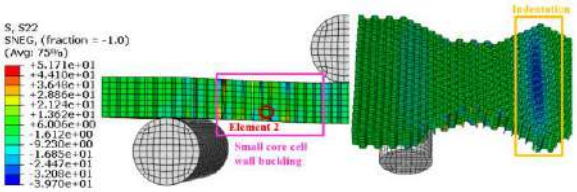

(III) Normal stress S22.

(b) Point A: Dis.=3.4 mm, F=1520 N.

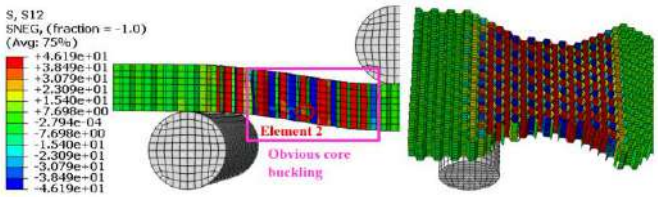

(I) Shear stress S12.

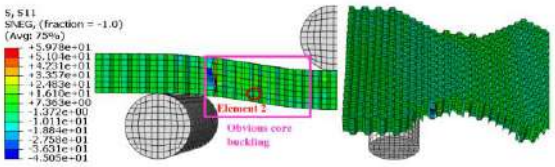

(II) Normal stress S11.

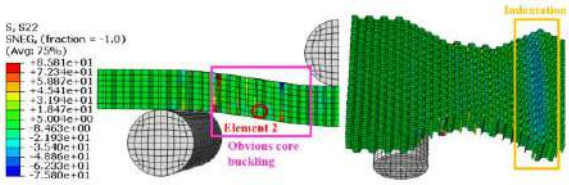

(III) Normal stress S22.

(c) Point B: Dis.=6.2 mm, F=1721 N.

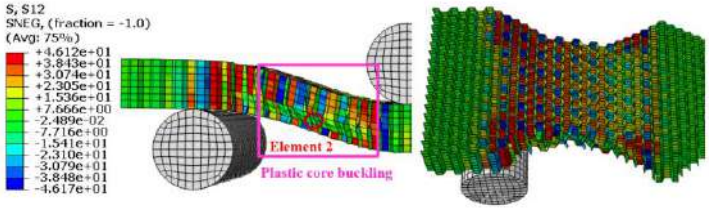

(I) Shear stress S12.

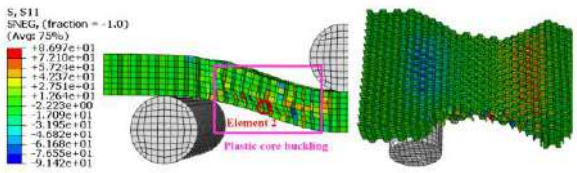

(II) Normal stress S11.

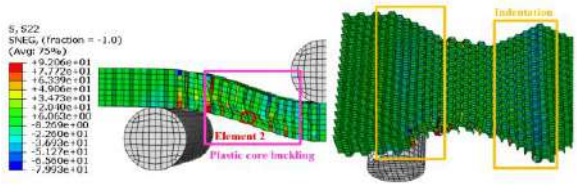

(III) Normal stress S22.

(d) Point C: Dis.=14.0 mm, F=1221 N.

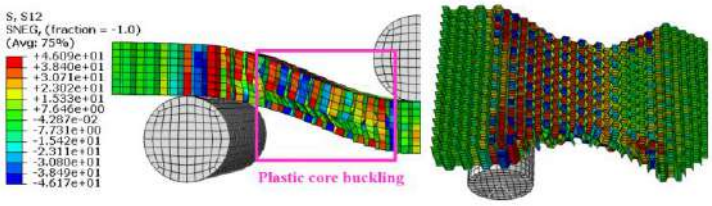

(I) Shear stress S12.

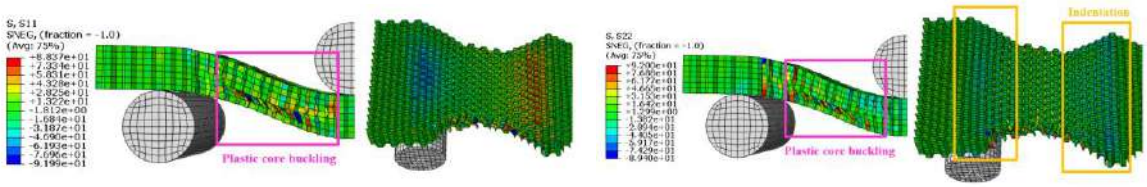

(II) Normal stress S11. (III) Normal stress S22.

(e) After C: Dis.=20 mm, F=1311 N.

Fig. 4-22. Stress distributions in zone 2 of wet sandwich by Abaqus simulation model Wet HS3.

Fig. 4-23 and Fig. 4-24 further plot the stress variation of the most deformed cell 1 of dry sandwich and cell 2 of wet sandwich as a function of displacement of the sandwich in the four stages, in order to observe the shear and compressive stresses corresponding to point A, B and C in Fig. 4-18. It is interesting to find the shear stress S12 increases almost linearly until 58 MPa for dry sandwich and 46 MPa for wet sandwich at point A, and then it keeps almost stable until point B, and it begins to decrease after point B, until zero near point C.

The normal stress S22 (in compression) begins to increase only after point A, and it continues to increase until the maximum 17 MPa for dry sandwich and 19 MPa for wet sandwich at point D, and then it begins to decrease until zero near point C. The normal stress S11 (in compression) begins to increase only after point B, and it continues to increase until the maximum 10 MPa for dry sandwich and 10 MPa for wet sandwich near point D, and then it begins to decrease until zero near point C.

Thus, for both dry and wet sandwich, in stage AB, shear stress S12 is much higher than normal stresses S11 and S22 which mainly causes the local core shear cracks. In stage BD, the shear stress S12 is also higher than normal stresses, so the core shear cracks are predominant, but the normal stresses have increased a lot. The normal stress S22 may cause the core wrinkling. After point D, the normal stress S22 is higher than the shear stress S12, so more obvious core wrinkling can be found. After point C, all the stresses become zero, so the final platform appears.

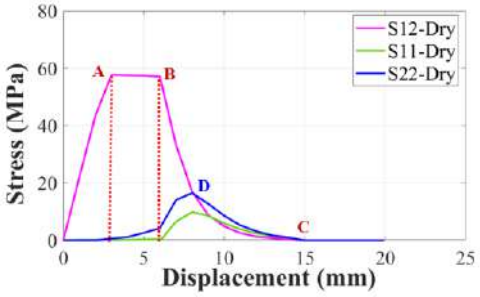

Fig. 4-23. Stress variation of Cell 1 in zone 2 of dry sandwich by Abaqus simulation model Dry HS1.

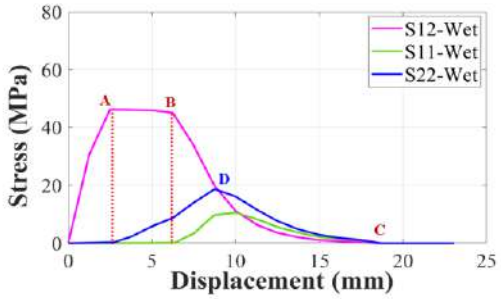

Fig. 4-24. Stress variation of Cell 2 in zone 2 of wet sandwich by Abaqus simulation model Wet HS3.

Combined with the previous microscope, IRT and AE observations, the normal stress S22 in the wet sandwich has become more predominant in stage AC, which will result in the more obvious core wrinkling near the loading application regions. But the core shear stress S12 become less important in wet sandwich, thus resulting in the less severe core shear cracks. It is also obvious that the decreasing rates of the shear and normal stresses of wet sandwich in stage BC seem smaller than those of the dry sandwich, which agree well with the tendency of Force/Displacement curves in Fig. 4-18.

4.3.4. Numerical conclusions

To conclude, to predict the non-linear 4-point bending behavior of CFRP-honeycomb sandwich, the equivalent progressive elastic-plastic isotropic material model and shear damage criterion have been chosen to approximately simulate the damage initiation and evolution process of honeycomb core, as well as the bending stiffness and strength. Based on the proposed new methodology to evaluate elastic modulus variation of CFRP skin due to moisture absorption by AE wave velocity in Chapter 2, moisture effects on elastic modulus, yield stress, fracture strain and fracture energy rate of Nomex honeycomb are introduced into Abaqus models to improve the prediction accuracy of wet sandwich.

In addition, damage localizations and evolution tendency predicted by Abaqus models agree well with IRT and AE observations, which have been demonstrated by the shear and compressive stress distributions.

4.4. Chapter summary

In summary, in this chapter, moisture effects on bending stiffness/strength and the damage mechanisms of CFRP-honeycomb sandwich under 4-point bending have been discussed, based on the observations by the microscope, IRT and AE. Although IRT has met some difficulty in identifying damages of wet sandwiches, some useful conclusions can be made.

Firstly, by the microscope observations, it can be seen that moisture absorption can result in the more obvious honeycomb cell wall wrinkling near the loading application regions in zone 2, but less severe

core shear cracks in zone 2. The damage localizations of dry sandwich by IRT agree well with the those observed by AE and Abaqus models. For IRT, in order to improve the quality of thermal images by IRT, the better image processing is necessary for wet sandwich, to consider the correlations between thermal field change, honeycomb shear/compressive damage evolution and moisture content variation.

By AE, it is demonstrated by cumulative energy that wet honeycomb core damages have released lower energy. Cumulative counts have been proven to be also useful for the identification of initiation of the four stages of bending behaviors of honeycomb sandwich, including the first linear elastic stage before yield point A, the second pre-buckling stage before max force point B, the third post-buckling stage BC, and the final platform after point C.

The numerical models show good agreement with experimental observations of bending stiffness, strength, damage localization and evolution. It verifies that the new proposed method in Chapter 2 can be effective for prediction of bending stiffness of wet CFRP-honeycomb sandwich by measuring AE wave velocity. However, the material property of honeycomb core is simplified by a homogenous isotropic model, and only equivalent elastic-plastic and shear damage criterion has been used. Therefore, further simulations considering the buckling damage model shall be studied to accurately simulate the honeycomb core damage mechanisms. In addition, future work shall be done to introduce the other damage modes, including the composite skin damages and skin/core debonding, to improve the simulation accuracy.

Conclusions and Perspectives

In this PhD thesis, moisture effects on bending behaviors and damage mechanisms of GFRP-balsa sandwich and CFRP-honeycomb sandwich have been investigated by static 4-point bending tests combining the microscope, IRT and AE observations. Different numerical models have been developed to simulate the bending behaviors and damage evolution of the two kinds of sandwich structures. The numerical simulations and experimental results show good agreements in the bending stiffness, strength and damage localizations. The main contributions of this work can be summarized as follows:

1. By the preliminary Hsu-Nielsen tests, a new strategy of rapid determination of AE wave propagation velocity in any direction is firstly proposed for GFRP-balsa sandwich and CFRP-honeycomb sandwich, based on the measurements of velocity in only one direction in the corresponding composite skin. It validates that the propagation direction farther away from the most fiber orientation of composite laminates and sandwiches will result in the lower wave velocity, which shall not be ignored when localizing damages under loading. These conclusions can serve the more accurate damage localizations in the most commonly used sandwich under loading.

2. Based on the relationships between Moisture Content, AE wave velocity and elastic modulus of the sandwich obtained in preliminary Hsu-Nielsen tests, a new methodology is proposed to predict the elastic modulus of the skin of the wet GFRP-balsa sandwich and wet CFRP-honeycomb sandwich. This new method has been applied through introducing the variation of mechanical properties of the skin of the sandwich as a function of MC into the Progressive Damage Analysis (PDA) model for GFRP-balsa sandwich and equivalent Elastic-plastic progressive damage model for CFRP-honeycomb sandwich in Abaqus, to improve the simulation accuracy of the bending stiffness of the wet sandwich structures. Finally, the numerical bending stiffnesses agree well with the experimental results, which verifies that the proposed methodology can be useful for the stiffness variation evaluation of the sandwich structure, to save a lot of cost and time.

3. For the application of IRT and AE on GFRP-balsa sandwich under 4-point bending, a damage characterization approach coupling the characteristics of AE amplitude, peak frequency and duration via K-means clustering algorithm is developed to identify the damage sequence and classify damage modes of GFRP-balsa sandwich under bending loading. It verifies that IRT can be useful for identifying when and where the damages with high energy appear, for example, fiber breakage. AE can effectively identify and classify different microscopic and macroscopic damage mechanisms, to explain clearly when, where and what kind of damages appear. These conclusions lay very important

foundations for the further applications of IRT and AE techniques on the composite sandwich structures.

4. For the application of IRT and AE on CFRP-honeycomb sandwich under 4-point bending, it demonstrates that the localizations of honeycomb core damages by IRT, AE and numerical models have good concordance. The four stages in the Force/Displacement curves mainly due to honeycomb core buckling behavior can be identified by the AE cumulative counts. In addition to experimental analysis, the developed numerical models for honeycomb cores have been accurate and fast enough to simulate the bending stiffness, strength and core damage evolution, showing obvious four stages, finally to save a lot of time and cost.

This PhD thesis ends here, however, due to the limited time, there are still many research works that we can do in the future, which are listed as:

1. Considering the proposed model to determine AE wave velocity in any direction of the sandwich and the new methodology to predict elastic modulus variation of the skin based on the relationships between Moisture Content, AE wave velocity and elastic modulus of the sandwich, they shall be further validated on other sandwich materials and specimens, such as, foam cored sandwich, CFRP-balsa sandwich, GFRP-honeycomb sandwich, and not only on dog-bone shape specimens, but also on larger sandwich panels.

2. For the study of GFRP-balsa sandwich, IRT can detect clearly the skin damage initiation and evolution process, but AE has met some difficulty in localizing all the damages, due to the decrease of wave velocity because of the damage accumulation under loading and the high attenuation, so the damage localization shall be further studied. In order to improve it, one possible solution will be reducing the sensor distance to make sure that the sensor is nearer to the damage source, or adding more sensors to localize the damages not linearly but triangularly in the plane. Furthermore, the correction of the AE wave velocity as a function of damage evolution index under 4-poing bending loading shall be integrated into the localization setup. In addition, larger triple dog-bone sandwich specimens can be fabricated to repeat the tests and leave more space for the sensors.

3. For the study of CFRP-honeycomb sandwich, IRT has met some difficulties when localizing damages in the wet sandwich, due to moisture absorption. So further tests on the wet CFRP-honeycomb sandwich shall be repeated to improve the damage localization by IRT. Correlations between thermal field change, honeycomb shear/compressive damage evolution and moisture content variation shall be investigated in the future, to classify the different damage modes. In addition, the honeycomb core shall be painted as black to better measure the surface temperature.

And the cumulative heat source field corresponding to irreversible damages shall be calculated by considering all the thermal parameter variations as a function of Moisture Content.

4. For the application of AE on CFRP-honeycomb sandwich under bending, the damage localization is better than that in GFRP-balsa sandwich because more signals have been received. However, further clustering analysis shall be finished in order to classify the honeycomb core buckling, wrinkling and microscopic skin damages more clearly.

5. For the moisture effects on the balsa core, honeycomb core and skin/core interface, further tests shall be added to validate the conclusions in this thesis. For example, debonding fracture tests can be done on the wet GFRP-balsa sandwich, to study the physical reason of the increase of strength of skin/core interface of wet GFRP-balsa sandwich. The influence of the strength of interfaces of different balsa/balsa blocks on the bending strength of the wet sandwich as a function of time shall be also investigated, by comparing the bending responses of wet balsa sandwich specimens with different balsa block interface positions.

6. For the numerical analysis of GFRP-balsa sandwich, further models considering more damage modes shall be developed to improve the accuracy of the prediction, such as, the skin/core debonding and balsa core damages. For the numerical analysis of CFRP-honeycomb sandwich, further simulations considering the buckling damage model shall be studied to accurately simulate the honeycomb core damage mechanisms. In addition, CFRP skin damages and skin/core debonding shall be also considered.

7. Finally, considering the moisture effects on the bending behaviors of the sandwich structure, the relationships of the moisture absorption behavior (Moisture Content as a function of time) and the variation of material parameters such as elastic modulus, strength and fracture energy rate, the AE wave velocity and amplitude attenuation, and the thermal parameters, which shall be further investigated, can be introduced into the numerical models to simulate more accurately the bending behavior of the wet sandwich. In this way, the numerical bending behaviors as a function of water immersion time or Moisture Content can be found.

References

[1] Deane S, Avdelidis N P, Ibarra-Castanedo C, Zhang H, Nezhad H Y,Williamson A A, Mackley T, Davis M J, Maldague X, Tsourdos A. Application of NDT thermographic imaging of aerospace structures. Infrared Physics & Technology 2019; 97: 456-466.

[2] Mrazova M. Advanced composite materials of the future in aerospace industry. Incas bulletin 2013; 5(3): 139.

[3] Ochola R O, Marcus K, Nurick G N, Franz T. Mechanical behaviour of glass and carbon fibre reinforced composites at varying strain rates. Composite Structures 2004; 63(3-4): 455-467.

[4] Sharma S, Sudhakara P, Nijjar S, Saini S, Singh G. Recent progress of composite materials in various novel engineering applications. Materials Today: Proceedings 2018; 5(14): 28195-28202.

[5] Zenkert D. An introduction to sandwich construction. Engineering materials advisory services 1995; 1-82.

[6] Madziara S, Najbert S, Wozniak M, Kubiak P, Ozuna G, De La Fuente P, Jozwiak P. Design and Build Vehicle with Solar Drive for World Solar Challenge Competition. Mechanization in agriculture & Conserving of the resources 2015; 61(11): 23-26.

[7] Vinson J R. Sandwich Structures. Applied Mechanics Reviews 2001; 54(3): 2001.

[8] Birman V, Kardomateas G A. Review of current trends in research and applications of sandwich structures. Composites Part B: Engineering 2018; 142: 221-240.

[9] Thomsen O T. Sandwich structures 7: advancing with sandwich structures and materials: Proceedings of the 7th International Conference on Sandwich Structures. Aalborg University, Aalborg, Denmark, 29-31 August, 2005.

[10] Cantwell W J, Scudamore R, Ratcliffe J, Davies P. Interfacial fracture in sandwich laminates. Composites Science and Technology 1999; 59(14): 2079-2085.

[11] Mohammadi M S, Nairn J A. Balsa sandwich composite fracture study: Comparison of laminated to solid balsa core materials and debonding from thick balsa core materials. Composites Part B: Engineering 2017; 122: 165-172.

[12] Senthil K, Arockiarajan A, Palaninathan R, Santhosh B, Usha K M. Defects in composite structures: Its effects and prediction methods-A comprehensive review. Composite Structures 2013; 106: 139-149.

[13] Elanchezhian C, Ramnath B V, Hemalatha J. Mechanical behaviour of glass and carbon fibre reinforced composites at varying strain rates and temperatures. Procedia Materials Science 2014; 6: 1405-1418.

[14] Steeves C A, Fleck N A. Material selection in sandwich beam construction. Scripta materialia 2004; 50(10): 1335-1339.

[15] Kirollos B W M, Trede R, Lampen P. The experimental static mechanical performance of ironed repaired GFRP-honeycomb sandwich beams. Journal of Sandwich Structures & Materials 2012; 14(6): 694-714.
[16] Cantwell W J, Broster G, Davies P. The influence of water immersion on skin-core debonding in GFRP-balsa sandwich structures. Journal of reinforced plastics and composites 1996; 15(11): 1161-1172.
[17] Banhart J. Manufacture, characterisation and application of cellular metals and metal foams. Progress in materials science 2001; 46(6): 559-632.
[18] Aviles F, Aguilar-Montero M. Mechanical degradation of foam-cored sandwich materials exposed to high moisture. Composite Structures 2010; 92(1): 122-129.
[19] Sypeck D J, Wadley H N G. Cellular metal truss core sandwich structures. Advanced Engineering Materials 2002; 4(10): 759-764.
[20] Wang B, Wu L, Ma L, Sun Y. Mechanical behavior of the sandwich structures with carbon fiber-reinforced pyramidal lattice truss core. Materials & Design (1980-2015) 2010; 31(5): 2659-2663.
[21] Borrega M, Gibson L J. Mechanics of balsa (Ochroma pyramidale) wood. Mechanics of Materials 2015; 84: 75-90.
[22] Da Silva A, Kyriakides S. Compressive response and failure of balsa wood. International Journal of Solids and Structures 2007; 44(25): 8685-8717.
[23] Vural M, Ravichandran G. Dynamic response and energy dissipation characteristics of balsa wood: experiment and analysis. International Journal of Solids and structures 2003; 40(9): 2147-2170.
[24] Osei-Antwi M, De Castro J, Vassilopoulos A P, et al. Shear mechanical characterization of balsa wood as core material of composite sandwich panels. Construction and Building Materials 2013; 41: 231-238.
[25] Soden P D, McLeish R D. Variables affecting the strength of balsa wood. The Journal of Strain Analysis for Engineering Design 1976; 11(4): 225-234.
[26] Amraei M, Shahravi M, Noori Z, Lenjani A. Application of aluminium honeycomb sandwich panel as an energy absorber of high-speed train nose. Journal of Composite Materials 2014; 48(9): 1027-1037.
[27] Karakoç A, Freund J. Experimental studies on mechanical properties of cellular structures using Nomex® honeycomb cores. Composite Structures 2012; 94(6): 2017-2024.
[28] Wang Z, Zhang Y, Liu J. Comparison between five typical reinforced honeycomb structures. 5th International Conference on Advanced Engineering Materials and Technology. Guangzhou, China, 22-23 August, 2015.

[29] Fogarty J H. Honeycomb core and the myths of moisture ingression. Applied Composite Materials 2010; 17(3): 293-307.
[30] Chen Z, Yan N. Investigation of elastic moduli of Kraft paper honeycomb core sandwich panels. Composites Part B: Engineering 2012; 43(5): 2107-2114.
[31] Zhang X, Chen Y, Hu J. Recent advances in the development of aerospace materials. Progress in Aerospace Sciences 2018; 97: 22-34.
[32] Thomsen O T. Sandwich materials for wind turbine blades—present and future. Journal of Sandwich Structures & Materials 2009; 11(1): 7-26.
[33] Mouritz A P, Gellert E, Burchill P, Challis K. Review of advanced composite structures for naval ships and submarines. Composite structures 2001; 53(1): 21-42.
[34] Bergan P G, Buene L, Echtermeyer A T, Hayman B. Assessment of FRP sandwich structures for marine applications. Marine structures 1994; 7(2-5): 457-473.
[35] Earl J S, Shenoi R A. Hygrothermal ageing effects on FRP laminate and structural foam materials. Composites Part A: Applied science and manufacturing 2004; 35(11): 1237-1247.
[36] Legrand V, TranVan L, Jacquemin F, Casari P. Moisture-uptake induced internal stresses in balsa core sandwich composite plate: Modeling and experimental. Composite Structures 2015; 119: 355-364.
[37] Veazie D R, Robinson K R, Shivakumar K. Effects of the marine environment on the interfacial fracture toughness of PVC core sandwich composites. Composites Part B: Engineering 2004; 35(6-8): 461-466.
[38] Kolat K, Neşer G, Özes Ç. The effect of sea water exposure on the interfacial fracture of some sandwich systems in marine use. Composite Structures 2007; 78(1): 11-17.
[39] Herrmann A S, Zahlen P C, Zuardy I. Sandwich structures technology in commercial aviation, Sandwich structures 7: Advancing with sandwich structures and materials. Springer, Dordrecht, 2005: 13-26.
[40] Jerome P. Composite materials in the airbus A380-from history to future. Proceedings 13th International Conference on Composite Materials (ICCM-13). Beijing, China, 25-29 June, 2001.
[41] Alila F. Analyse de la tenue en fatigue de structures composites sandwich. PhD Thesis, Nantes, 2017.
[42] Li C, Cantarel A, Gong X, Liang D. Numerical Simulation of Characteristic of Resin Infusion at Micro-scale. 21st International Conference on Composite Materials, Xi'an (2017) 1-10.
[43] Munoz Cuartas V. Identification de mécanismes d'endommagement de stratifiés carbone-époxyde par couplage de l'émission acoustique et de la thermographie infrarouge. PhD Thesis, Toulouse, 2015.

[44] Ghobadi A. Common type of damages in composites and their inspections. World Journal of Mechanics 2017; 7(2): 24-33.
[45] Daniel I M, Abot J L. Fabrication, testing and analysis of composite sandwich beams. Composites Science and Technology 2000; 60(12-13): 2455-2463.
[46] https://www.3accorematerials.com/en/markets-and-products/baltek-balsa/baltek-sb-balsa.
[47] Galos J, Sutcliffe M, Newaz G. Design, fabrication and testing of sandwich panel decking for use in road freight trailers. Journal of Sandwich Structures & Materials 2018; 20(6): 735-758.
[48] Le Duigou A, Deux J M, Davies P, Baley C. PLLA/flax mat/balsa bio-sandwich manufacture and mechanical properties. Applied Composite Materials 2011; 18(5): 421-438.
[49] Shahdin A, Mezeix L, Bouvet C, Morlier J, Gourinat Y. Fabrication and mechanical testing of glass fiber entangled sandwich beams: A comparison with honeycomb and foam sandwich beams. Composite Structures 2009; 90(4): 404-412.
[50] Wadley H N G, Fleck N A, Evans A G. Fabrication and structural performance of periodic cellular metal sandwich structures. Composites science and technology 2003; 63(16): 2331-2343.
[51] Brechet Y, Bassetti D, Landru D, Salvo L. Challenges in materials and process selection. Progress in materials Science 2001; 46(3-4): 407-428.
[52] Atas C, Sevim C. On the impact response of sandwich composites with cores of balsa wood and PVC foam. Composite Structures 2010; 93(1): 40-48.
[53] Scudamore R J, Cantwell W J. The effect of moisture and loading rate on the interfacial fracture properties of sandwich structures. Polymer composites 2002; 23(3): 406-417.
[54] Goodrich T, Nawaz N, Feih S, Lattimer B Y, Mouritz A P. High-temperature mechanical properties and thermal recovery of balsa wood. Journal of wood science 2010; 56(6): 437-443.
[55] Sadler R L, Sharpe M, Panduranga R, Shivakumar K. Water immersion effect on swelling and compression properties of Eco-Core, PVC foam and balsa wood. Composite Structures 2009; 90(3): 330-336.
[56] Zaharia S M, Morariu C O, Nedelcu A, Pop M A. Experimental study of static and fatigue behavior of CFRP-balsa sandwiches under three-point flexural loading. BioResources, 2017; 12(2): 2673-2689.
[57] Hoff N J, Mautner S E. Bending and buckling of sandwich beams. Journal of the Aeronautical Sciences, 1948; 15(12): 707-720.
[58] Paik J K, Thayamballi A K, Kim G S. The strength characteristics of aluminum honeycomb sandwich panels. Thin-walled structures 1999; 35(3): 205-231.
[59] Lu C, Zhao M, Jie L, Wang J, Gao Y, Cui X. Stress distribution on composite honeycomb sandwich structure suffered from bending load. Procedia Engineering 2015; 99: 405-412.

[60] Mamalis A G, Spentzas K N, Pantelelis N G, Manolakos D E, Ioannidis M B. A new hybrid concept for sandwich structures. Composite Structures 2008; 83(4): 335-340.
[61] Arbaoui J, Schmitt Y, Pierrot J L, Royer X. Effect of core thickness and intermediate layers on mechanical properties of polypropylene honeycomb multi-layer sandwich structures. Archives of Metallurgy and Materials 2014; 59(1): 11-16.
[62] ASTM C393/C393M-06. Standard Test Method for Core Shear Properties of Sandwich Constructions by Beam Flexure. 2006.
[63] ASTM D7249/D7249M−12. Standard Test Method for Facing Properties of Sandwich Constructions by Long Beam Flexure. 2012.
[64] Rajaneesh A, Sridhar I, Rajendran S. Failure mode maps for circular composites sandwich plates under bending. International Journal of Mechanical Sciences 2014; 83: 184-195.
[65] Daniel I. Influence of core properties on the failure of composite sandwich beams. Journal of Mechanics of Materials and Structures 2009; 4(7): 1271-1286.
[66] Petras A, Sutcliffe M P F. Failure mode maps for honeycomb sandwich panels. Composite structures 1999; 44(4): 237-252.
[67] Daniel I M, Gdoutos E E, Wang K A, Abot J. Failure modes of composite sandwich beams. International journal of damage mechanics 2002; 11(4): 309-334.
[68] Li Z, Zheng Z, Yu J, Qian C, Lu F. Deformation and failure mechanisms of sandwich beams under three-point bending at elevated temperatures. Composite structures 2014; 111: 285-290.
[69] Sayahlatifi S, Rahimi G, Bokaei A. Experimental and numerical investigation of sandwich structures with balsa core and hybrid corrugated composite/balsa core under three-point bending using digital image correlation. Journal of Sandwich Structures & Materials 2021; 23(1): 94-131.
[70] Shi H, Liu W, Fang H. Damage characteristics analysis of GFRP-Balsa sandwich beams under Four-point fatigue bending. Composites Part A: Applied Science and Manufacturing 2018; 109: 564-577.
[71] Osei-Antwi M, De Castro J, Vassilopoulos A P, Keller. Fracture in complex balsa cores of fiber-reinforced polymer sandwich structures. Construction and Building Materials 2014; 71: 194-201.
[72] Hassinen P, Martikainen L, Berner K. On the design and analysis of continuous sandwich panels. Thin-Walled Structures 1997; 29(1-4): 129-139.
[73] Xie S, Feng Z, Zhou H, Wang D. Three-point bending behavior of Nomex honeycomb sandwich panels: Experiment and simulation. Mechanics of Advanced Materials and Structures 2021; 28(18): 1917-1931.
[74] Wu X, Yu H, Guo L, Zhang L, Sun X, Chai Z. Experimental and numerical investigation of static and fatigue behaviors of composites honeycomb sandwich structure. Composite Structures 2019; 213: 165-172.

[75] Palomba G, Crupi V, Epasto G. Collapse modes of aluminium honeycomb sandwich structures under fatigue bending loading. Thin-Walled Structures 2019; 145: 106363.
[76] Belouettar S, Abbadi A, Azari Z, Belouettar R, Freres P. Experimental investigation of static and fatigue behaviour of composites honeycomb materials using four-point bending tests. Composite Structures 2009; 87(3): 265-273.
[77] Li X, Weitsman Y J. Sea-water effects on foam-cored composite sandwich lay-ups. Composites Part B: Engineering 2004; 35(6-8): 451-459.
[78] Alomayri T, Assaedi H, Shaikh F U A, Low I M. Effect of water absorption on the mechanical properties of cotton fabric-reinforced geopolymer composites. Journal of Asian ceramic societies 2014; 2(3): 223-230.
[79] Katzman H A, Castaneda R M, Lee H S. Moisture diffusion in composite sandwich structures. Composites Part A: Applied Science and Manufacturing 2008; 39(5): 887-892.
[80] Célino A, Fréour S, Jacquemin F, Casari P. The hygroscopic behavior of plant fibers: a review. Frontiers in chemistry 2014; 1: 43.
[81] Gerhards C C. Effect of moisture content and temperature on the mechanical properties of wood: an analysis of immediate effects. Wood and Fiber Science 1982; 14(1): 4-36.
[82] Feng A, Zhang Y. Study on moisture absorption and sweat discharge of honeycomb polyester fiber. IOP Conference Series: Materials Science and Engineering, 2015; 87(1): 012095.
[83] Radtke T C, Charon A, Vodicka R. Hot/wet environmental degradation of honeycomb sandwich structure representative of F/A-18: Flatwise Tension Strength. Defence Science and Technology Organisation Melbourne, Australia, 1999.
[84] Veazie D R, Robinson K R, Shivakumar K. Effects of the marine environment on the interfacial fracture toughness of PVC core sandwich composites. Composites Part B: Engineering 2004; 35(6-8): 461-466.
[85] Scudamore R, Cantwell W J. The effect of moisture and loading rate on the interfacial fracture properties of sandwich structures. Polymer composites 2002; 23(3): 406-417.
[86] Gholizadeh S. A review of non-destructive testing methods of composite materials. Procedia Structural Integrity 2016; 1: 50-57.
[87] Adams R D, Cawley P. A review of defect types and nondestructive testing techniques for composites and bonded joints. NDT international 1988; 21(4): 208-222.
[88] Garnier C, Pastor M L, Eyma F, Lorrain B. The detection of aeronautical defects in situ on composite structures using Non-Destructive Testing. Composite structures 2011; 93(5): 1328-1336.
[89] Yang R, He Y, Zhang H. Progress and trends in nondestructive testing and evaluation for wind turbine composite blade. Renewable and Sustainable Energy Reviews 2016; 60: 1225-1250.

[90] Dwivedi S K, Vishwakarma M, Soni A. Advances and researches on nondestructive testing: A review. Materials Today: Proceedings 2018; 5(2): 3690-3698.
[91] Ibrahim M E. Nondestructive evaluation of thick-section composites and sandwich structures: A review. Composites Part A: Applied Science and Manufacturing 2014; 64: 36-48.
[92] Amenabar I, Mendikute A, López-Arraiza A, Lizaranzu M, Aurrekoetxea J. Comparison and analysis of non-destructive testing techniques suitable for delamination inspection in wind turbine blades. Composites Part B: Engineering 2011; 42(5): 1298-1305.
[93] Munoz V, Valès B, Perrin M, Pastor M L, Welemane H, Cantarel A and Karama M. Damage detection in CFRP by coupling acoustic emission and infrared thermography. Composites Part B: Engineering 2016; 85: 68-75.
[94] Perrin M, Yahyaoui I, Gong X. Acoustic monitoring of timber structures: Influence of wood species under bending loading. Construction and Building Materials 2019; 208: 125-134.
[95] Yahyaoui I. Contribution au suivi par émission acoustique de l'endommagement des structures multi-matériaux à base de bois. PhD Thesis, Université Paul Sabatier-Toulouse III, 2017.
[96] Scruby C B. An introduction to acoustic emission. Journal of Physics E: Scientific Instruments 1987; 20(8): 946.
[97] Gholizadeh S, Leman Z, Baharudin B T H T. A review of the application of acoustic emission technique in engineering. Structural Engineering and Mechanics 2015; 54(6): 1075-1095.
[98] Dahmene F, Yaacoubi S, Mountassir M E L. Acoustic emission of composites structures: story, success, and challenges. Physics Procedia 2015; 70: 599-603.
[99] Finlayson R D, Friesel M, Carlos M. Health monitoring of aerospace structures with acoustic emission and acousto-ultrasonics. Insight-Wigston then Northampton 2001; 43(3): 155-158.
[100] Ammar I B, Karra C, El Mahi A, El Guerjoumaa R, Haddarb M. Mechanical behavior and acoustic emission technique for detecting damage in sandwich structures. Applied Acoustics 2014; 86: 106-117.
[101] Behnia A, Chai H K, Shiotani T. Advanced structural health monitoring of concrete structures with the aid of acoustic emission. Construction and Building Materials 2014; 65: 282-302.
[102] De Rosa I M, Santulli C, Sarasini F. Acoustic emission for monitoring the mechanical behavior of natural fiber composites: A literature review. Composites part A: applied science and manufacturing 2009; 40(9): 1456-1469.
[103] Gorman M R. Plate wave acoustic emission. The Journal of the Acoustical Society of America 1991; 90(1): 358-364.
[104] Saeedifar M, Zarouchas D. Damage characterization of laminated composites using acoustic emission: A review. Composites Part B: Engineering 2020; 108039.

[105] Barile C, Casavola C, Pappalettera G, Kannan V P. Application of different acoustic emission descriptors in damage assessment of fiber reinforced plastics: A comprehensive review. Engineering Fracture Mechanics 2020; 107083.

[106] Kumar C S, Arumugam V, Sengottuvelusamy R, Srinivasan S, Dhakal H. Failure strength prediction of glass/epoxy composite laminates from acoustic emission parameters using artificial neural network. Applied Acoustics 2017; 115: 32-41.

[107] McCrory J P, Al-Jumaili S K, Crivelli D, Pearson M R, Eatona M, Featherston C A, Guagliano M, Holford K M, Pullin R. Damage classification in carbon fiber composites using acoustic emission: A comparison of three techniques. Composites Part B: Engineering 2015; 68: 424-430.

[108] Tuloup C, Harizi W, Aboura Z, Meyer Y. On the use of in-situ piezoelectric sensors for the manufacturing and structural health monitoring of polymer-matrix composites: A literature review. Composite Structures 2019; 215: 127-149.

[109] Pashmforoush F, Khamedi R, Fotouhi M, Hajikhani M, Ahmadi M. Damage classification of sandwich composites using acoustic emission technique and k-means genetic algorithm. Journal of Nondestructive Evaluation 2014; 33(4): 481-492

[110] Sause M G R, Gribov A, Unwin A R, Horn S. Pattern recognition approach to identify natural clusters of acoustic emission signals. Pattern Recognition Letters 2012; 33(1): 17-23.

[111] Momon S, Godin N, Reynaud P, et al. Unsupervised and supervised classification of AE data collected during fatigue test on CMC at high temperature. Composites Part A: Applied Science and Manufacturing, 2012, 43(2): 254-260.

[112] NOESIS Manual. ENVIROCOUSTICS S.A., Athens, GREECE, 2011.

[113] AEwin^{TM} Software User's Manual. Physical Acoustics Corporation, Princeton Jct., USA, 2004.

[114] Assarar M, Bentahar M, El Mahi A, et al. Monitoring of damage mechanisms in sandwich composite materials using acoustic emission. International Journal of Damage Mechanics 2015; 24(6): 787-804.

[115] Zhang Y, Zhou B, Yu F, Chen C. Cluster analysis of acoustic emission signals and infrared thermography for defect evolution analysis of glass/epoxy composites. Infrared Physics & Technology 2021; 112: 103581.

[116] Masmoudi S, El Mahi A, Turki S. Use of piezoelectric as acoustic emission sensor for in situ monitoring of composite structures. Composites Part B: Engineering 2015; 80: 307-320.

[117] Andrew J J, Arumugam V, Bull D J, Dhakal H N. Residual strength and damage characterization of repaired glass/epoxy composite laminates using AE and DIC. Composite Structures 2016; 152: 124-139.

[118] Oskouei A R, Zucchelli A, Ahmadi M, Minak G. An integrated approach based on acoustic emission and mechanical information to evaluate the delamination fracture toughness at mode I in composite laminate. Materials & Design 2011; 32(3): 1444-1455.
[119] Quispitupa A, Shafiq B, Just F, Serrano D. Acoustic emission based tensile characteristics of sandwich composites. Composites Part B: Engineering 2004; 35(6-8): 563-571.
[120] Fotouhi M, Saeedifar M, Sadeghi S, Najafabadi M A, Minak G. Investigation of the damage mechanisms for mode I delamination growth in foam core sandwich composites using acoustic emission. Structural Health Monitoring 2015; 14(3): 265-280.
[121] Tabrizi I E, Oz F E, Zanjani J S M, Mandal S K, Yildiz M. Failure sequence determination in sandwich structures using concurrent acoustic emission monitoring and postmortem thermography. Mechanics of Materials 2022; 164: 104113.
[122] Ciampa F, Meo M. A new algorithm for acoustic emission localization and flexural group velocity determination in anisotropic structures. Composites Part A: Applied Science and Manufacturing 2010; 41(12): 1777-1786.
[123] Sikdar S, Ostachowicz W, Pal J. Damage-induced acoustic emission source identification in an advanced sandwich composite structure. Composite Structures 2018, 202: 860-866.
[124] Romhány G, Czigány T, Karger-Kocsis J. Failure assessment and evaluation of damage development and crack growth in polymer composites via localization of acoustic emission events: a review. Polymer Reviews 2017; 57(3): 397-439.
[125] Abdulaziz A H, Hedaya M, Elsabbagh A, Holford K M, McCrory J P. Acoustic Emission Source Location in Composite-Honeycomb Sandwich Panel. International Journal of Renewable Energy Research 2021; 11(2): 851-860.
[126] Sikdar S, Mirgal P, Banerjee S, Ostachowicz W. Damage-induced acoustic emission source monitoring in a honeycomb sandwich composite structure. Composites Part B: Engineering 2019; 158: 179-188.
[127] Wu Y, Perrin M, Pastor M L, Casari P, Gong X. On the determination of acoustic emission wave propagation velocity in composite sandwich structures. Composite Structures 2021; 259: 113-231.
[128] Grammatikos S A, Kordatos E Z, Matikas T E. On the fatigue response of a bonded repaired aerospace composite using thermography. Composite Structures 2018; 188: 461-469.
[129] Huang J, Pastor M L, Garnier C, Gong X. Rapid evaluation of fatigue limit on thermographic data analysis. International Journal of Fatigue 2017; 104: 293-301.
[130] Doshvarpassand S, Wu C, Wang X. An overview of corrosion defect characterization using active infrared thermography. Infrared Physics & Technology 2019; 96: 366-389.

[131] Zhao Y, Addepalli S, Sirikham A, Roy R. A confidence map-based damage assessment approach using pulsed thermographic inspection. NDT & E International 2018; 93: 86-97.
[132] Čapka A, Vavilov V P, Rusnáková S, Fojtl L. Detecting water in composite sandwich panels by using infrared thermography. Materials Science Forum. Trans Tech Publications Ltd 2017; 891: 516-521.
[133] Larbi W B, Ibarra-Castanedo C, Klein M. Experimental comparison of lock-in and pulsed thermography for the nondestructive evaluation of aerospace materials. 6th International Workshop, Advances in Signal Processing for Non-Destructive Evaluation of Materials (IWASPNDE), Ontario, Canada, 2009.
[134] Qin Y W, Bao N K. Infrared thermography and its application in the NDT of sandwich structures. Optics and Lasers in Engineering 1996; 25(2-3): 205-211.
[135] Usamentiaga R, Venegas P, Guerediaga J. Infrared thermography for temperature measurement and non-destructive testing. Sensors 2014; 14(7): 12305-12348.
[136] Boccardi S. Infrared thermography to monitoring mechanical tests on composite materials: Experimental procedure and data analysis. PhD Thesis, Universidade do Porto, Portugal, 2017.
[137] Silva A J R. Detection and characterization of defects in composite materials using thermography. PhD Thesis, Universidade do Porto, Portugal, 2016.
[138] Grinzato E, Vavilov V, Kauppinen T. Quantitative infrared thermography in buildings. Energy and buildings 1998; 29(1): 1-9.
[139] Rosina E, Ludwig N, Redaelli V, Robison E. IRT techniques for the detection of timber moisture. Thermosense XXV, International Society for Optics and Photonics 2003; 5073: 100-108.
[140] Vavilov V, Marinetti S, Pan Y, Chulkov A. Detecting water ingress in aviation honeycomb panels: qualitative and quantitative aspects. Polymer Testing 2016; 54: 270-280.
[141] Naderi M, Kahirdeh A, Khonsari M M. Dissipated thermal energy and damage evolution of Glass/Epoxy using infrared thermography and acoustic emission. Composites Part B: Engineering 2012; 43(3): 1613-1620.
[142] Pastor M L, Balandraud X, Grédiac M, Robert J L. Applying infrared thermography to study the heating of 2024-T3 aluminum specimens under fatigue loading. Infrared Physics & Technology 2008; 51(6): 505-515.
[143] Valès B, Munoz V, Welemane H, Pastor M L, Trajin B, Perrin M, Cantarel A, Karama M. Heat source estimation in anisotropic materials. Composite Structures 2016; 136: 287-296.
[144] Vavilov V, Pan Y Y, Nesteruk D. Infrared thermographic inspection of water ingress in composite honeycomb panels. Applied optics 2016; 55(34): D120-D125.
[145] Chen D, Zeng Z, Tao N, Zhang C, Zhang Z. Liquid ingress recognition in honeycomb structure by pulsed thermography. The European Physical Journal-Applied Physics 2013; 62(2).

[146] Chrysafi A P, Athanasopoulos N, Siakavellas N J. Damage detection on composite materials with active thermography and digital image processing. International journal of thermal sciences 2017; 116: 242-253.
[147] Ibarra-Castanedo C, Marcotte F, Genest M. Detection and characterization of water ingress in honeycomb structures by passive and active infrared thermography using a high-resolution camera. 11th International Conference on Quantitative InfraRed Thermography. Naples, Italy, 11-14 June, 2012.
[148] Matsumura H, Ogata T, Hirasawa H, Uchiyama M. Method for detecting moisture in a honeycomb panel. U.S. Patent 5,433,106. 1995; 1-16.
[149] Zhao S, Zhang C, Wu N. Pulsed thermography detection of water and hydraulic oil intrusion in the honeycomb sandwich structure composite. International Symposium on Photoelectronic Detection and Imaging 2011: Advances in Infrared Imaging and Applications. International Society for Optics and Photonics 2011; 8193: 819337.
[150] Wagner D, Ranc N, Bathìas C, Paris P C. Fatigue crack initiation detection by an infrared thermography method. Fatigue & Fracture of Engineering Materials & Structures 2010; 33(1): 12-21.
[151] Amiri M, Khonsari M M. Rapid determination of fatigue failure based on temperature evolution: Fully reversed bending load. International Journal of Fatigue 2010; 32(2): 382-389.
[152] Colombo C, Libonati F, Pezzani F, Salerno A, Vergani L, et al. Fatigue behavior of a GFRP laminate by thermographic measurements. Procedia Engineering 2011; 10: 3518-3527.
[153] Sinan Şahin Ö, Selek M, Kahramanlı Ş. Investigation of bending fatigue of composite plates by using infrared thermography. Advanced Materials Research. Trans Tech Publications Ltd 2011; 268: 406-411.
[154] Wang X G, Crupi V, Guo X L, Zhao Y. Quantitative Thermographic Methodology for fatigue assessment and stress measurement. International Journal of Fatigue 2010; 32(12): 1970-1976.
[155] Saeedifar M, Najafabadi M A, Zarouchas D, Toudeshky H H, Jalalvandd M. Clustering of interlaminar and intralaminar damages in laminated composites under indentation loading using Acoustic Emission. Composites Part B: Engineering 2018; 144: 206-219.
[156] Boccardi S, Carlomagno G M, Meola C. The added value of infrared thermography in the measurement of temperature-stress coupled effects. Sensors & Transducers 2016; 201: 43-51.
[157] Dattoma V, Giancane S. Evaluation of energy of fatigue damage into GFRC through digital image correlation and thermography. Composites Part B: Engineering 2013; 47: 283-289.
[158] Steinberger R, Leitão T I V, Ladstätter E, Pinter G, Billinet W. Infrared thermographic techniques for non-destructive damage characterization of carbon fibre reinforced polymers during tensile fatigue testing. International Journal of Fatigue 2006; 28(10): 1340-1347.

[159] Østergaard R C, Sørensen B F, Brøndsted P. Measurement of interface fracture toughness of sandwich structures under mixed mode loadings. Journal of Sandwich Structures & Materials 2007; 9(5): 445-466.

[160] Kordatos E Z, Aggelis D G, Matikas T E. Monitoring mechanical damage in structural materials using complimentary NDE techniques based on thermography and acoustic emission. Composites Part B: Engineering 2012; 43(6): 2676-2686.

[161] Wang W, Dulieu-Barton J M, Thomsen O T. A methodology for characterizing the interfacial fracture toughness of sandwich structures using high speed infrared thermography. Experimental Mechanics 2016; 56(1): 121-132.

[162] Fruehmann R K, Dulieu-Barton J M, Wang W. Debond damage assessment in foam/composite sandwich structures. 18th international conference on composite materials (ICCM-18). Jeju, Korea, 21-26 August, 2011.

[163] Fan J, Guo X, Wu C. A new application of the infrared thermography for fatigue evaluation and damage assessment. International Journal of Fatigue 2012; 44: 1-7.

[164] AbaqusV6.10. Analysis user's manual. Providence, RI, USA: Abaqus Inc.; 2019.

[165] Medina S A, Meza J M, Kawashita L F. Damage sequence of honeycomb sandwich panels under bending loading: Experimental and numerical investigation. Journal of Reinforced Plastics and Composites 2020; 39(5-6): 175-192.

[166] Piovár S, Kormaníková E. Sandwich beam in four-point bending test: experiment and numerical models. Advanced Materials Research. Trans Tech Publications Ltd 2014; 969: 316-319.

[167] Kreja I. A literature review on computational models for laminated composite and sandwich panels. Open Engineering 2011; 1(1): 59-80.

[168] Irfan S, Siddiqui F. A review of recent advancements in finite element formulation for sandwich plates. Chinese Journal of Aeronautics 2019; 32(4): 785-798.

[169] Foo C C, Chai G B, Seah L K. Mechanical properties of Nomex material and Nomex honeycomb structure. Composite structures 2007; 80(4): 588-594.

[170] Hosseini S M H, Gabbert U. Numerical simulation of the Lamb wave propagation in honeycomb sandwich panels: a parametric study. Composite Structures 2013; 97: 189-201.

[171] Gharib M, Hassanieh A, Valipour H, et al. Three-dimensional constitutive modelling of arbitrarily orientated timber based on continuum damage mechanics. Finite Elements in Analysis and Design, 2017, 135: 79-90.

[172] Barbero E J, Cosso F A, Roman R, Weadon T L. Determination of material parameters for Abaqus progressive damage analysis of E-glass epoxy laminates. Composites Part B: Engineering 2013; 46: 211-220.

[173] Camanho P, Davila C. Mixed-mode decohesion finite elements for the simulation of delamination in composite materials. NASA/TM-2002-211737; 2002; 1–37.
[174] Hashin Z, Rotem A. A fatigue failure criterion for fiber reinforced materials. Journal of composite materials 1973; 7(4): 448-464.
[175] Lapczyk I, Hurtado J A. Progressive damage modeling in fiber-reinforced materials. Composites Part A: Applied Science and Manufacturing 2007; 38(11): 2333-2341.
[176] Xin H, Mosallam A, Liu Y, Wang C, Zhang Y. Analytical and experimental evaluation of flexural behavior of FRP pultruded composite profiles for bridge deck structural design. Construction and Building Materials 2017; 150: 123-149.
[177] Zhao L, Gong Y, Zhang J, Chen Y, Fei B. Simulation of delamination growth in multidirectional laminates under mode I and mixed mode I/II loadings using cohesive elements. Composite Structures 2014; 116: 509-522.
[178] Camanho P P, Davila C G, De Moura M F. Numerical simulation of mixed-mode progressive delamination in composite materials. Journal of composite materials 2003; 37(16): 1415-1438.
[179] Fan C, Jar P Y B, Cheng J J R. Cohesive zone with continuum damage properties for simulation of delamination development in fibre composites and failure of adhesive joints. Engineering Fracture Mechanics 2008; 75(13): 3866-3880.
[180] Turon A, Camanho P P, Costa J, Dávila C G. A damage model for the simulation of delamination in advanced composites under variable-mode loading. Mechanics of materials 2006; 38(11): 1072-1089.
[181] Malek S, Gibson L J. Multi-scale modelling of elastic properties of balsa. International Journal of Solids and Structures 2017; 113: 118-131.
[182] Qiu L P, Zhu E C, Van de Kuilen J W G. Modeling crack propagation in wood by extended finite element method. European Journal of Wood and Wood Products, 2014, 72(2): 273-283.
[183] Matsumoto N, Nairn J A. Fracture toughness of wood and wood composites during crack propagation. Wood and Fiber Science 2012; 44(2): 121-133.
[184] Mackenzie-Helnwein P, Eberhardsteiner J, Mang H A. A multi-surface plasticity model for clear wood and its application to the finite element analysis of structural details. Computational Mechanics, 2003, 31(1): 204-218.
[185] Toson B, Viot P, Pesqué J J. Finite element modeling of Balsa wood structures under severe loadings. Engineering structures 2014; 70: 36-52.
[186] De Dios Rodriguez-Ramirez J, Castanié B, Bouvet C. Experimental and numerical analysis of the shear nonlinear behaviour of Nomex honeycomb core: Application to insert sizing. Composite Structures 2018; 193: 121-139.

[187] Pavlopoulou S, Roy S S, Gautam M, Bradshaw L, Potluri P. Numerical and experimental investigation of the hydrostatic performance of fiber reinforced tubes. Applied Composite Materials 2017; 24(2): 417-448.
[188] Shinde D, Kimbro E, Mohan R, Kelkar A. Mechanical properties of woven fiberglass Composite interleaved with glass nanofibers. Carbon 2013; 2(166.8): 13-5.
[189] Dahle G A, James K R, Kane B, Grabosky J C, Detter A. A review of factors that affect the static load-bearing capacity of urban trees. Arboriculture and Urban Forestry 2017; 43(3): 89-106.
[190] Baydoun S K, Voigt M, Jelich C, Marburg S. A greedy reduced basis scheme for multifrequency solution of structural acoustic systems. International Journal for Numerical Methods in Engineering 2020; 121(2): 187-200.
[191] Alila F, Fajoui J, Kchaou M, Casari P, Wali N, Gerard R. Mechanical characterization of sandwich composite structure using a new experimental approach. Advanced Composites Letters 2016; 25(5): 096369351602500502.
[192] Alila F, Casari P. Fatigue damage and failure analysis of honeycomb sandwich. Procedia Structural Integrity 2019; 19: 101-105.
[193] Prosser W H. Applications of advanced waveform-based ae techniques for testing composite materials. Proceedings of the SPIE Conference on Nondestructive Evaluation Techniques for Aging Instructure and Manufacturing: Materials and Composites. Scottsdale, Arizona, 2-5 December, 1996.
[194] Khon H, Bashkov O V, Zolotareva S V, Solovev D B. Modeling the Propagation of Elastic Ultrasonic Waves in Isotropic and Anisotropic Materials When Excited by Various Sources. Materials Science Forum. Trans Tech Publications 2019; 945: 926-931.
[195] Gorman M R, Prosser W H. AE source orientation by plate wave analysis. Journal of Acoustic Emission 1991; 9(4): 283-288.
[196] Li Y, Yu S S, Dai L, Luo T F, Li M. Acoustic emission signal source localization on plywood surface with cross-correlation method. Journal of wood science 2018; 64(2): 78-84.
[197] Noiret D, Roget J. Calculation of wave propagation in composite materials using the Lamb wave concept. Journal of composite materials 1989; 23(2): 195-206.
[198] Morscher G N, Gyekenyesi A L. The velocity and attenuation of acoustic emission waves in SiC/SiC composites loaded in tension. Composites science and technology 2002; 62(9): 1171-1180.
[199] ISO 12571. Hygrothermal performance of building materials and products-determination of hygroscopic sorption properties. 2013.
[200] ASTM D5229. Standard Test Method for Moisture Absorption Properties and Equilibrium Conditioning of Polymer Matrix Composite Materials. 2004.
[201] Barreira E, Almeida R, Delgado J. Infrared thermography for assessing moisture related phenomena in building components. Construction and building materials 2016; 110: 251-269.

[202] Kee Paik J, Thayamballi A K, Sung Kim G. The strength characteristics of aluminum honeycomb sandwich panels. Thin-Walled Structures 1999; 35(3): 205-231.
[203] Célino A, Fréour S, Jacquemin F, Casari P. Characterization and modeling of the moisture diffusion behavior of natural fibers. Journal of Applied Polymer Science 2013; 130(1): 297-306.
[204] Belingardi G, Martella P, Peroni L. Fatigue analysis of honeycomb-composite sandwich beams. Composites Part A: applied science and manufacturing 2007; 38(4): 1183-1191.
[205] Guzman V A, Brondsted P. Effects of moisture on glass fiber-reinforced polymer composites. Journal of Composite Materials 2015; 49(8): 911-920.
[206] Li H, Li S, Wang Y. Prediction of effective thermal conductivities of woven fabric composites using unit cells at multiple length scales. Journal of Materials Research 2011; 26(3): 384-394.
[207] Li H, Wang N, Han X, Fan B, Feng Z, Guo S. Simulation of Thermal Behavior of Glass Fiber/Phenolic Composites Exposed to Heat Flux on One Side. Materials 2020; 13(2): 421.
[208] Ludwig N, Redaelli V, Rosina E, Augelli F. Moisture detection in wood and plaster by IR thermography. Infrared Physics & Technology 2004; 46(1-2): 161-166.
[209] Belingardi G, Martella P, Peroni L. Fatigue analysis of honeycomb-composite sandwich beams. Composites Part A: applied science and manufacturing 2007; 38(4): 1183-1191.
[210] Wu Y, Pastor M L, Perrin M, Casari P, Gong X. A new methodology to predict moisture effects on mechanical behaviors of GFRP-balsa sandwich by acoustic emission and infrared thermography. Composite Structures 2022; 287: 115-342.
[211] Manalo A C, Aravinthan T, Karunasena W, Islam M M. Flexural behaviour of structural fibre composite sandwich beams in flatwise and edgewise positions. Composite Structures 2010; 92(4): 984-995.
[212] Pavlopoulou S, Roy S S, Gautam M, Bradshaw L, Potluri P. Numerical and experimental investigation of the hydrostatic performance of fibre reinforced tubes. Applied Composite Materials 2017; 24(2): 417-448.
[213] Shinde D, Kimbro E, Mohan R, Kelkar A. Mechanical properties of woven fiberglass Composite interleaved with glass nanofibers. Carbon 2013; 2(166.8): 13-5.

Annex 1

Acoustic emission parameters are as following:

Amplitude: maximum amplitude in dB

Energy: energy generated within the material under test in $mV \cdot \mu s$

Duration: time between the first and the last crossing of the threshold in microseconds

Rise time: time between the onset of the hit and maximum amplitude in microseconds

Counts: number of counts that exceed the detection threshold

Counts to peak: number of counts between the onset of the hit and the maximum amplitude

Average frequency: the number of counts of the hit divided by its duration

Reverberation frequency: the ratio between the number of counts of the hit decay and its duration

Initiation frequency: the ratio between the number of counts of the initiation phase and its duration

Frequency centroid: frequency barycenter of the hit

Peak frequency: maximum frequency corresponding to the peak of the Fourier transform

ASL: effective voltage in dB

RMS: effective voltage in volt

Annex 2

Sensitivity curves of acoustic emission sensors:

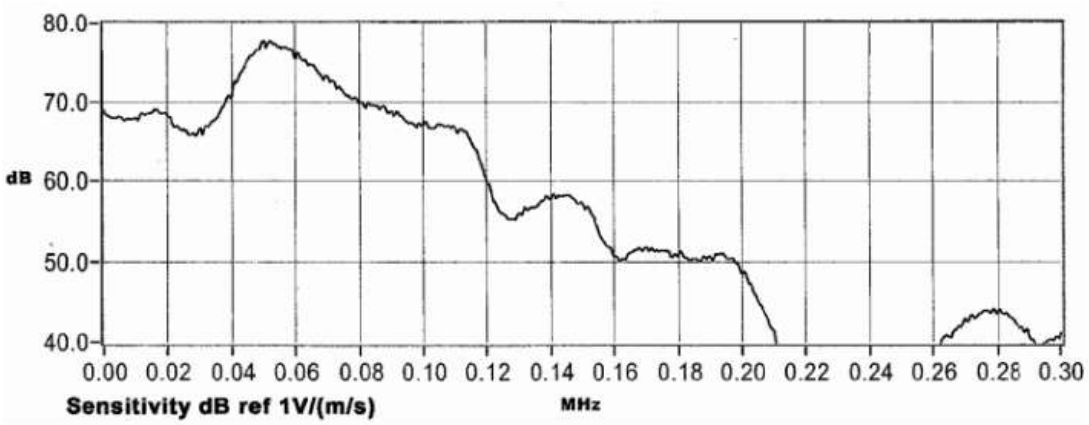

Fig. A. Sensitivity of R6α sensor.

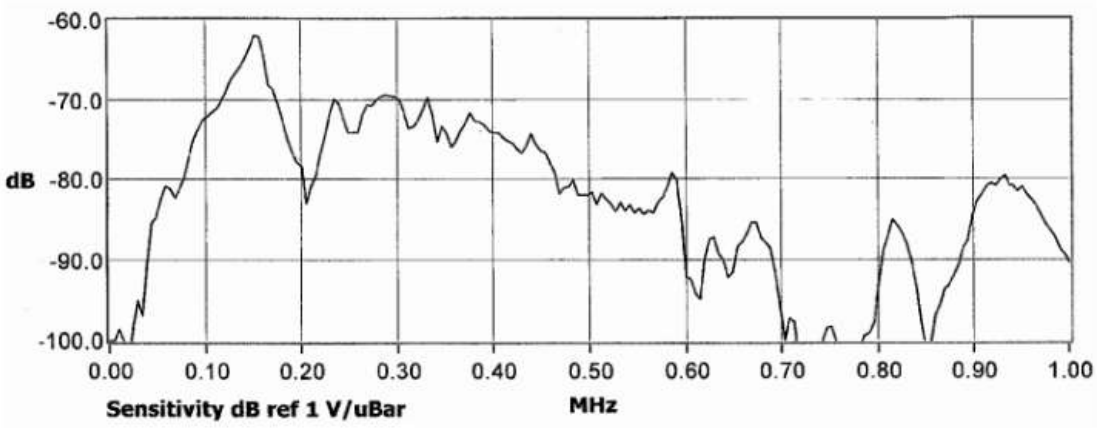

Fig. B. Sensitivity of R15α sensor.

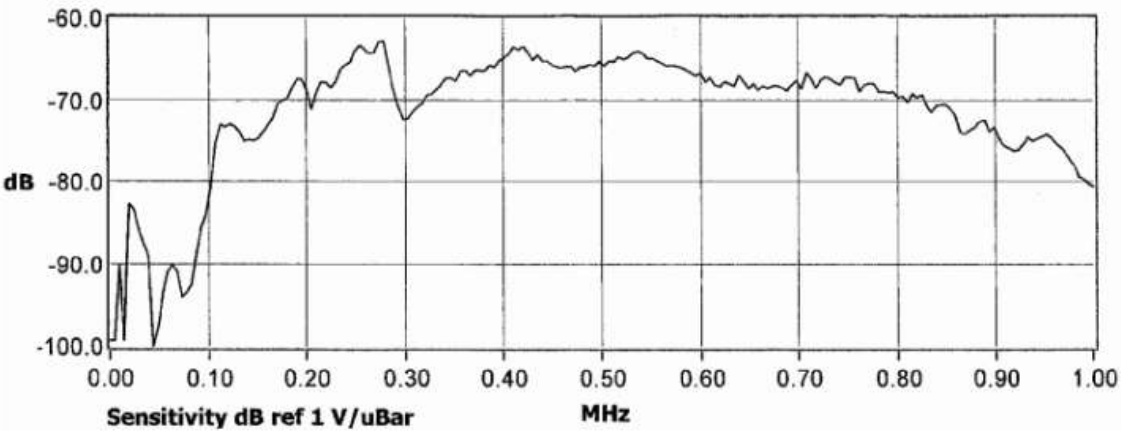

Fig. C. Sensitivity of WD sensor.

Annex 3

Large microscope images of skin/core damage surface of dry and wet GFRP-balsa sandwich:

- **Images of specimen Dry 1:**

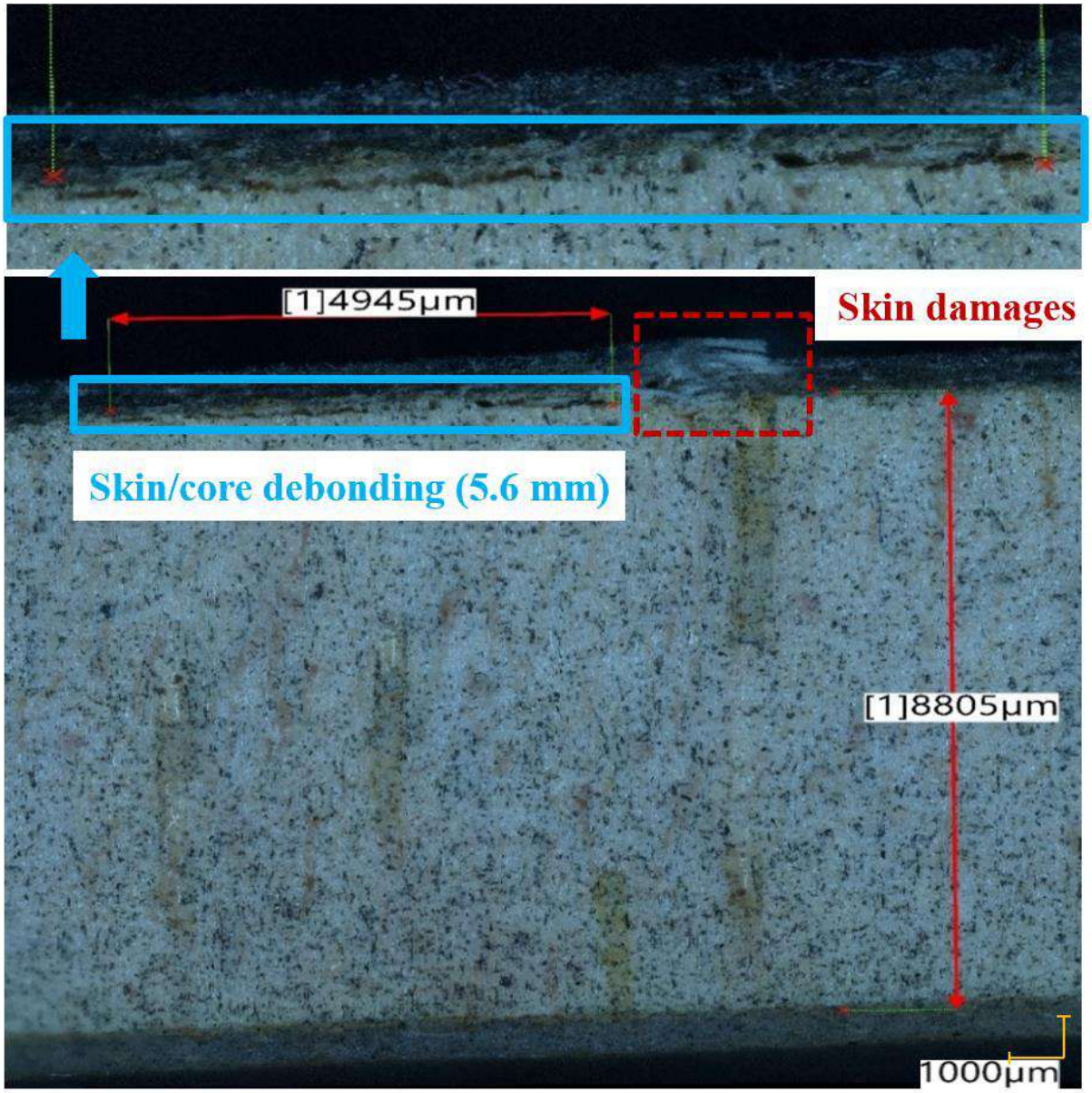

Fig. A. Skin/core debonding crack of Dry 1.

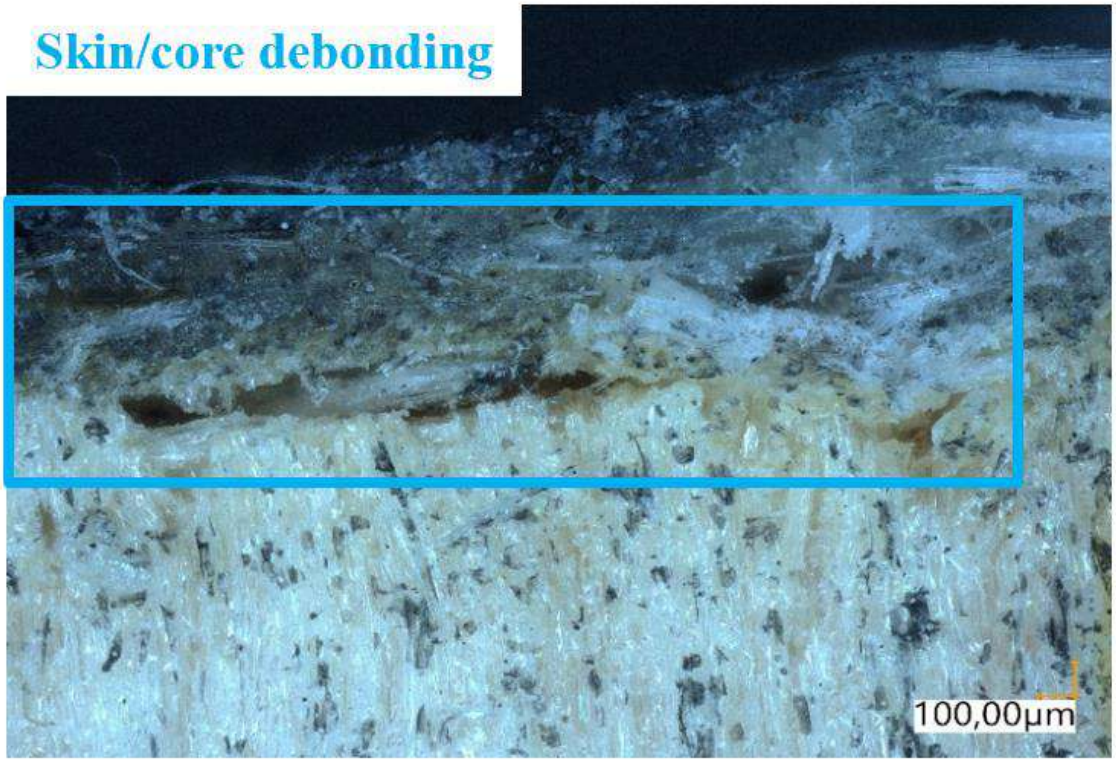

Fig. B. Zoom of skin/core debonding crack of Dry 1.

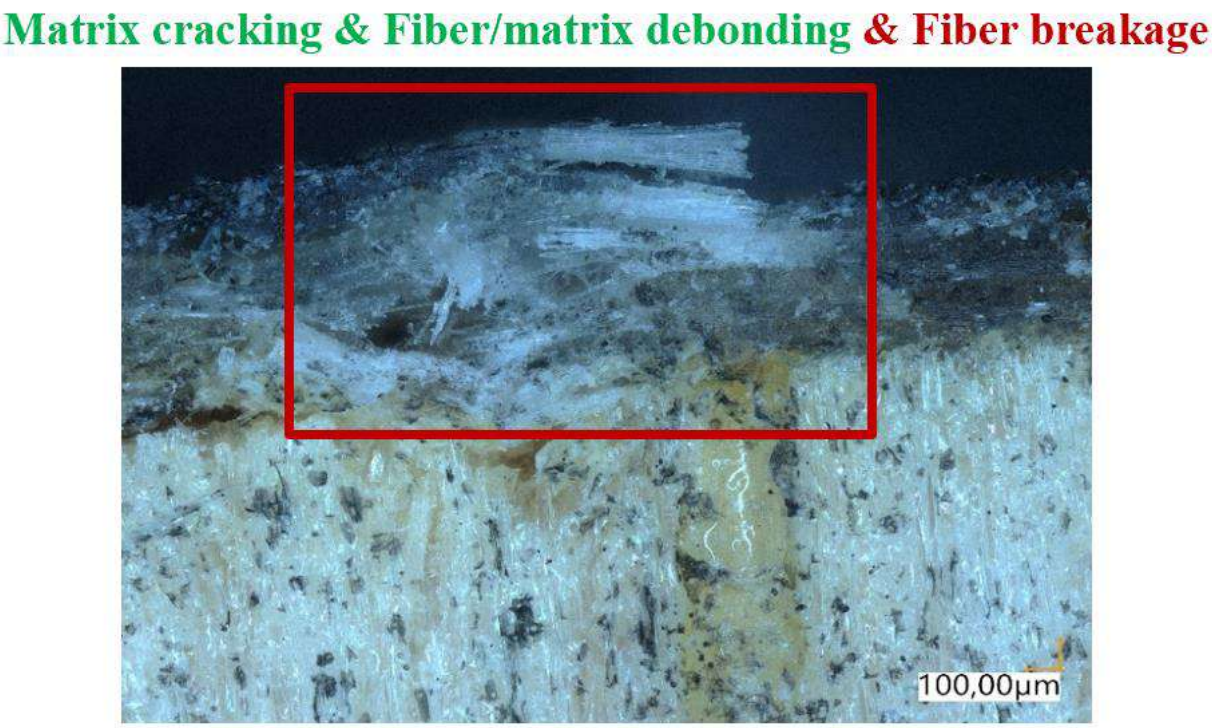

Fig. C. Zoom of skin damages of Dry 1.

- **Images of 50% MC specimen Wet 2:**

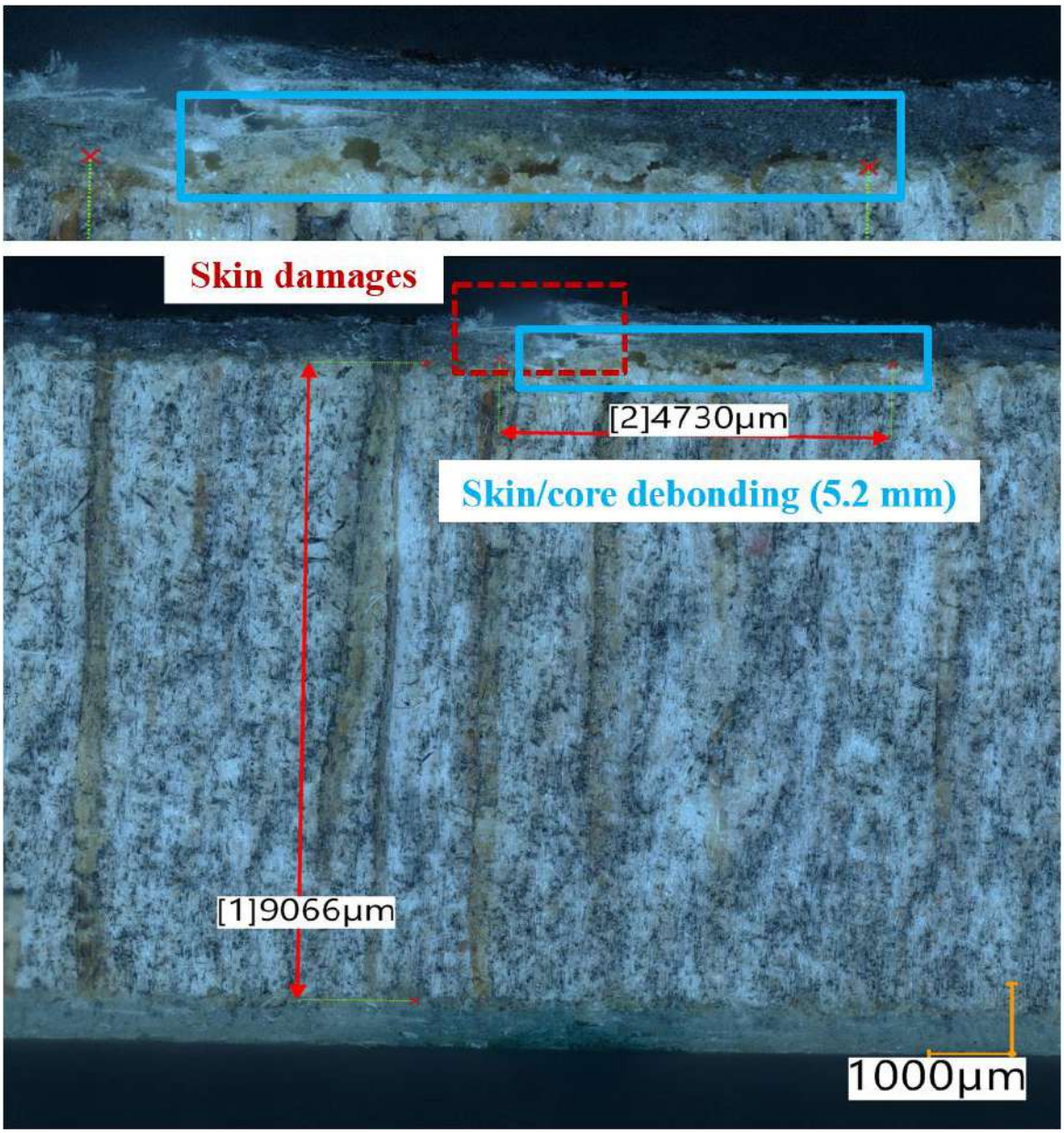

Fig. A. Skin/core debonding crack of 50% MC specimen Wet 2.

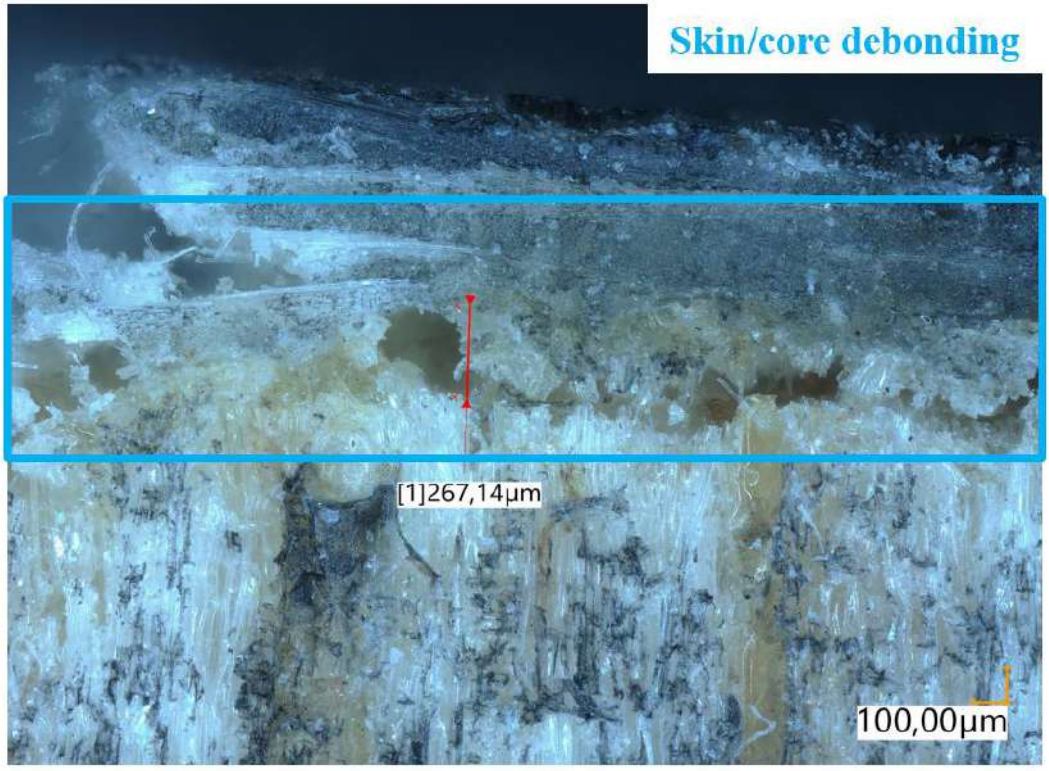

Fig. B. Zoom of skin/core debonding crack of 50% MC specimen Wet 2.

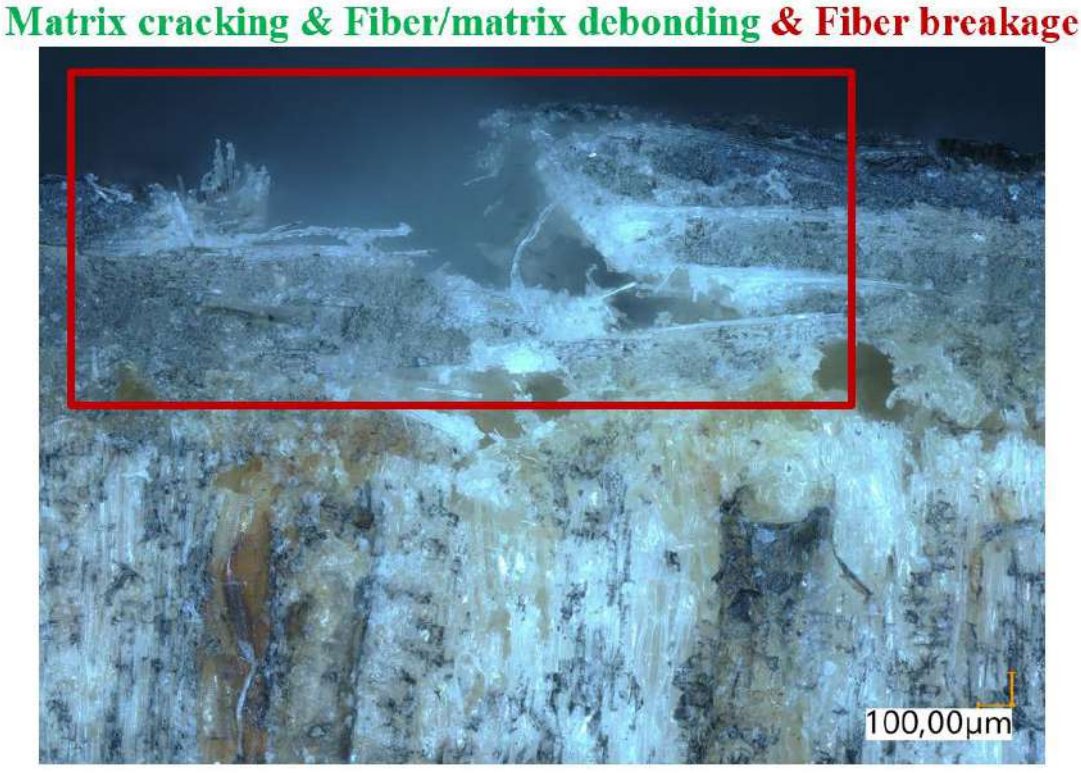

Fig. C. Zoom of skin damages of 50% MC specimen Wet 2.

- **Images of 120% MC specimen Wet 5:**

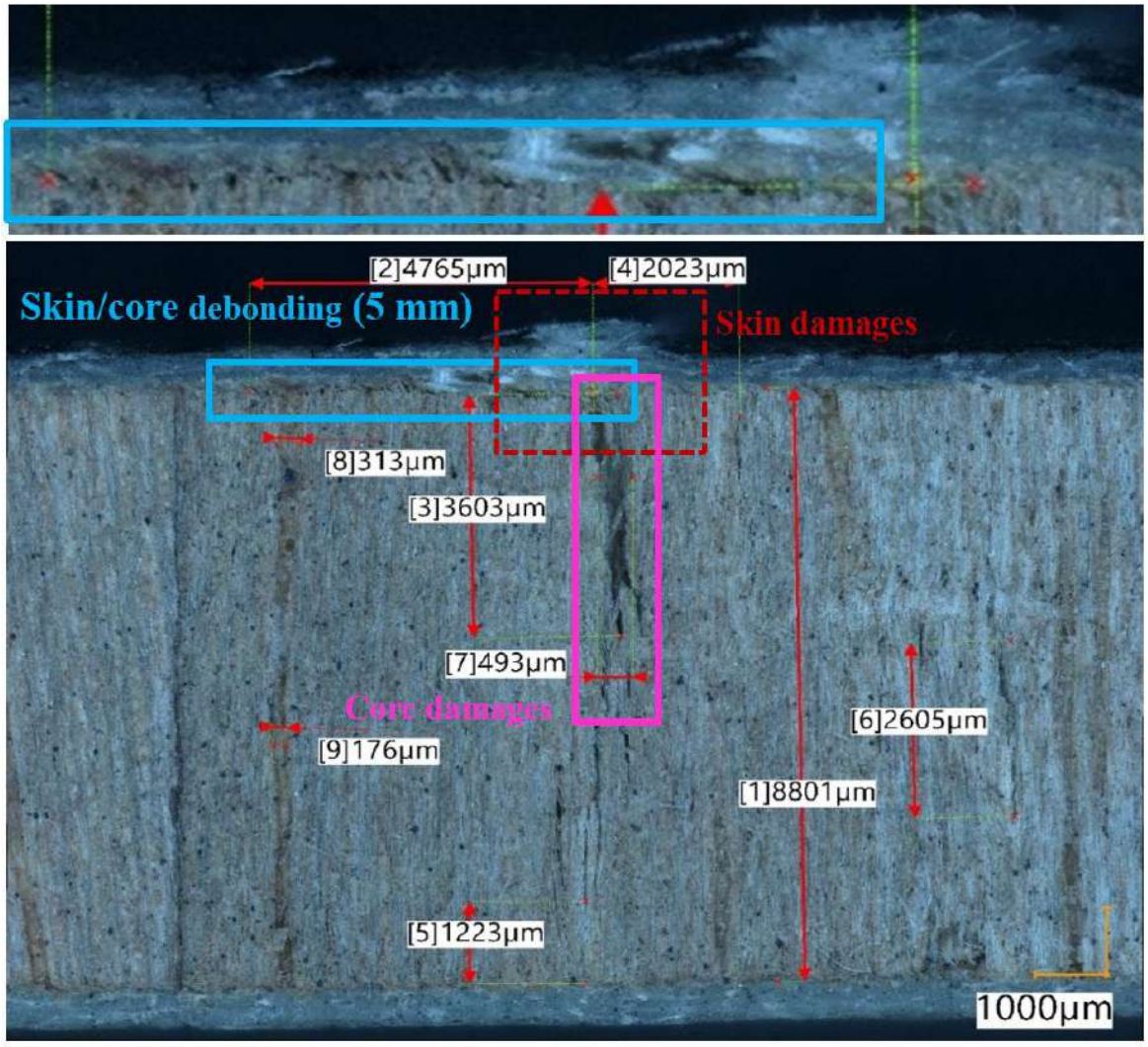

Fig. A. Skin/core debonding crack of 120% MC specimen Wet 5.

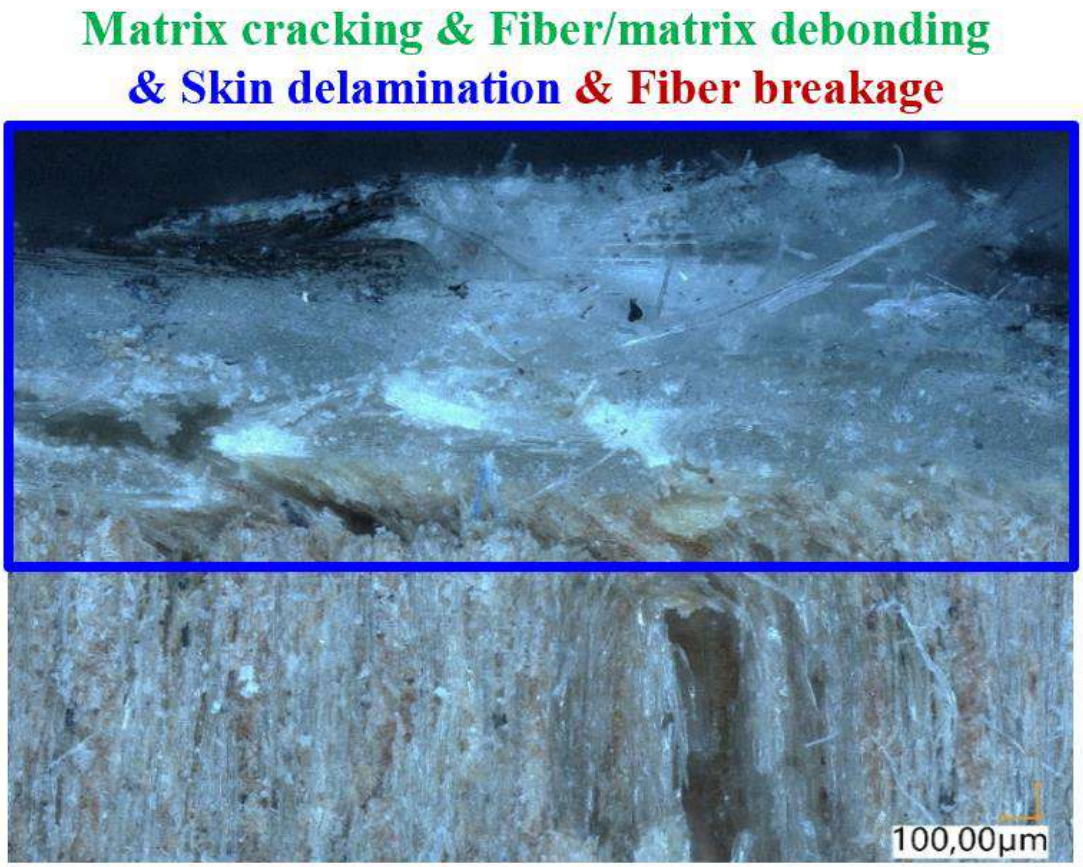

Fig. B. Zoom of skin damages of 120% MC specimen Wet 5.

Relevant Publications

Articles

[1] Wu Y, Perrin M, Pastor M L, Casari P, Gong X. On the determination of acoustic emission wave propagation velocity in composite sandwich structures. Composite Structures, 2021, 259: 113231.

[2] Wu Y, Pastor M L, Perrin M, Casari P, Gong X. A new methodology to predict moisture effects on mechanical behaviors of GFRP-BALSA sandwich by acoustic emission and infrared thermography. Composite Structures, 2022, 287: 115342.

[3] Wu Y, Perrin M, Pastor M L, Casari P, Gong X. A comprehensive acoustic emission analysis approach for characterization of damage mechanisms of GFRP-balsa sandwich under 4-point bending. Composite Structures, 2022, submitted.

Conferences

[1] Wu Y, Perrin M, Pastor M L, Casari P, Gong X. Moisture effects on monitoring GFRP-balsa sandwich structure by acoustic emission [C]. CompTest-2021(10th International Conference on Composites Testing and Model Identification), 18-20 May, 2021, France, online.

[2] Wu Y, Pastor M L, Perrin M, Casari P, Gong X. Caractérisation des mécanismes d'endommagement des structures sandwich GFRP-balsa sous flexion 4 points par couplage d'émission acoustique et de thermographie infrarouge [C]. JNC 22 (22èmes Journées Nationales sur les Composites), 28-30 juin, 2021, France, conference virtuelle.

[3] Wu Y, Perrin M, Pastor M L, Casari P, Gong X. Moisture effects on 4-point bending behavior of GFRP-balsa sandwich by acoustic emission and infrared thermography [C]. 10er Journées Scientifiques du GDR Sciences du Bois, 17-19 Novembre, 2021, Montpellier, France.

[4] Wu Y, Pastor M L, Perrin M, Casari P, Gong X. Moisture effects on monitoring GFRP-balsa sandwich structure by acoustic emission and infrared thermography [C]. ICSS-13 (13th International Conference on Sandwich Structures), 23-26 October, 2022, University of Tennessee, Knoxville, USA.